Development of Early Warning Methods for Electric Power Systems

Jóhannsson, Hjörtur; Nielsen, Arne Hejde; Østergaard, Jacob

Publication date:
2011

Document Version
Publisher's PDF, also known as Version of record

Technical University of Denmark

Hjörtur Jóhannsson

Development of Early Warning Methods for Electric Power Systems

PhD Thesis

DTU Electrical Engineering
Department of Electrical Engineering

Hjörtur Jóhannsson

Development of Early Warning Methods for Electric Power Systems

PhD Thesis

Development of Early Warning Methods for Electric Power Systems

This report was prepared by
Hjörtur Jóhannsson

Supervisors
Arne Hejde Nielsen
Jacob Østergaard

Department of Electrical Engineering
Centre for Electric Technology (CET)
Technical University of Denmark
Elektrovej building 325
DK-2800 Kgs. Lyngby
Denmark

www.elektro.dtu.dk/cet
Tel: (+45) 45 25 35 00
Fax: (+45) 45 88 61 11
E-mail: cet@elektro.dtu.dk

Release date:	June 14, 2011
Category:	1 (public)
Edition:	First
Comments:	This report is a part of the requirements to achieve the PhD degree in Electrical Engineering at the Technical University of Denmark.
Rights:	©Hjörtur Jóhannsson, 2011
ISBN:	978-87-92465-95-5

Abstract

This thesis concerns the development of methods that can provide, in real-time, an early warning for an emerging blackout in electric power systems. The blackout in E-Denmark and S-Sweden on September 23, 2003 is the main motivation for the method development. The blackout was caused by occurrence of two severe system disturbances within a time interval of five minutes. Following the second disturbance where initial oscillations had damped out, a period of approximately $80\,s$ with slowly decaying voltage magnitude was observed, before a system blackout was experienced. It was of interest to develop methods, that could, in such situations, give an early warning for the emerging blackout.

After investigation of data and plots taken from the time of the blackout, it was decided to focus the development on assessment of aperiodic small signal stability. In order to assess the system generators aperiodic small signal stability, expressions for stability boundaries were algebraically derived in the injection impedance plane. A method for detecting aperiodic small signal stability was established, which was based on one of the derived boundaries. The method carries out an element-wise assessment of the system aperiodic small signal stability where each generator is assessed specifically by using the value of its injection impedance and its corresponding system Thevenin impedance.

For the purpose of obtaining distance-to-instability information, the generators operating point were visualized in the injection impedance plane. A mapping of the different operating points into a normalized injection impedance plane was derived, which enabled a visualization of multiple operating points on the same screen. Such visualization provides system operators a new mean of graphically assessing the system conditions in respect of aperiodic small signal stability and enables a quick identification of critical generators.

The assessment method was implemented in an algorithm, that could effectively determine the required information for carrying out the stability assessment. The algorithm received a PMU-snapshot of the system conditions as an input and determined the injection and Thevenin system impedances

for all system generators. A test bench software was written for the purpose of testing the developed algorithm. A large scale test of the assessment method was carried out where a simulation of the blackout in E-Denmark and S-Sweden September 23, 2003 was used as a test case scenario. The simulation results were used to generate a synthetic PMU-snapshots of the system conditions which were used as an input to the assessment algorithm. The test results showed that the loss of aperiodic small signal stability of one machine was detected approximately $54\,s$ before the simulated blackout was experienced.

The developed assessment method was therefore capable of providing, in real-time, an early warning for the occurrence of the emerging simulated blackout almost a minute before it occurred.

Resumé

Denne afhandling omhandler udviklingen af metoder der kan give en tidlig varsel for forekomsten af en omfattende strømafbrydelse i elforsyningen. Strømafbrydelsen på Sjælland og i Sydsverige i 2003 har været en særlig motivation for metodeudviklingen. Strømafbrydelsen var forårsaget af to alvorlige systemforstyrrelser der skete indenfor et tidsinterval på fem minutter. Som følge af den anden forstyrrelse, blev et langsomt spændingsfald observeret i en periode af ca. 80 sekunder før strømafbrydelsen skete. Formålet med projektet var at udvikle en metode, der kunne give en tidlig varsel for forekomsten af en omfattende strømafbrydelse, når systemet befinder sig i sådan en kritisk driftstilstand.

Efter en undersøgelse af måledata fra strømafbrydelsen, blev det besluttet at metodeudviklingen skulle fokuseres på metoder, der kan vurdere aperiodisk små-signal stabilitet i systemet. Til det formål blev et analytisk udtryk for systemets stabilitetsgrænser fundet. En af disse grænser blev herefter anvendt som en basis for en ny metode der kan detektere og overvåge aperiodisk små-signal stabilitet i realtid.

Metoden blev software implementeret via en algoritme der effektivt kunne bestemme den nødvendige information for at udføre en stabilitetsvurdering. Som input får algoritmen et PMU-snapshot af systemets strømme og spændinger, og returnerer en vurdering af systemets aperiodiske små-signal stabilitet.

For at teste metoden, blev en simulering af 2003 strømafbrydelsen på Sjælland og i Sydsverige udført. Resultaterne fra simuleringen blev brugt for at generere syntetisk PMU-data, som blev anvendt som input til algoritmen der skulle testes. Resultaterne fra testen viste, at den første maskine der krydsede den kritiske stabilitetsgrænse, gjorde det ca. 54s før den omfattende strømafbrydelse skete.

Den udviklede overvågningsmetode kunne derfor give en tidlig varsel for forekomsten af den simulerede strømafbrydelse, næsten et minut før dens forekomst.

Acknowledgement

First of all, I would like to thank my supervisors at Arne Hejde Nielsen and Jacob Østergaard, for their consistent support and advice throughout the project.

Energinet.dk are acknowledged for funding the PhD project. I would also like to thank the follow-up group from Energinet.dk, especially Per Lund, Carsten Strunge and Samuel Thomasson for their involvement through follow-up meetings.

I would also like to thank Pacific Northwest National Laboratories (PNNL) for making my research stay there professionally rewarding. Special thanks to Yuri Makarov and Mark Morgan at PNNL.

Finally I would like to thank my family for their support, especially my parents who have always been very supportive and my two children who have also unknowingly supported me in a great way. At last but not least I would like to thank my wife for her endless support, good advices and assistance.

Preface

This thesis was prepared at the Centre for Electric Technology, Department of Electrical Engineering, the Technical University of Denmark in partial fulfillment of the requirements for acquiring the PhD degree in electrical engineering. The research has been conducted from the 1st of April 2007 to the 30th of September 2010.

The project was funded by Energinet.dk and the Technical University of Denmark. The thesis deals the development of stability assessment methods, which can provide an early warning for an emerging blackout in electric power systems.

Hjörtur Jóhannsson

Lyngby, October 2010

Contents

Chapter 1

Introduction

A stable and secure operation of electric power systems and a supply of energy at competitive prices is of fundamental importance for all modern societies. It is one of the cornerstones of sustainable development, providing the foundation for societies' social and economic well-being. The series of blackouts occurring in 2003, demonstrated the modern societies' complete dependence on safe and reliable supply of electricity.

The aftermath of the 2003 blackouts was that investigation teams were established which studied the causes of the blackouts and recommended actions that would minimize the possibility of similar blackouts to occur again. The final reports from the investigations teams include, among others, recommendations for an increased use of synchronized real-time measurements for the purpose monitoring the system state.

In the final report from the Investigation Committee on the blackout in Italy September 28, 2003 (Vandenberghe et al. 2004, p.95), it is recommended that a focus is put on accelerating the ongoing wide-area measurement system (WAMS) installation program for the purpose of providing support for dynamic analysis and monitoring of the UCTE[1] system.

In the final report from the U.S. - Canada Power System Outage Task-Force, it was recommended, among others, that the focus should be increased on research of reliability related tools and technologies, including development of practical real-time applications for wide-area system monitoring using phasor measurements and other synchronized measuring devices (Liscouski & Elliot 2004, p.149).

A real-time application, that uses wide-area system measurements for monitoring system stability boundaries could have been useful in the moments before the blackout in E-Denmark and S-Sweden on September 23, 2003. The blackout was caused by occurrence of two severe system disturbances within a time interval of five minutes. As the initial oscillations following the

[1] Union for the Coordination of Transmission of Electricity

second disturbance damped out, a period of approximately 80 s with slowly decaying voltage magnitude was observed, before a system blackout was experienced.

During this period, it would have been very valuable to have a trustworthy real-time monitoring of the system stability boundaries. Such real-time monitoring of the stability boundaries could have been used for obtaining an early warning for the occurrence of the emerging stability problem, thereby providing an increased time window for applying appropriate countermeasures that prevent the emerging blackout.

1.1 Project Objective

The overall purpose of the project is to develop methods that can provide, in real-time, an early warning for an emerging stability problem. The 2003 blackout in E-Denmark and S-Sweden is a case scenario for motivation of the work. For achieving this overall objective, several goals are defined that together contribute to an early warning method:

- Express system stability boundaries in variables that can easily be obtained from wide-area PMU-observations.
- Derive methods for stability assessment, which are capable of detecting when stability boundaries are crossed and quantify the margin from a given operating point to its critical boundary.
- Visualize the observed system conditions such that the distance of an operating point to its stability boundary is represented, which thereby provides a mean of visual identification of critical elements.
- Develop algorithms that enable real-time usage of the developed assessment method.

1.2 Contributions

The main contributions of the work presented in the thesis are listed below:

- *Assessment of the limitations associated with the use of voltage phase angles for stability assessment:* Analysis of why observations of system phase angles cannot alone be used for accurate assessment of the

power system operating conditions and two examples provided that illustrate the limitations of the use of voltage phase angles alone for stability assessment.

- *Analytical expressions derived for the appearance of critical system boundaries and characteristic lines in the injection impedance plane:* A simple two bus system was considered where the boundaries described by the conditions where $\partial P/\partial V$, $\partial Q/\partial V$, $\partial P/\partial Q$, $\partial V/\partial Q$, $\partial V/\partial P$ and $\partial Q/\partial P$ become zero, were derived in terms of injection impedance. Furthermore, analytical expressions for lines of constant voltage magnitude, constant voltage phase angle, constant active power injection and reactive power injection were derived in the injection impedance plane.

- *A method developed for real-time assessment of aperiodic small signal stability*[2]*:* A method for element-wise assessment of individual generators was developed. The developed method utilizes the derived critical boundaries in the injection impedances for the assessment of the generators aperiodic small signal stability.

- *Mapping of multiple operating points into normalized impedance plane for visualization:* A mapping of an arbitrary generators operating point was determined such way that the stability boundary for the mapped points appears as unit circle in the normalized injection impedance plane. This enables visualization of multiple operating points in the same plane where all points have the same unit circle as their stability boundaries.

- *Development of test-bench software for wide-area stability assessment algorithms:* A C++ software was developed that is used for implementation and test of wide-area stability assessment algorithms. The software automatically generates synthetic PMU-data from PSS/E simulation of a instability case scenario and uses it to test the considered assessment method. The software provides capability of visualizing the system operating points and their distance to the stability boundary of concern.

- *Fast algorithms developed and implementation of the stability assessment method:* A fast algorithm was developed that determines the

[2]Definition of aperiodic small signal stability is detailed in chapter 2

information required for carrying out the assessment from a PMU-snapshot of the system conditions. The algorithm was implemented in the test-bench software and tested on a system containing 488 nodes and 672 branches and 144 generators where the aperiodic small signal stability of all 144 generators was determined in 7.86 *ms*.

- *Large Scale Test of the assessment method:* A test of the assessment method was carried out where a simulation of the blackout in E-Denmark and S-Sweden September 23, 2003 was carried out. The simulation results were used to generate a synthetic PMU-snapshots of the system conditions which were used as an input to the assessment algorithm. The test results showed that the loss of aperiodic small signal stability of one the machines was detected approximately 54 *s* before the system blackout was experienced.

1.3 List of Publication

Journal submissions and prepared manuscripts during the project period:

J1 **H. Jóhannsson**, A.H. Nielsen, J. Østergaard, *Shortcomings of the use of Voltage Phase Angle Observations for Stability Assessment*, International Journal of Electrical Power and Energy, submitted for publication. Manuscript Number: IJEPES-D-10-00151.

J2 **H. Jóhannsson**, A.H. Nielsen, J. Østergaard, *Interpretations of the term Voltage Collapse in Textbooks and Scientific Papers*, European Transactions on Electrical Power, submitted for publication.

J3 **H. Jóhannsson**, A.H. Nielsen, J. Østergaard, *Description Procedure for Voltage Instability Related Blackouts*, European Transactions on Electrical Power, submitted for publication.

J4 **H. Jóhannsson**, A.H. Nielsen, J. Østergaard, *Identification of Critical Transmission Limits in Injection Impedance Plane*, International Journal of Electrical Power and Energy, submitted for publication. Manuscript Number: IJEPES-D-10-00388.

J5 **H. Jóhannsson**, A.H. Nielsen, J. Østergaard, *Method for Real-Time Assessment of Aperiodic Small Signal Rotor Angle Stability*, Manuscript.

J6 **H. Jóhannsson**, A.H. Nielsen, J. Østergaard, *Fast Algorithm for Real-Time Aperiodic Small Signal Stability Assessment,* Manuscript.

Conference Submission:

C1 **H. Jóhannsson**, R. Garcia-Valle, *Real-Time Stability Assessment based on PMUs, IEEE Trondheim PowerTech 2011*, June 19-23, 2011, Trondheim, Norway. Submitted.

The author had a minor contribution in the report listed below:

R1 P. E. Sørensen, M. Togeby, T. Ackermann, D. K. Chandrashekhara, J. P. F. Horstmann, **H. Jóhannson**, A. H. Nielsen, J. Østergaard, and et al. Ecogrid.dk Phase 1 WP4 report: New measures for integration of large scale renewable energy. Technical report, Forskningscenter Risø, 2008.

1.4 Thesis Organization

The topics treated in the papers written during the project period are incorporated into to the thesis and therefore, the papers are not provided in an appendix. The the thesis is categorized into five parts as follows:

- Part I - Background, Theory and State of the Art:
  - Chapter 2: Provides a description of the stability terms used in the thesis and an overview of the anatomy of power system blackouts.
  - Chapter 3: Provides a description of PMUs, their potentials and limitations for stability assessment and a overview over the state of the art for real-time stability assessment methods.
  - Chapter 4: Discussion regarding potential approaches for obtaining real-time assessment of the system stability from wide-area PMU measurements.
- Part II - Development of Real-Time Stability Assessment Methods:
  - Chapter 5: Concerns the analytical derivation of expressions for critical stability boundaries and characteristic lines in the injection impedance plane.

  - Chapter 6: Describes a method for an element-wise assessment of aperiodic small signal stability.
  - Chapter 7: Describes how stability margin can be quantified in meaningful manner and how an informative visualization of multiple operating points in the same screen shot can be obtained by normalizing each of the points in appropriate manner.

- Part III - Algorithms and Implementation:
  - Chapter 8: Describes the development of a test-bench software that can test wide-area stability assessment methods.
  - Chapter 9: Describes algorithm suitable for real-time stability assessment and the implementation of the method into the test-bench software.

- Part IV - Test of Method:
  - Chapter 10: The developed method is tested where a blackout scenario, simulated in PSS/E is used as a test case.

- Part V - Conclusion and Perspective:
  - Chapter 11: Conclusion and perspective on future research.

Part I

Background, Theory and State of the Art

Chapter 2

Blackouts in Electric Power Systems

This chapter provides an overview of basic concepts and definitions related to power system stability as it is used in the following chapters. Furthermore, a general description of how blackouts occur in electric power systems together with a description of an actual example of a system blackout are provided.

2.1 Power System Stability Definitions

In 2004, an IEEE/CIGRE joint task force on stability terms and definitions published a report (Kundur et al. 2004) where the problem of defining and classifying power system stability was addressed. The aim of the report was to define power system stability more precisely than before and provide a systematic basis for stability classification.

The terminology related to power system stability that is used in the following chapters is based on the suggestions from (Kundur et al. 2004). The overall electric power system stability is defined as:

> *Power system stability is the ability of an electric power system, for a given initial operating condition, to regain a state of operating equilibrium after being subjected to a physical disturbance, with most system variables bounded so that practically the entire system remains intact.*

The overall power system stability problem is essentially a single problem, which can be classified into several subcategories. The classification is based on considerations regarding (Kundur et al. 2004):

- The physical nature of the resulting instability as indicated by observed physical system variable that reflect the appearance of the instability.
- The size on the disturbance considered.
- The time span of the devices and processes that have a considerable

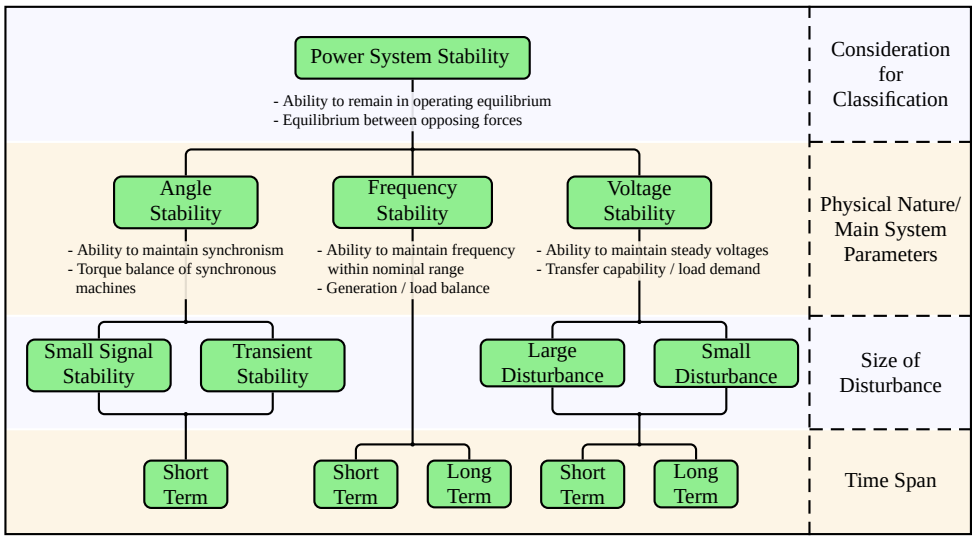

Figure 2.1: Classification of the overall power system stability problem into subcategories (Kundur et al. 2004).

contribution to the resulting instability

An overview of the overall stability problem and its classification into subcategories is provided in figure 2.1.

The overall stability problem is divided into three main categories (Kundur et al. 2004):

Rotor Angle Stability: Refers to the ability of synchronous machines to remain in synchronism after being subjected to a disturbance. Rotor angle stability is further divided into two subcategories; a *small signal* (or *small disturbance*) *rotor angle stability* and *transient* (or *large disturbance*) *rotor angle stability*. The small signal rotor angle stability concerns the stability of the system equilibrium point (or steady state point). Small signal rotor angle instability may appear in two forms: a) as an aperiodic (non-oscillatory) increase of the rotor angle due to lack of synchronizing torque, or b) rotor oscillations of increasing amplitude due to lack of sufficient damping torque. Transient rotor angle stability concerns the ability of system to maintain synchronism when subjected to a severe disturbance. The instability is usually in form of

aperiodic angular separation due to insufficient synchronizing torque, manifesting as first swing instability.

Frequency Stability: Relates to the ability of a power system to maintain steady frequency following a severe system disturbances resulting in a significant imbalance between generation and load.

Voltage Stability: Refers to the ability of a power system to maintain steady voltages at all busses in the system after being subjected to a disturbance from a given initial operating condition. Voltage stability is dependent on the system ability to restore an equilibrium between load demand and supply. Voltage instability may appear in progressive fall or rise of voltages at some busses. In relation to voltage stability, the term *voltage collapse* is commonly used. It is described as the process by which a sequence of events accompanying voltage instability leads to abnormally low voltages in a significant part of the power system or to a blackout.

In addition to the power system stability terminology provided in (Kundur et al. 2004), the phrase *aperiodic small signal stability* will be used in the following chapters to refer to the ability of the system generators to establish sufficient synchronizing torque for a given equilibrium condition. An *aperiodic small signal instability* appears as aperiodic (non-oscillatory) increase of the rotor angle and subsequent loss of synchronism following a very small disturbance (could be a small increase in applied mechanical power to a generator, or small changes in the system loading). In early literature on electric power system stability the term *steady state stability* was used to cover the area of *aperiodic small signal stability* (Crary 1945, Kimbark 1956). The *aperiodic small signal stability* can be considered as an subcategory of the rotor angle small signal stability category shown in figure 2.1.

The above given definition of the term *voltage collapse*, recommended by the joint IEEE/CIGRE task force on stability terms and definitions, is not the only interpretation of the phenomenon that appears in scientific papers. This inconsistency in terminology is addressed next.

2.1.1 Inconsistent Usage of the term Voltage Collapse

The interpretations of the term *voltage collapse* appearing in technical literature and papers dealing with the topic of voltage stability are inconsistent where few different interpretations of *voltage collapse* can be identified. In

the following, three different textbook descriptions of the phenomena will be introduced and afterwards, it is investigated wherefrom the different interpretations originate and it is studied which interpretation of the term *voltage collapse* is most commonly used in papers published in IEEE Transactions on Power System.

Textbook Descriptions of the Voltage Collapse Phenomena

Voltage stability in electric power systems has been a research topic for several decades. The focus on the topic was greatly intensified during the late eighties and is still today a field with high research activities. The research has been successful for identifying mechanisms causing voltage instability, establishing useful terminology related to voltage stability problems and for providing several methods for analyzing voltage stability problems. As the research progressed, several textbooks were written where the topic of voltage stability is covered (Taylor 1994, Cutsem & Vournas 1998, Kundur 1994). In all of the three textbooks, the consistency in the terms used to describe voltage stability problems is in general good. There is though one term, *voltage collapse*, where different interpretations and descriptions of phenomena appear in each book.

In Carson Taylor's book (Power System Voltage Stability,1994) a definition of voltage collapse is provided where it is stated that a system undergoes a *voltage collapse* if, for a given operating state and a given disturbance, the post-disturbance equilibrium voltages are below acceptable limits. Furthermore, it is mentioned in the book that the terms *voltage instability* and *voltage collapse* are used somewhat interchangeably by most engineers. For example, the decline in voltage magnitude due to under-load tap transformer action in a voltage unstable situation is denoted as *voltage collapse* if the resulting voltage levels are below some acceptable limits.

In Prahba Kundur's book (Power System Stability and Control, chapter 14, 1994), it is stated that voltage instability is essentially a local phenomena where its consequences may have a widespread impact. Furthermore it is said that *voltage collapse* is more complex than simple voltage instability. *Voltage collapse* is referred to as the process by which a sequence of events accompanying voltage instability leads to a low voltage profile in a significant part of the power system.

In Van Cutsem's and Costas Vournas's book (Voltage Stability of Electric

Power Systems, 1998), *voltage collapse* is related to a sudden catastrophic transition in voltage. Furthermore it is said that *voltage collapse* may or may not be the final outcome of voltage instability.

The difference between these descriptions is significant, where in (Kundur 1994) the term *voltage collapse* is related to a process that results in system wide low voltage profile while in (Cutsem & Vournas 1998) *voltage collapse* is related to collapse in voltage magnitude over short period of time. The difference between the usage of the term is illustrated graphically in figure 2.2.

Voltage collapse, as defined in (Cutsem & Vournas 1998), is illustrated in figure 2.2.(b). A sudden transition in voltage magnitude, as illustrated in plot can be caused by different phenomena. For example could such behavior be observed on busses connected to large induction motor that suddenly stalls due to insufficient voltage levels at the motor terminals. Another phenomena that could result in observations of sudden transition in voltage magnitude is when two subgroups of generators approach an angular separation of 180°, following a loss of synchronism. In such situation, rapid voltage drop can be observed at busses close to the electrical center between the subgroups of generators.

Figure 2.2.(a) illustrates a potential outcome of a voltage collapse as defined in (Kundur 1994). The plot illustrates system wide voltage profile, where an initially voltage unstable situation at a single bus has resulted in that the automatic control actions of a tap changing transformer gradually caused a decline in the system voltages. This decline in the system voltages resulted in that the neighboring busses became as well voltage unstable resulting in further decline in the system voltage that continued until the tap transformers hit their limits. This process is a simple example of voltage collapse according to the definition in (Kundur 1994) where the final outcome of such process could be a low voltage profile in a significant part of the power system as illustrated on in figure 2.2.(a) or a system blackout.

The Origins of the Different Interpretations

In all of the three above mentioned textbooks covering the topic of voltage stability, extensive references to technical papers are provided as a base for the theory presented. Since the interpretation of the term *voltage collapse* varies between the three books, it was of interest to analyze how the term

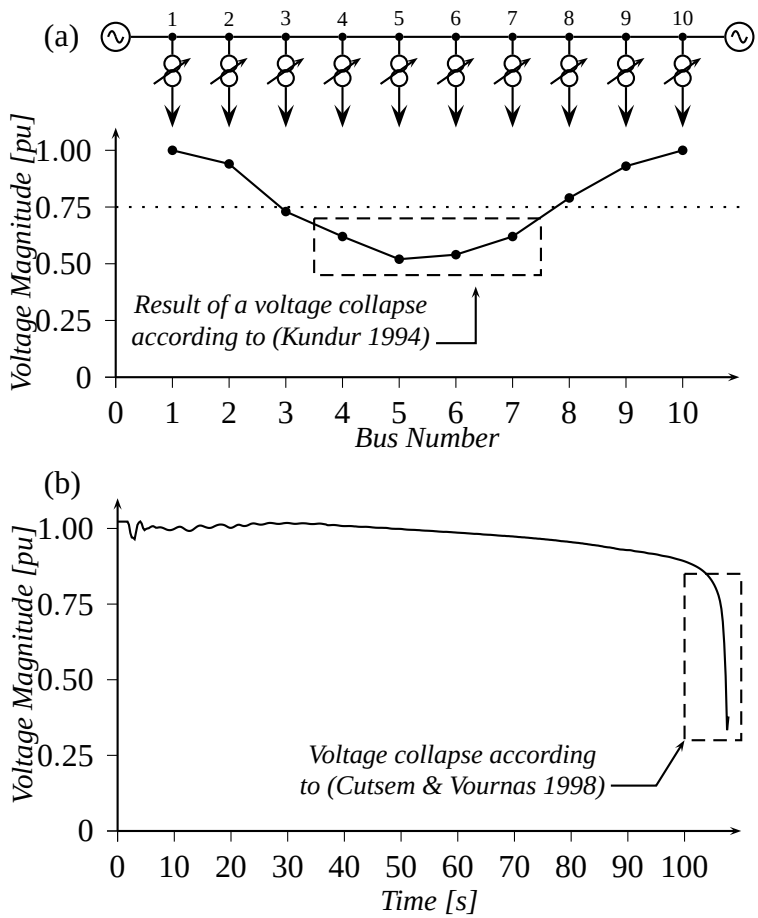

Figure 2.2: Graphical interpretation of the two different definitions of the term *voltage collapse* as used in (Kundur 1994) on one hand and in (Cutsem & Vournas 1998) on the other hand. The definition in (Kundur 1994) relates *voltage collapse* to a process that causes a low voltage profile in the system as illustrated in (a), while the definition in (Cutsem & Vournas 1998) the phenomena related to the sudden transition in the voltage magnitude at a given bus as illustrated in time domain in (b).

voltage collapse had been used in scientific and technical papers written in the past.

In early papers concerning voltage instability in electric power systems, the terms *voltage instability* and *voltage collapse* were used somewhat interchangeably (Nagao 1975, Barbier & Barret 1980). In (Barbier & Barret 1980), the phenomena of *voltage collapse* is explained by considering the decline in voltage due to an unstable control action taken by under-load tap changing transformer when operating below the locus of critical points on the PV-curves. This usage of the term *voltage collapse* resembles the statement in (Taylor 1994) that *voltage instability* and *voltage collapse* are used somewhat interchangeably by most engineers.

In the late 80's and in the early 90's, a great increase in the research activities within the field of voltage stability began. Different approaches for the analysis of voltage stability problems emerged and in this period, bifurcation analysis was introduced as a potentially useful tool for voltage stability analysis. In several papers concerning the usage of bifurcation analysis for voltage stability studies, a different formulation of the term *voltage collapse* began to appear. In these papers, the process of voltage collapse was explained as an event characterized by a slow decline in the system voltage until a sharp collapse in voltage occurs (Brucoli et al. 1985, Dobson & Chiang 1989). These interpretations of the phenomena are similar to the definition from (Cutsem & Vournas 1998).

The usage of the Term Voltage Collapse in Technical Papers

For the purpose of analyzing which interpretation of the term *voltage collapse* is most widely used in papers covering the topic of voltage stability, all *IEEE Transactions on Power Systems* papers in the period 1987-2009, containing the term *voltage collapse* were investigated. It was analyzed which of the three interpretation of the term *voltage collapse* the authors used. The results from the analysis are shown in figure 2.3. The figure contains a histogram where the number of papers published each year containing the term voltage collapse is shown. Each individual paper is represented as a citation inside a square bracket.

The citations are marked in different ways, depending on which interpretation of the term *voltage collapse* is used. Citations that are marked with a squared box denote papers where *voltage collapse* is explained in same way

as in Van Cutsem's and Vournas's book (Cutsem & Vournas 1998). Citations marked with a circle represents papers where the interpretation of *voltage collapse* is similar to the statement from Taylor's book (Taylor 1994) where *voltage collapse* and *voltage instability* are used somewhat interchangeably, while the papers marked with a hexagon explain *voltage collapse* in similar way as done in Kundur's book (Kundur 1994).

The majority of the citations in the histogram are unmarked. An unmarked citation represents a paper where no further explanations are provided for the term *voltage collapse* (assumed as common knowledge), or as in some papers where there is referred to all of the three previously mentioned textbooks for further details concerning the term *voltage collapse*.

The figure reveals the inconsistency in the usage of the term *voltage collapse* in scientific papers over a long period. It is even more interesting to see that in the majority of the papers, it is assumed that the term *voltage collapse* is a common knowledge and no further explanations or references are provided.

As previously mentioned, an IEEE/CIGRE joint task force on stability terms and definitions published a report (Kundur et al. 2004) where the problem of defining and classifying power system stability was addressed. In the report, the term *voltage collapse* is explained as the process by which the sequence of events accompanying voltage instability leads to a blackout or abnormally low voltages in a significant part of the power system. Furthermore, it is stated that a stable operation at low voltage may continue after transformer tap changers reach their boost limit, with intentional and/or unintentional tripping of some load. This definition of the term *voltage collapse* resembles the one given in Kundur's book (Kundur 1994).

In the report, it is mentioned that a rapid fall in voltage magnitude (as mentioned in the definition of *voltage collapse* in (Cutsem & Vournas 1998)) can be associated with rotor angle instability. The voltage can drop rapidly at intermediate points close to the electrical center between two subgroups of generators when the angular separation between the groups is approaching 180 degrees.

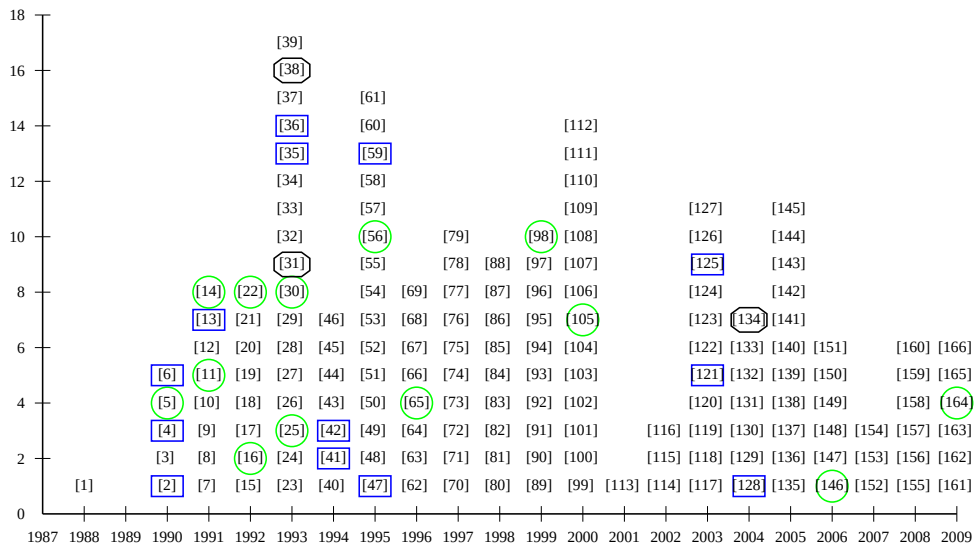

Figure 2.3: Histogram over number of papers per year from the IEEE Transactions on Power Systems where the term *voltage collapse* is used. The citations located inside a box denote papers where the definition of *voltage collapse* from (Cutsem & Vournas 1998) is used, the citations inside a circle represent papers where *voltage collapse* and *voltage instability* are used somewhat interchangeably as mentioned in (Taylor 1994) while the citations inside the hexagons represent a papers where the *voltage collapse* is defined as in (Kundur 1994). Unmarked citations indicate a papers where no further explanations were given for the term voltage collapse or where it was referred to all three books for an explanation of the phenomena. A list over the involved references can be found in appendix B.

2.2 The Anatomy of a Blackout

The U.S - Canada Power System Outage Task-Force, which was established to investigate the causes of the blackout on August 14, 2003 and recommend actions that would minimize the possibility of similar blackouts, published a final report concerning the blackout (Liscouski & Elliot 2004). In the report it was recommended, among others, that the focus should be increased on research of reliability-related tools and technologies, including development of practical real-time applications for wide-area system monitoring using phasor measurements and other synchronized measuring devices (Liscouski & Elliot 2004, p.149).

When new solutions are to be developed that aim at avoiding large scale blackouts to occur, it is important to understand causes and involved mechanisms in the process leading to a blackout. Figure 2.4 is derived from (Pourbeik et al. 2006, Voropai & Efimov 2008) and illustrates a general sequence of events that can lead to a blackout. It is common that the operating conditions are normal and in compliance with system operating policies prior to the ensuing events that lead to a blackout. Major system blackouts are most of the time initiated by a single severe disturbance (loss of generator or a tripping of a critical line) or even a multiple related event such a fault and a subsequent relay misoperation. Following the initiating event, a proper automatic or operator remedial control actions could ensure a stable operation of the system. If proper operational planning criteria are followed, most systems are designed in such way that the system stability is maintained for such single outages. The system might, however, enter an emergency state if the severity of the disturbance is great, particularly during peak load hours. The normal operating state can be restored by applying a system readjustment, such as generation shifting and increase of spinning power reserve. The time frame for such system readjustment is usually in tens of minutes.

If proper automatic control actions or operator intervention are not taken following a severe disturbance, the system may enter a state of severe emergency where it can be exposed to further failures and cascading outages. The system can also enter this state if a second severe disturbance occurs when remedial actions have ensured stable operation following the initial disturbance and before the system readjustment has been carried out. The blackout in Sweden and Denmark on September 23, 2003 is an example

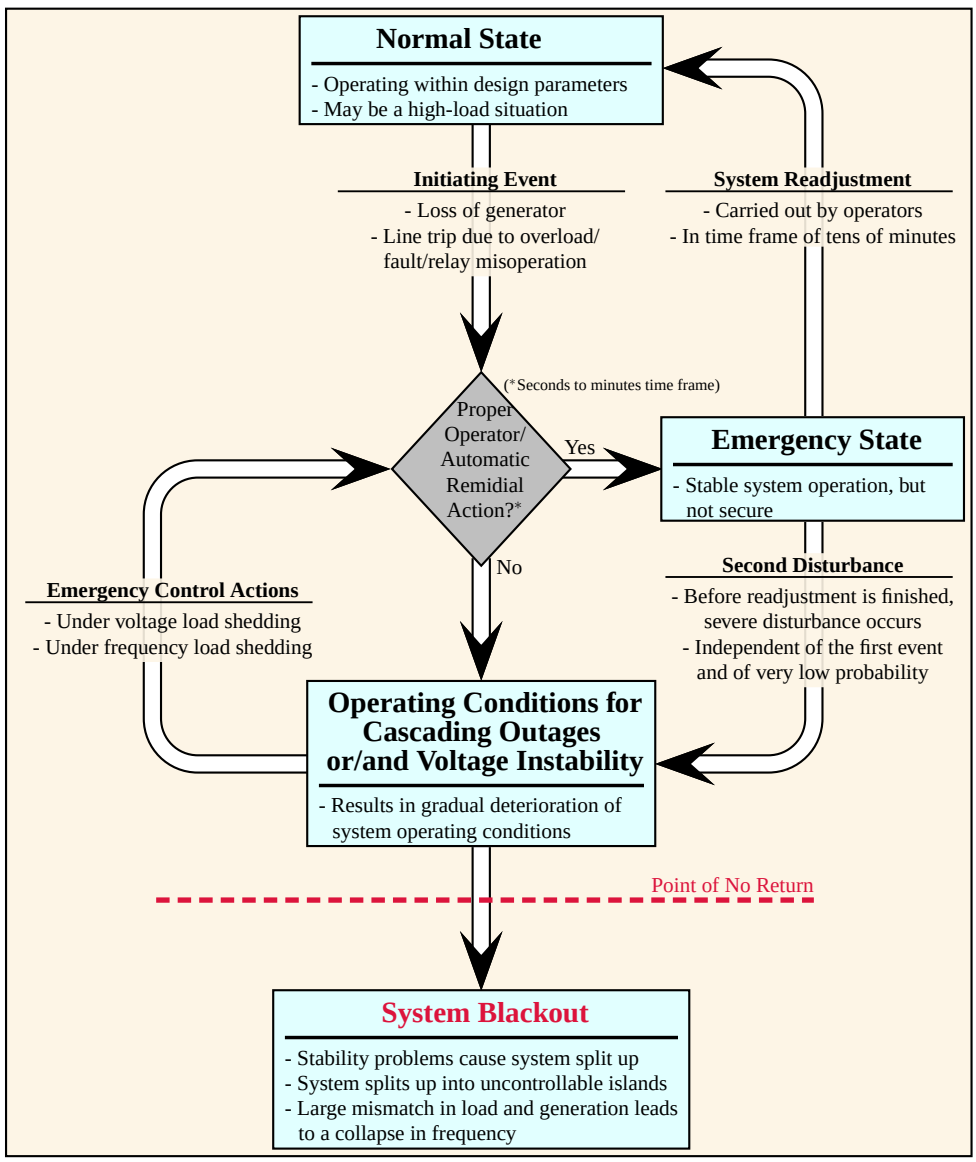

Figure 2.4: General sequence of events leading to a blackout. The diagram is derived from (Pourbeik et al. 2006) and (Voropai & Efimov 2008).

of such blackout scenario, where a second severe disturbance occurred approximately five minutes after the initiating disturbance and where the two disturbances were independent of each other.

When the system is in the state of a severe emergency, a system blackout can ensue due to many different instability mechanisms. For the most simple cases, the initial disturbance causes redistribution of power flow resulting in increased loading on other lines. The actions of ULTC-transformer, thermostats and other load regulation devices tend to gradually restore load which causes further loading and eventually overloading of critical transmission lines. This can lead to a process of cascading line outages, which at some point causes the system to be prone to dynamic performance issues. The increase in the impedance between the load and generation, as transmission lines trip, can lead to a number of stability problems (Pourbeik et al. 2006):

- *Transient Rotor Angle instability:* The initial large disturbance (e.g., transmission system fault) will lead to deviations in generator rotor angles. If this is then followed by inadequate electrical coupling between groups of generators (due to the loss of transmission lines), it may lead to a lack of synchronizing power and thus an inability for generators in different regions of the system to keep in synchronism with each other. This phenomenon has a time frame of few seconds.

- *Oscillatory Small Signal Instability:* Due to the weakening of the transmission system associated with high power transfer levels can lead to uncontrolled growing electromechanical oscillations between groups of generators. The growing oscillations in power continue until line protection reacts causing further partitioning of the system. The phenomenon may have a time frame from several seconds to tens of seconds.

The above unstable phenomena can lead to partitioning of the system into smaller islands with a large imbalance between load and generation. Eventually, a point of no return is reached when a rapid chain reaction of load and generation tripping leads to the system blackout.

When the system is in the state of severe emergency, voltage instability can as well be the driving mechanism in the evolution of a system blackout. Voltage instability has been considered to be the main mechanism driving

the evolution of many actual system blackouts where for example in (Taylor 1994) a list of 17 voltage instability related blackouts in the years 1965-1987 is provided. Voltage stability is still today a research topic of high focus. A detailed description of how a blackout can unfold from the point when conditions for voltage instability occurs, is provided in next section.

2.2.1 From Voltage Instability to System Blackout

For the purpose of visualizing some of the interrelationships between events that cause a blackout to unfold from a initially voltage unstable operating condition, figure 2.5 contains a state diagram that outlines some of the involved mechanisms.

Conditions for voltage instability occur when the point of maximum deliverable power to a given system node have been reached and such conditions are represented as initial state of operation in the top left corner of the state diagram in figure 2.5. During such conditions, the occurrence of voltage instability is dependent on, among others, the longer term voltage dependency of the system load and the voltage control equipment at the node of concern. A tap action of a ULTC-transformer connected to a voltage unstable node, results in further deterioration of the system operating conditions where the voltage on the load side is reduced while the supplied current is increased. This results in lowered system voltages, increased line currents and hence an increased reactive power demand which is met by increased reactive power output from the system generators. The ULTC-transformer will continue its attempts to raise the voltage on the low-voltage side which results in further deterioration of the system conditions with each change in tap-position. The lowered system voltages gradually lead to neighboring busses becoming voltage unstable as well, which escalates the deterioration further.

The gradual increase in generator reactive power output, due to reduced system voltages, results in that overexcitation current limiters (OXLs) become activated as the generators begin to hit their reactive power capability limits one by one. When a generator's OXL is activated, it is no longer capable of maintaining a constant voltage at its terminal and its share of reactive power loading is transferred to the other generators which can lead to a cascading overloading of the machines.

The increase in line currents due to the gradually deteriorating operating contrition introduces as well the risk of cascading line tripping. A line that

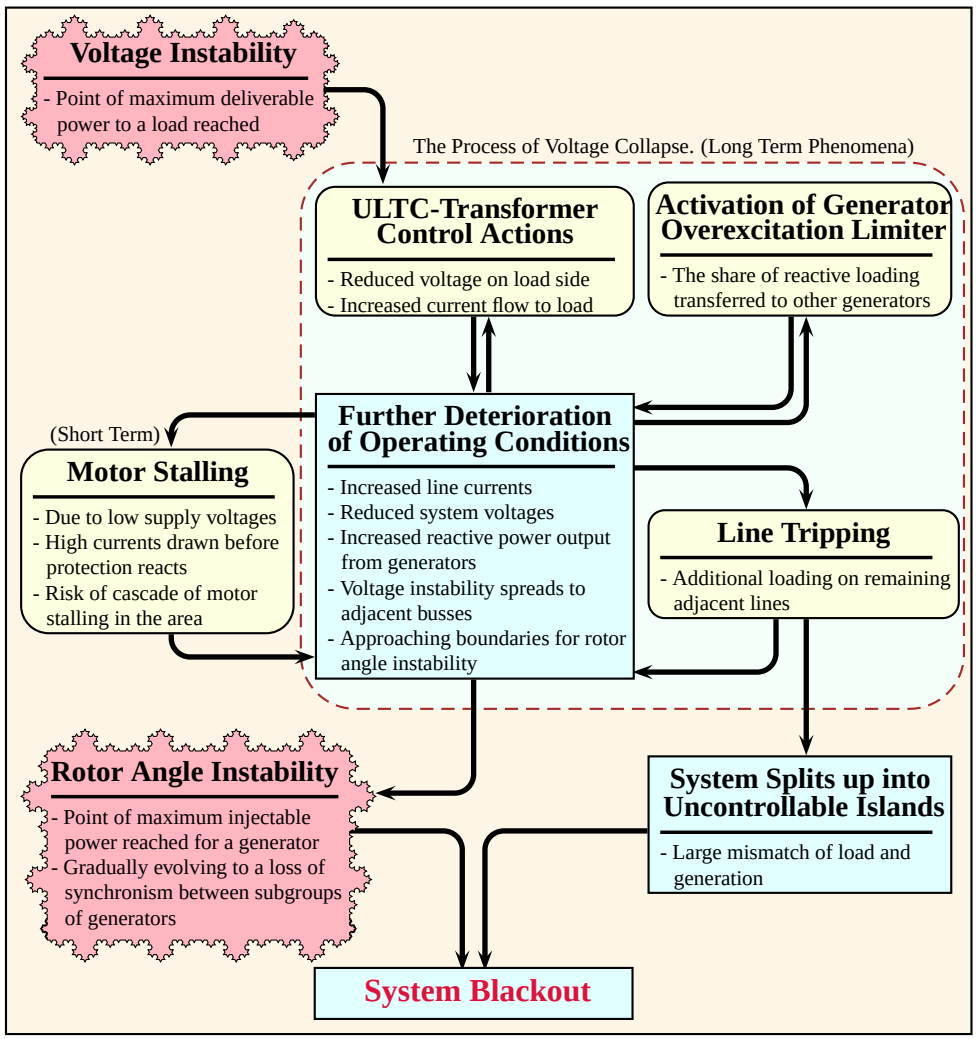

Figure 2.5: State diagram illustrating how the occurrence of voltage instability can evolve into a system blackout. Various mechanisms (ULTC-transformer control actions, line tripping or activation of OXLs) cause gradual deterioration of the system conditions. In the figure, the deterioration continues until a) the point of maximum injectable power from a given generator is reached resulting in a loss of synchronism of the generator, which can gradually evolve into a loss of synchronism between subgroups of generators and a subsequent blackout, or until b) when trip of a critical line results in partitioning of the system into uncontrollable islands with large imbalance between load and generation resulting in blackout.

trips results in additional loading of adjacent lines that might gradually lead to a cascade of line outages.

The gradual deterioration of the system condition due to above mentioned mechanism is an example of a voltage collapse process. It is a long term process where the system deterioration can gradually continue for several minutes. As the voltage collapse process continues, it is possible that induction motors begin to stall at voltage unstable busses due to low supply voltage, resulting in high current to be drawn resulting in further deterioration. If the motor protection does not react quickly enough, this could lead to cascade of motor stallings in the area.

The voltage collapse process might stop when transformer tap changers reach their boost limit, where stable operation continues after intentional or unintentional tripping of some load. On the other hand, the system deterioration due to the voltage collapse might reach a point, before the transformer tap changers reach their limit, where a system blackout unavoidable. This could be due to that the cascading outages have resulted in the formation of an uncontrollable island where a large mismatch between the island generation and load results in a blackout. Another possibility is that the gradual system deterioration have resulted in operating condition where a loss of synchronous operation between subgroup of generators occurs followed by system separation and a blackout.

Voltage instability is associated with the operating conditions where the maximum deliverable power (in steady state) to a given system node has been reached while the point of maximum injectable power into a system node (in steady state) is on the other hand related to aperiodic small signal stability of the power injecting machine. The limits for maximum injectable power into a given node are dependent on both the strength of the grid and the system loading. The gradual deterioration of the system condition due to the voltage collapse process, lead to a reduction of maximum amount of power that can be injected into a given system node and eventually can lead to conditions for the loss of aperiodic small signal stability. The resulting instability can be observed as initially slowly growing angular shift between groups of generators. As the two regions separate in voltage phase angle, the voltage in between the two regions will be reduced and potentially leading to transmission line protective relays tripping lines and possible separating the two regions two regions resulting in a blackout.

2.3 The Blackout in Sweden and Denmark September 23, 2003

At noon September 23rd 2003, a sequence of disturbances occurred that eventually caused a blackout of the eastern part of Denmark and the southern part of Sweden. The blackout affected approximately 2.4 million persons in E-Denmark and approximately 1.6 million persons in S-Sweden. The outage resulted in that $18GWh$ of energy were not delivered to the customers.

In the following, a description of the events that caused the blackout and a time line of events is established. The information provided in the following is mainly gathered from two official reports concerning the blackout, one in Danish (Elkraft System 2003) and the other in Swedish (Svenska Kraftnät 2003*a*).

2.3.1 The Swedish and the Danish Power System (2003)

Figure 2.6 shows the $400kV$ transmission system in Sweden and E-Denmark along with the major thermal and hydro power plants in the system.

The Swedish transmission system is characterized by a strong transmission grid between the northern part and the central and southern part of Sweden, which enables utilization of the large amount of hydro power resources in the northern part of the country. The hydro energy resources in Sweden are mainly located in the northern part of Sweden, while the consumptions areas are mainly located in the central and the southern part of Sweden. When the construction of nuclear plants was being planned it was chosen to locate the plants near the large consumptions areas for two reasons; a short transmission distances to consumption areas and an easy access to cooling water.

In E-Denmark (Zealand) the distance between the main power plants and the main consumption areas is short. The generation consists of large coal-fired units (up to $650MW$), combined heat and power plants and a significant amount of wind power. The Swedish grid and the E-Denmark grid are connected through a pair of $400kV$ cables and another pair of $132kV$ cables. The total capacity of the connection between Sweden and Zealand is $1900MW$.

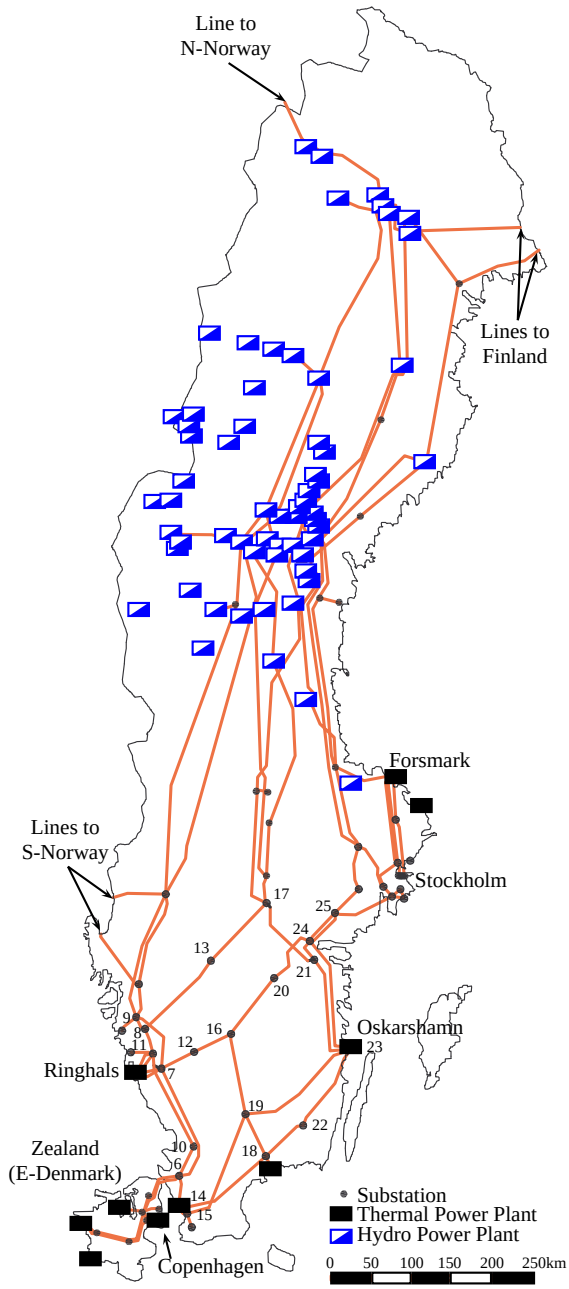

Figure 2.6: The 400*kV* system in Sweden and Zealand (E-Denmark). The system is characterized by a strong connection between the hydro-generation in northern part of Sweden and the consumption areas in central and S-Sweden. The numbered substations in the figure correspond to the bus numbers from figure 2.7.

2.3.2 Pre-fault Conditions

Prior to the blackout, few production units and transmissions lines were not in operation due to maintenance. In E-Denmark, the DC-connection to Germany (Kontek) was out of order due to a planned maintenance, few 132kV lines and one 400kV were disconnected and three thermal plant units were not in operation. In the southern part of Sweden, both of the DC-connections to the continent were out of order due to planned maintenance, two 400kV lines were disconnected due to maintenance and revision, and three power plant blocks were not operating due to an extended maintenance. Based on these conditions, the operation conditions were considered to be stable and well within the constraint laid out in operational planning and grid security assessment (Svenska Kraftnät 2003*b*).

In figure 2.6, the pre-fault condition in S-Sweden and E-Denmark are shown. The figure shows the 400kV transmission system and which major generating units were in operation. Prior to the first disturbance, the production from power plants in E-Denmark was approximately 1.800MW and production from wind turbines was approximately 450MW. This production covered a consumption of 1.850MW in E-Denmark and a 400MW export to Sweden. The available reserves in E-Denmark were 775MW which was more than sufficient to cope with the loss of any of the operating production units in E-Denmark (Elkraft System 2003).

The Swedish power system was moderately loaded prior to the first disturbance with a total consumption in Sweden of approximately 15.000MW which is almost half of the maximum yearly consumption (Svenska Kraftnät 2003*a*). The consumption in the southern part of Sweden was approximately 3.000MW (Elkraft System 2003).

2.3.3 Involved Events/Disturbances

First Event: Oskarshamn

The initiating event, which played a role for the evolution of the blackout was the loss of a 1200MW nuclear unit at the Oskarshamn nuclear plant (bus 23 in figure 2.7). Internal valve problem in the feedwater circuits of the power plant made it necessary to manually lower the production from 1.176MW to 800MW in less than 10s. When the attempts to solve the valve problem

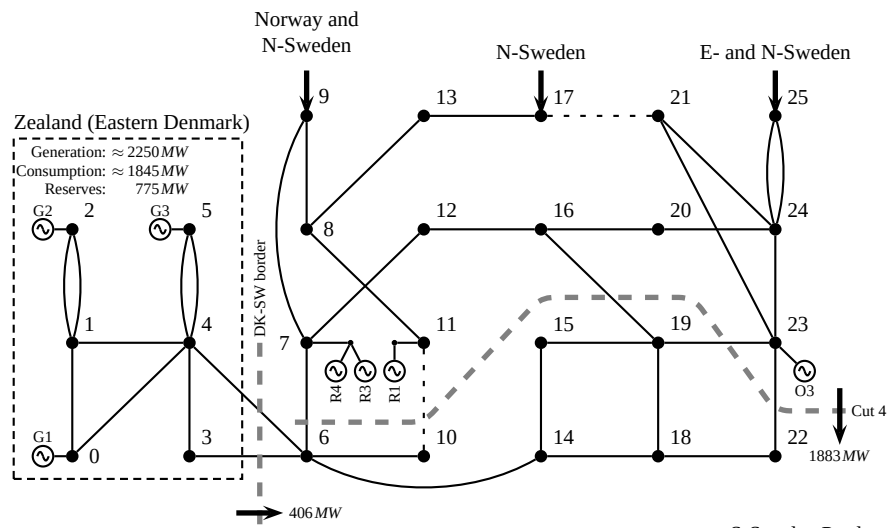

Bus #	Name
0	Ishøj
1	Bjærskov
2	Asnæs
3	Gørløse
4	Hove
5	Kyndby
6	Söderåsen
7	Horred
8	Stenkullen

Bus #	Name
9	Kilanda
10	Breared
11	Strömma
12	Uddebo
13	Timmersdala
14	Barsebäck
15	Sege
16	Tenhult
17	Hallsberg

Bus #	Name
18	Hjemsjö
19	Alvesta
20	Kolstad
21	Kimstad
22	Nybro
23	Oskarshamn
24	Glan
25	Hedenlunda

S-Sweden Prod.

Unit	Production
R1	845 MW
R3	884 MW
R4	877 MW
O1	1176 MW

Figure 2.7: The pre-fault operating conditions in the the 400*kV* Network in E-Denmark and S-Sweden. The Generators in Zealand represent an aggregation of several generators in corresponding area, while the generators in Swedish part represent the individual generating units that were operating prior to the blackout.

failed, the reactor scrammed to a full shut-down and stopped after another 10s.

The loss of the production unit at Oskarshamn resulted in frequency dip to $49.66Hz$ whereafter the frequency stabilized in the range $48.80 - 48.85Hz$. The drop in frequency caused an automatic activation of the hydro power reserves in Norway, northern Sweden and Finland along with emergency reserves from Jutland (W-Denmark). The disturbance resulted in that the voltage dropped approximately by $5kV$ in the southern part of Sweden but remained within the $405 - 409kV$ level which is by no means critical. Following the activation of the reserves in the northern part of Sweden and in the neighboring countries, the frequency was slightly below the normal operating limit of 49,90Hz and therefore, actions were initiated to raise the frequency.

The fault at Oskarshamn caused a redistribution of the power flow in the south-eastern part of Sweden. This redistribution caused more power flowing in the western part of Sweden to supply the demand in south (more flow through bus 25 in figure 2.7). The transmission voltage level were though still within the predetermined security constrains. A loss of a single unit is regarded as a standard contingency and active and reactive power reserves shall be able to cope with this kind of disturbance without any subsequent supply interruptions.

Second Event: Horred

Only five minutes after the loss of the Oskarshamn unit, a severe double busbar fault occurred in a $400kV$ substation in Horred on the western coast of Sweden (bus 7 in figure 2.7). The fault resulted in the tripping of four 400kV lines, which again resulted in isolation of two $900MW$ nuclear units at Ringhals from the system and a subsequent shut down of the units. Figure 2.8 shows the situation in the southern part of Sweden after the fault in Horred. Two of the four disconnected lines made an important connection from central Sweden to S-Sweden (lines 7-9, and 7-12 in figure 2.8). The loss of the two Ringshals units resulted in practically no power being produced in the southern part of Sweden. Additionally, one of the DC-connections from Jutland (Konti-Skan 1) was lost following the disturbance, resulting in a loss of 250MW import.

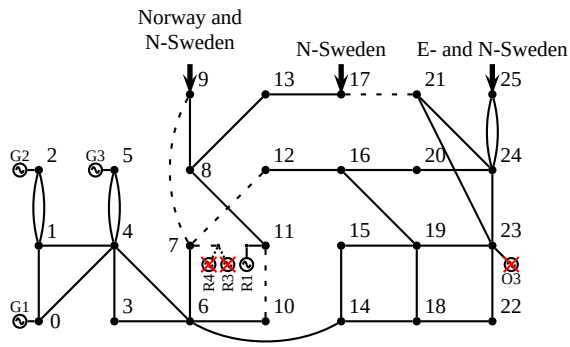

Figure 2.8: The system condition after the double busbar fault in Horred (bus 7). As a consequence, practically no local production was available in the southern part of Sweden (busses 6,7,10,14-16,18-24). The power was either supplied from Denmark (through bus 6) or from the eastern and northern part of Sweden (through bus 25).

From figure 2.8, it can be seen that the only operating nuclear unit in the area (Ringhals block 1) had no longer a connection to the South along the western coast of Sweden. The power supply of the southern part of Sweden had to come from either E-Denmark through Söderåsen (through bus 6) or from north, through the Hedenlunda substation (through bus 25) in the eastern part of Sweden. The disturbance resulted in a very high power transfer from mid to southern Sweden on the remaining 400kV lines in the SE-Sweden.

In the following seconds after the fault in Horred, powerful electromechanical oscillations caused a large voltage drop in the southern part of Sweden. At Simpervarp (substation at Oskarshamn), the voltage fell to approximately 300kV and at Söderåsen to approximately 320kV whereafter the voltage level got stabilized in the range of 360kV -370kV in the area from Söderåsen through Sege in south to Hall and Åker (in north of bus 25 in figure 2.7).

Approximately 10s after the fault in Horred, the voltage in the area began to sink slowly over a period of 80s until a level below 320kV was reached in the area from Sege in south to Hall and Åker in North. The voltage level was lowest in Simpevarp.

The explanations provided in (Svenska Kraftnät 2003*a*, p.14) for the slowly decreasing voltage is related to the voltage dependency of the load. Initially, the load decreased when the voltage decreased on all levels level in the net. Gradually the voltage levels at the consumer side got adjusted by the use of

feeder transformer tap changers in the net, which resulted in an increase in the load and thereby an increase of the power flowing into the area.

Third Event: Disconnection of 400*kV* **lines**

The decreasing transmission system voltage magnitudes and strongly increased power flow from north to south resulted in that the distance relays on the lines between central and south Sweden considered the situation as a distant short circuit, leading to cascading tripping of 400*kV* lines resulting in separation of southern part of Sweden from the rest of Sweden.

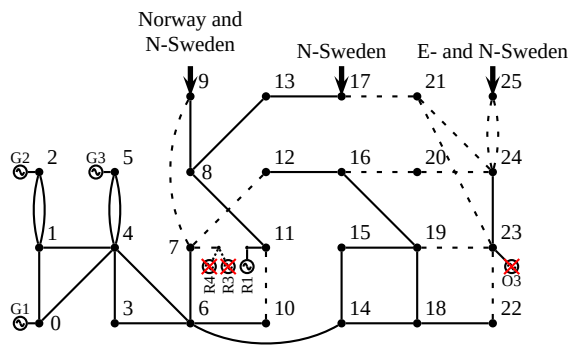

Figure 2.9: The system condition after the disconnection of the 400kV lines in the eastern part of Sweden. After the disconnection of the lines the southern part of Sweden (busses 6,7,10,12,14,15,16,18,19 and 22) was supplied from Denmark (busses 0-5).

Figure 2.9 shows the situation after the disconnection of the lines. The lines between E-Denmark and Sweden remained connected resulting in that S-Sweden was supplied from Denmark. Consequently, the system experienced a blackout of both E-Denmark and S-Sweden.

2.3.4 Time line of Events

As a summary, the involved events and disturbances that played a role in the process causing the blackout are listed on the time line of events in figure 2.10. The time line is derived from data presented in the two official reports covering the blackout incident (Elkraft System 2003, Svenska Kraftnät 2003*a*).

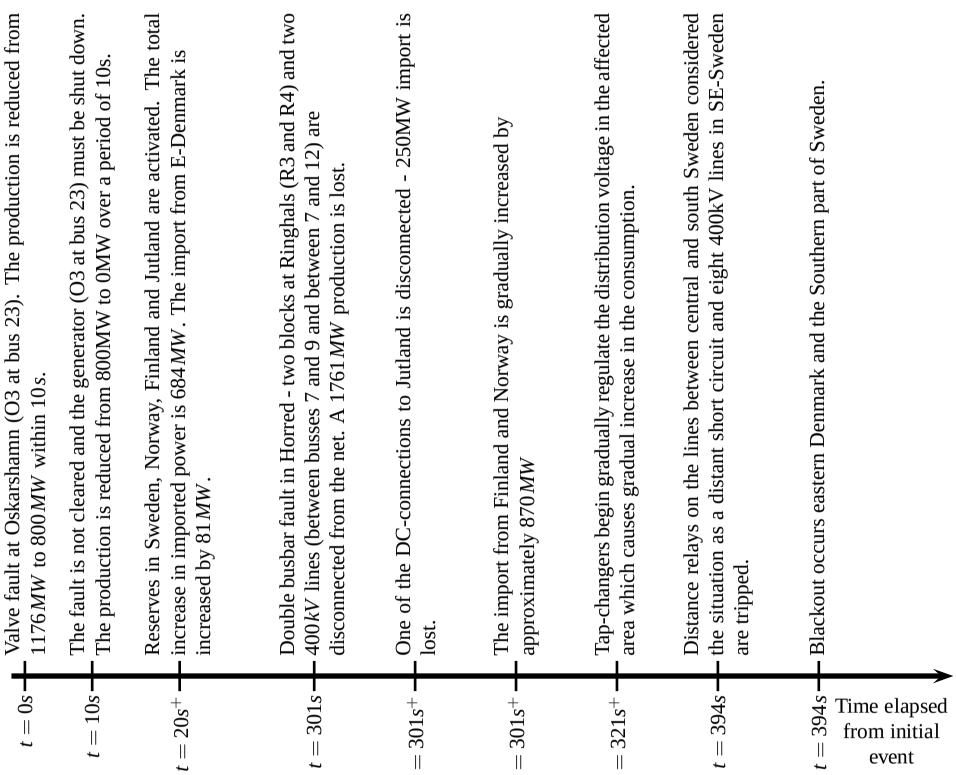

Figure 2.10: The time line of events that played a role for the occurrence of the blackout in Sweden and Denmark on September 23, 2003.

Chapter 3

Phasor Measurement Units and Methods for Real-Time Stability Assessment

In 1893 Charles Proteus Steinmetz revolutionized the AC circuit analysis by introducing the concept of complex phasors (Steinmetz 1894), a simplified mathematical representation of a sinusoidal waveform. The introduction of phasors greatly simplified the analysis of AC circuits. Prior to this time, AC circuit analysis had to be carried out using calculus, a difficult and time consuming process involving integrals and derivatives of sinusoids. With the introduction of phasors, the problem was reduced to a simple problem in algebra where an AC circuit could be represented in terms of complex impedances for the purpose of analysis.

Complex phasors of voltages and currents are used for the analysis of a given stationary operating condition in electric power systems. In three phase electric power systems, the positive sequence voltage phasor at a power system bus has become parameter of vital significance. It is a common practice to describe a given stationary or a quasi-stationary system operating condition in terms of positive sequence bus voltages and neglecting the negative sequence and zero components. A set of all positive sequence bus voltage phasors is provided as an output from load flow analysis and state-estimation, and thereby an unique description of a given system operating conditions is obtained. The set of bus voltage phasors can be used, together with the knowledge about the network impedances to determine the currents and power flowing in the system.

Following the US Northeast Blackout of 1965, increased focus was on developing methods and tools for monitoring the system operating conditions in real-time. After a few years of research and development, weighted least square state estimators were introduced which made a real-time network analysis possible (Savulescu 2006). The estimation of the system state was carried out by estimating the system bus voltages from a set measurements of several system parameters. The development of state estimators was the initial step in the development of real-time static security assessment methods

that utilized the estimated operating conditions as input data.

Phadke et al. (1983) presented a new measurement technique that enabled measurements of positive sequence voltage phasors in real-time. In 1986 a prototype phasor measurement unit (PMU) was produced at Virginia Tech and in 1991 a commercial production of PMUs began with the introduction of the Macrodyne 1690 unit. Since the development of the first PMU, many other models have become available with a wide range range of options. At the present there are over 20 commercial manufactures of PMUs world wide and PMUs have been installed in power systems through out the world (Phadke & de Moraes 2008).

The aim of this chapter is to explore the basic principle of PMUs and investigate their added value to the system operation as well as their limitations when used for stability assessment. Furthermore, an overview is provided over few existing methods that can deploy PMU measurement for real-time assessment of the system stability and security.

3.1 Phasor Measurement Units (PMUs)

A phasor measurement unit (PMU) is a device that provides synchronized measurements, in real-time, of voltage and current phasors along with a measurement of frequency. Synchronism between the individual PMUs is achieved by the use of a common synchronizing signal from GPS satellites. The synchronization of the sampling process for different waveforms, measured at locations that may be hundreds of kilometers apart, makes it possible to put their phasors on the same phasor diagram and use directly for circuit analysis of the system.

Figure 3.1 illustrates the concept of PMUs, where a sinusoidal waveform is sampled at two different system busses. A GPS signal ensures synchronization of the sampling process, which makes it possible to represent the sampled waveforms as phasors in the same complex plane.

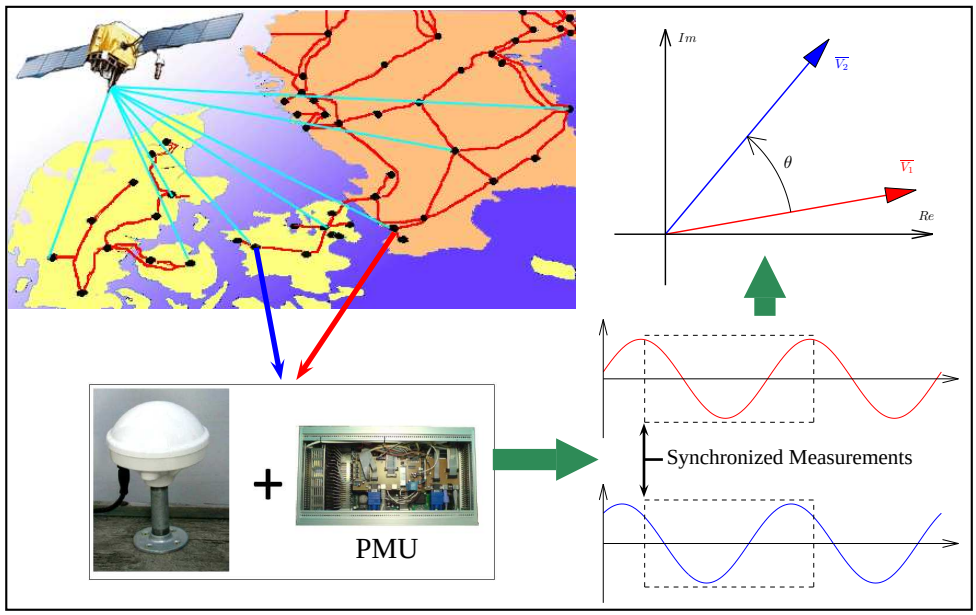

Figure 3.1: Phasor Measurements in electric power systems. PMUs installed in substations dispersed over a wide-area in a power system receive a GPS signal that ensures a time synchronization of the phasor measurement. The synchronizing signal ensures that the sampled voltage or current waveform can be used to derive the phasor values that can be put in the same complex plane for the purpose of analysis.

3.1.1 Accuracy of Phasor Measurements

According to IEEE standard for PMUs, the accuracy limits of PMUs is defined in terms of Total Vector Error (TVE) which is defined as:

$$TVE = \sqrt{\frac{(X_r(n) - X_r)^2 + (X_i(n) - X_i)^2}{X_r^2 + X_i^2}} \tag{3.1}$$

Where $X_r(n)$ and $X_i(n)$ are the real and imaginary part of the phasor given by the measuring device and X_r and X_i are the theoretical real and imaginary phasor values of the input signal at the time of measurement. Accuracy limits of PMUs, expressed as TVE should be within 1%. This implies a phase error within ± 0.01 rad ($\pm 0.57^\circ$) or a maximum time error of $26.5\mu s$ at $60\,Hz$ and $31.8\mu s$ at $50\,Hz$ (Martin et al. 2008).

This high accuracy of the PMU elevates the standards of power system monitoring, control, and protection to a new level. The introduction of PMUs

provides a possibility for development of new methods for real-time stability assessment, which might benefit from that a large scale deployment of PMUs in electric power systems where a full observability of the system operating conditions can be obtained in real-time, with a high repetition rate.

3.1.2 Wide-Area Measurement Systems (WAMS) and Phasor Data Concentrators (PDC)

Wide-area measurement systems (WAMS) focus on collecting the synchronized system measurements in real-time and distribute them further to applications that make use of the data. A basic structure of a WAMS is illustrated in figure 3.2. The figure shows a WAMS consisting of PMUs, communication links, and data concentrators which are needed to fully exploit the benefits of synchronized phasors measurements. The PMU measurements are transmitted immediately to a receiving unit, usually a phasor data concentrator (PDC). The data is then sent without delay to real-time applications and to data storage for off-line use. The WAMS provide the possibility of serving all measurement applications through different choice of data rates.

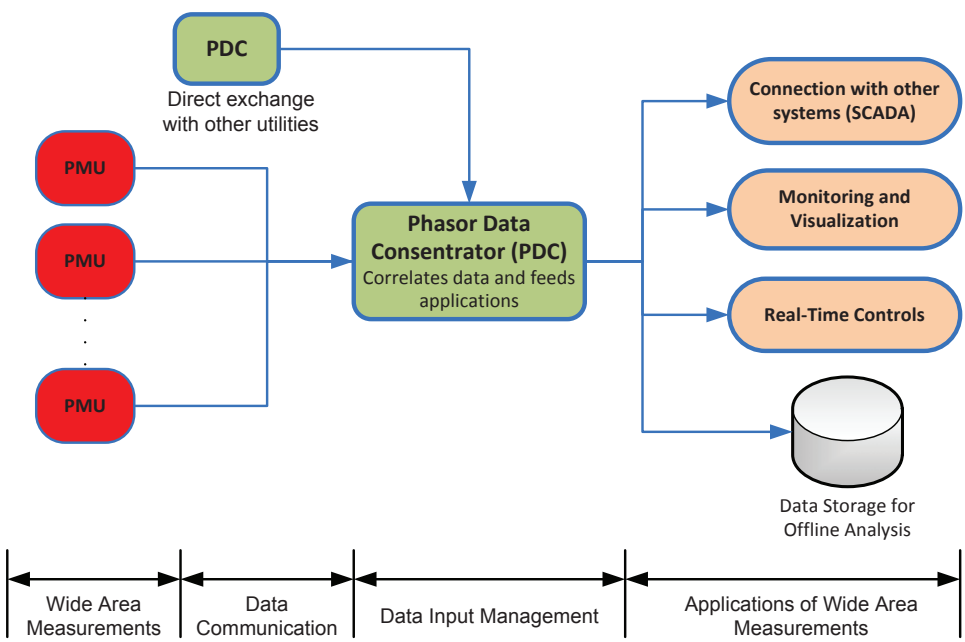

Figure 3.2: General overview of wide-area measurement systems.

In the figure, PMUs provide measured phasors in a data stream that are transmitted to a PDC. The measurement data from different location may not arrive simultaneously, since different communication technologies may be used (Naduvathuparambil et al. 2002). For this reason, the one of the most important function of a PDC is to gather data from different locations and align the data by time-tags before it is sent to appropriate applications.

PDCs from different utilities may also share data among them to support wide-area applications. In large scale power systems, a Super Phasor Data Concentrator (A PDC that gathers data from several other PDCs) can be used to correlate data from several utilities within a power grid, thereby providing platform for application that assess the overall condition of the whole system.

3.1.3 Added Value of PMUs

The PMU technology has matured in recent years and consequently, new installations of PMUs have been gradually increasing in power systems through out the world (Phadke & de Moraes 2008). The objective of the installations is to reach for hierarchical WAMS, in which system measurements from various substations are collected at central locations. The practical value of wide-area PMU data, collected in a WAMS, is given by applications that utilize the data. Few examples over existing and suggested applications are listed below (Skok et al. 2007, Rehtanz & Pouyan 2006):

Real-Time Monitoring and Control: One of the benefits of PMUs is the ability to inform not only operators that they face problems in their control areas, but as well neighboring operators of a stressed grid. In (Taylor et al. 2005) a wide-area stability and voltage control system (WACS) is presented that is intended to provide a flexible platform for rapid implementation of generator tripping and reactive power compensation switching for transient stability and voltage support of a large power system.

Power System State Estimation: PMUs offer a number of benefits to the State Estimation application such as improved accuracy and robustness of bad data detection, and an availability of a faster numerical solution to a linear problem (Zhao & Abur 2005, Nuqui 2001).

Real-Time Congestion Management: Real-time congestion management is usually carried out by comparing a pre-calculated Nominal Transfer

Capability (NTC) to the actual flow in a line or a path. The calculations of the NTC based on stability limitations, voltage level limitation of thermal limitations, whichever is the most restrictive for the given stress direction. The assumptions used in NCT calculations are often conservative. This can result in that excessive margins are introduced which may lead to unused transfer capability and thereby a lost opportunity to reduce costs in the dispatch process (Leirbukt et al. 2005, Mao et al. 2005). The high repetition rate and accuracy of PMU-measurements contributes to speed and quality enhancement of real-time algorithms that enable rapid computation of Real-time Transfer Capability (RTC). On many lines or paths such RTCs will exceed their corresponding NTCs which reduces the need for congestion curtailments in real-time (Breidablik et al. 2003).

Benchmarking, validation and fine-tuning of system models: The implementation of phasor measurement based tools, methods and applications provides a means of improving existing models. The availability of precise and time synchronized measurements from various locations in the power system provides new opportunities for identifying errors in system modeling data and for fine tuning power system models utilized throughout the industry for both on-line and off-line applications (Hiskens 2001, Hauer et al. 2005).

Post-Disturbance Analysis: The aim of a post-disturbance analysis is to identify the sequence of events which caused that a given power system interruption occurred. This is usually carried out by a team of engineers that study measurements from various data recorders from locations dispersed throughout the system. Since the recorders are not synchronized, this job of understanding the process causing the disturbance and reconstructing a time line of events is a time consuming job. A utilization of synchronized measurements can make this process significantly easier (Skok et al. 2007).

Power System Restoration: Under the process of power restoration, large phase angle difference can occur across a breaker that connects two adjacent substations. Closing a breaker on a large angle difference can cause severe equipment damage, and eventually lead to a reoccurrence of the system outage. The PMUs are capable of providing on-line monitoring of system voltage phase angles and are therefore useful

during a power restoration. The PMU can reduce the time needed during a restoration process.(Skok et al. 2007)

Online Monitoring of Global and Inter-Area Oscillations: Several methods, which utilize PMU data, have been suggested for both online and offline analysis of power system oscillations. Methods that have been applied for the detection and identification of oscillations are among others based on prony analysis and wavelet analysis (Breulmann et al. 2000, Rehtanz & Pouyan 2006).

Adaptive Protection: Certain relays and protection schemes could be made to adapt to prevailing system conditions observed from wide-area PMU data and thereby enhance their performance (Skok et al. 2007).

Thermal Monitoring: By measuring voltage and current phasors at each end of a transmission line, the line parameters can accurately be determined. Utilizing that the line resistance R is temperature dependent, the average temperature of the entire line between the two measurement points can be estimated where the temperature reflects the actual situation of ambient conditions like wind speed, sun and line current (Weibel et al. 2006).

3.2 Potentials and Limitations of the usage of PMUs for Stability Assessment

When new applications, which rely on PMU-data, are to be developed, it is appropriate to identify the benefits and the limitations associated with the usage of PMU-data. Some of the main advantages associated with the utilization of PMU-data for stability assessment are listed below:

- A PMU-snapshot, which provides full observability of the network, can be obtained in real-time at a repetition rate of once per cycle of system frequency.
- The high repetition rate of PMU measurements makes it possible to capture system dynamics over a wide-area. Previously, a wide-area observability was provided from a SCADA system that had a repetition rate that was too slow to capture any but the slowest dynamics.

The above mentioned benefits of PMU measurements contribute to a strong base for the development of methods intended for wide-area assessment of the system operating conditions in real-time. A PMU-snapshot, which provides a full observability of a system, can be directly used to update a system model that is used for assessment of the the system state. The step of estimating unobserved system variables is not needed when the measurements provide full observability of the network and therefore, a significant reduction in assessment time can be obtained.

The high repetition rate opens as well up the possibility for real-time tracing the system dynamics which can eventually be used for prediction of future states. The dynamics captured in PMU data must though be sufficiently slow such that the PMUs repetition rate is sufficient for providing a good representation of the actual system trajectory.

Some of the limitations of PMUs can be related to the concept of phasors, which is a simplified representation of a stationary sinusoidal waveform. This simplification results in that some information from the actual observed waveform is lost. This imposes limitations on what complex phasors can be used for, which in fact imposes limitation on what kind of applications PMU-data can be used. To mention some of the limitation associated with the usage of PMU data for assessment of the system conditions, the following is outlined:

- Since PMUs are limited to a repetition rate of once per cycle of system frequency, applications focusing on assessment of very fast phenomena cannot use PMU data if the repetition rate is too slow for capturing the dynamics of interest.
- The PMUs provide a measurement of the positive sequence component of the observed waveforms, which limits their usage to applications that can manage without the knowledge of the negative sequence or the zero sequence components.
- The performance of PMUs under transient conditions, where the magnitude and relative phase angle of the observed waveform can change significantly during one period, is not standardized. It is uncertain which voltage magnitude or phase angle the PMU phasor should represent during such conditions, bearing in mind that phasors are a simplified representation of a stationary sinusoidal waveform. It is not

clear whether PMU measurements from a period involving fast dynamics can be used for accurate assessment of system stability.

It has been proposed, that real-time observations of system voltage phase angles can be used for stability or security assessment observed system conditions. In the following, the shortcomings of methods only relying on phase angle observations for system assessment are pointed out.

3.2.1 Shortcomings of the use of Voltage Phase Angles Observations for Stability/Security Assessment

In a power system where PMUs are covering a large part of the system busses, a snapshot of the system operating conditions can be obtained if the measurements are continually gathered at a control center. For the purpose of utilizing the wide-area information obtained from such a set of PMU measurements for stability assessment, several applications and ideas have been suggested. One idea sometimes suggested is to use phase angle measurements for assessing the system operating conditions. In (Venkatasubramanian et al. 2009) it is suggested that a set of measured voltage phase angles can be useful for assessing system stress and in (Dobson et al. 2010, Dobson & Parashar 2010) phase angles across a cutset area are used as a measure of the system stress.

The suggestions for using voltage phase angle measurements for assessing system stress are often based on practical experience where stability/security problems seem to occur when bus voltage phase angle differences exceeds some particular value. In (Dobson & Parashar 2010), it is mentioned that simulations of the grid before the Northeast blackout of August 2003 showed an increasing angle differences between the Cleveland and West Mahican, which are said to indicate that large angle differences could be a blackout risk precursor.

The usage of a measurement data set consisting only of system voltage phase angles, for the purpose of assessing the system operating condition has some disadvantages compared to a data set containing both the voltage magnitude and phase information. In the following, arguments are provided for why observations of system phase angles cannot alone be used for accurate assessment of the power system operating conditions.

In order to assess the stability or security of a given operating point from

a set of measured system variables, it is important that the observed system variables provide a unique representation of the system operating conditions. The term *unique representation* is used to denote a set of observed system variables which can only be obtained from one specific operating point. This means that the observed set of system variables provides full observability of the system. If not sufficiently many system variables are observed, the observed variable set cannot be used to represent one specific operating point. In such cases, other operating points exist that would result in an identical set of observed variables.

A unique representation of power system operating conditions can be obtained in different ways. As an example, for a system with N busses and M branches a unique description of a given operating point can be obtained if the network impedances are known together with all of the N bus voltage phasors or together with all the currents flowing in the M branches along with the voltage magnitude at one bus in the system. With the network configuration known, all other network variables can be determined from these sets of the M complex current variables and one voltage magnitude ($2M+1$ real variables) or from the N complex bus voltage variables ($2N$ real variables).

In power system analysis it is common practice to represent a specific system operating point, by determining the N bus voltage phasors. The reason for this is that in practical power system, the number of branches is greater than the number of busses and hence, a larger number of independent equations are needed to determine the M currents, than the N voltages.

Each operating point can be uniquely described by the N voltage phasors or $2N$ real variables (consisting of N voltage magnitudes and N angles). The number of required variables needed to provide a complete description of a system operating point can be reduced by applying constraints to some of the variables. For example, one of the bus voltage phasors can be used as an angle reference which reduces the number of voltages phase angle variables to $N-1$. It could be assumed that the voltages at n busses is maintained constant (by e.g. AVRs or SVCs) which would reduce the number of required variables to a set of $N-n$ bus voltage magnitudes.

When the stability (or security) of a specific operating point is to be assessed from an observed set of N (or $N-1$) bus voltage phase angles in the system, then the $N-n$ independent voltage magnitude variables are missing in

order to have unique representation of the observed operating point. This introduces $N - n$ degrees of freedom to the description of the current operating point. It is therefore obvious that the observed set of phase angles cannot provide a unique description of the system operating point and in fact a given set of $N - 1$ phase angles can both represent a stable situation and an unstable situation all depending on the values of the $N - n$ free variables (the bus voltage magnitudes).

In order to illustrate the difficulties associated with stability or security assessment based only on voltage phase angle observations, the following two examples are provided.

Example I - Simple 3-bus system

The aim of this example is to illustrate why information about the voltage phase angles in an electric power system is not alone sufficient for assessing the system operating conditions. The system used in this example is shown in figure 3.3.a. The system consists of three busses and two lines where two of the buses are connected to a voltage source while the third bus is a load bus.

In this example, the term critical operating point is used to denote when the point of maximum deliverable power to the load has been reached when some specific constrains are applied to the system. It is though noted that an operating point might be considered to be critical for several other reasons. For example a given operating point could be considered critical when thermal limits of a transmission line or a generator are reached or when the voltage magnitude at some point in the system goes below some specified limits for minimum voltage magnitude. For the sake of simplicity of this analysis, the maximum deliverable power to the load will only be used to denote critical points since this maximum is critical for voltage stability in electric power systems.

In order to determine whether a given operating point is critical or not, some knowledge concerning the system behavior and control is needed. The point of maximum deliverable power through a network to a load is dependent on several factors such as how the production from the involved generators changes as the system load is increased and how the relationship is between active power consumption and reactive power consumption as the loading increases (whether the power factor is varying or fixed). For example, if

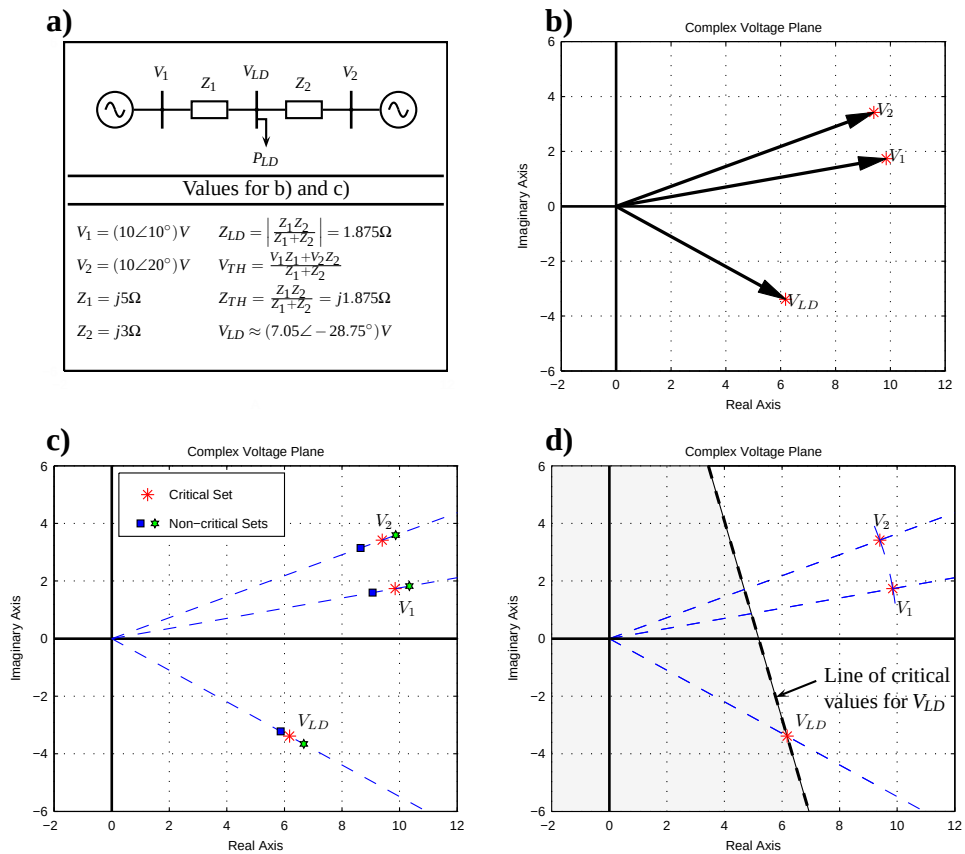

Figure 3.3: a) Simple three bus system used to explain why the values of voltage phase angles is not alone sufficient to asses whether a given operating point is critical or not. Calculations are provided to show how the voltage phasors in b) were determined. b) Representation of a critical operating condition for the system in a) when the supply voltage is fixed and the load has a fixed load angle. The critical operating conditions (point of maximum deliverable power) occur when the system Thevenin impedance is equal the load impedance. c) Three different operating conditions where in all cases the phase angles are the same, but the operating conditions represented are either critical or non-critical all dependent on the bus voltage magnitudes. d) Illustration which values of V_{LD} represent a non-critical situation (non-shaded area to the right of the line of critical values) when the supply voltages are fixed (both angle and magnitude) and the load is increased at fixed load angle.

the relationship between active and reactive power consumption is linear (fixed power factor) the point of maximum deliverable power will be different than if there was a nonlinear relationship between active and reactive power consumption. Different specifications or assumption for the behavior of the devices connected to the network, result in that an operating point which is critical for one specific set of system constrains might not be critical for another set of constrains.

In this example, the following constrains are used to describe the system behavior; the load angle is maintained fixed as the loading is increased and the voltage magnitude and phase angle are maintained constant (generator dynamics neglected). It is clear that these constrains do not reflect a practical situation. On the other hand, this selection of system constrains makes it easy to illustrate why the phase angle information alone is not sufficient to describe a given operating condition. By this selection, it is ensured that the system is stressed in specific way and that each operating condition can be described by two free variables which are the phase angle and the voltage magnitude at the load bus.

Figure3.3.b shows an example of a critical operating point in voltage plane, when the above mentioned constrains are applied to the system. If the idea of using phase angle observations for stability assessment of this situation would be applied here, it would mean that whenever exactly the same set of phase angles differences would be observed, the system conditions would be considered to be critical.

Figure 3.3.c illustrates three different operating points, where all of them have identical phase angle values. Only one of these points is critical while the two others are non-critical. The only difference between the critical and non-critical points is that the voltage magnitudes are different. From the figure, it is evident that the information about the voltage magnitude is needed in order to determine whether a given point is critical or not.

In figure 3.3.d the line of all possible critical values of $\overline{V}_{LD}$ have been determined for the previously mentioned system constrains. The set of critical points are represented by the border line between the shaded region and the unshaded region. This picture clearly illustrates that it is not possible to use phase angle information alone to determine whether the observed operating point is critical or not since the limits are both phase angle and voltage

magnitude dependent.

Example II - 2×10 **bus system**

In this example, the 20 bus system in figure 3.4 is used to illustrate how large variations there can be in observations of system phase angle for two different critical operating points of the system. In this section, the static voltage stability boundaries, characterized by the non-solution of the power-flow equation (Venkatasubramanian et al. 2009) are used as the critical operating conditions. The system consists of 10 generators and 10 loads where all of the lines are purely reactive with line reactance $X_{LN} = 1\,pu$. In the following, the system will be gradually stressed according to two different schemes.

In figure 3.4 the load/generation participation factors λ_i for the two cases are shown. The participation factors indicate the increment in power injection at each bus when the total system load is increased by one unit. For a total system load increment of ΔP the partial increment at bus i is $\Delta P_i = \Delta P \cdot \lambda_i$, where negative values correspond to increased generation and positive values denote increased load. The voltage at the generator busses is maintained fixed during the analysis and the loads are purely resistive.

In the first scheme (case a in figure 3.4) the generator participation is highest for the left most generator, and is gradually decreasing for generators at busses to the right. The load participation factors are, opposite to the generator participation factors, highest for loads furthest to the right in the figure and become gradually smaller for busses to the left. This selection of load and generation participation factors results in power flow in the system from left to right. This means that a path of positive power flow can be found from the generator at bus 1 to the load at bus 19.

The resulting plot of the system bus voltages is shown in figures 3.5 and 3.6. The bus voltages are shown by a dot and the lines connecting the dots represent the voltage drop over the transmission line between two adjacent busses. In the leftmost plot in figure 3.5, the bus voltages are plotted when the system has been loaded up to 60% of its maximum, the plot in the middle shows the situation when the system has been stressed to 80% of its maximum and the plot to the right illustrates the critical operating point for the system when stressed according to the participation factors for case a in figure 3.4. By examining these three plots it can be seen how the system phase

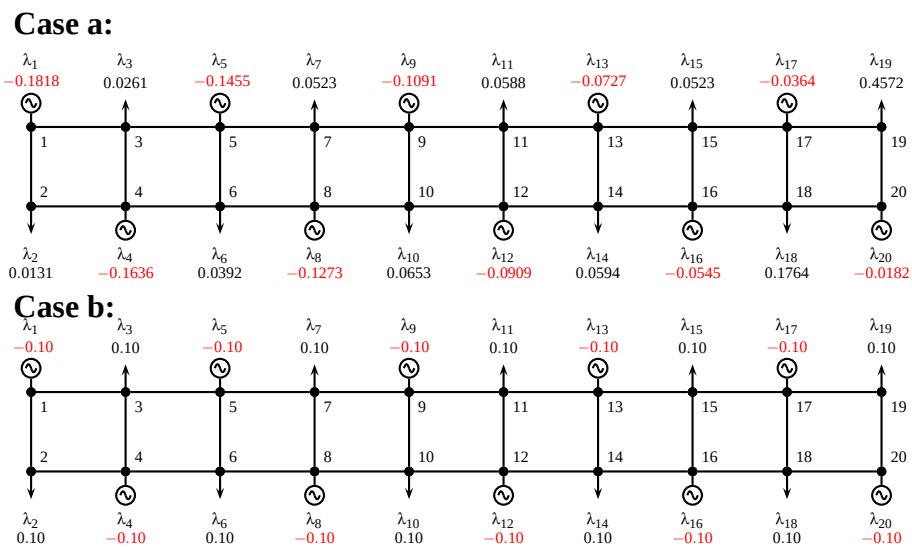

Figure 3.4: A 20 bus system with 10 generators and 10 loads. The load/generation participation factors for cases a) and b) are shown where a negative number corresponds to an increment in production and positive number corresponds to a increment in load. For a total system load increment of ΔP the partial increment at bus i is $\Delta P_i = \Delta P \cdot \lambda_i$. Each branch in the network is purely reactive with a unit line reactance $X_{LN} = 1\,pu$.

angle differences gradually increase as the system stress is increased. It can be seen from the plot of the critical operating point that the applied stress pattern causes large separation in the phase angles, where the maximum phase angle separation in the data set is close to 360 degrees.

In the second participation scheme (case b in figure 3.4) all participation factors are equal. When this scheme is applied the paths of positive power flow can only be traced from generator busses to the adjacent load busses. The three plots in figure 3.6 show the system bus voltages as the loading is gradually increased to the critical point. It can be seen that the phase angle separation as the system stress is increased is very different from the previous case and the maximum phase angle separation in the data set is much smaller in this case (approximately 50 degrees).

The difference between the two cases stems from the fact that in case a, the power flow in the branches was from the left to the right which resulted in long paths of positive power flow could be traced in the network while in case b the power was generally transmitted over short distances. When power is transferred through a long path consisting of purely inductive elements the voltage phase angles decreases on the busses in the path from the sending end to the receiving end.

These two cases demonstrated that the difference in phase angle separation of the bus voltages for two different critical operating points of the system can be very substantial. If only the information about phase angle separation was to be used for assessment of the critical operating condition, it would be impossible to identify the different critical situations. It is evident that more information is required than only the phase angles in order to assess the stability/security of such system.

It is interesting to compere the above results to suggested stability criteria in publications describing stability constrained power flow. Nguyen & Pai (2003) suggest when a relative rotor angle $\delta_{ij} = \delta_i - \delta_j$ exceeds 180 degrees, the system is considered unstable. Gan et al. (2000) refer to this criteria as an extreme case and an even lower threshold for δ_{ij} suggested. The above example illustrates that it is not possible to define a fixed phase angle difference δ_{ij} to accurately represent the system stability boundary. The system boundary depends on the both the network topology and how the system is loaded. A set voltage phase angles where δ_{ij} is high, could be an indication

Case a:

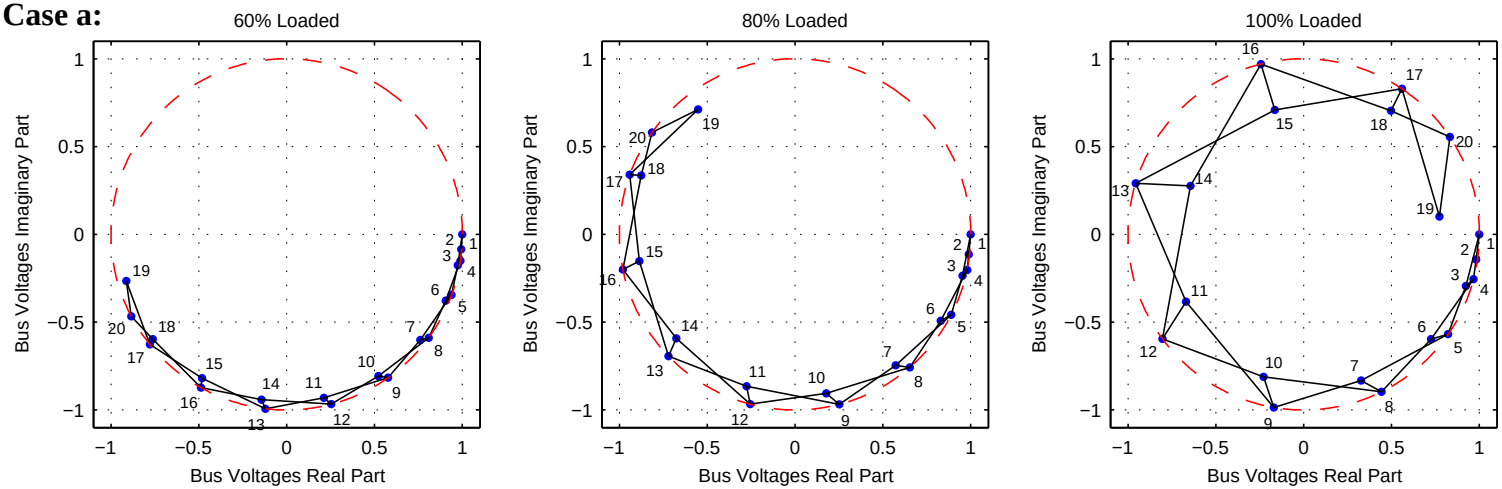

Figure 3.5: Plot of the system bus voltages for the system in figure 3.4. The leftmost plot shows bus voltages when the system is loaded to 60% of the maximum loading, when the participation factors from figure 3.4.a are applied. The middle plot shows the situation when loaded to 80% and the right plot are the bus voltages for the maximum possible loading.

Case b:

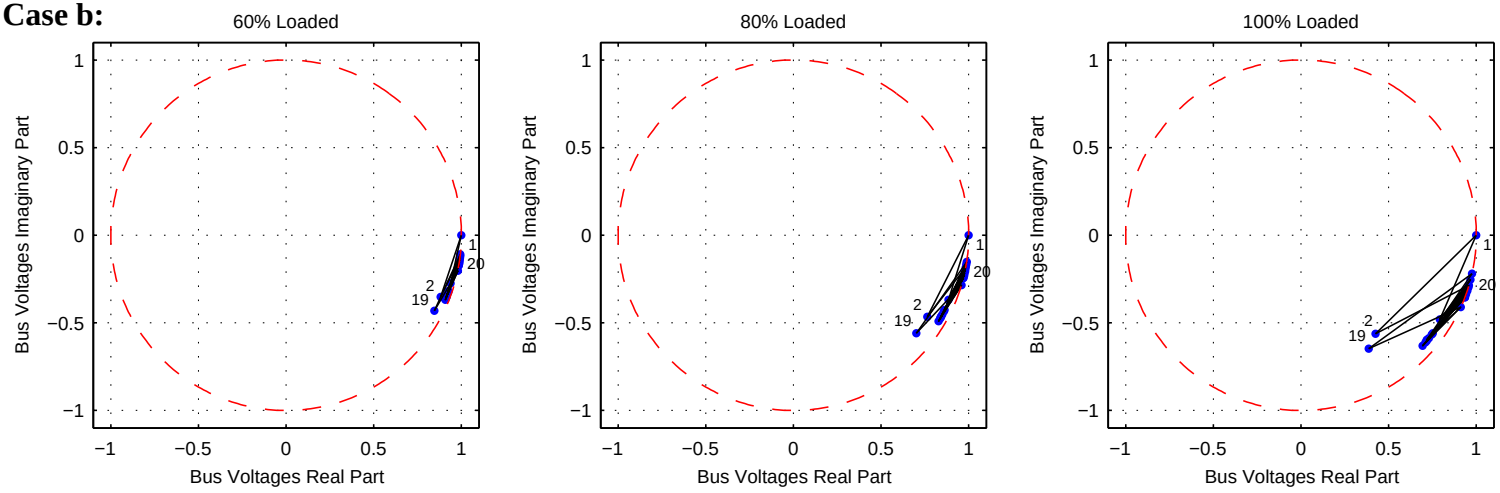

Figure 3.6: Plots for the same loading levels as in figure 3.5 when the participation factors figure 3.4.b are applied. There is a great difference between the two critical cases when the voltage phase angle separation of the bus voltages is investigated. In case a (figure 3.5), the maximum phase angle separation in the data is approximately 360 degrees while in case b it is approximately 50 degrees.

of that the path of positive power flow can be traced through a long distance in the system rather than a specific indication of a stressed system condition.

It should though be noted, that the idea of using maximum phase angle difference δ_{ij} as stability criteria is often suggested by utility engineers that observe that stability related problem seem to occur when δ_{ij} exceeds some practical limit. One potential explanation why utility engineers observe problems when δ_{ij} exceeds the practical limit, is that the system generation and consumption patterns of the bulk power system are usually very similar on daily basis. If the two, similar sets of participation factors were applied on the system in figure 3.4, the observed value of critical δ_{ij} might as well be similar.

Even though similar system generation and consumption patterns are experienced on daily basis, the usage such experience based stability criteria for δ_{ij} might be unreliable during some critical operating condition. This especially applies for stressed situations where the system topology might have been changed due to a trip of a transmission line, or when a loss of a large generator has resulted in redistribution of the power flow, such that a longer path of positive power flow is experienced. In such situations, the actual value for the critical δ_{ij} might be significantly different from practical experience based limits and result in either a false alarm for stability problems, or that the stability problem occurs before the practical limit is reached.

3.3 Existing Methods for Wide-Area Assessment in Real-Time

In the following, examples of method that utilize wide-area measurements for stability or security assessment are provided.

3.3.1 Wide-Area Detection of Voltage Instability

In (Glavic & Van Cutsem 2008, Glavic & Van Cutsem 2009*a*, Glavic & Van Cutsem 2009*b*) a method is presented that focusses on detecting the onset of voltage instability triggered by large disturbances. For this purpose, the method utilizes PMU system snapshots of the post-disturbance conditions. It is assumed the snapshot provides observability of the whole region which is prone to voltage instability. The voltage stability assessment is based on the singularity conditions of a computed Jacobian matrix derived

from an extended set of equilibrium equations. The short term dynamics of generators are not traced, but replaced by accurate equilibrium conditions. The assessment is based on system model where the effects of machine AVRs and OXLs are considered as well as the effects of other voltage control equipment in the system. No assumptions are made about the load behavior since it is directly measured.

A coupling between time domain simulation and eigenvalue analysis of the Jacobian has been suggested before (Moriso et al. 1993, Van Cutsem et al. 1995). The suggested method basically aims at replacing the off-line noise-free computations of the Jacobian sensitivities by a one carried out in real-time and based on the PMU snapshots.

A case study provided in (Glavic & Van Cutsem 2009*b*) shows that the method is capable of detecting when conditions for voltage instability occur. The method is though not capable of identifying the actual voltage stability boundaries and therefore not capable of assessing the distance to the boundaries in real-time.

3.3.2 Wide-Area Nomograms

In (Makarov et al. 2010), an approach for real-time security assessment is presented, where a multidimensional security region is determined for a specified operational base case. The security region boundary is represented using its piecewise linear hyperplanes in a multi-dimensional space, consisting of system parameters that are critical for security analysis. The security regions are pre-calculated off-line in a time-consuming process where the security region is derived for one particular system configuration. The derived multidimensional security region represents a set of operating points for which constrains thermal overloading, voltage levels, voltage stability, transient and oscillatory stability are satisfied.

A real-time assessment of the system security margin is obtained by monitoring the operating point in real-time and comparing it against the pre-calculated security boundaries. The method provides a very accurate multidimensional representation of the system security boundaries which provides confidence for operating the system closer to the security boundaries than before.

A drawback of the approach is that the boundaries are determined for a specific base case and fixed system topology. If the system is subjected to any

topological changes (e.g. few lines out of order due to maintenance), the actual approach may introduce an inaccuracy for the assessment of the security margin, as it has been based on the non-changed topological structure.

3.3.3 Monitoring System Stress by Cutset Angles

In (Dobson et al. 2010, Dobson & Parashar 2010) an approach is presented where the system stress is assessed by monitoring so called cutset angles.

A power system, with DC load flow approximation is considered where the topology and the impedances of the base case are known. A voltage phase angle at a bus i is denoted θ_i, the phase angle difference across the branch j is denoted $\hat{\theta}_j$ and the branch susceptance is b_j. A cutset of branches c that divides the network into area 1 and area 2 is chosen. Since a DC load flow approximation of the network is considered, the power flowing through the cutset c can be determined as:

$$P_c = \sum_{j \in c} b_j \hat{\theta}_j \tag{3.2}$$

The cutset susceptance:

$$b_c = \sum_{j \in c} b_j \tag{3.3}$$

And the cutset angle is defined as:

$$\hat{\theta}_c = \sum_{j \in c} \frac{b_j}{b_c} \hat{\theta}_j \tag{3.4}$$

Then (3.2),(3.3) and (3.4) imply that $P_c = b_c \hat{\theta}$ which represents the power flow through the cutset c derived from the cutset angle and the cutset susceptance.

The real-time assessment of the system stress is obtained by monitoring the cutset angle $\hat{\theta}_c$, which yields specific information about changes to the grid with respect to the chosen cutset.

The disadvantage of this approach is that it does not assess system stability in an accurate way, it only provides an indicator of stressed system conditions. Furthermore, as previously pointed out, by utilizing only the voltage phase angles from a given PMU-set and discarding the voltage magnitude

observations, results in reduced observability of the system conditions. A reduction of the system observability introduces greater uncertainty for the assessment of critical operating conditions.

Chapter 4

Real-Time Stability Assessment - Considerations

This chapter presents practical considerations related to real-time stability assessment where an element-wise stability assessment is presented as a potential approach for real-time monitoring of the system stability boundaries.

4.1 Monitoring Multidimensional Stability Boundaries

Traditionally, power system stability analysis is carried out by utilizing a variety of different methods which cover among others time domain simulations and static analysis. Depending of the scope of the study, different aspects are examined. For example, an analysis of transient stability involves investigation of whether, for a given operating point, the system can withstand of severe contingencies. The analysis of voltage stability for a given operating condition focusses on investigation of two aspects; the proximity to voltage instability and mechanisms of voltage instability. For that purpose, static methods such as continuation methods and QV-sensitivity analysis are applied.

For the purpose of monitoring the overall system stability or security boundaries, multidimensional nomograms have been suggested (Makarov et al. 2010). The critical boundaries are determined in an offline analysis where critical multiple critical boundary points are determined by stressing the system in various directions away from a given base operating point X_0, where $X_0 \in \mathbb{R}^N$. After each step increase of the system stress in a particular stress direction, a wide range of assessment method are applied to determine whether the new operating point is secure and/or stable. The stepwise increase of the system stress is continued until one of the applied assessment methods indicates that the current operating point is no longer stable or secure whereafter the point is used to represent a critical boundary point in

the multidimensional parameter space $\mathbb{R}^N$. The security (or stability) region boundary is represented using its piecewise linear hyperplanes in a multi-dimensional space where the hyperplanes are determined from the critical points determined by the offline analysis. Figure 4.1 depicts a piecewise linear approximated security region.

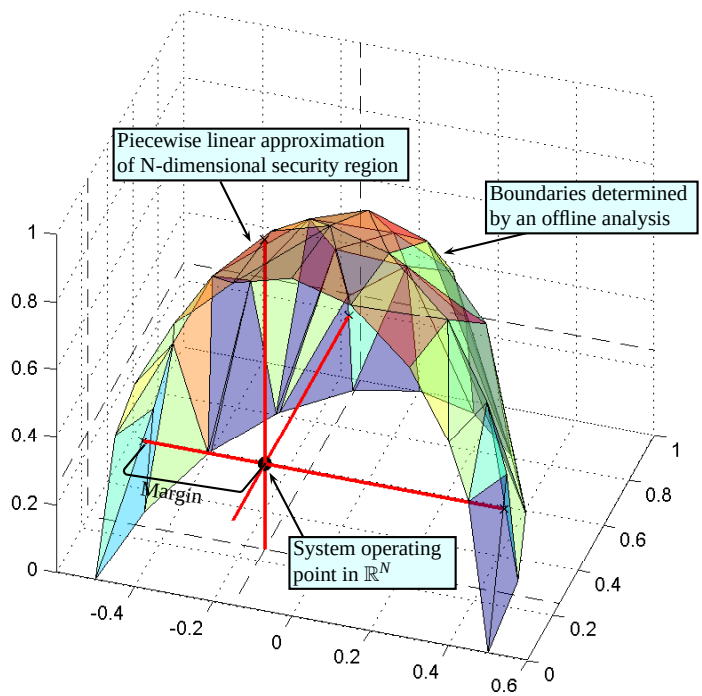

Figure 4.1: Assessment of a multidimensional operating point (in $\mathbb{R}^N$) against its boundaries. The boundaries are determined by offline analysis, while the operating point is monitored in real-time.

The derived security/stability region is used for real-time assessment of the system operating condition where the multidimensional operating point is monitored in real-time and held against the boundaries. In this way, a multidimensional security/stability margin can be obtained. This approach provides an overall-assessment of power system stability from observation of single multidimensional operating point.

Another approach for stability assessment, instead of monitoring a multidimensional operating point, would be to monitor multiple operating points where each point is associated to a specific element in a power system.

4.2 Element-Wise Assessment of Individual Mechanisms of Stability

One approach for real-time stability assessment, is to focus on assessment of one particular mechanism of instability that is related to a specific element in the system. Such element-wise assessment of individual mechanisms of stability could for example consist of determining the boundaries for the maximum amount of power that can be delivered to the terminal of specific ULTC-transformer. Another example could be an assessment of the maximum steady-state electrical torque T_e that a specific generator can apply for a given steady state situation.

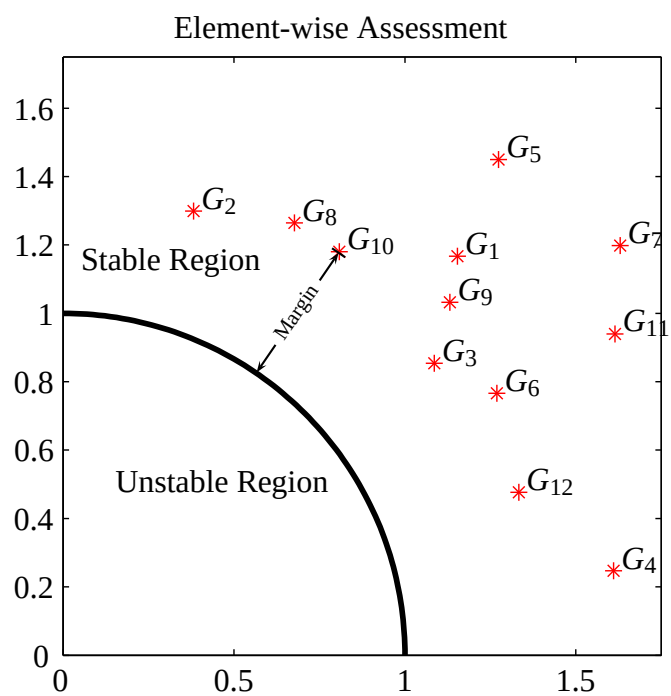

Figure 4.2: Element-wise assessment of stability, where the one particular mechanism of instability is assessed explicitly for each relevant system element. An individual operating point is associated with each element (in this case generators G_i) is held against its stability boundary.

Figure 4.2 illustrates the concept of such *element-wise assessment of indi-*

vidual stability mechanisms. In this case, the stability of a given system element is evaluated in respect to a given mechanism of stability. This could for example be the assessment of when generator (G_i) reaches its limit of maximum injectable power in steady state condition. The limits for maximum injectable power represents the stability limit for aperiodic small signal stability for the machine of concern. The assessment concept is illustrated in figure 4.2, where each operating point is associated to one generator and the point is held against a critical boundary for a given mechanism of stability (the boundary could be presented in $\mathbb{R}^2$ or even $\mathbb{R}$).

By assessing the conditions of a one particular system element in respect to one particular mechanism of stability offers possibilities for obtaining reduced computational time for carrying out the assessment. The reduction in computational time is related to that the system description can be tailored such that only factors that have a significant influence on the stability mechanism of concern are represented in the system model. Furthermore, when the assessment of a particular system element is being carried out, the network representation can potentially be reduced such that the areas that have little influence on the element of concern are represented by a simplified equivalent. Such reduction of the system network can lead to reduced computational efforts required for the assessment.

Another benefit of an element-wise assessment of stability is that the critical system elements are quickly identified which provides a good background for choosing appropriate remedial action for improving the observed system operating conditions.

4.2.1 Overall Assessment of Stability

An overall real-time assessment of system stability can be obtained by dividing the assessment process into several subtasks, where in each subtask the aim is to assess one particular mechanism of instability. Figure 4.3 gives an overview over the suggested assessment process.

Wide-area observations of the system operating conditions are used as an input to several different assessment methods, where each method concerns the assessment of a single mechanism of instability. The assessment of the different mechanisms of instability can be executed in parallel on different processors where the output from all methods is gathered and investigated for an overall assessment of the system stability. The division of the stability

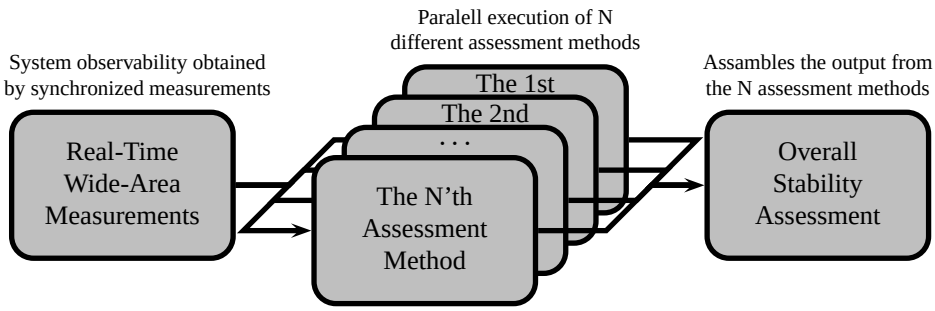

Figure 4.3: Schematic overview over real-time stability assessment process.

assessment problem into subtasks offers several benefits when being used in real-time:

- The system description can be tailored to the stability mechanism that is being addressed. This enables model reduction where system dynamics, that have a limited or no effect on the addressed stability mechanism, can be neglected. Hence, a reduction in the computational efforts is obtained.
- Since each assessment method is focussing on a particular mechanism of stability, it becomes easy to identify where in the system a problem is emerging, and what kind of stability problem is emerging.
- The parallel execution of several assessment methods provides improved speed of the assessment

Part II

Development of Real-Time Stability Assessment Methods

Chapter 5

Critical Boundaries and Characteristic Lines in Injection Impedance Plane

The main topic of this chapter concerns the mappings of some useful characteristics of a three dimensional PQV-surface, for a simple two bus system, into the injection impedance plane. The derived expressions for the characteristic boundaries are used as foundations for a method providing situational awareness that utilizes the derived expressions in this chapter for stability assessment and for an informative visualization of the observed system conditions in real-time.

5.1 Benefits of Describing Critical Boundaries in Terms of Injection Impedance

The representation of stability boundaries in injection impedance plane for the purpose of stability assessment has several advantages compared to representation of the boundaries in terms of other system variables. First of all, as will be shown in the following, the critical boundaries and other characteristic lines appear as circles in the impedance plane. This makes it possible to visualize multiple operating points on the same screen when the operating points have been normalized such that their critical boundary is represented by a unit circle.

Furthermore, characteristic lines of constant voltage magnitude, phase angle, active power and reactive power appear as well as circles in the injection impedance plane which provides a good basis for providing a meaningful and informative visualization of the system operating conditions.

5.2 Mapping of Critical Boundaries

In Figure 5.1 a diagram of a two bus system is presented which contains the notations of the system variables used in the following. The relationship between receiving and sending voltage, active and reactive power is formulated

in (5.1):

$$V^4 + V^2\left(2(RP + XQ) - E^2\right) + (R^2 + X^2)(P^2 + Q^2) = 0 \qquad (5.1)$$

The derivation of (5.1) is provided in appendix A.

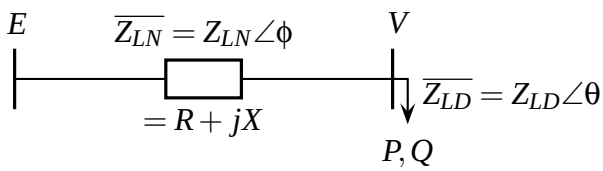

Figure 5.1: The simple two bus system and the notations used for deriving the critical boundaries in the injection impedance plane. E denotes the sending end voltage magnitude, V is the receiving end voltage magnitude, P and Q are the active and reactive power at the receiving end. $\overline{Z_{LN}}$ and $\overline{Z_{LD}}$ represent the line and the injection impedance respectively. The angle ϕ is used to denote the angle of $\overline{Z_{LN}}$ and θ is the angle of $\overline{Z_{LD}}$.

In order to construct a PQV-surface a solution for either P, Q are V has to be found. Rearranging (5.1) and solving the active power P results in the following two solutions:

$$P_{[1]} = -\frac{RV^2 - \sqrt{-Q^2(R^2+X^2)^2 + (R^2+X^2)(E^2 - 2QX)V^2 - X^2V^4}}{R^2+X^2} \qquad (5.2)$$

$$P_{[2]} = -\frac{RV^2 + \sqrt{-Q^2(R^2+X^2)^2 + (R^2+X^2)(E^2 - 2QX)V^2 - X^2V^4}}{R^2+X^2} \qquad (5.3)$$

By assuming $R \geq 0$ and $X > 0$, then the solution $P_{[2]}$ corresponds to solution where P is negative while $P_{[1]}$ describes the solutions for P values that can be positive as well as negative. All solutions for positive values of P are therefore described by $P_{[1]}$, given the above constrains for R and X.

The two solutions $P_{[1]}$ and $P_{[2]}$ describe the entire PQV-surface. If the region S contains all points on the PQV-surface and the subregions S_1 and S_2 contain the solutions of $P_{[1]}$ and $P_{[2]}$ respectively, then $S = S_1 \cup S_2$ is valid. This means that S represents the entire injection impedance plane.

Solutions for Q and V, can as well be obtained by manipulating (5.1):

$$Q_{[1]} = -\frac{XV^2 + \sqrt{-P^2\left(R^2+X^2\right)^2 + \left(R^2+X^2\right)\left(E^2-2RP\right)V^2 - R^2V^4}}{R^2+X^2} \tag{5.4}$$

$$Q_{[2]} = -\frac{XV^2 - \sqrt{-P^2\left(R^2+X^2\right)^2 + \left(R^2+X^2\right)\left(E^2-2RP\right)V^2 - R^2V^4}}{R^2+X^2} \tag{5.5}$$

$$V_{[1]} = \sqrt{-(RP+XQ) + \frac{E^2}{2} + \sqrt{\frac{E^4}{4} - (XP-RQ)^2 - E^2(RP+XQ)}} \tag{5.6}$$

$$V_{[2]} = \sqrt{-(RP+XQ) + \frac{E^2}{2} - \sqrt{\frac{E^4}{4} - (XP-RQ)^2 - E^2(RP+XQ)}} \tag{5.7}$$

$$V_{[3-4]} = -\sqrt{-(RP+XQ) + \frac{E^2}{2} \pm \sqrt{\frac{E^4}{4} - (XP-RQ)^2 - E^2(RP+XQ)}} \tag{5.8}$$

It can be seen that two different solutions exist for Q and four solutions for V exists. Two of the four solutions for V result in negative values for V which gives no physical meaning and therefore, only solutions for positive values for V are of interest ($V_{[1-2]}$).

In the following, the regions S_3 and S_4 represent the set of points described by the solutions $Q_{[1]}$ and $Q_{[2]}$ respectively and the regions S_5 and S_6 represent the set of points described by the solutions $V_{[1]}$ and $V_{[2]}$ respectively. In the same way as above, $S = S_3 \cup S_4 = S_5 \cup S_6$ are valid.

For the purpose of visualizing the relationship between P, Q and V, a three dimensional surface can be plotted by utilizing one of the expressions provided in (5.2)-(5.6) and keeping the values of R, X and E fixed. In figure 5.2 a plot of such surfaces can be found where the values $E = 1, X = 0.1$ and $R = 0.01$ are used. The surfaces are shown for positive values of P.

In figure 5.2.(a) several lines on the surface are shown that represent constant load power factor (that is the path on the surface where θ remains constant). A projection of those lines onto the PV-plane results in the traditional nose curves (PV-curves), which are often used in voltage stability analysis. Figure 5.2.(b) contains a set of lines which represent constant receiving end power P. A projection of these lines onto the QV-plane results in the QV-curves which also often are used in voltage stability analysis. The corresponding PV-curves and PQ-curves for the surfaces in figure 5.2.(a) and (b) can be found in figure 5.3.(a) and (b) respectively.

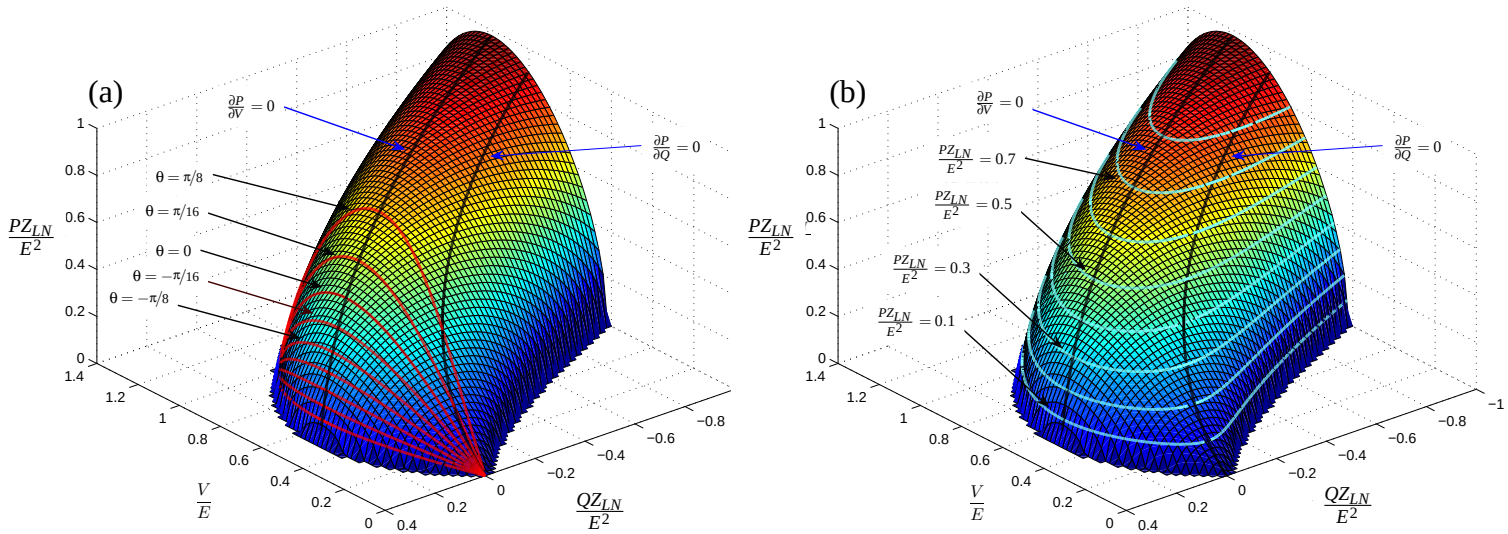

Figure 5.2: Illustration of the relationship between receiving end power and reactive power (P and Q) and the receiving end voltage V when the sending end voltage E and the line parameters (R and X) are kept constant. Two surfaces are shown in the figure, where in (a) lines of constant power factor are shown for different values of θ while in (b) lines of constant power P are shown. Figure 5.3 shows the projection of these lines onto the PV-plane and the VQ-plane respectively. Lines which illustrate where the partial derivatives $\partial P/\partial V$ and $\partial P/\partial Q$ respectively become zero are shown on both surfaces.

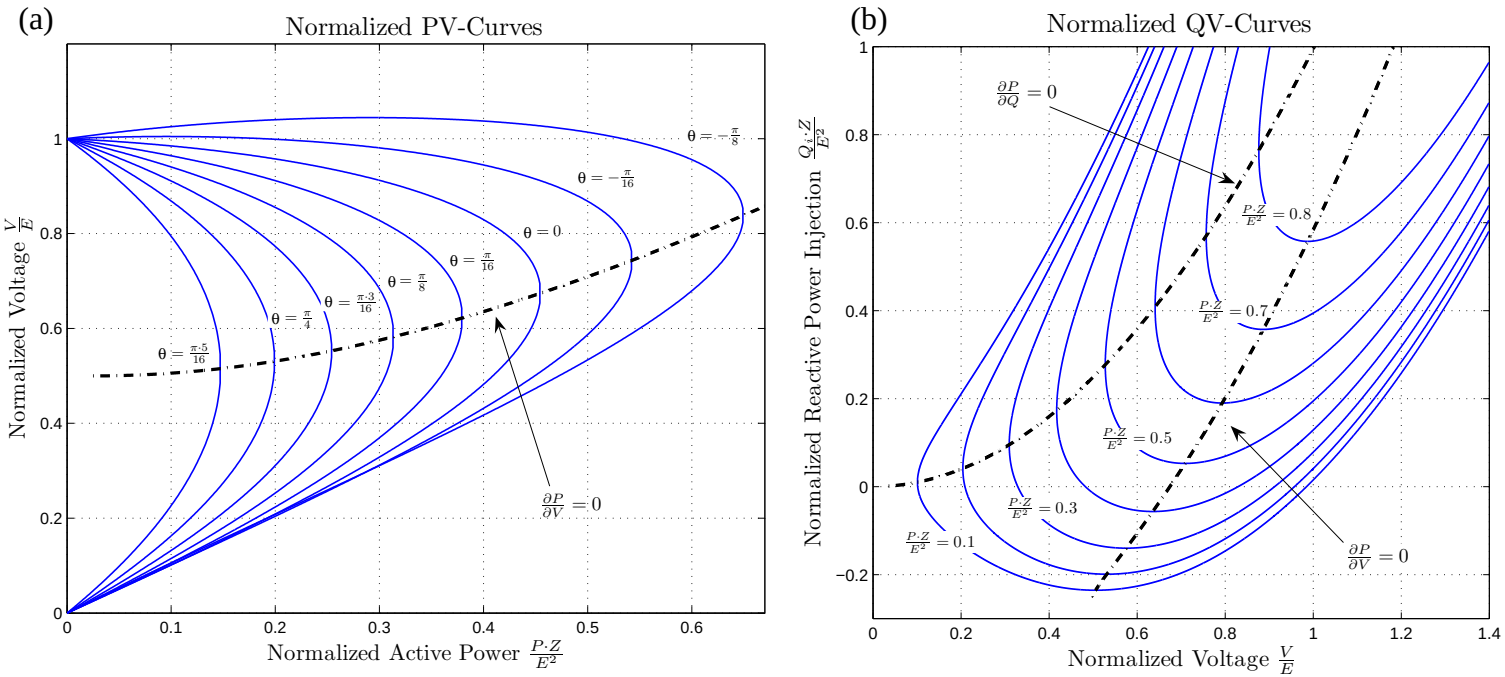

Figure 5.3: PV-curves and QV-curves. These curves are the results of the projection of the lines of constant power factor in figure 5.2.(a) onto the PV-plane and the projection of the lines of constant power in figure 5.2.(b) onto the QV-plane respectively. Note that y-aksis in (b) shows the reactive power injection Q_i and has therefore opposite sign to Q in figure 5.2.(b).

Apart from the lines of constant power factor and constant power, two lines that are of critical importance for stability studies are shown. The first line, the one which intercepts the lines of constant power factor when P is at maximum, is the line where the partial derivative $\frac{\partial P}{\partial V}$ is zero. The second line represents the set of points where $\frac{\partial P}{\partial Q} = 0$.

Both of these line represent the limits for maximum deliverable power P for a given system condition. The line $\frac{\partial P}{\partial V} = 0$ represents the maximum deliverable power when the sending end voltage is fixed and the relationship between P and Q is linear (that is changes in P are proportional to changes in Q). It is as well the maximum deliverable power when the value reactive power Q is fixed.

The line $\frac{\partial P}{\partial Q} = 0$ represents the maximum deliverable power when the receiving end voltage V is fixed. This could represent the maximum deliverable power between to systems, where the voltage in each end is maintained constant.

For voltage stability, it is the line where $\frac{\partial P}{\partial V} = 0$ that is of central importance since it represents the situation when there can not be delivered more power P to the load for the given value of Q. Whether a voltage instability is experienced when the operating point crosses this limit line is dependent on the dynamic behavior of the load. The line $\frac{\partial P}{\partial V} = 0$ is therefore only a borderline between a safe region and unsafe region.

For the purpose of developing an early warning system which monitors voltage stability in power systems, it would be interesting to determine the distance between an operating point and the critical borderline where $\frac{\partial P}{\partial Q} = 0$. It would as well be interesting to determine the "velocity" and direction of the operation point and predict the time it takes for the operating point to cross the borderline. It is not convenient to monitor multiple operating points in the system on a PQV-surface, since the shape of PQV-surface is dependent on the value of $\overline{Z}_{LN}$ for each transmission line. A mapping of the PQV-surface into the injection impedance plane enables the monitoring of multiple operating points. Before the mapping of lines on the PQV-surface can be be derived, it is necessary to identify some important characteristics of the PQV-surface that enable the derivation.

5.3 Characteristics of the surface

As necessary background for the mapping of the critical lines of the PQV-surface into the injection impedance plane, the following relationship must be valid:

$$\text{When} \quad \frac{\partial P}{\partial V} = 0, \quad \text{then} \quad \frac{\partial Q}{\partial V} = 0. \tag{5.9}$$

$$\text{When} \quad \frac{\partial P}{\partial Q} = 0, \quad \text{then} \quad \frac{\partial V}{\partial Q} = 0. \tag{5.10}$$

$$\text{When} \quad \frac{\partial Q}{\partial P} = 0, \quad \text{then} \quad \frac{\partial V}{\partial P} = 0. \tag{5.11}$$

In the following subsections it will be shown that the statements above are valid.

5.3.1 Proof of when $\partial P/\partial V = 0$ then $\partial Q/\partial V = 0$

Differentiating the expression for $P_{[1]}$ in (5.2) with respect to V yields:

$$\frac{\partial P}{\partial V} = -\frac{2RV}{R^2+X^2} + \frac{V\left(E^2-2QX\right)\left(R^2+X^2\right)-2X^2V^3}{\left(R^2+X^2\right)\sqrt{-Q^2\left(R^2+X^2\right)^2+\left(R^2+X^2\right)\left(E^2-2QX\right)V^2-X^2V^4}} \tag{5.12}$$

Setting $\frac{\partial P}{\partial V} = 0$ and solving for Q results in:

$$Q_{(\partial P/\partial V=0)} = \frac{X\left(E^2-2V^2\right) \pm ER\sqrt{4V^2-E^2}}{2\left(R^2+X^2\right)} \tag{5.13}$$

Using the expression for $P_{[2]}$ instead of the expression for $P_{[1]}$ when determining the partial derivative in (5.12) results in the same expressions for the solution for Q as in (5.13). From (5.13), it can be seen that there are two solutions for Q, that describe the line where $\partial P/\partial V = 0$. This partial derivative becomes zero when P is either at its maximum its minimum.

It can be seen that (5.13) is valid for V in the range $[E/2, \infty[$. A description of the entire PQV-surface can be obtained by equations 5.2 and 5.3 which correspond to the subregions S_1 and S_2 respectively. By inspection of (5.13)

it can be seen that the solution with the negative sign lies entirely in the region S_1 while the solution with the positive sign lies partly in S_1 and S_2. The values of $Q_{(\partial P/\partial V=0)}$ obtained by the solution with the positive sign should be applied into $P_{[1]}$ when the voltage V is in the range $[E/2, E/(2\sin\phi)]$ and applied into $P_{[2]}$ when V is in the range $[E/2\sin\phi, \infty[$. If the values of $Q_{(\partial P/\partial V=0)}$ are not applied in $P_{[1]}$ and $P_{[2]}$ as described, then they do not represent the set of points on the PQV-surface where $\partial P/\partial V = 0$.

The aim is to show that when $\frac{\partial P}{\partial V} = 0$ then $\frac{\partial Q}{\partial V} = 0$. Differentiation of the expression for $Q_{[1]}$ in (5.4) in respect to V results in:

$$\frac{\partial Q}{\partial V} = -\frac{2XV}{R^2+X^2} - \frac{V\left(E^2-2PR\right)\left(R^2+X^2\right)-2R^2V^3}{\left(R^2+X^2\right)\sqrt{-P^2\left(R^2+X^2\right)^2+\left(R^2+X^2\right)\left(E^2-2PR\right)V^2-R^2V^4}} \tag{5.14}$$

Setting $\partial Q/\partial V = 0$ and solving for P results in:

$$P_{(\partial Q/\partial V=0)} = \frac{R\left(E^2-2V^2\right) \pm EX\sqrt{4V^2-E^2}}{2\left(R^2+X^2\right)} \tag{5.15}$$

The results are the same as the one that would be obtained if $Q_{[2]}$ would have been used instead of $Q_{[1]}$ in (5.14).

An analysis of the two solutions for $P_{(\partial Q/\partial V=0)}$ reveals that the expression is valid for V in the range $[E/2, \infty[$.

Inspection of the solutions for (5.15) it can be seen that the solution with the positive sign lies entirely in the region S_1 while the solution with the positive sign lies partially in S_1 and S_2. The values of $P_{(\partial Q/\partial V=0)}$ obtained by the solution with the negative sign represent points in S_1 when the voltage V is in the range $[E/2, E/(2\sin\phi)]$ and represent points in S_2 when V is in the range $[E/(2\sin\phi), \infty[$.

By constraining expression for $P_{[1]}$ in (5.2) by inserting the expression with

the positive sign for $Q_{(\partial P/\partial V=0)}$ in (5.13) (which lies entirely in S_1) gives:

$$\begin{aligned} P &= \frac{-2RV^2+\sqrt{2XE^2\sqrt{R^2E^2\left(2V-E\right)\left(2V+E\right)}+E^4R^2+4X^2V^2E^2-X^2E^4}}{2(R^2+X^2)} \\ &= \frac{-2RV^2+E\sqrt{\left(RE+X\sqrt{\left(2V-E\right)\left(2V+E\right)}\right)^2}}{2(R^2+X^2)} \\ &= \frac{R\left(E^2-2V^2\right)+EX\sqrt{4V^2-E^2}}{2\left(R^2+X^2\right)} \end{aligned} \tag{5.16}$$

The above expression for P, which is constrained by $\partial P/\partial V = 0$, is the same as the expression for P with the positive sign in (5.15) where $\partial Q/\partial V = 0$. It is therefore proven that the line on the surface where $\partial Q/\partial V = 0$ is the same line as the one where $\partial P/\partial V = 0$.

5.3.2 Proof of when $\partial P/\partial Q = 0$ then $\partial V/\partial Q = 0$

Differentiation of the expression for $P_{[1]}$ in (5.2) with respect to Q yields:

$$\frac{\partial P}{\partial Q} = \frac{-Q(R^2+X^2)-XV^2}{\sqrt{-Q^2\left(R^2+X^2\right)^2+\left(R^2+X^2\right)\left(E^2-2QX\right)V^2-X^2V^4}} \tag{5.17}$$

Setting $\partial P/\partial Q = 0$ and solving for Q yields:

$$Q_{(\partial P/\partial Q=0)} = -\frac{XV^2}{R^2+X^2} \tag{5.18}$$

This result would be obtained as well if $P_{[2]}$ would have been differentiated in (5.17) instead of $P_{[1]}$. By inspecting the expressions for $Q_{[1]}$ and $Q_{[2]}$ in (5.4) and (5.5) it can be seen than the expression for $Q_{(\partial P/\partial Q=0)}$ is identical to $Q_{[1]}$ and $Q_{[2]}$ when the term under the root is equal zero. This means the the line representing $\partial P/\partial Q = 0$ is at the boundary of regions described by $Q_{[1]}$ and $Q_{[2]}$ (S_3 and S_4 respectively). Therefore, the expression for $Q_{(\partial P/\partial Q=0)}$ represents the intersection between $Q_{[1]}$ and $Q_{[2]}$ ($Q_{(\partial P/\partial Q=0)} = S_3 \cap S_4$). This results in (5.18) being valid for all values of V in both expressions for $Q_{[1]}$ and $Q_{[2]}$ in (5.4) and (5.5) respectively.

The aim of this subsection is to show that when $\partial P/\partial Q = 0$ then $\partial V/\partial Q = 0$. Expressions for the positive voltage magnitudes ($V_{[1]}$ and $V_{[2]}$) were derived

in (5.6) and (5.7). Differentiation of the expression for $V_{[1]}$ in respect to Q yields:

$$\frac{\partial V}{\partial Q} = \frac{2R(XP - RQ) - E^2X - X\sqrt{d}}{\sqrt{2d\sqrt{d} + 2d(E^2 - 2(RP + QX))}} \tag{5.19}$$

Where $d = -4(RQ - XP)^2 + E^2(E^2 - 4(RP + QX))$. Setting $\partial V/\partial Q = 0$ and solving for P results in:

$$P_{(\partial V/\partial Q=0)} = \frac{RQ \pm E\sqrt{-QX}}{X} \tag{5.20}$$

This expression would have been obtained as well, if any one of the four solutions for the voltages ($V_{[1-4]}$ in (5.6)-(5.8)) would have been differentiated in (5.19) and used to determine $P_{(\partial V/\partial Q=0)}$. Equation 5.20 is valid for negative Q if X is positive (inductive) and vice versa.

In order to show that when $\partial P/\partial Q = 0$ then $\partial V/\partial Q = 0$, the expression for $Q_{(\partial P/\partial Q=0)}$ from (5.18) is put into the expression for the expression for $P_{[1]}$ given by (5.2). Doing this results in:

$$P_{[1]} = \frac{\left(-RV + \sqrt{R^2E^2 + X^2E^2}\right)V}{R^2 + X^2} \tag{5.21}$$

This expression can be achieved by inserting the expression for $Q_{(\partial P/\partial Q=0)}$ from (5.18) into the expression for $P_{(\partial V/\partial Q=0)}$ with the positive sign given by (5.20):

$$\begin{aligned} P_{(\partial V/\partial Q=0)} &= \frac{RQ_{(\partial P/\partial Q=0)} + E\sqrt{-Q_{(\partial P/\partial Q=0)}X}}{X} \\ &= \frac{\left(-RV + \sqrt{R^2E^2 + X^2E^2}\right)V}{R^2 + X^2} \end{aligned} \tag{5.22}$$

Since the same result is obtained by constraining the surface described by $P_{[1]}$ with $Q_{(\partial P/\partial Q=0)}$ as by constraining the line described by $P_{(\partial V/\partial Q=0)}$ with

$Q_{(\partial P/\partial Q=0)}$, it is proven that the line on the surface where $\partial V/\partial Q = 0$ is the same as line where $\partial P/\partial Q = 0$.

5.3.3 Proof of when $\partial Q/\partial P = 0$ then $\partial V/\partial P = 0$

Differentiation of the expression for $Q_{[1]}$ in (5.4) with respect to P yields:

$$\frac{\partial Q}{\partial P} = \frac{RV^2 + P(R^2+X^2)}{\sqrt{-P^2(R^2+X^2)^2 + (V^2E^2 - 2V^2RP)(R^2+X^2) - R^2V^4}} \tag{5.23}$$

Rearranging and solving for P, when $\frac{\partial Q}{\partial P} = 0$ results in.

$$P_{(\partial Q/\partial P=0)} = -\frac{RV^2}{R^2+X^2} \tag{5.24}$$

This is the same result as would have been obtained if $Q_{[2]}$ in (5.5) would have been differentiated in (5.23) instead of $Q_{[1]}$. By inspection of equations (5.2) and (5.3) for $P_{[1]}$ and $P_{[2]}$ respectively, it can be seen that $P_{(\partial Q/\partial P=0)}$ is identical to $P_{[1]}$ and $P_{[2]}$ when the term under the root is equal zero. This means that the line representing $\partial Q/\partial P = 0$ at the boundaries of $P_{[1]}$ and $P_{[2]}$ ($\partial Q/\partial P = 0$ at $S_1 \cap S_2$). Therefore (5.24) is valid for all values of V in either $P_{[1]}$ or $P_{[2]}$.

The aim is to show that when $\partial Q/\partial P = 0$ then $\partial V/\partial P = 0$. Differentiating the expression for $V_{[1]}$ in (5.6) in respect to P yields:

$$\frac{\partial V}{\partial P} = \frac{2X(RQ - XP) - E^2R - R\sqrt{d}}{\sqrt{2d\sqrt{d}) + 2d(E^2 - 2(RP+QX))}} \tag{5.25}$$

where $d = -4(RP - QX)^2 + E^2(E^2 - 4(RP+QX))$.

Rearranging and solving for Q, when $\frac{\partial V}{\partial P} = 0$ results in.

$$Q_{(\partial V/\partial P=0)} = \frac{PX \pm E\sqrt{-RP}}{R} \tag{5.26}$$

This expression would have been obtained as well, if any one of the four solutions for the voltages ($V_{[1-4]}$ in (5.6)-(5.8)) would have been differentiated in (5.25) and used to determine $Q_{(\partial V/\partial P=0)}$. Equation 5.26 is valid for negative P if R is positive and vice versa.

By inserting the expression for $P_{(\partial Q/\partial P=0)}$ from (5.24) into the expressions for $Q_{[1]}$ and $Q_{[2]}$ in (5.4-5.5) results in:

$$Q_{[1]} = -\frac{XV^2 + EV\sqrt{R^2+X^2}}{R^2+X^2} \tag{5.27}$$

$$Q_{[2]} = -\frac{XV^2 - EV\sqrt{R^2+X^2}}{R^2+X^2} \tag{5.28}$$

These are the same results which would be obtained if the expression for $Q_{(\partial V/\partial P=0)}$ in (5.26) would have been constrained by inserting $P_{(\partial Q/\partial P=0)}$ from (5.24). This proves that the line on the PQV-surface where $\partial Q/\partial P = 0$ is the same as the line where $\partial V/\partial P = 0$.

5.4 Transformation of Critical Lines into Injection Impedance Plane

In the following sections the lines on the PQV-surface that represents the set of points where the partial derivatives are zero, become transformed into the impedance plane.

5.4.1 Transformation of $\partial P/\partial V = \partial Q/\partial V = 0$ into Injection Impedance Plane

Previously, it has been shown that the expression for $P_{(\partial Q/\partial V=0)}$ in (5.15) and the expression for $Q_{(\partial P/\partial V=0)}$ in (5.13) describe the same line on the PQV-surface where $\partial P/\partial V = \partial Q/\partial V = 0$.

Furthermore, it was stated in section 5.3.1 that the solution for $P_{(\partial Q/\partial V=0)}$ with the negative sign lies entirely on the same surface as the solution of $Q_{(\partial P/\partial V=0)}$ with the positive sign. By rewriting and manipulating the solutions for $P_{(\partial Q/\partial V=0)}$ and $Q_{(\partial P/\partial V=0)}$ that lie on the same surface gives:

$$P_{(\partial Q/\partial V=0)} = \frac{R\left(E^2-2V^2\right) - XE\sqrt{4V^2-E^2}}{2\left(R^2+X^2\right)} = \frac{RA-XB}{C} \tag{5.29}$$

$$Q_{(\partial P/\partial V=0)} = \frac{X\left(E^2-2V^2\right) + RE\sqrt{4V^2-E^2}}{2\left(R^2+X^2\right)} = \frac{XA+RB}{C} \tag{5.30}$$

Where $A = \left(E^2 - 2V^2\right)$, $B = E\sqrt{4V^2 - E^2}$ and $C = 2\left(R^2 + X^2\right)$. The aim is to derive an expression for the line where $\partial P/\partial V = \partial Q/\partial V = 0$. For that purpose, the following relationship is utilized:

$$\left(\frac{V^2}{Z_{LD}}\right)^2 = P^2 + Q^2 \tag{5.31}$$

Inserting the expressions for P and Q in (5.30-5.29) into (5.31) gives:

$$\begin{aligned}\left(\frac{V^2}{Z_{LD}}\right)^2 &= \frac{R^2A^2 - 2RXAB + X^2B^2}{C^2} + \frac{X^2A^2 + 2RXAB + R^2B^2}{C^2} \\ &= \frac{(R^2 + X^2)(A^2 + B^2)}{C^2} \\ &= \frac{(A^2 + B^2)}{4(R^2 + X^2)} \\ &= \frac{V^4}{Z_{LN}^2}\end{aligned} \tag{5.32}$$

and solving for Z_{LD} results in:

$$Z_{LD} = Z_{LN} \tag{5.33}$$

Hence, the set of points on the PQV-surface that describe $\partial P/\partial V = \partial Q/\partial V = 0$ appear as a circle in the RX-plane with center at the origin and radius equal to the magnitude of Z_{LN}.

5.4.2 Transformation of $\partial P/\partial Q = \partial V/\partial Q = 0$ into Injection Impedance Plane

By writing the expression for $Q_{(\partial P/\partial Q=0)}$ from (5.18) in terms of apparent injection impedance Z_{LD} results in:

$$Q_{(\partial P/\partial Q=0)} = -\frac{XV^2}{R^2 + X^2} = \frac{V^2 \sin\theta}{Z_{LD}} \tag{5.34}$$

and solving for Z_{LD} results in:

$$Z_{LD} = -\frac{Z_{LN}\sin\theta}{\sin\phi} \tag{5.35}$$

From (5.35) it can be seen that the line that represents $\partial P/\partial Q = \partial V/\partial Q = 0$ is mapped as a circle in the RX-plane. The circle intercepts the origin of the plane, the complex conjugate of the line impedance and the negative of the line impedance. That is, the line where $\partial P/\partial Q = \partial V/\partial Q = 0$ appears as a circle with center in the impedance plane at $(R_{LD} = 0, X_{LD} = -r)$ where r is the radius of the circle and can be expressed as:

$$r = \frac{Z_{LN}}{2\sin\phi} \tag{5.36}$$

5.4.3 Transformation of $\partial Q/\partial P = \partial V/\partial P = 0$ into Injection Impedance Plane

By writing the expression for $P_{(\partial Q/\partial P=0)}$ where $\partial Q/\partial P = \partial V/\partial P = 0$ from (5.24) in terms of apparent injection impedance Z_{LD} results in:

$$P = -\frac{RV^2}{R^2+X^2} = \frac{V^2\cos\theta}{Z_{LD}} \tag{5.37}$$

and solving for Z_{LD} yields:

$$Z_{LD} = -\frac{Z_{LN}\cos\theta}{\cos\phi} \tag{5.38}$$

From (5.38) it can be seen that the line that represents $\partial Q/\partial P = \partial V/\partial P = 0$ is mapped as a circle in the RX-plane. The circle intercepts the origin of the plane, the real conjugate of the line impedance and the negative of the line impedance. That is, the line where $\partial Q/\partial P = \partial V/\partial P = 0$ appears as a circle with center in the impedance plane at $(R_{LD} = -r, X_{LD} = 0)$ where r is the radius of the circle and can be expressed as:

$$r = \frac{Z_{LN}}{2\cos\phi} \tag{5.39}$$

5.4.4 Graphical Representation of the Critical Lines in the Injection Impedance Plane

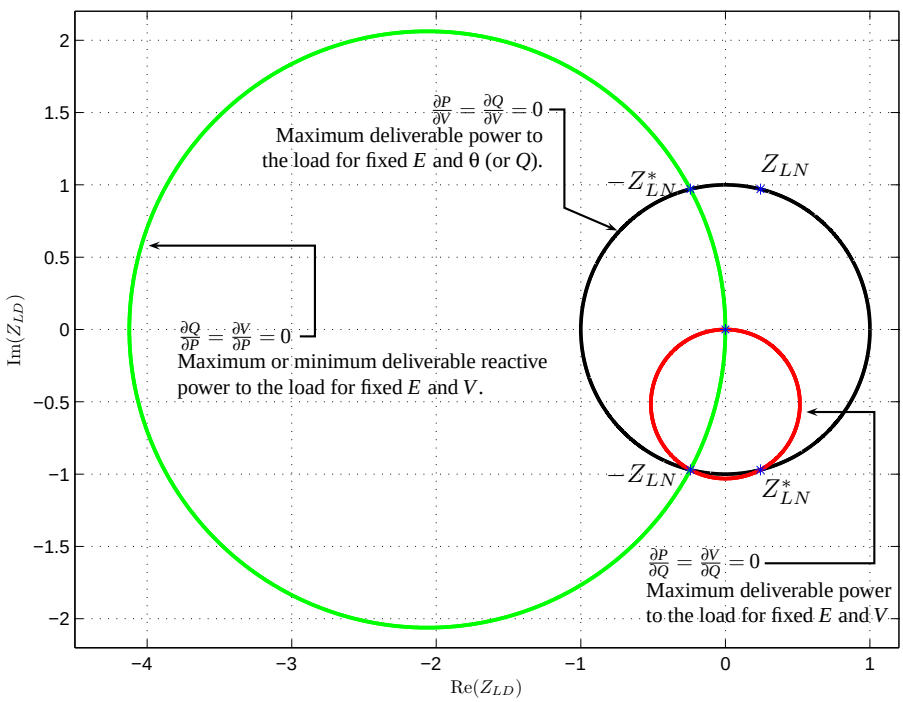

Figure 5.4: Graphical representation of the critical lines in the injection impedance plane.

Figure 5.4 shows a plot of the three borderlines of interest. It has been shown that the line where $\partial P/\partial V = \partial Q/\partial V = 0$ appears as a circle in the impedance plane with its center at the origin and a radius equal the size of the line impedance Z_{LN}. This line is plotted as a black circle in the impedance plane and it can be said to represent the maximum deliverable power through Z_{LN} when the sending end voltage is maintained fixed as well as θ or Q.

The line where $\partial P/\partial Q = \partial V/\partial Q = 0$ is plotted as a red circle in the figure. This borderline represents the maximum deliverable power through the line impedance Z_{LN} when both the sending end and the receiving end voltages are fixed. This borderline could be useful in determining the maximum transferrable power between two subsystems where the voltage in each subsystem is maintained constant by local generators.

The third line shown in figure 5.4 (green line) represents the situation where $\partial P/\partial Q = \partial V/\partial Q = 0$. This borderline represents the situation where maximum or minimum reactive power is transferred through Z_{LN} when both the sending end and receiving end voltage is fixed. This line is of limited interest when studying stability in power system.

5.5 Transformation of Other Characteristic Lines on the *PQV*-Surface into the Impedance Plane

The previously derived mappings of the critical lines on the PQV-surface, where all the partial derivatives are zero, are useful for stability studies. For the purpose of establishing meaningful visualization of a given operating condition in injection impedance plane, the mapping of lines of constant P, Q, V and δ become of interest. In the following section, the mapping of those lines are derived.

5.5.1 Lines of Constant *P*

In order to derive expressions for lines of constant P in the injection impedance plane, the expression (5.6) is used. In order to relate the values of P to Z_{LD},it is necessary to express V and Q as a function of those variables. Expressing V and Q in terms of the injection impedance and the receiving end power gives:

$$V^2 = \frac{Z_{LD}P}{\cos\theta} \tag{5.40}$$

$$Q = P\tan\theta \tag{5.41}$$

An expression for values of constant P described as a function of Z_{LD} can be obtained by putting (5.6) into powers of two and inserting the expressions for V^2 and Q from (5.40) and (5.41). After some manipulation, an expression of Z_{LD} as circle in polar coordinates can be obtained:

$$Z_{LD} = r_0 \cdot \cos(\theta - \varphi) \pm \sqrt{r^2 + r_0^2 \cdot \sin^2(\theta - \varphi)} \tag{5.42}$$

where:

$$\begin{aligned} r &= \sqrt{\frac{E^4 - 4E^2RP}{4P^2}} \\ r_0 &= \sqrt{X^2 + R^2 + \frac{E^4}{4P^2} - \frac{RE^2}{P}} \\ \tan\varphi &= \frac{-X}{-\left(R - \frac{E^2}{2P}\right)} \end{aligned}$$

The expression in (5.42) represents the set of points in the injection impedance plane where the receiving end power P is constant. Lines of constant power appear as circles in the injection impedance plane where r_0 is the distance from the origin to the center of the circle, r is the radius of the circle and φ is the angle between the positive real axis and the line connecting the origin and the center of the circle.

5.5.2 Lines of Constant Q

In order to derive expressions for lines of constant Q in the injection impedance plane, the expression in (5.6) is used again along with the following expressions for V^2 and Q:

$$V^2 = \frac{Z_{LD}Q}{\sin\theta} \tag{5.43}$$

$$P = \frac{Q}{\tan\theta} \tag{5.44}$$

Inserting (5.43) and (5.43) into the square of (5.6) and solving for Z_{LD} results in the following expression in polar coordinates:

$$Z_{LD} = r_0 \cdot \cos(\theta - \varphi) \pm \sqrt{r^2 + r_0^2 \cdot \sin^2(\theta - \varphi)} \tag{5.45}$$

where:

$$\begin{aligned} r &= \sqrt{\frac{E^4 - 4E^2XQ}{4Q^2}} \\ r_0 &= \sqrt{X^2 + R^2 + \frac{E^2}{4Q^2} - \frac{XE}{Q}} \\ \tan\varphi &= \frac{-\left(X - \frac{E^2}{2Q}\right)}{-R} \end{aligned}$$

For a fixed value of Q, equation 5.45 represents a circle in the injection impedance plane where r_0 is the distance from the origin to the center of the circle, r is the radius of the circle and φ is the angle between the positive real axis and the line connecting the origin and the center of the circle.

5.5.3 Lines of Constant V

In order to derive expressions for lines of constant V in the injection impedance plane, the expression (5.3) is used along with the following expressions for P and Q:

$$P = \frac{V^2}{Z_{LD}}\cos\theta \tag{5.46}$$

$$Q = \frac{V^2}{Z_{LD}}\sin\theta \tag{5.47}$$

By inserting (5.46) and (5.46) into (5.3) and solving for Z_{LD} results in the following expression in polar coordinates.

$$Z_{LD} = r_0 \cdot \cos(\theta - \varphi) \pm \sqrt{r^2 + r_0^2 \cdot \sin^2(\theta - \varphi)} \tag{5.48}$$

where:

$$\begin{aligned} r &= \frac{EV\sqrt{R^2+X^2}}{V^2-E^2} \\ r_0 &= \frac{V^2\sqrt{R^2+X^2}}{V^2-E^2} \\ \tan\varphi &= \frac{-X}{-R} \end{aligned}$$

Again, it can be seen that that the lines of constant voltage are represented as circles in the injection impedance plane. As before, r_0 is the distance from the origin to the center of the circle, r is the radius of the circle and φ is the angle between the positive real axis and the line connecting the origin and the center of the circle.

5.5.4 Lines of Constant Voltage angle δ

In order to derive expressions for lines of constant bus voltage phase angle δ in the injection impedance plane, the following expressions for P and Q are used:

$$P = \frac{V^2}{Z_{LD}}\cos\theta \tag{5.49}$$

$$P = \frac{EV\cos(\delta+\phi)-V^2\cos(\phi)}{Z_{LN}} \tag{5.50}$$

$$Q = \frac{V^2}{Z_{LD}}\sin\theta \tag{5.51}$$

$$Q = \frac{EV\sin(\delta+\phi)-V^2\sin(\phi)}{Z_{LN}} \tag{5.52}$$

By setting (5.49) equal (5.50) and solving for V results in:

$$V = \frac{EZ_{LD}\cos(\delta+\phi)}{Z_{LN}\cos\theta+Z_{LD}\cos\phi} \tag{5.53}$$

Similar results are obtained by setting (5.51) equal (5.52) and solving for V:

$$V = \frac{EZ_{LD}\sin(\delta+\phi)}{Z_{LN}\sin\theta+Z_{LD}\sin\phi} \tag{5.54}$$

Setting (5.53) equal (5.54) and solving for Z_{LD} yields:

$$Z_{LD} = -\frac{Z_{LN}}{\sin\delta} \cdot \sin(\delta + \phi - \theta) \tag{5.55}$$

This equation represents a circle in the injection impedance plane when δ is constant. The circle represented in (5.55) has a diameter equal $Z_{LN}/\sin\delta$ and intercepts the origin of the injection impedance plane and the point $\overline{Z_{LD}} = -\overline{Z_{LN}}$ for all values of constant δ.

It can be seen that (5.55) represents the same circles in the impedance plane for $\delta = \delta_0$ and $\delta = -180 + \delta_0$ where δ_0 is arbitrary. Therefore, it must be investigated which part of the circles represents constant $\delta = \delta_0$ and which part represents constant $\delta = -180 + \delta_0$. For simplicity, it is assumed that $0^\circ \leq \delta_0 < 180^\circ$. If $\delta_0 = 0^\circ$, it can be seen from (5.55) that the circle representing $\delta = \delta_0$ and $\delta = -180 + \delta_0$ has a radius going towards infinity; eg. these conditions are represented by the straight line that intercepts the origin and the point where $\overline{Z_{LD}} = \overline{Z_{LN}}$. By inspection it can be seen that the part of the line between the two singular points (eg. the origin and the point where $\overline{Z_{LD}} = -\overline{Z_{LN}}$ represents the condition where $\delta = \pm 180^\circ$ while the other parts of the line represents the points in injection impedance plane where $\delta = 0^\circ$.

If the line intercepting the origin and $\overline{Z_{LD}} = -\overline{Z_{LN}}$ is used to split the impedance plane into two halves, it can be seen by inspection that all of the circles represented constant δ lie in both halves. The lines of constant δ where $\delta = \delta_0$ are represented by the part of the circle laying in the left half while the part of the circle laying in the right half represents the condition where $\delta = -180 + \delta_0$. In figure 5.5 it is illustrated how the same circle in the impedance plane represents two different conditions of constant phase angle, depending on in which half plane the circle parts lie in.

5.5.5 Graphical Representation of the Characteristic Lines in the Injection Impedance Plane

Figures 5.6.a, 5.6.b, 5.7.a and 5.7.b illustrate how lines of constant *P*,*Q*, *V* and δ appear in the injection impedance plane. The figures represent the situation where $\overline{Z_{LN}} = (1\angle\phi)$ and $\phi = 75^\circ$.

Figure 5.6.a shows how the lines of constant receiving end power *P* appear in the complex injection impedance plane. By inspecting the lines of constant

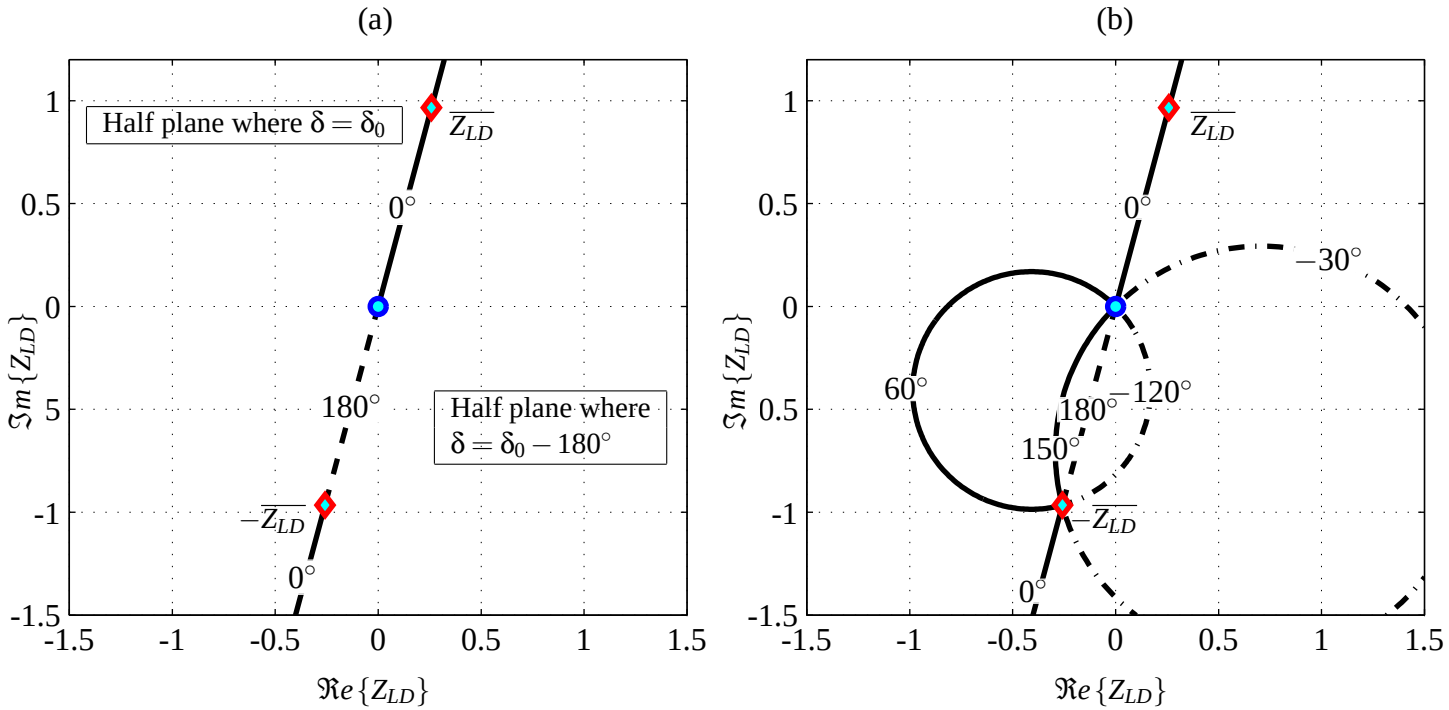

Figure 5.5: Illustration of how lines of constant δ are represented in the injection impedance plane. In (a) a plot of the line of constant δ according to (5.55) for the special case when δ is either $0°$ or $180°$. The line of constant δ is represented by a straight line, where the part of the line between the origin and $-Z_{LD}$ represents the value where $\delta = \pm 180°$ while others parts of the line represents points where $\delta = 0°$. In (b) it is shown how the parts of the same circle represent two different values of constant δ depending on which side of the line $\delta = 0°$ the parts are located. By defining $0 \leq \delta_0 < 180$ it can be seen that the condition $\delta = \delta_0$ is represented by the part of the circle lying in the left half plane while the condition $\delta = \delta_0 - 180°$ is represented by the same circle, just by the part lying in the right half plane.

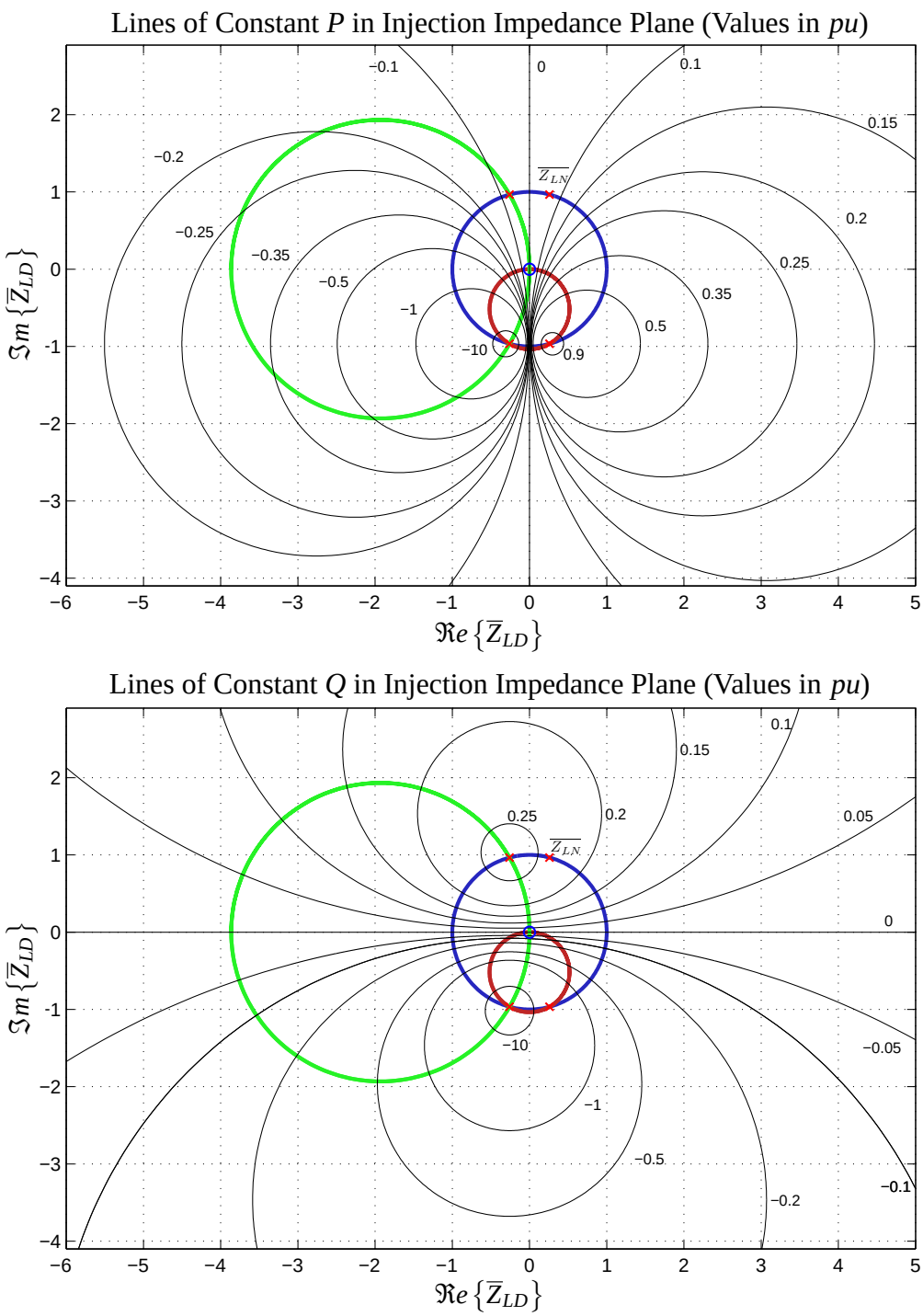

Figure 5.6: Lines of constant active and reactive power in the complex injection impedance plane derived from (5.42) and (5.45), when $\overline{Z_{LN}} = (1\angle 75^\circ)$. The values of P and Q are per unit values of where $S_{base} = {}^{E^2}/_{Z_{LN}}$ is used as base value.

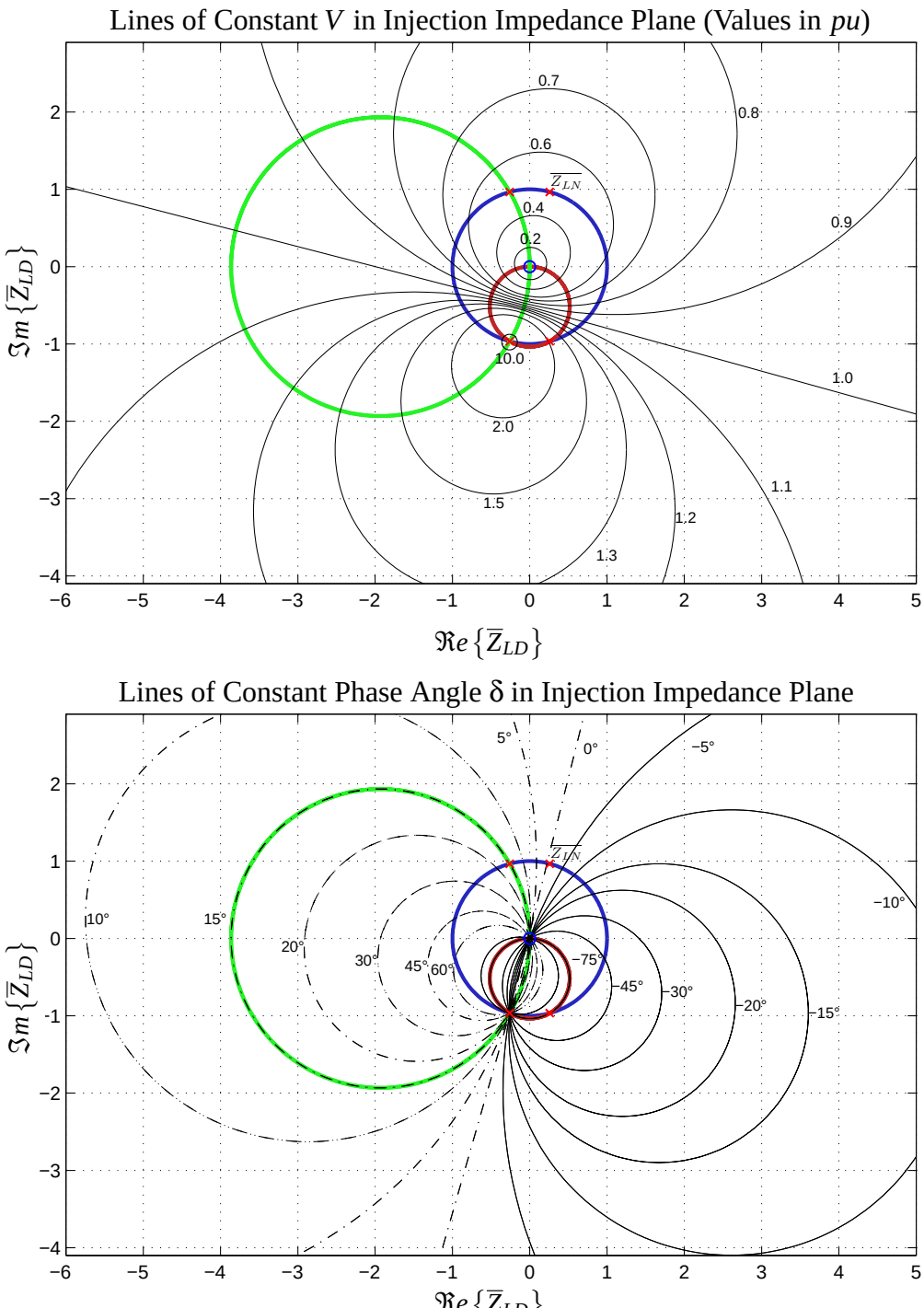

Figure 5.7: Lines of constant voltage magnitude V and voltage phase angle δ in the complex injection impedance plane derived from (5.48) and (5.7), when $\overline{Z_{LN}} = (1\angle 75^\circ)$. The values shown for the lines of constant voltage magnitude are in per unit, where sending end voltage E is used as base value.

P, some sort of symmetric appearance can be recognized. Constant positive values of the receiving end power appear as circles in the right half plane where the radius of the circle gradually decreases as the power is increased towards the point of maximum deliverable power. The point of maximum deliverable power appears where the injection impedance is equal the complex conjugate of the line impedance. Values of constant negative power at the receiving end are represented in the right half pane of the injection impedance plane. The radius of the circles representing constant negative power (positive bus injection) gradually decreases as the absolute value of the power increases. The point of minimum deliverable power (maximum bus injection) occurs at the singular point where the injection impedance is equal to the negative of the line impedance. At this point the receiving end power goes towards $-\infty$. The set of points representing the situation where P is zero, appears as straight line that satisfies $R_{LD} = 0$.

Figure 5.6.b shows how the lines of constant Q appear in the complex injection impedance plane. The lines for constant Q have a similar appearance as lines of constant P. The circles for constant positive values of Q appear in the upper half plane, where the radius of the circles gradually decreases until the point of maximum positive Q is obtained. The point of maximum Q occurs when the value of the injection impedance is equal to the real conjugate of the line impedance ($X_{LD} = X_{LN}$ and $R_{LD} = -R_{LN}$). The circles representing negative constant values of Q appear in the lower half plane and the minimum occurs at the singular point where the injection impedance is equal to the negative of the line impedance. At the singular point, the value of Q goes towards $-\infty$. The set of points representing the situation where Q is zero, appears as straight line that satisfies $X_{LD} = 0$.

Figure 5.7.a shows how lines of constant V appear in the injection impedance plane. From the figure it can be seen that circles representing constant values of the receiving end voltage V have center points on the lines intercepting the origin of the injection impedance plane and the singular point where $\overline{Z_{LD}} = -\overline{Z_{LN}}$. The set of points where $V = {}^{E}/_{2}$ appears as straight line that is perpendicular to the line between the origin and $\overline{Z_{LD}} = -\overline{Z_{LN}}$ and intercepts this line in the point where $\overline{Z_{LD}} = -{}^{\overline{Z_{LN}}}/_{2}$. The line representing $V = E$ divides the injection impedance plane into to half planes, where constant voltages lower than E appear as circles in the half plane containing the origin, while voltages higher than E appear as circles in the half containing

the singular point $Z_{LD} = -Z_{LN}$.

The lines of constant voltage phase angle δ appear as circles in the injection impedance plane where all circles intercept the origin and the singular point where $\overline{Z_{LD}} = -\overline{Z_{LN}}$. The part of the circles going in clockwise direction from the origin to $Z_{LD} = -Z_{LN}$ represents positive angles of δ (if δ is defined as $-180^\circ < \delta \leq 180^\circ$) while the part of the circle going in counter clockwise direction from the origin to $Z_{LD} = -Z_{LN}$ represents the points where δ is negative.

Furthermore, it can be noted that the circle where the partial derivative $\partial P/\partial Q = 0$ is the same as the circle representing fixed phase angle where $\delta = -\phi$ and $\delta = 180 - \phi$. This means that the point of maximum deliverable power to the receiving end in figure 5.1 when V and E are fixed occurs when $\delta = -\phi$ and the point of minimum deliverable power (maximum injectable power) to the receiving end for fixed V and E occurs for the conditions when:

$$\delta = 180 - \phi \tag{5.56}$$

Similarly, it can be seen that the circle where the partial derivative $\partial Q/\partial P = 0$ is the same as the circle representing fixed phase angle where $\delta = -90^\circ - \phi$ and $\delta = 90^\circ - \phi$. This means that the part of the circle where $\delta = -90^\circ - \phi$ represents the points of maximum deliverable reactive power when V and E are fixed, while $\delta = 90^\circ - \phi$ represents the minimum deliverable (maximum reactive power injection) reactive power for the same conditions.

5.6 Example - Analytical Load Flow for two Bus System

The expressions for the PQV-characteristics of the system in figure 5.1 in the injection impedance plane can be used to provide an analytical solution of the simple two bus system. By using the sending end as a reference bus, power flow solutions can be obtained analytically by considering where the circles of constant P and Q intercept in the injection impedance plane.

Equation 5.42 describes the lines of constant P as function of E, R, X and θ. With values of P and Q specified, θ is known and the injection impedance values corresponding to the load flow solutions can be determined directly

from (5.42). With the injection impedance known, the receiving end bus complex voltage can be determined.

Chapter 6

Method for Early Warning Against System Blackout

The purpose of this chapter is to describe a method that can determine the aperiodic small signal stability boundaries for the system generators from a set of PMU-data that provides a full observability of the system grid. The presented method enables real-time monitoring of stability boundaries and the corresponding margin to the observed operating point, which is used to provide an early warning for emerging stability problems.

The chapter begins by providing the background for the presented assessment method, followed by a description of the method and how synchronous machines should be represented so that effects of different excitation control, effects of saliency and iron saturation are included. Finally, a simple test of the method is carried out, where the method's capability of detecting the occurrence of aperiodic small signal instability is validated.

6.1 Background

As described in chapter 2, the principal causes and involved mechanism that provoke blackouts in electric power systems can be of various nature. The challenge of providing, in real-time, an awareness for a potentially emerging blackout would require an assessment of many different mechanisms that can contribute to the evolution of a system blackout. Such real-time situational awareness could for example require that the system voltage stability and the risk of voltage collapse is assessed, that the risk of cascading outages is evaluated and that a measure of the proximity to system stability boundaries can be determined in real-time. The establishment of such real-time awareness tool would require research efforts within several fields, where methods for real-time assessment of specific mechanisms contributing to the occurrence of blackouts are to be developed.

The blackout in E-Denmark and S-Sweden on September 23, 2003 has been the motivation for the following work, which concerns the development of

a method that can provide an awareness, or an early warning, for impeding stability problems and a subsequent blackout. The method development is focused on detection and assessment of the instability mechanisms that were the driving forces in evolution of the blackout.

The principal causes of the blackout in E-Denmark and S-Sweden were two severe system disturbances, independent of each other, that occurred within a time frame of five minutes. In an official report concerning the incident (Svenska Kraftnät 2003*a*), it is stated that it was a voltage collapse process (as illustrated in figure 2.5 in chapter 2) that eventually lead to the system blackout. It is difficult to point out specific indicators from system recordings or other data, provided in the two official reports concerning the incident, which clearly indicate that voltage collapse was the driving mechanism leading to the blackout.

In order to develop real-time assessment method, which can provide an early warning for the occurrence of a blackout similar to the one in E-Denmark and S-Sweden, it is important to identify the driving mechanism for the occurrence of the blackout. Figure 6.1 is taken from (Svenska Kraftnät 2003*a*, appendix 3) and shows recordings of the bus voltage magnitude and system frequency measured at the Odensala substation (close to the Stockholm area) for the period spanning before the fault in Horred occurred until after the system partitioning and the subsequent blackout.

An inspection of the two plots reveals the following:

- As the initial oscillations following the disturbance damped out, a period with slowly decreasing voltage magnitude can be identified from $t \approx 20\,s$ to $t \approx 80 - 85\,s$.
  - Such decline in voltage can be explained by considering the long term dynamics of the system load. The ULTCs of substation transformers try to restore voltages to pre-fault voltage levels. With each tap-change operation results in further decrease of voltages at the transmission system levels. Another factor potentially contributing the gradual voltage decline is load dynamics due to electric heating. The lowered voltage following the disturbance results in that thermostatically controlled load has to be turned on for a longer period of time to reach the level called by the thermostats. This leads to a gradual increase in the number of

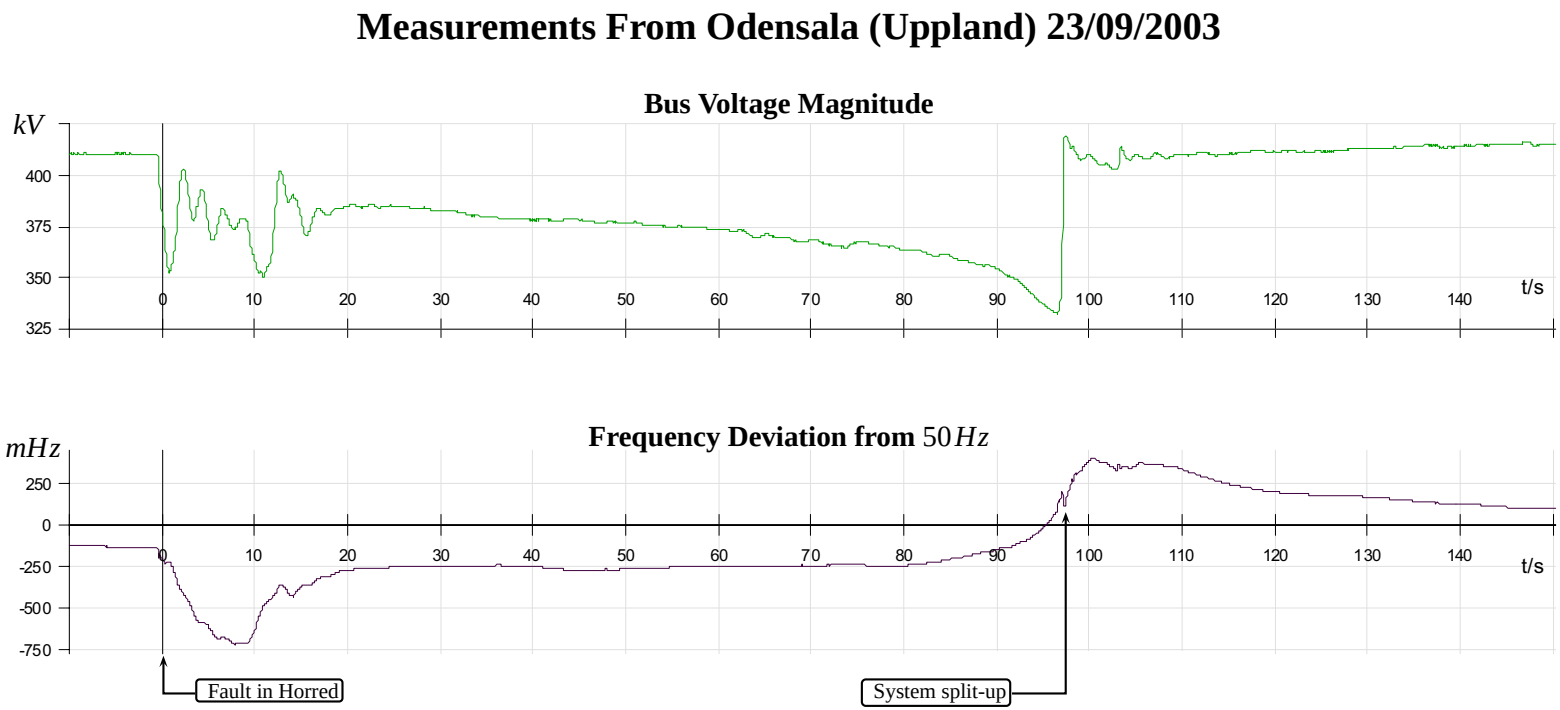

Figure 6.1: Measurements of bus voltages and frequency from the Odensala substation (near Stockholm) from the blackout in E-Denmark and S-Sweden on September 23, 2003. The measurements span the period from before the occurrence of the double busbar fault in Horred and until after the split-up of the system and the subsequent blackout. The plots are taken from (Svenska Kraftnät 2003*a*, appendix 3).

such devices connected at any given time which results in further decrease of the system voltages.

  - Voltage instability is not a necessary condition for such slow decline in voltage to occur.

- During the last seconds before the system partitioning, the voltage is decaying more rapidly.
  - That could be an indication of a loss of synchronism between two subgroup of generators.
  - Such rapid fall in voltage magnitude is experienced at intermediate points between two subgroups of generators that are approaching angular separation of 180 degrees.
- The measured system frequency begins to increase rapidly from approximately $t = 80\,s$ which indicates that system load is being heavily reduced. Such load reduction could occur:
  - when voltage instability is experienced at system load busses. The automatic control actions of ULTC-transformers would result in reduced voltage on the load side and hence reduced consumption at that bus.
  - when phase angle separation between two subgroups of generators is increasing. This causes the voltage to decline over a large area between the groups of generators. The reduction in the voltage magnitude is directly reflected into the distribution grid, resulting in an immediate load reduction.

It is not likely that the rapid increase in frequency (from $t = 80\,s$) could be explained from voltage instability mechanisms. The actions of the ULTC-transformers would decrease the system loading in relatively small discrete steps, repeated at intervals that could be few tens of seconds. The rapid increase in the frequency indicates that the load is decreasing more rapidly than can be explained by mechanisms of voltage instability.

On the other hand, a loss of synchronous operation between the group of generators in E-Denmark and the remaining generators in north of the disturbed area, provides a likely explanation for the observed rapid increase in frequency. As the phase angle difference between the two groups of genera-

tors increases, the voltage in the southern part of Sweden decreases, causing further reduction in consumption in the area. As the angular separation approaches 180 degrees, the voltage begins to fall more rapidly resulting in large decrease in the area consumption and consequently rapid increase in the observed frequency.

During the period between the fault in Horred and the occurrence of the blackout, the system entered a state of severe emergency. It is not possible to determine, from the data available in official reports concerning the blackout, whether a state of voltage instability had been experienced in the southern part of Sweden during this period. On the other hand, based on the above considerations, it can be argued that a state of aperiodic small signal instability occurred in this period.

When the system was in the state of severe emergency, it would have been of great value, if real-time time monitoring of the system stability boundaries would have been available. If, for example, the boundaries for generators aperiodic small signal stability would have been monitored, critical machines could have been identified in time before the boundaries were crossed. By this, valuable information could have been obtained concerning the instantaneous operating conditions that might be used for determining appropriate emergency control actions that could have avoided the emerging blackout.

Based on the above, it was decided to focus the research on methods for real-time assessment of aperiodic small signal stability. In the remains of this chapter, one such method is presented.

6.2 Assessment Method for Aperiodic Small Signal Stability

In the following, a method for determining boundaries of aperiodic small signal stability is presented. The method is based on the availability of real-time measurement set of the system operating conditions, which provides full observability of the system grid. The full network observability is used to establish a deterministic representation of the system conditions. The system conditions are represented as a network of impedances which have the following characteristics:

- All power injections into the system enter the network in a node of constant steady state voltage magnitude.
  - Might result in the introduction of additional network nodes and branches depending on the type of machine excitation control and state of machine protection equipment.
- The system loads are represented as impedances in the network.
  - Longer term load dynamics due to the voltage dependency of the load are not represented.
  - The method evaluates the instantaneous operating conditions, therefore the instantaneous impedance as seen from the generators is used.
  - When the stability boundary is crossed, the resulting instability is in short time frame. Therefore a short term representation of the load is used.

The benefit of representing the power injections at nodes of constant steady state voltage magnitude is that the point of maximum injectable power, into a given node, can be expressed in terms of the voltage phase angle. If power injections would not have been represented to enter the system at nodes of constant steady state voltage magnitude, the point of maximum injectable power would have been a function of both the voltage magnitude and the phase angle at the node of injection. The chosen representation of system conditions results in a reduction of the degrees of freedom associated with the determination of the boundaries for aperiodic small signal stability.

In the following, the system in figure 6.2 will be considered when deriving boundaries for aperiodic small signal stability. The figure shows a system where all loads are represented as constant impedances and where all generators are assumed to maintain a constant terminal voltage. With all system impedances known, the system operating conditions can be determined from the generators terminal voltages ($\overline{V}_1, \overline{V}_2, \overline{V}_3$ and $\overline{V}_4$).

The boundaries for aperiodic small signal stability are reached when the point of maximum power that a given generator can inject into a system node in steady state is reached. In the following, the point for maximum injectable power will be determined for a given steady state condition described by the

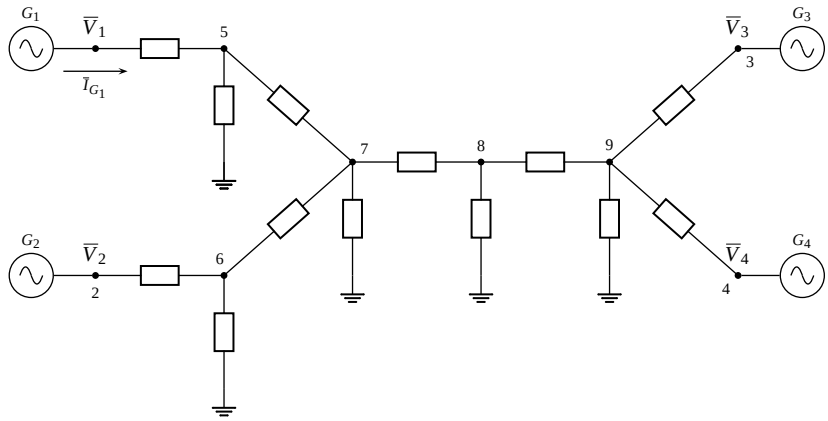

Figure 6.2: System used when deriving equations for maximum injectable power. The system loads are represented as impedances and the generators are assumed to maintain constant terminal voltage in the following derivations.

impedance network and the four complex voltage phasors ($\overline{V}_1, \overline{V}_2, \overline{V}_3$ and $\overline{V}_4$). Since the voltage magnitude at the nodes of injection is constant, only changes in voltage phase angles at injection busses can result in changes in power injection. The boundary of maximum injectable power for G_1 will be determined by fixing $\overline{V}_2, \overline{V}_3$ and $\overline{V}_4$ and determine at which phase angle δ_1 ($\overline{V}_1 = (V_1 \angle \delta_1)$) the point of maximum injectable power occurs.

The changes in current injection into node 1 can be determined by applying the superposition principle. The voltage at the point of constant voltage magnitude for G_1 will be changed from $V_1 \angle \delta_1$ to $V_1 \angle \delta_1 + \Delta\delta$. By applying the superpositions principle, the current from G_1 ($\bar{I}_{G_1}$) can be expressed as the sum of the current flowing from G_1 when all other nodes of constant voltage magnitude are shorted ($\bar{I}_{sup,G1}$) plus the current contributions due to all other nodes of constant voltages when node 1 is shorted.

$$\bar{I}_{G_1} = \bar{I}_{sup,G1} + \sum_{i=2}^{N} \bar{I}_{sup,Gi} \tag{6.1}$$

Here $N = 4$ is the number of generators. For a small change in the angle δ_1, the sum in 6.1 will remain unchanged since it is independent of voltage $\overline{V}_1$. The current due to V_1 when all other sources are shorted ($\bar{I}_{sup,G1}$) does, on the other hand, have the same magnitude but its angle will change by $\Delta\delta$.

The apparent power S_{G1} injected into node 1 can be expressed as:

$$\overline{S}_{G1} = \overline{V}_1 \overline{I}^*_{G_1} = \overline{V}_1 \overline{I}^*_{sup,G1} + \overline{V}_1 \sum_{i=2}^{N} \overline{I}^*_{sup,Gi} \tag{6.2}$$

For small changes in δ_1, the apparent power due the term $\overline{V}_1 \overline{I}^*_{sup,G1}$ will be constant since the magnitudes of $\overline{I}_{sup,G1}$ and $\overline{V}_1$ and their relative angle remains the same. Therefore the additional increase in injected power comes from the current component represented by the sum in (6.2). It is apparent that the point of maximum injectable power into node 1, occurs when the voltage $\overline{V}_1$ (of constant magnitude) is aligned with the current phasor, represented by the sum in (6.2).

By considering figure 6.2 it should be noted that the impedance that G_1 looks into, when all other points of constant voltage are shorted is the same as the Thevenin impedance between node 1 and one of the other nodes of constant voltages. Utilizing this, the current $\overline{I}_{G_1}$ can be expressed as:

$$\overline{I}_{G_1} = \frac{\overline{V}_1}{\overline{Z}_{th}} - \sum_{i=2}^{N} \frac{\overline{V}_{th,Gi}}{\overline{Z}_{th}} = \frac{\overline{V}_1}{\overline{Z}_{th}} - \frac{\overline{V}_{th}}{\overline{Z}_{th}} \tag{6.3}$$

Where $\overline{V}_{th} = \sum_{i=2}^{N} \overline{V}_{th,Gi}$ and $\overline{V}_{th,Gi}$ is the Thevenin voltage behind the Thevenin impedance that can be used to determine the current component due to the voltage source at bus i. As mentioned above, the maximum injectable power occurs when the current contribution represented by the sum in (6.1) is aligned with $\overline{V}_1$. Therefore, the maximum injectable power occurs when:

$$\arg \overline{V}_1 = \arg - \frac{\overline{V}_{th}}{\overline{Z}_{th}} \tag{6.4}$$

If $\overline{V}_{th}$ is used as phase angle reference, the above conditions for the point of maximum injectable power can be expressed as:

$$\delta_1 = 180^\circ - \phi_{th} \tag{6.5}$$

Where ϕ_{th} is the angle of the system Thevenin impedance $\overline{Z}_{th}$. The result in (6.5) is identical to the previous observation presented by (5.56) in chapter

5. There it was shown that the point of maximum injectable power into a two bus system occurs when the phase angel difference between the two bus voltages is equal $180^\circ - \phi$. The obtained expression in (6.5) means that the stability boundaries, represented by (5.35), derived for the simple two bus system in chapter 5, can be applied to an arbitrary system. This results in that the boundaries for aperiodic small signal stability of a given machine can be determined if the system Thevenin impedance, seen from the node of injection, and the corresponding injection impedance are known.

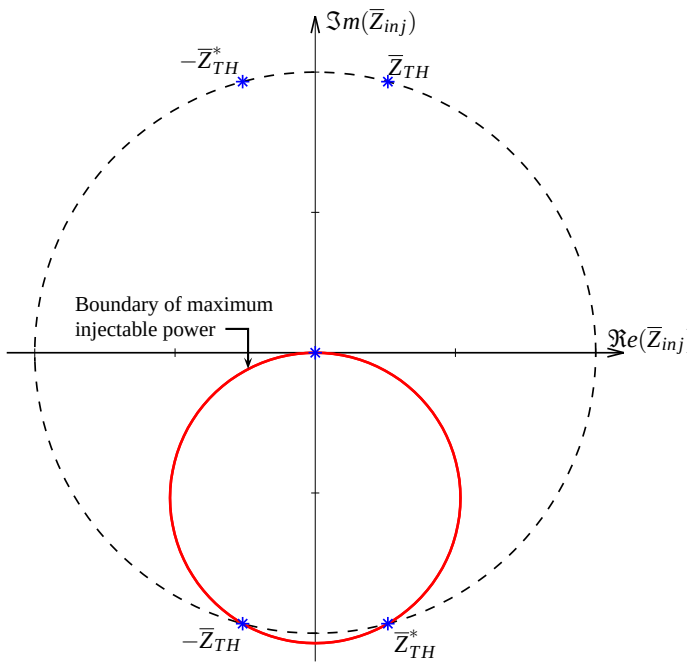

Figure 6.3: The boundary of aperiodic small signal stability (red circle) in the injection impedance plane. The boundary is described in terms of the system Thevenin impedance by equation 6.6.

Figure 6.3 shows how the stability boundary for aperiodic small signal stability appears in the injection impedance plane. The boundary is derived from (5.35), which is rewritten below:

$$Z_{inj} = -\frac{Z_{th}\sin\theta}{\sin\phi_{th}} \tag{6.6}$$

The boundary appears as an circle with radius $r = {Z_{th}}/{(2\sin\phi_{th})}$. An operation outside the circle indicates a stable operation where a relative increase in the phase angle at the bus of injection results in an increased injection. An operation inside the circle represents unstable conditions characterized by a decrease in the injected power as the phase angle increases at the bus of injection. By utilizing (6.6), the aperiodic small signal stability of a given generator can therefore be described by the following set of inequalities:

$$\left|\frac{\overline{Z}_{inj}\cdot(2\sin\phi_{th})+j\cdot Z_{th}}{Z_{th}}\right| \quad \begin{cases} >1 & \text{Stable operation} \\ =1 & \text{On the stability boundary} \\ <1 & \text{Unstable operation} \end{cases} \tag{6.7}$$

Based on the above analysis, a method for assessing the aperiodic small signal stability of the system generators can be outlined consisting of the steps shown as algorithm 6.1.

Algorithm 6.1: An outline of aperiodic small signal stability assessment.

Input: Continuous sequence of system PMU-snapshots

foreach *System Snapshot* **do**
  foreach *Generator* $j = 1 : K$ **do**
    Determine the injection impedance $\overline{Z}_{inj,j}$;
    Determine the Thevenin impedance $\overline{Z}_{th,j}$ seen from the injection node;
    Apply (6.7) to assess the generator aperiodic small signal stability;
  end
end

The most computational demanding step in the suggested approach, is the determination of the Thevenin impedance $\overline{Z}_{th,j}$ for each of the generators from a given snapshot of the system conditions. This problem is treated in chapter 9, where efficient algorithms are presented that can effectively determine the Thevenin impedances for each of the K system generators.

From the knowledge of a generator's injection impedance $\overline{Z}_{inj,j}$ and the corresponding Thevenin impedance $\overline{Z}_{th,j}$, an information concerning the machine's stability boundary and the location of the machine's operating point relative to the boundary can be derived. This means that an impedance margin from a given operating point to its corresponding stability boundary can

be determined for a given observed system conditions. In the following, the notation $\left\{\overline{Z}_{inj,j}, \overline{Z}_{th,j}\right\}$ is used to denote an operating point for generator G_j.

In chapter 7 it is addressed how the impedance margin from an observed operating point to its corresponding stability boundary can be expressed in other useful system quantities. The information concerning the generators margin to their stability boundary is a highly useful early warning indicator for emerging stability problems.

Before it is studied how impedance margins can be interpreted in terms of useful system quantities, it is appropriate to test whether the derived boundaries for aperiodic small signal stability in (6.6), can be used to detect when a given generator experiences aperiodic small signal instability. Therefore, the remaining of the chapter is focused on how the synchronous machine can be appropriately represented so their power injections occur into a node of constant steady state voltage magnitude. Furthermore, a simple test of the assessment method is carried out for the purpose of verifying the concept of detecting the occurrence of aperiodic instability, merely by using the observed values of the system Thevenin impedance and the generator's injection impedance.

6.3 Representation of the Synchronous Machine

The following sections concern how the synchronous machine can be appropriately represented in the previously suggested stability assessment method. The method aims at determining the maximum amount of power that, in steady state, can be injected into a node of constant voltage. Therefore, it is of importance that a real or fictitious node of constant voltage magnitude is used to represent the point where a given machine injects the power into the system. The representation of the appropriate point of constant voltage magnitude for power injection is dependent on the control and protection of the machine as well as physical characteristics of the machine, such as rotor saliency and magnetic saturation in the machine rotor and stator iron.

6.3.1 Mathematical Model and Steady State Operation

Extensive literature exist that concerns the modeling of synchronous machines, which offer various approaches for deriving a set of differential equations that describe the performance of the synchronous machine. In (Kundur

1994) such equations are derived for the machine stator and rotor circuits shown in figure 6.4.

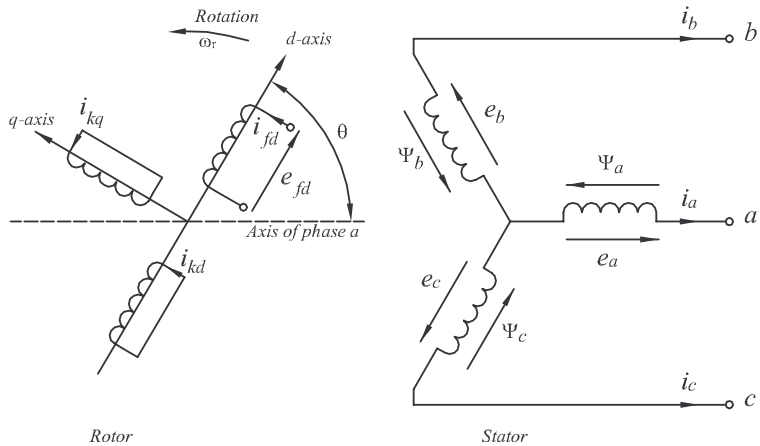

a,b,c:	Stator phase windings	k:	$1,\ldots,n$; n = number of amortisseur circuits
fd:	Field Winding	ω_r:	Rotor angular velocity
kd:	d-axis amortisseur circuit	θ:	Angle by which d-axis leads
kq:	q-axis amortisseur circuit		the magnetic axis of phase a

Figure 6.4: Stator and rotor circuits of a synchronous machine for which a mathematical model is derived in (Kundur 1994).

The figure shows the three-phase stator windings carrying the stator currents i_a, i_b and i_c and the rotor circuits which comprise a field winding and d- and q-axes amortisseur windings. After establishing basic equations of a synchronous machine, applying dq0-transformation and normalizing them using the L_{ad}-base reciprocal per unit system, the per unit machine equations in dq-reference frame are expressed as:

$$e_d = p\Psi_d - \Psi_q\omega_r - R_a i_d \quad (6.8)$$

$$e_q = p\Psi_q + \Psi_d\omega_r - R_a i_q \quad (6.9)$$

$$e_0 = p\Psi_0 - R_a i_0 \quad (6.10)$$

$$e_{fd} = p\Psi_{fd} + R_{fd} i_{fd} \quad (6.11)$$

$$0 = p\Psi_{1d} + R_{1d} i_{1d} \quad (6.12)$$

$$0 = p\Psi_{kq} + R_{1q} i_{1q} \quad (6.13)$$

where:

$$p = \frac{1}{\omega_{base}} \frac{d}{dt}$$

In the above equations, the windings' flux-linkages are used as state variables, and only one amortisseur winding is included on each each axis. The

d- and q-axes flux-linkages can be related to the d-and q-axes currents respectively, in the following way:

$$\begin{bmatrix} \Psi_d \\ \Psi_{fd} \\ \Psi_{1d} \end{bmatrix} = \begin{bmatrix} -(L_l + L_{ad}) & L_{ad} & L_{ad} \\ -L_{ad} & L_{ffd} & L_{f1d} \\ -L_{ad} & L_{f1d} & L_{11d} \end{bmatrix} \begin{bmatrix} i_d \\ i_{fd} \\ i_{1d} \end{bmatrix} \tag{6.14}$$

$$\begin{bmatrix} \Psi_q \\ \Psi_{1q} \end{bmatrix} = \begin{bmatrix} -(L_l + L_{aq}) & L_{aq} \\ -L_{aq} & L_{11q} \end{bmatrix} \begin{bmatrix} i_q \\ i_{1q} \end{bmatrix} \tag{6.15}$$

and the per unit air-gap torque can be expressed as:

$$T_e = \Psi_d i_q - \Psi_q i_d \tag{6.16}$$

All of the above machine equations are expressed in per unit quantities. The stator and rotor voltage equations (6.8)-(6.13) together with the flux-linkage equations (6.14)-(6.15), and the torque equation (6.16) describe the electrical dynamic performance of the machine.

For balanced steady-state conditions, the performance of synchronous machines can be analyzed by utilizing (6.8)-(6.13) where all time derivatives are put equal to zero. During steady state conditions, the rotating magnetic field due to stator currents is stationary with respect to rotor and therefore all amortisseur currents are zero. Utilizing (6.8)-(6.13) and (6.14)-(6.15), the machine equations under balanced steady state conditions can be written as:

$$e_d = -\Psi_q \omega_r - R_a i_d \quad (6.17) \qquad \Psi_d = -L_d i_d + L_{ad} i_{fd} \quad (6.20)$$

$$e_q = \Psi_d \omega_r - R_a i_q \quad (6.18) \qquad \Psi_q = -L_q i_q \quad (6.21)$$

$$e_{fd} = R_{fd} i_{fd} \quad (6.19) \qquad \Psi_{fd} = L_{ffd} i_{fd} - L_{ad} i_d \quad (6.22)$$

In the above equations the per unit reactances can be used instead of the per-unit inductances, since their values are equal in per unit. Rearranging (6.18) and substituting Ψ_d by utilizing (6.20), the following expression for the steady state field current is obtained:

$$i_{fd} = \frac{e_q + R_a i_q + X_d i_d}{X_{ad}} \tag{6.23}$$

In the above equations, the dq0-transformation was carried out using the scaling factors $k_d = k_q = 2/3$. This selection ensures that for a balanced steady state operation, the peak value of the stator current is equal the maximum value of which the corresponding d- and q-axis current can have. This results in that a complex phasor representation of the stator currents and voltages appears as phasors of same magnitude when transformed into dq-reference frame. This makes it possible to apply a phasor representation of the steady state values of dq-components of the armature quantities in conventional AC-circuit analysis of the system network. The stator terminal voltages can be expressed as complex phasor:

$$\overline{E}_t = e_d + je_q \tag{6.24}$$

By utilizing (6.17), (6.18), (6.20) and (6.21), e_d and e_q can be written as:

$$e_d = -\Psi_q \omega_r - R_a i_d = X_q i_q - R_a i_d \tag{6.25}$$
$$e_q = \omega_r \Psi_d - R_a i_Q = -X_d i_d + X_{ad} i_{fd} - R_a i_q \tag{6.26}$$

and similarly, the terminal current can be expressed as phasor in terms of d- and q-axes components:

$$\bar{I}_t = i_d + ji_q \tag{6.27}$$

by letting δ be the angle by which the q-axis leads $\overline{E}_t$ and ϕ be the load angle, i_d and i_q can be expressed as:

$$i_d = I_t \sin(\delta + \phi) \tag{6.28}$$
$$i_q = I_t \cos(\delta + \phi) \tag{6.29}$$

A mean of relating the terminal voltage and current phasors to the q-axis is to define a voltage $\overline{E}_q$ as:

$$\overline{E_q} = \overline{E}_t + (R_a + jX_q)\bar{I}_t = e_d + je_q + (R_a + jX_q)(i_d + ji_q) \tag{6.30}$$

substituting (6.25 and (6.25) into (6.30) yields:

$$\overline{E_q} = j(X_{ad} i_{fd} - (X_d - X_q) i_d) \tag{6.31}$$

It can be seen from the above expression that $\overline{E_q}$ is purely imaginary, and lies therefore along the q-axis. If saliency is neglected ($X_d = X_q$), then (6.31) represents a constant steady state voltage behind the synchronous reactance X_s ($X_s = X_d = X_q$) if the applied field voltage is constant. Figure 6.5 shows a steady state phasor diagram of the machine when machine saliency is neglected.

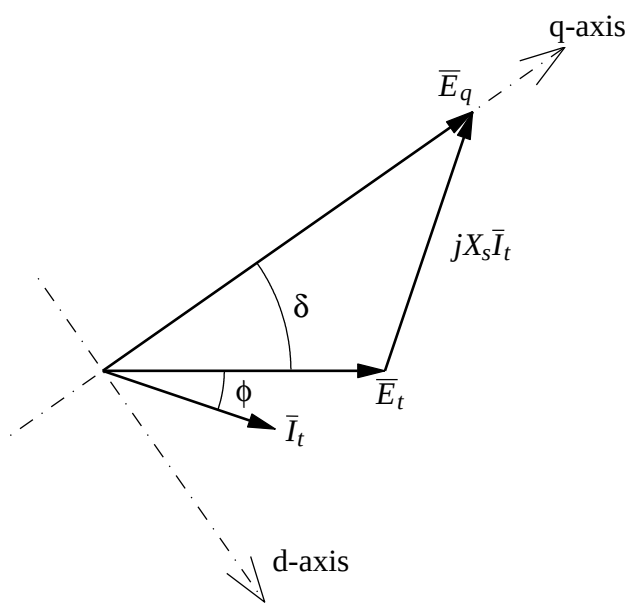

Figure 6.5: Phasor diagram of the synchronous machine when saliency is neglected. If the machine is manually excited (constant field voltage), the steady state values of the internal voltage $\overline{E}_q$ behind the synchronous reactance X_s will be constant.

Points of Constant Voltage Magnitude in Steady State

In the previous section it was shown that a synchronous machine can be represented as a constant voltage behind the synchronous reactance X_s when saliency is neglected and a constant field voltage E_{fd} is applied to the field winding. If the machine is equipped with a automatic voltage regulator (AVR) which maintains a constant voltage at the terminal of the machine

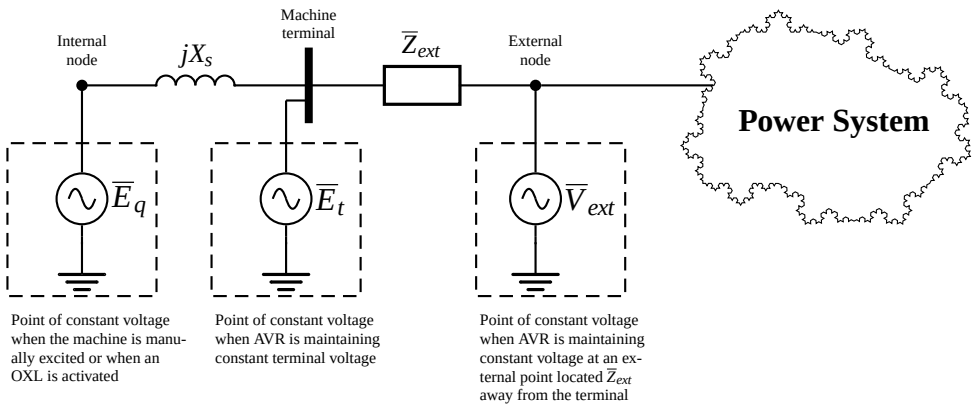

Figure 6.6: The point of constant steady state voltage magnitude for a synchronous machine dependent on the excitation control and protection used. The points of constant voltage determine wherefrom system impedances and injection impedances are calculated.

or at a point external from the generator, the machine can be represented as a source of constant voltage magnitude at its node of voltage control. When an overexcitation limiter is activated, the generator field current becomes limited to a constant value. The activation of an OXL results in the point of constant steady state voltage being behind the synchronous reactance X_s.

Figure 6.6 shows how the synchronous machine can be represented depending on its excitation control and the status of its overcurrent protection.

In the previously presented stability assessment method, the synchronous generators have to be represented as voltage sources of constant steady state voltage magnitude. This means that if the generator is manually excited, the node behind the synchronous reactance X_s must be added to the network. On the other hand, if an AVR maintains a constant voltage at a distance $\overline{Z}_{ext}$ away from the machine terminals, both $\overline{Z}_{ext}$ and the terminal node are excluded from the network equations.

Treatment of Saliency in Synchronous Machines

Figure 6.7 shows a phasor diagram for a salient pole machine, derived from equation 6.31. When the machine is manually excited, the saliency results in that the fixed voltage component due to $jX_{ad}i_{fd}$ (represented by point c) can no longer be described as an internal voltage behind a fixed reactance.

Furthermore, the voltages behind X_d (point *a*) and X_q (point *b*) will not maintain a constant steady state magnitude for changes in δ when the machine is manually excited.

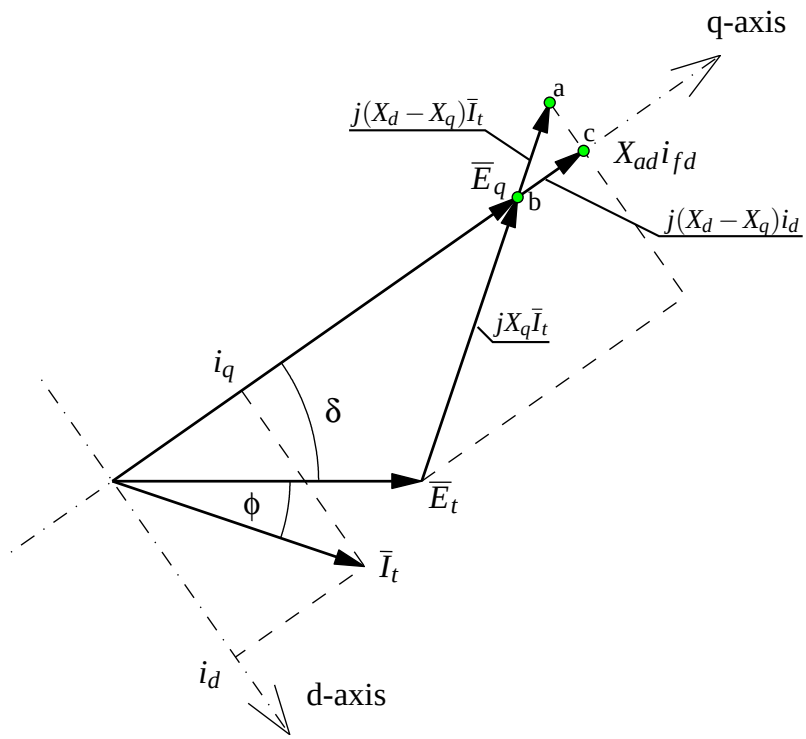

Figure 6.7: Phasor diagram over the steady state operation of a salient pole synchronous machine. The points *a* and *b* represent the voltage behind X_d and X_q respectively. Neither of these two points represents a constant steady state voltage magnitude for different operating conditions, when the machine is manually excited. The point *c* represents voltage that will be fixed for different operating conditions, but its effective impedance to the machine terminal will vary for different operating conditions.

In order to investigate the effect that rotor saliency has on the assessment method, a simple test is carried out on the system shown in figure 6.8. The system consists of a manually excited salient pole generator connected to an infinite bus through the external impedance $\overline{Z}_{ext}$.

The changes in the steady state magnitudes of the voltages behind X_d and X_q (points *a* and *b* in figure 6.7) will be investigated for six different system configurations. It will be studied how the excitation voltage $X_{ad}i_{fd}$ (point

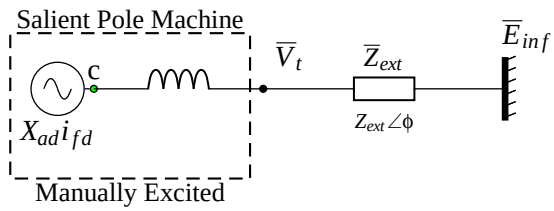

Figure 6.8: The system used for illustrating the effect that rotor saliency has on the assessment method. The effect is investigated for variations in the external impedance (both in Z_{ext} and ϕ), and variations in the ratio between two terms $X_{ad}i_{fd}$ (point *c* in figure 6.7) and E_{inf}.

c in the phasor diagram) and the value of the external impedance influence the effect that the rotor saliency has on the assessment method. Table 6.1 provides an overview of the six different system configurations used in the test.

Case:	X_d	X_q	Z_{ext}	ϕ	$X_{ad}i_{fd}$	E_{inf}
(a)	1.0	0.5	1.0	90°	1.8	1.0
(b)	1.0	0.5	**0**	90°	1.8	1.0
(c)	1.0	0.5	**3.0**	90°	1.8	1.0
(d)	1.0	0.5	1.0	90°	**1.0**	1.0
(e)	1.0	0.5	1.0	90°	**2.8**	1.0
(f)	1.0	0.5	1.0	**60**°	1.8	1.0

Table 6.1: The six different system configuration, corresponding to the system in figure 6.8, for which the effect of rotor saliency on the assessment method is investigated. All impedance and voltage values are in per unit.

The six considered cases have the following characteristics:

(a) a base case for the investigation

(b) a case with zero external impedance to the infinite bus

(c) a case with larger external impedance than in (a)

(d) a case with lower excitation voltage than in (a)

(e) a case with higher excitation voltage than in (a)

(f) a case were significant resistance is introduced in the external impedance

Figure 6.9 shows the results for the different scenarios described in table 6.1 The voltage magnitude behind X_d is plotted in blue and the voltage magnitude behind X_q is plotted in red. In all plots, the corresponding voltage magnitude when $\delta = 0^\circ$ is used to normalize the plots. The plots reveal that the voltage magnitude behind X_d is closer to a constant voltage as δ changes than the voltage behind X_q. By comparing plots (a)-(c) it can be seen that the larger the external impedance, the smaller is the effect of the saliency. Case (b) represents a situation where no external impedance is present and is provided here to illustrate a worst case scenario. This case is not of concern, since in practical power system there will always exist an external Thevenin system impedance, seen from the terminal of the machine.

Plots (d) and (e) illustrate that an increased excitation of the salient pole machines causes reduction in the effect that saliency has on the approximation of constant voltage behind X_d. The last case (f), indicates that if the resistive part of the Thevenin system impedance is significant (here shown for an impedance angle $\phi = 60^\circ$), the deviation from the constant voltage assumption increases.

In all plots (a)-(f) an information is provided regarding which effect the assumption of constant voltage behind X_d has on the suggested assessment method. In each case, the difference between when the assessment method would detect the occurrence instability and when the actual boundaries are crossed is given in degrees. Bearing in mind that (b) does not represent a practical situation, the error is quite small (below 1.5° for all except (b)). This can be considered to be quite insignificant especially since the change in injected power per a change in degree is very small when operating close to the limits of maximum injectable power.

The detection error introduced, by using the voltage behind X_d to represent the point of constant voltage magnitude for a manually excited salient pole machine, will result in instability being detected before the actual stability boundary is crossed. This introduces a slight conservatism for the stability assessment when the method is used.

The machine saliency introduces uncertainties when the machine's aperiodic small signal stability is to be assessed by the suggested method. It can though

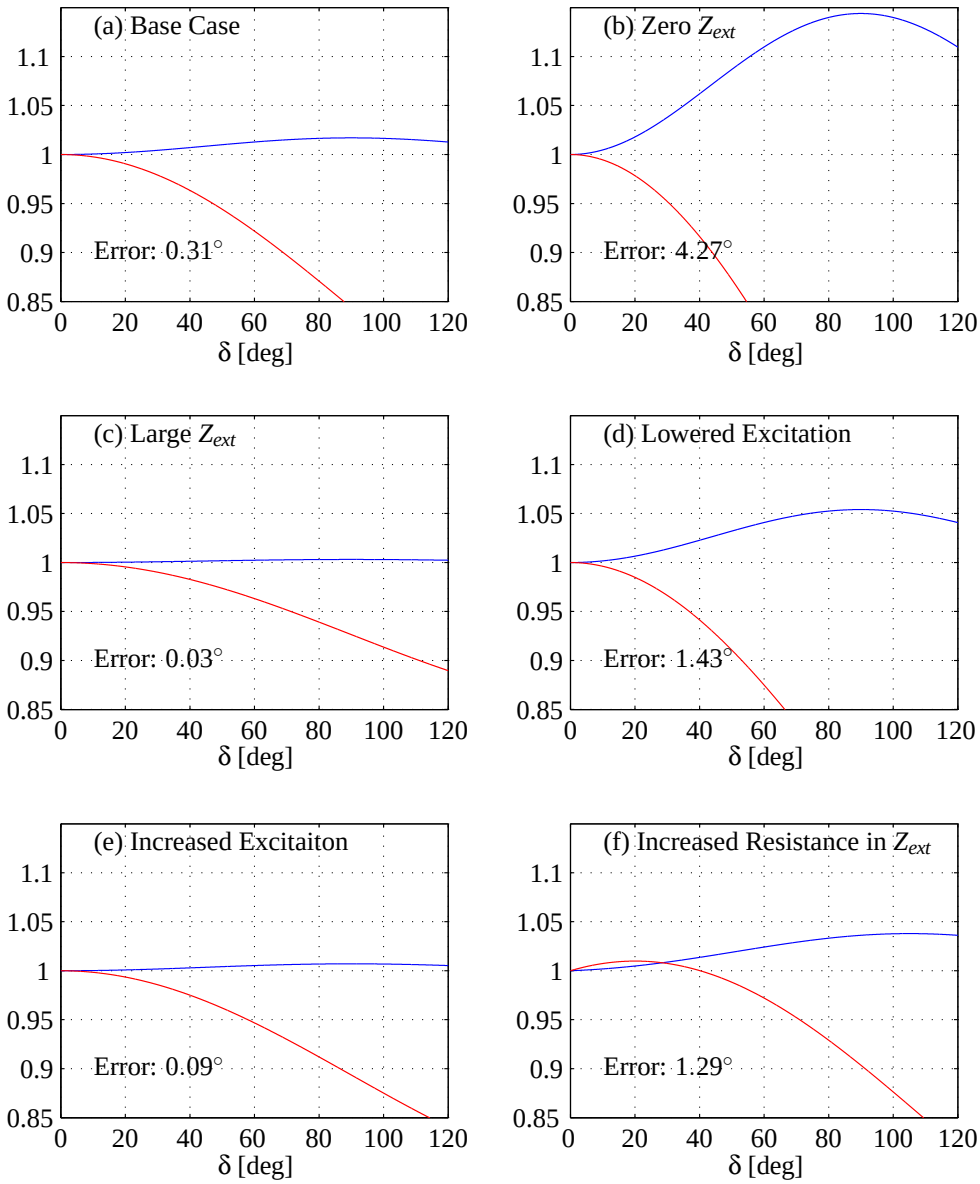

Figure 6.9: Plot of the voltage magnitude behind X_d (blue line) and X_q (red line) as function of δ for the different situations described in table 6.1. The voltages are normalized in such a way that the voltage magnitude at $\delta = 0°$ is 1 *pu*. The error in degrees by which the assessment method would detect instability before it actually occurred is shown in each plot when the voltage behind X_d is used to denote the point of constant voltage.

be argued, that the effect of the saliency will have a limited effect on the accuracy of assessment method for the following reasons:

- For the situations, when the machine terminal voltage is controlled by an AVR, the terminal of the machine is represented as the point of injection and therefore the internal impedance is not used for the stability assessment.

- When a salient pole machine is manually excited, or when an OXL is active, the machine's internal reactance has to be considered. Since the machine is connected to a system, which can be represented by a Thevenin voltage behind the system Thevenin impedance, the effect of the saliency is reduced.

Based on the above investigations it is chosen to represent salient pole machines, when manually excited or when an OXL is active, as a voltage source behind the direct axis reactance X_d. In worst case, this introduces a slight conservatism for the detection of stability boundary crossover which is though preferred rather than a late detection of the boundary crossover.

Treatment of Machine Saturation

The values of machine inductances are dependent on the saturation level of the iron in the machine. It is therefore important that the machine iron saturation is considered in order to obtain the actual value of the machine reactance for a given operating conditions. In stability studies, the representation of saturation is usually based on the following assumptions (Kundur 1994):

- The leakage inductances are usually independent of saturation. The leakage fluxes are in air for large portion of their paths so that they are not significantly affected by saturation of the iron portion. This means that the only machine inductances that saturate are the mutual inductances L_{ad} and L_{aq}.

- The leakage fluxes do not contribute to the iron saturation. This is based on that the leakage fluxes are usually small and share a path with that of the main flux for only small portion and hence the saturation is determined by the air-gap flux linkage.

- The saturation relationship between the resulting air-gap flux and the mmf under loaded conditions can be considered to be the same as un-

der no-load conditions. This allows the use of the open circuit saturation curve to represent the saturation characteristics.

- There is no magnetic coupling between d- and q- axes.

Based on the above assumptions, the effects of saturation can be expressed by letting the superscript *s* denote saturated values:

$$L_d^s = L_l + L_{ad}^s \tag{6.32}$$
$$L_q^s = L_l + L_{aq}^s \tag{6.33}$$

where:

$$L_{ad}^s = K_{sd} L_{adu} \tag{6.34}$$
$$L_{aq}^s = K_{sq} L_{aqu} \tag{6.35}$$

The saturation factors K_{sd} and K_{sq} describe the degree of saturation on the d- and q-axes respectively. For salient-pole machines the saturation in the q-axes is usually negligible, and therefore K_{sq} is considered to be at unity. For a round-rotor machine, K_{sd} and K_{sq} are different in principle, but closer to each other. In most practical cases, a q-axis saturation is not available and K_{sd} is taken to be equal K_{sq} (Kundur 1994).

The saturation factor K_{sd} can be determined from the open circuit characteristics (OCC) that relates the open circuit terminal voltage to the field current. Figure 6.10 shows a typical OCC that is used to represent the saturation characteristics of a loaded generator. The air-gap line represents the field current required to overcome the reluctance of the air-gap. The OCC deviates from the air-gap line as the field current increases, which indicates a saturation in the rotor and stator iron.

In order to represent the deviation of OCC from the air-gap line, the saturation *S*, at a given air-gap flux linkage Ψ_{at}, is defined as:

$$S_{(\Psi_{at})} = \frac{I - I_0}{I_0} \tag{6.36}$$

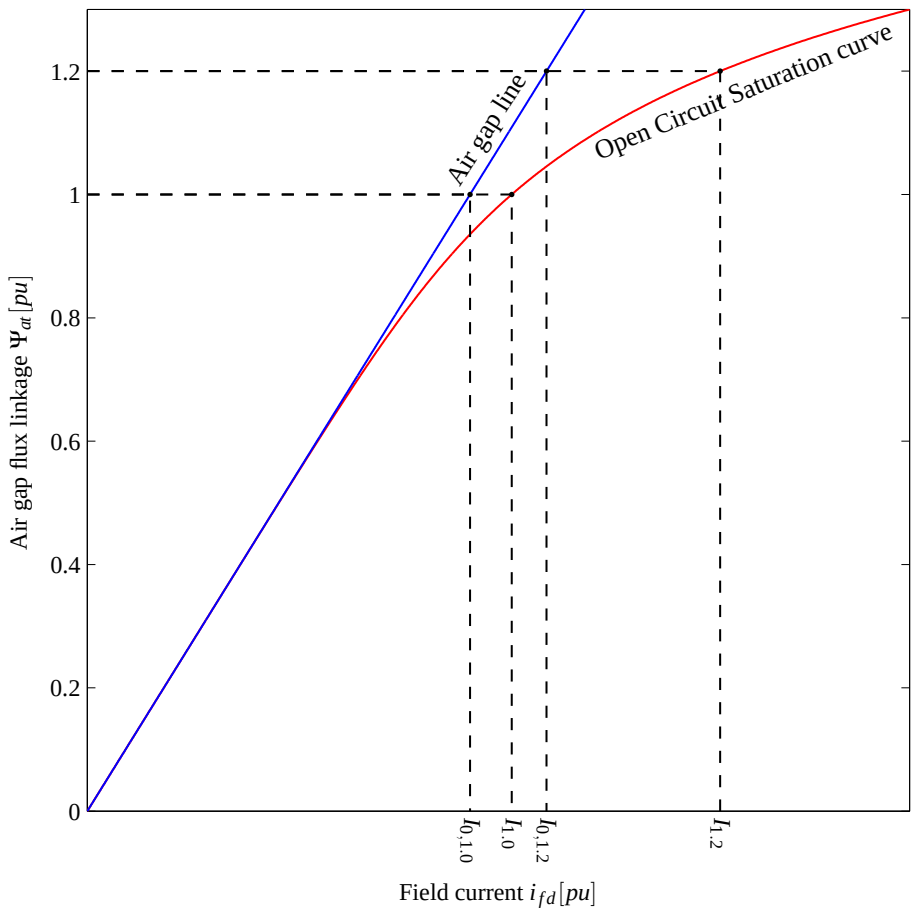

Figure 6.10: Typical open circuit characteristic (OCC) of a synchronous generator. The straight line is the air gap line, which indicates the field current needed to overcome the reluctance of the air gap. The deviation of the OCC from the air gap line gives an indication of the level of rotor and stator iron saturation.

where I_0 and I are the field currents required to generate Ψ_{at} for the unsaturated and saturated characteristics in the OCC. In several power system simulation tools, the machine saturation is specified by providing two different values of the machine saturation, $S_{1.0}$ and $S_{1.2}$, which represent the saturation when Ψ_{at} is equal to $1.0\,pu$ and $1.2\,pu$ respectively. $S_{1.0}$ can be determined from figure 6.10 as:

$$S_{1.0} = \frac{I_{1.0} - I_{0,1.0}}{I_{0,1.0}} \tag{6.37}$$

There exist many different approaches for representing saturation effects. In PSS/E, the standard synchronous machine models GENROE and GENSAE assume the saturation curve to be exponential, where the saturation S is determined by:

$$S = S_{1.0}\Psi_{at}^{\left(\frac{\ln(S_{1.2})-\ln(S_{1.0})}{\ln(1.2)}\right)} \tag{6.38}$$

The saturation factor K_{sd}, for a given operating point is defined as:

$$K_{sd} = \frac{I_0}{I} = \frac{1}{S+1} \tag{6.39}$$

If the machine terminal voltage and current phasors are measured by a PMU, the saturation factor K_{sd} can be determined. The air gap voltage can be determined as:

$$\overline{E}_a = \overline{V}_t + \overline{I}_t(R_a + jX_l) \tag{6.40}$$

Utilizing that Ψ_{at} in per unit is equal to the per unit air-gap voltage ($\Psi_{at} = E_a$), the corresponding level of saturation S can be determined by (6.38) and subsequently K_{sd} can be found by utilizing (6.39). For the previously presented assessment method, the saturated value of the machine inductance should be used to represent the point of constant voltage when the machine is manually excited. This requires that the saturation coefficient K_{sd} has to be determined for every system snapshot obtained.

6.4 Simple Example - Test of Methodology

In the following, it is tested whether the suggested assessment method is capable of detecting when the boundaries of aperiodic small stability are crossed. For that purpose, a time domain simulation of an aperiodic small signal instability scenario is carried out and the simulation output used to generate a sequence of synthetic PMU-snapshots of system conditions. The synthetic PMU-snapshots are at last used to test the suggested assessment method. A description of the case study, simulation results and the test results is provided in the following.

6.4.1 Case Description

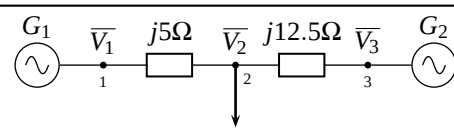

Model parameters for G_1			
MVA:	50	X_d:	2.54
T'_{do}:	3.00	X_q:	2.54
T''_{do}:	0.025	X'_d:	0.360
T'_{qo}:	2.00	X'_q:	0.468
T''_{qo}:	0.025	X''_d:	0.183
H	5.97	X''_q:	0.183
D	0.0	X_l:	0.10

Initial conditions	
$\overline{V_1}$:	$(20.00\angle\text{-}7.76°)$ kV
$\overline{V_2}$:	$(18.53\angle\text{-}27.36°)$ kV
$\overline{V_3}$:	$(20.00 \angle 0°)$ kV
P_{G1}:	24.87 MW
P_{G2}:	13.63 MW
P_{LD}:	38.50 MW
Q_{LD}:	0.0 MVAr

Figure 6.11: The three-bus system, used to test the suggested assessment method. The system voltage is $20\,kV$ line-to-line and the generator G_3 represents an infinite bus ($H \to \infty$). Generator G_1 is manually excited and is operated with constant mechanical power input.

Figure 6.11 shows the system used to test the suggested assessment method. The system consists of three $20kV$ busses, two generator busses and one load bus. Generator G_2 at bus 3, represents an infinite bus where the voltage at bus 3 is constant during the analysis. Generator G_1 is a $50\,MVA$ round rotor machine that is manually excited and operated with a constant mechanical power input. The dynamic model parameters for G_1 are provided in figure 6.11.

The initial conditions for the simulation are provided in the figure, where the load is purely resistive of $38.5\,MW$ for which the generators share the burden. The generators terminal voltage magnitude is $20kV$ line-to-line. In

the following, a loss of synchronous operation of G_1 is provoked by applying to two minor disturbances in the form of increase in load demand on bus 2.

6.4.2 Analysis of the Initial Condition

For the purpose of investigating the initial operating conditions, the system in 6.11 will be represented in such a way that the generator G_1 is represented as a source of constant voltage magnitude behind X_d, the voltage at the infinite bus is assumed constant and the load at bus 2 is represented by its impedance value. Figure 6.12 illustrates the extended system representation for the initial conditions provided in figure 6.11.

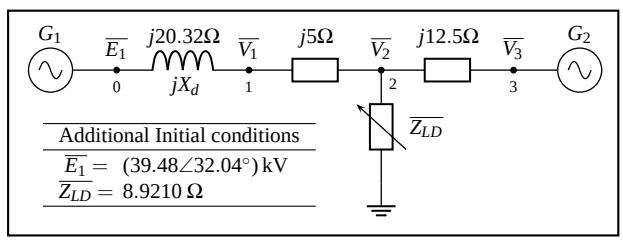

Figure 6.12: Representation of the system used for testing the stability assessment method. The manually excited generator G_1 is represented as voltage source of constant magnitude E_1 behind the direct axis reactance X_d and the load at bus 2 is represented as the impedance $\overline{Z_{LD}}$. The point of constant voltage for G_2 is at its terminal since it represents an infinite bus.

Since the steady state voltage magnitudes at the points of injections are constant, all potential operating conditions (for the chosen manual excitation of the machine) can be determined from the knowledge of the value of the phase angle difference betweens the two nodes of constant voltage ($\Delta\delta$) and the value of load impedance ($\overline{Z_{LD}} = R_{LD} + jX_{LD}$). In other words, the constrained system represented in figure 6.12 only has three degrees of freedom ($\Delta\delta, R_{LD}$ and X_{LD}). If the load impedance is constrained in such way that the load angle is fixed, the system operating point can be described by the knowledge of $\Delta\delta$ and the load impedance magnitude Z_{LD}.

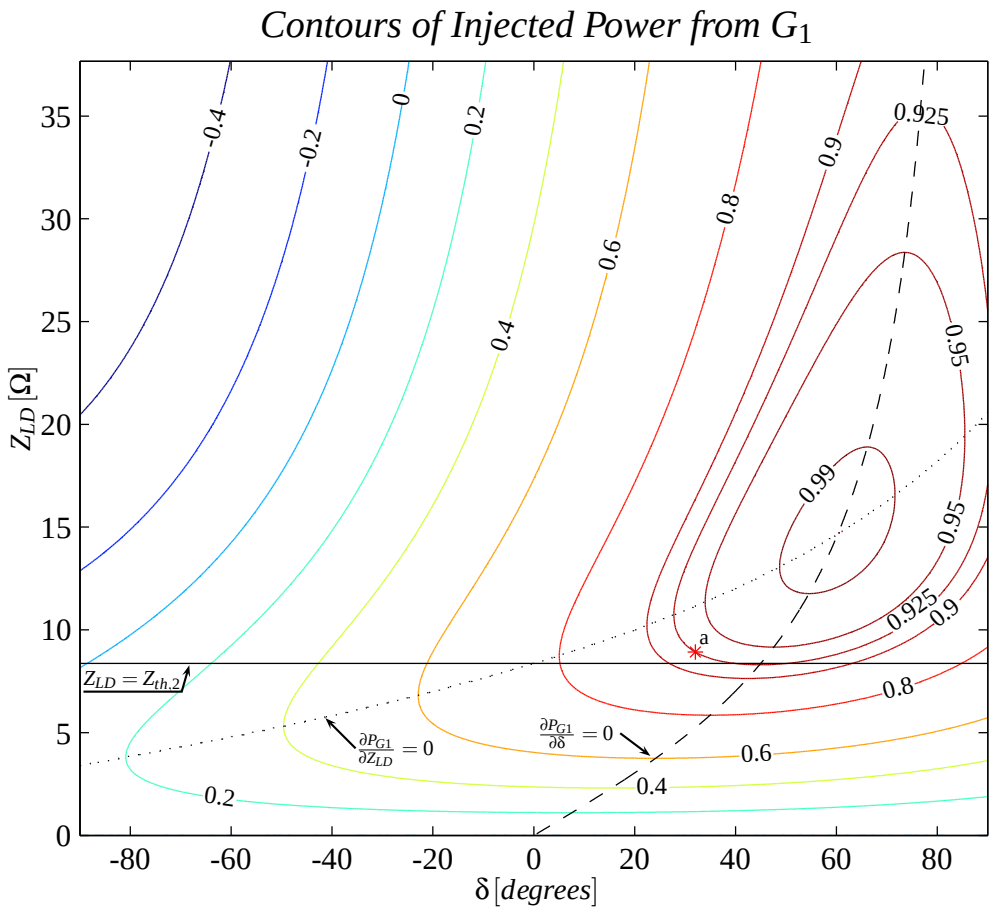

Figure 6.13: Contours of constant injected power in the δ-Z_{LD} plane for G_1 in figure 6.12. The dashed line represents the boundary of maximum injectable power for a fixed Z_{LD}, the dotted line represents maximum injectable power for a fixed δ and the straight line represents the conditions when the load impedance Z_{LD} is equal to the Thevenin impedance magnitude seen from bus 2. The contours show per unit values where the maximum injectable power is used as a base value.

In the following analysis the load angle is constant ($\phi = 0°$), and the power injection from G_1 into the node of constant voltage (node 0) is inspected in respect to variations of $\Delta\delta$ and Z_{LD}. Figure 6.13 shows how the power injection from G_1 varies as a function of these two variables. For simplicity, the phase angle of the infinite bus is chosen as angle reference resulting in that $\Delta\delta = \delta$ where δ is the angle of $\overline{E_1}$

The figure shows contours of constant injected power in the Z_{LD} - δ plane.

The contours have been normalized in such a way, that the value of maximum injectable power is used as per unit base. The initial conditions, from figure 6.11, are represented at the point *a*, which is on the contour where $P = 0.925\,pu$ (equivalent to $P_{G1} = 24.87\,MW$). The figure contains three characteristic lines; a dotted line representing the conditions where the maximum injectable power for a fixed value of delta occur (where $\partial P_{G1}/\partial Z_{LD} = 0$), a dashed line where the maximum amount of injectable power for a fixed value of Z_{LD} occurs (where $\partial P_{G1}/\partial \delta = 0$) and a straight line representing where the load impedance Z_{LD} is equal to the magnitude of system Thevenin impedance, seen from the load at bus 2 ($Z_{th,2}$).

In this study, it is the dashed line (where $\partial P_{G1}/\partial \delta = 0$) that is of interest. The dashed line represents the aperiodic small signal stability boundary for machine G_1. For any fixed value of the load impedance Z_{LD}, it can be seen that an increase in δ causes a reduced power injection into the system if the operating point is to the right of the dashed line in figure 6.13. For such conditions, a small increase of δ would lead to acceleration of the machine causing further increase in the angle δ. Since the machine acceleration increases with increasing δ, an operation on the right side of the dashed line is unstable and would gradually lead to a loss of synchronous operation of G_1 with the infinite bus.

In the example, the machine G_1 is operated with a constant mechanical power input. This means that the contour where $P = 0.925\,pu$ in figure 6.13 represents the trace of possible steady state operating points as a function of Z_{LD}. That is, if the initial conditions are considered (point *a* in figure 6.13), a small decrease in the load impedance Z_{LD} (corresponding to increased load demand) would result in a new steady state operating point, located on the contour $P = 0.925\,pu$ closer to the critical stability boundary.

In the following section, it will be shown how a loss of aperiodic small signal stability of G_1 is provoked by applying two small step decreases in the load impedance Z_{LD}. The effect of the two disturbances is illustrated in figure 6.14 which shows an enlarged view of the contour plot in figure 6.13. In the figure, point *a* represents the initial operating conditions. The first disturbance to be applied is a decrease in Z_{LD} from 8.9210Ω to 8.3039Ω which results in that G_1 will approach a new equilibrium represented by the point *b*. The post-disturbance equilibrium at point *b* is stable, but very close to the stability boundary. The second disturbance applied, is the very small

decrease in Z_{LD} from 8.3039Ω to 8.2936Ω which results in the loss of aperiodic small signal stability of machine G_1. The effect of the disturbance can be seen by considering the box containing an enlarged view of the region close to point *b*.

It can be seen that the contour of constant P_{G1} and the line representing new value of Z_{LD} do not intersect following the second disturbance, which results in that no equilibrium can be obtained and consequently the machine eventually looses synchronism.

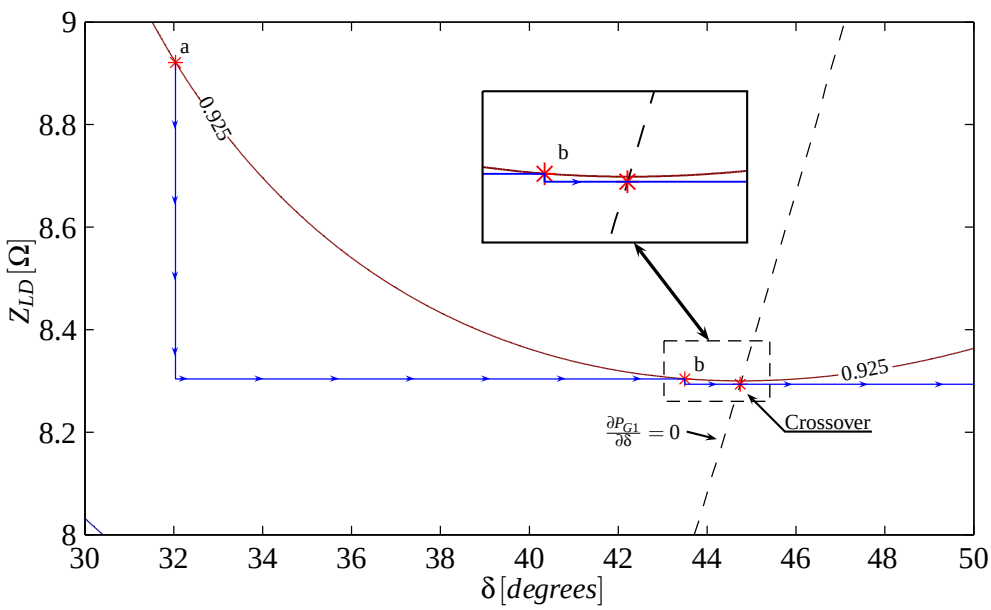

Figure 6.14: Enlarged view of figure 6.13. Point *a* represents the initial steady state operating conditions and point *b* shows the new equilibrium point following first disturbance. Point *b* is very close to the critical stability boundary and when the second disturbance is applied, no intersection can be found for the contour of constant P_{G1} and the line representing the new value for Z_{LD} following the disturbance (shown in further enlarged view inside the box). Therefore the second disturbance results in that G_1 looses synchronism.

6.4.3 Simulation Results

This section contains the results from a time domain simulation, carried out in PSS/E (version 30), of the system in figure 6.11 where previously mentioned disturbances were applied to provoke an aperiodic small signal instability. Figure 6.15 contains plot of the simulation results. Plot (i) shows

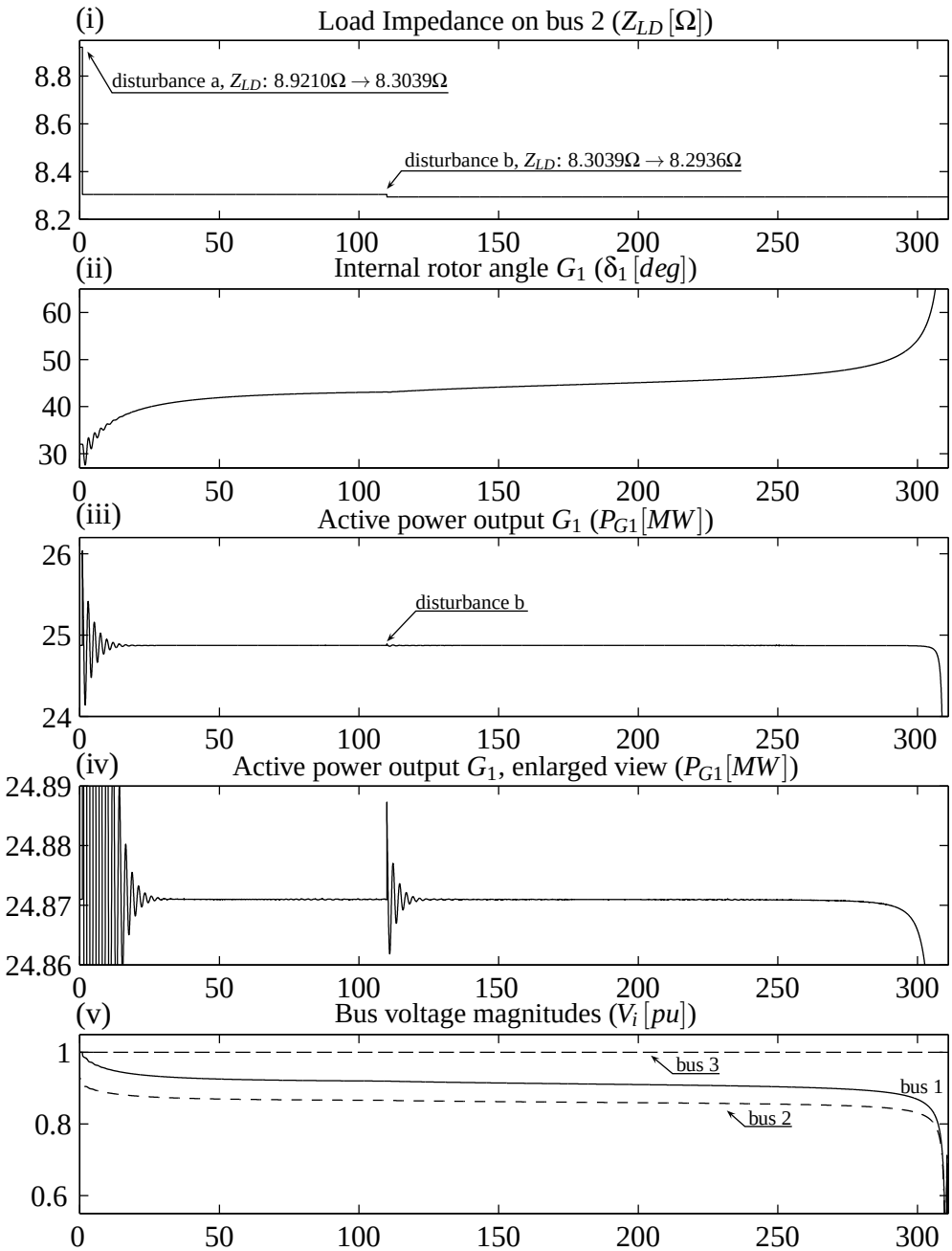

Figure 6.15: Simulation results. plot (i) shows the two applied disturbances and in (ii)-(v) are plots of the internal rotor angle and active power output from machine G_1 and the bus voltage magnitudes. Disturbance a, brings machine G_1 very close to its stability boundaries, whereafter the tiny disturbance b, causes eventual loss of rotor angle stability.

the applied changes in the load impedance that eventually caused the system instability. The first disturbance was applied at $t = 1s$ where the load impedance was changed from 8.9210Ω to 8.3039Ω. The second disturbance was applied at the time $t = 110s$ where the impedance was changed from 8.3039Ω to 8.2936Ω. It can be seen from the other plots that approximately $200s$ passed from the second disturbance until a sudden decrease in the system voltages occurred.

Plot (ii) shows the internal rotor angle of G_1, where the infinite bus is used as an angle reference. When the second disturbance is applied ($t = 110s$), a very slow increase in the rotor angle was experienced over a period of approximately $200s$ until a sharp increase in the rotor angle occurred. This result is in good accordance with the above provided description of the instability process.

Plots (iii) and (iv) show the power output from G_1 (P_{G1}). Plot (iv) provides an enlarged view of plot (iii). The second disturbance can barely be seen in (iii), but yet, it is sufficient to cause G_1 to lose its synchronous operation. In plot (iv), the size of the second disturbance can more clearly be seen. It is worth noticing, that the power output from G_1 was constant following the second disturbance until the sudden sharp decrease in the power output occurred. The emerging stability problems of G_1 are not reflected in the power output from the machine and could therefore not have been identified from observations P_{G1} alone.

Plot (v) in figure 6.15, shows the bus voltage magnitudes in the system. Following the first disturbance, the bus voltages on busses 1 and 2 appear to be very slowly decreasing until a sharp decrease occurs. It is interesting to notice that these plots resemble the plot of bus voltage magnitude from the Odensala substation in figure 6.1, for the last 80 seconds before the blackout in E-Denmark and S-Sweden.

6.4.4 Test of the Assessment Method

The time domain simulation was carried out in such a way that values of, among others, line flows and bus voltages were stored in an output file for every $20ms$ of the simulated time interval. The output data was used to generate synthetic PMU-measurements of voltage and current phasors. In that way, a snapshot of the system operating conditions for every $20ms$ was obtained.

In order to test the previously suggested assessment method, the synthetic PMU-data was used to determine the value of the injection impedance for G_1 ($\overline{Z}_{inj}$) and the value of the system line and load impedances shown in figure 6.12. With all network impedances known, the system Thevenin impedance $\overline{Z}_{th}$, as seen from the point of injection, could be determined. The values of $\overline{Z}_{inj}$ and $\overline{Z}_{th}$ are determined for every PMU-snapshot and then it is investigated when the stability boundaries, represented by (6.6), are crossed.

The results from the test are shown in figure 6.16. The figure shows four plots, where in (i) a time domain plot of the voltage magnitude at bus 2 is shown. The dots on the plotted line are used to illustrate a fixed interval of time where the distance between two adjacent dots represents $\Delta t = 5\,s$. Three events are marked on the plots, where points *a* and *b* denote the time when the two disturbances were applied and point *c* is used to denote when the stability boundary was crossed. The time of detected instability occurred approximately $71\,s$ after the second disturbance had been applied. It is worth noticing that the time elapsed from the detection of the boundary crossover until the sharp decline in voltage magnitude occurred is approximately $130\,s$.

Plots (ii)-(iv) in figure 6.16 show all the same trajectory of the injection impedance $\overline{Z}_{inj}$, but in different level of detail. The value of the injection impedance $\overline{Z}_{inj}$ is normalized in such a way that stability boundary, at any instant of time, always appears as a circle with a diameter at unity. In plot (ii), the trajectory of the injection impedance can be seen for nearly the whole time interval shown in (i). It can be seen that the initial conditions (point *a*) are quite close to the stability boundary, and when the disturbances are applied the trajectory slowly moves towards the boundary. The boundary are crossed at point *c* whereafter the the machine gradually accelerates and looses synchronism with the infinite bus.

Plot (iii) shows enlarged view of the trajectory from *a* through *b* to *c*. It can be seen that the system gradually approaches the operating point *b* following the first disturbance where the distance between two dots (that denote time interval of $5\,s$) gradually gets shorter and shorter. A gradual decrease in the distance between two points indicates that the machine is gradually decelerating and approaching an equilibrium point and a synchronous speed.

Plot (iv), provides a further enlarged view of the injection impedance trajectory from the occurrence of the second, very small disturbance, and until

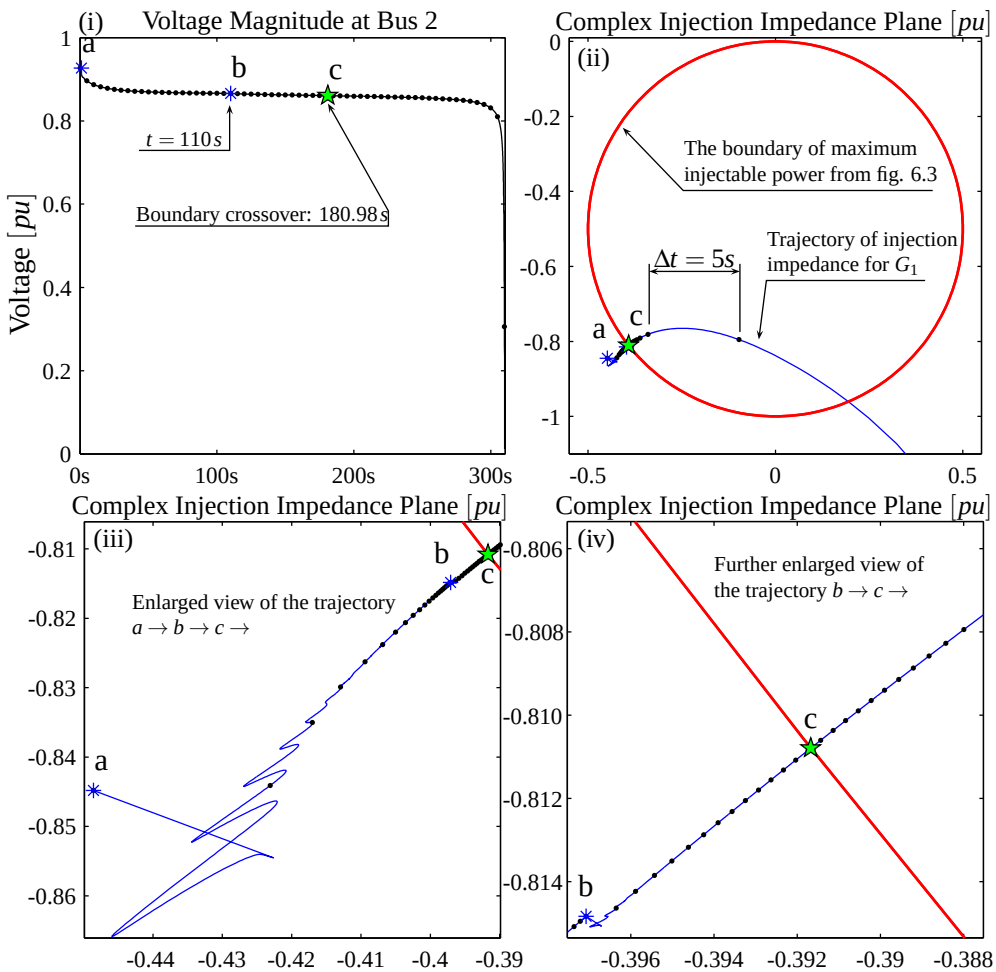

Figure 6.16: Test results. (i) plot of the voltage magnitude on bus 2 where the two disturbances are marked with *a* and *b* respectively, and the time when the boundaries are crossed is marked *c*. (ii)-(iv) the corresponding trajectory of the injection impedance for generator G_1. The injection impedance values are normalized in such a way that the stability boundary has a diameter at unity at any instance of time.

after the boundary was crossed. If the trajectory from *b* to *c* is studied, it can be seen that the disturbance initially caused increase in the average angular velocity of the machine, which is reflected by a gradual movement of the system operating point towards the boundary. As the operating point moves closer to the boundary (from *b* to *c*), the distance between adjacent dots is gradually decreasing, which indicates that the machine is slowly decelerating towards synchronous speed during that period. When the boundary is crossed, it can be noticed that the distance between the dots is gradually increasing. This indicates that the machine is accelerating, which is expected behavior when the boundary for aperiodic small signal instability has been crossed.

The test result in figure 6.16 shows that the suggested assessment method accurately detects, for the studied system, when the boundary of aperiodic small signal stability is crossed.

Furthermore, it is interesting to see how long it can take from when the stability boundary is crossed until the sharp decline in the voltage magnitude occurs. During this time interval the machine is slowly but gradually accelerating, yet it is very difficult to identify that the machine was unstable merely by inspecting the plots of the system voltage magnitude and power output in figure 6.15.

6.5 Voltage instability vs Rotor Angle Instability

In the previous example it was illustrated how the suggested assessment method was capable of detecting when the generator G_1 crossed the critical boundary for aperiodic small signal stability. In the example, voltage instability was of no concern since the system load was represented as fixed impedance and no voltage control equipment was included in the example. This means that no mechanisms were present that could cause a voltage instability at the load bus, even if the point of maximum deliverable power to the load would have been reached.

In the following, it is investigated where the boundary for voltage instability appears in the previous example, if the load bus would have been equipped with an ideal ULTC-transformer. In such situation, the boundary of voltage instability at bus 2 is reached when the point of maximum deliverable power to the load is reached.

A few methods for detecting the point of voltage instability have been suggested that are based on comparison of the load impedance Z_{LD} at a given bus to the system Thevenin impedance seen from the same bus. The concept is that the maximum deliverable power to the load occurs when the magnitude of the load impedance becomes equal to the magnitude of the system Thevenin impedance. This would be true, if the system Thevenin voltage magnitude would remain constant as the value of the load impedance changes. For practical power systems this is not the case and it will be shown in the following that, for the system in previous example, the point of maximum deliverable power to the load occurs well before the magnitude of Z_{LD} becomes equal the magnitude of $Z_{th,2}$.

The boundary of maximum deliverable power to the load, when G_1 is supplied with constant mechanical input power, can be investigated by considering two different contour plots; one showing contours of delivered power to the load (P_{LD}) and the other showing contours of injected power by G_1 (P_{G1}). Figure 6.17 contains those two plots. In the upper left plot, contours of constant delivered power to the load P_{LD} are shown in per unit where the peak value of P_{LD} is used as per unit base. Inspection of the plot reveals that the maximum deliverable power to the load, when the angle δ is fixed, occurs when Z_{LD} is equal $Z_{th,2}$. A fixed value of δ as Z_{LD} changes results in that the system Thevenin voltage, seen from bus 2, remains constant and therefore does the point of maximum deliverable power to the load P_{LD} occur when Z_{LD} is equal $Z_{th,2}$. Furthermore, it can be seen that the maximum amount of power delivered to the load for a fixed value of Z_{LD} occurs when $\delta = 0^\circ$. The reason for this is that the system Thevenin voltage magnitude is at its maximum, for the considered system, when $\delta = 0^\circ$.

Contours of constant injected power from G_1, P_{G1}, are revisited in the upper right plot. When G_1 is operated with constant mechanical power, the contours represent the trajectory of the system steady state operating points as a function of the parameters δ and Z_{LD}. It should be noticed that, for a constant value of P_{G1}, the value of δ changes as Z_{LD} changes. The changes in δ results in that the system Thevenin voltage magnitude will vary with changes in Z_{LD} and therefore, the point of maximum deliverable power to the load cannot be described by the straight line where $Z_{LD} = Z_{th,2}$.

For the purpose of illustrating where the boundary of maximum deliverable power to the load is located, when the generator G_1 is operated with constant

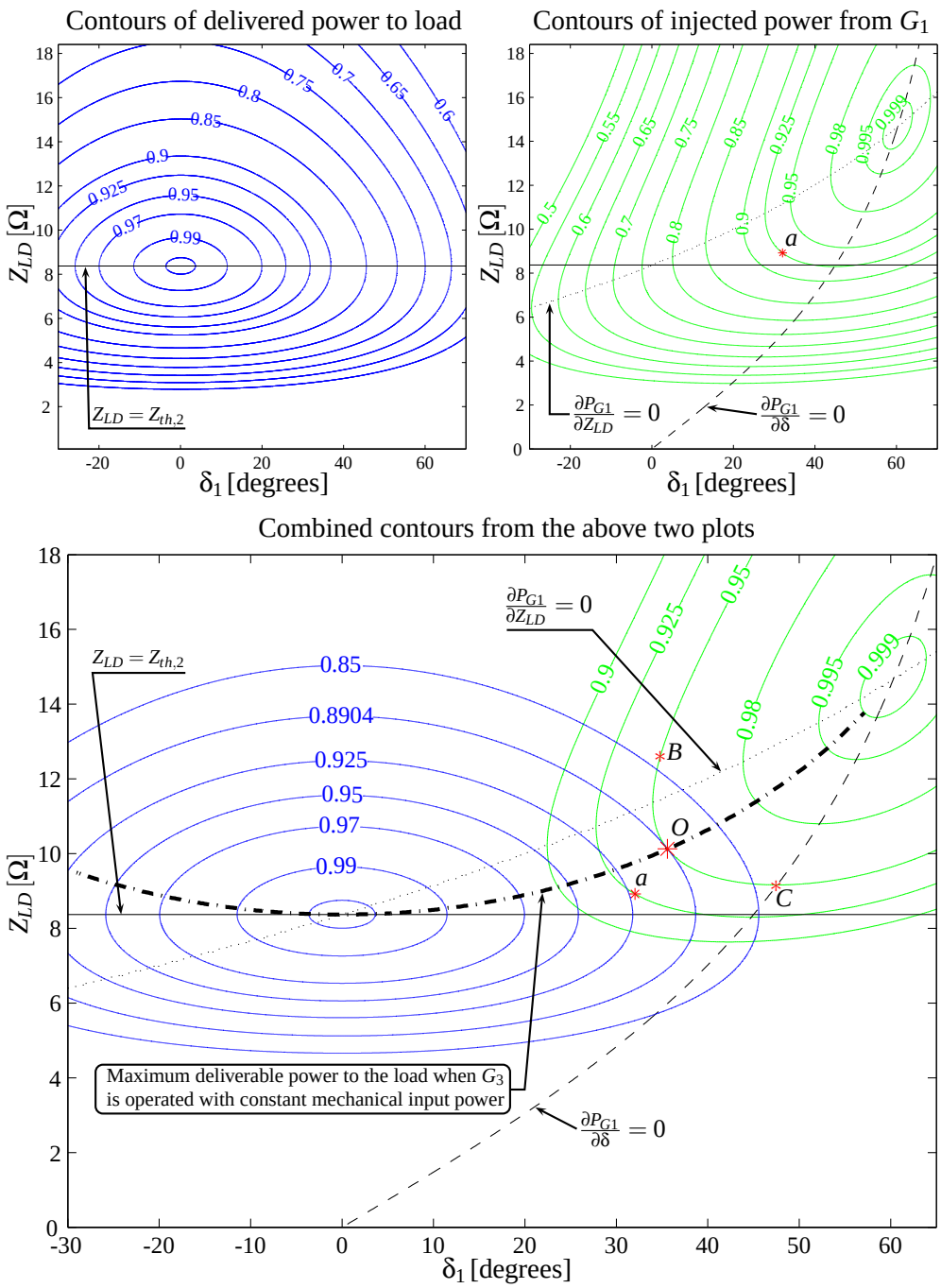

Figure 6.17: Contours of constant delivered power to load (P_{LD}) and contours of constant injected power from G_1 (P_{G1}) combined into one plot for visualizing the boundary for maximum deliverable power to the load when G_1 is operated with constant mechanical input power.

mechanical power input, the bottom plot in figure 6.17 is considered. In the plot, the contours from the two above plots have been combined into one. In order to determine the boundaries of maximum deliverable power to the load, it is useful to consider the contour where $P_{G1} = 0.95\,pu$, starting from the point *B*. As the load impedance Z_{LD} decreases, the operating point moves along the contour $P_{G1} = 0.95\,pu$ towards the point *O* resulting in an increase of the delivered power to the load. When Z_{LD} has reached the a value corresponding to the point *O*, it can be seen that the maximum deliverable power to the load has been reached. A further decrease in Z_{LD}, beyond the point *O*, results in a reduction of the power delivered to the load. It can be seen that the point *O*, which represents maximum deliverable power to the load when $P_{G1} = 0.95\,pu$ occurs at a value for Z_{LD} that is significantly higher than the system Thevenin impedance $Z_{th,2}$.

The locus of maximum deliverable power to the load, when G_1 is operated with constant mechanical power is shown as a dashed-dotted line in the plot. This line would be the boundary for voltage instability, if an ULTC-transformer would have been attempting to maintain a constant voltage at the load side on bus 2. It can be seen that actual border line for voltage instability deviates significantly from the line where Z_{LD} equals $Z_{th,2}$. This shows that methods, which assess the system voltage instability by comparing system load impedance Z_{LD} to the Thevenin impedance $Z_{th,2}$ (e.g. (Julian et al. 2000)) would fail for the system in context.

In fact, if the case $P_{G1} = 0.95\,pu$ is considered, both the boundary of voltage stability (at point *O*) and the boundary for aperiodic small signal stability (at point *C*) would be crossed, before the conditions $Z_{LD} = Z_{th,2}$ are reached. This means that the control actions of an ULTC-transformer at bus 2 would continually decrease the load impedance Z_{LD} when the actual voltage stability boundaries are crossed. This automatic deterioration of the system operating conditions would results in that machine G_1 looses synchronism and eventual blackout occurs before a voltage stability assessment method, which uses the $Z_{LD} = Z_{th,2}$ criteria, would detect voltage instability.

6.6 Partial Conclusion

A method suitable for real-time monitoring of aperiodic small signal stability boundaries has been presented. The method utilizes the boundaries

for maximum injectable power into a two bus system derived in chapter 5. The assessment method uses the system Thevenin impedance, seen from the node of injection, and the injection impedance seen from the same node. The Thevenin impedance is used to derive the generator's stability boundary, while the injection impedance determines the position of the machine's operating point in respect to the boundary.

The method is based on a linear network representation of the system conditions, which are represented in terms of impedances and constant voltage magnitudes at the nodes of injection. By representing the synchronous machine as a constant voltage behind a reactance introduces some inaccuracy for the detection of stability crossover compared to when the machine nonlinearity due to saliency and saturation effects are considered. The effects of the machine saliency is reduced and can even be neglected if the system Thevenin impedance is large compared to the machine's direct axis reactance and if the internal voltage magnitude is significantly higher than the system Thevenin voltage behind the Thevenin impedance.

At last it was shown by a simple example, where both saliency and saturation were excluded, that the presented assessment method accurately detects when the boundaries for aperiodic small signal stability are crossed.

Since it has been verified that the analytically derived stability boundaries can be used for instability detection, the boundaries will therefore be used for providing early warning for an emerging stability problem, where the margin from the generators injection impedances to the boundary is monitored. It is though important, that the monitored stability margin is represented in terms of meaningful system quantities. The following chapter covers, among others, how stability margins in terms of injection impedance can be related to meaningful system quantities.

Chapter 7

Visualizing the System Operating Conditions

This chapter provides a description of how multiple operating points for all of the system generators, can be visualized in a single plot. The visualization of the operating conditions enables visual identification of critical machines and its corresponding margin to the boundaries of aperiodic small signal stability.

7.1 Interpreting Stability Margins

It was shown in the previous chapter that the presented assessment method for aperiodic small signal stability is capable of detecting when the stability boundary is crossed by a given generator. For the purpose of obtaining an early warning for an emerging stability problem, it is not sufficient to merely detect when the stability boundary is crossed. It is necessary that the early warning is received in time before that actual boundaries are crossed, such that appropriate remedial control actions can be taken to avoid instability.

For the purpose of providing an early warning for an emerging stability problem, the margin from an observed operating point to its corresponding stability boundary may become a useful indicator. In the suggested assessment method, the stability boundary related to a given operating point $\left\{\overline{Z}_{inj,i}, \overline{Z}_{th,i}\right\}$, is presented in the injection impedance plane. A margin from the point $\overline{Z}_{inj,i}$ to its critical boundaries expressed in term of injection impedance does not provide a useful physical interpretation of the closeness to instability. For that purpose, it is more useful to derive margins that are expressed in quantities such as active power or as percentage power margin to the maximum.

In chapter 6 it was shown that the stability boundary is represented by a line of constant phase angle where $\delta = 180 - \phi_{th}$. By utilizing this, the margin from a observed operating point $\left\{\overline{Z}_{inj,i}, \overline{Z}_{th,i}\right\}$ to its corresponding boundaries can be expressed in several different ways. For the purpose of deriving one such margin, the apparent power injection is expressed in terms

of Thevenin voltage and the Thevenin impedance:

$$\overline{S}_{inj} = \left(\frac{\overline{E}_{th} - \overline{V}}{\overline{Z}_{th}} \right)^{\star} \overline{V} = \frac{E_{th} V}{Z_{th}} e^{j(\delta + \phi_{th})} - \frac{V^2}{Z_{th}} e^{j(\phi_{th})} \tag{7.1}$$

Where $\overline{E}_{th}$ is used as phase angle reference. The active power injection becomes:

$$P_{inj} = \frac{E_{th} V}{Z_{th}} \cos(\delta + \phi_{th}) - \frac{V^2}{Z_{th}} \cos(\phi_{th}) \tag{7.2}$$

A power injection is represented by a negative value of P_{inj}. As mentioned previously, the maximum injected power occurs when $\delta = 180^{\circ} - \phi_{th}$ and can therefore be expressed as:

$$P_{inj,max} = -\frac{E_{th} V}{Z_{th}} - \frac{V^2}{Z_{th}} \cos(\phi_{th}) \tag{7.3}$$

An active power margin ΔP_{inj} becomes:

$$\Delta P_{inj} = P_{inj,max} - P_{inj} = -\frac{E_{th} V}{Z_{th}} (\cos(\delta + \phi_{th}) + 1) \tag{7.4}$$

The above can be expressed as a percentage margin to the maximum $\%\Delta P_{inj}$ in the following way:

$$\%\Delta P_{inj} = \frac{\Delta P_{inj}}{P_{inj,max}} \cdot 100\% = \frac{\cos(\delta + \phi_{th}) + 1}{1 + \left| \frac{\overline{Z}_{inj}}{\overline{Z}_{th} + \overline{Z}_{inj}} \right| \cos(\phi_{th})} \cdot 100\% \tag{7.5}$$

The above margins describe how much the active power injection can be increased as the phase angle δ is increased to its critical value at $\delta = 180 - \phi_{th}$, while other system variables are fixed. The margin is therefore derived considering changes in only one system variable, the voltage phase angle δ.

This is different from how stability margins are derived by means of continuation methods where the system is stressed in a particular direction by applying some pre-defined loading and dispatch patterns. The stress patterns are usually based on operational experience, where the daily consumption patterns are usually the same and well known by the system operators.

Even though the above suggested stability margins, derived from the phase angle margin $\Delta\delta$, are not obtained by applying specific "normal" stress patterns they do anyhow provide a useful information. The method is intended to provide a stability assessment during emergency operating conditions. During such conditions, it is not likely that the normal stress patterns would give the most likely stress direction of the system, since many other control and load restoration mechanisms have a more significant role in such situations. The actual stress direction might be dominated by the actions of ULTC-transformers and other devices that try to restore the pre-disturbance consumption. This means that the "normal" stress direction is not suitable for determining a margin to the system stability boundary. On the other hand, the element-wise margins (7.4)-(7.5) provide a valuable information concerning which of the system generators is operating close to, or approaching its stability boundaries. Such information could be used to take remedial actions to avoid an emerging instability.

7.2 Normalizing Multiple Operating Points

The suggested method performs an element-wise assessment of the generators aperiodic small signal stability. In a system having k generators, k individual Thevenin impedances $\overline{Z}_{th,i}$ $(i = 1,\ldots,k)$ are determined resulting in that k different stability boundaries are used for the assessment. In chapter 5 it was shown that the stability boundaries are circular, and therefore it is possible to normalize all the k boundaries in such way that they appear as a circle with radius at unity centered at the origin of the normalized impedance plane. By doing so, all of the k operating points for the generators can be visualized in the same normalized injection impedance plane where all of the points are held against the same stability boundary.

In chapter 5 it was shown how several characteristic lines of constant P,Q,V and δ could be represented in the injection impedance plane, if only the system Thevenin impedance is known. It would be desirable if some characteristic lines could be derived in a normalized injection impedance plane, such that the lines provide a useful information regarding the operating conditions of all normalized operating points.

In the following, it will be shown how a given operating point $\left\{\overline{Z}_{inj,i},\overline{Z}_{th,i}\right\}$ can be mapped into a normalized injection impedance plane such that the

voltage phase angle margin $\Delta\delta$ to the critical stability boundary and the lines of constant $V/E_{th,i}$ ratio are preserved.

7.2.1 Mapping of lines of constant V and $\Delta\delta$

In this section, the lines of constant phase angle margin $\Delta\delta$ and normalized voltage V/E_{th} in the injection impedance plane for an arbitrary $\overline{Z}_{th}$ will be mapped into a plane where the boundaries are derived from Thevenin impedance having the same magnitude as $\overline{Z}_{th}$ and purely inductive. That is, the operating point $\left\{\overline{Z}_{inj,0}, \overline{Z}_{th,0}\right\}$ is mapped as the point $\left\{\overline{Z}_{inj,\star}, (Z_{th,0}\angle 90^\circ)\right\}$ in the injection impedance plane as illustrated in figure 7.1.

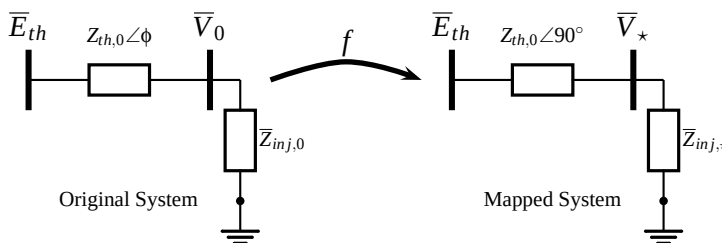

Figure 7.1: It is desired to derive the mapping of a original operating point $\left\{\overline{Z}_{inj,0}, \overline{Z}_{th,0}\right\}$ (represented by the system to the left) to an equivalent point $\left\{\overline{Z}_{inj,\star}, (Z_{th,0}\angle 90^\circ)\right\}$ (represented by the system to the right). The characteristics of the mapped operating point should be such that the normalized voltage magnitude is preserved ($V_0/E_{th} = V_\star/E_{th}$) and the phase angle margin $\Delta\delta$ is as well preserved after the mapping.

In the following, the mapping:

$$f : \left\{\overline{Z}_{inj,0}, \overline{Z}_{th,0}\right\} \rightarrow \left\{\overline{Z}_{inj,\star}, (Z_{th,0}\angle 90^\circ)\right\} \tag{7.6}$$

is determined where the following properties of the mapped operating point are preserved:

- The normalized voltage magnitude V/E_{th} is the same for both operating points
- The phase angle margin $\Delta\delta$ to the critical boundary is preserved after the mapping

In the subsequent derivations, $\overline{Z}_{inj,0}, \overline{Z}_{th,0}, \overline{V}_0$ and δ_0 are used to denote original variables while $\overline{Z}_{inj,\star}, \overline{Z}_{th,\star}, \overline{V}_\star$ and $\delta_\star$ denote the mapped variables. It is

desired that the phase angle difference from operating point to the boundary is preserved after the mapping which results in:

$$\Delta\delta = 180^\circ - \phi - \delta_0 = 90^\circ - \delta_\star \tag{7.7}$$

It is also desirable that the normalized voltage magnitude is the same. For that purpose, the following relation between the original voltage phasor $\overline{V}_0$ and the mapped voltage phasor $\overline{V}_\star$ can be utilized:

$$\frac{\overline{V}_\star}{E_{th}} = \frac{\overline{V}_0 e^{j(\delta_\star - \delta_0)}}{E_{th}} = \frac{\overline{V}_0 e^{j(\phi - 90^\circ)}}{E_{th}} \tag{7.8}$$

The normalized voltage magnitude can be expressed in terms of variables shown in figure 7.1:

$$\frac{\overline{V}_\star}{E_{th}} = \frac{\overline{Z}_{inj,\star}}{Z_{th,0}e^{j90^\circ} + \overline{Z}_{inj,\star}} = \frac{\overline{Z}_{inj,0}}{\overline{Z}_{th,0} + \overline{Z}_{inj,0}} e^{j(\phi - 90^\circ)} \tag{7.9}$$

Utilizing that $Z_{th,0}e^{j90^\circ}e^{j(\phi-90^\circ)} = \overline{Z}_{th,0}$ and solving for $\overline{Z}_{inj,\star}$ gives:

$$\overline{Z}_{inj,\star} = \frac{1}{\frac{1}{\overline{Z}_{inj,0}} + \frac{1}{\overline{Z}_{th,0}}\left(1 - e^{j(\phi-90^\circ)}\right)} = \frac{1}{\overline{Y}_{inj,0} + \overline{Y}_{th,0}\left(1 - e^{j(\phi-90^\circ)}\right)} \tag{7.10}$$

Equation 7.10 describes the mapping in (7.6) such that the above mentioned characteristics are preserved after the mapping.

Figure 7.2 illustrates the effect of the mapping of injection impedances according to (7.10). The plot to the left shows an equally meshed grid in the injection impedance plane, the stability boundary when $\overline{Z}_{th,0} = 1\angle 70^\circ$ (the black circle) and line of constant $\Delta\delta$ that is 36° away from the boundaries (light blue circle). Additionally, several reference points are marked on the circles for illustrating the effect of the mapping.

The plot to the right shows the results of the mapping when (7.10) is applied. Each of the mapped injection impedance points is such that the voltage magnitude and the phase angle difference to the critical boundary has

been preserved. The stability boundary appears now as a circle with diameter at unity, which is the same as the boundary obtained when $\overline{Z}_{th} = 1\angle 90^\circ$ and the blue line represents the line of constant phase angel when $\delta = 54^\circ$ which corresponds to a phase angle margin $\Delta\delta = 36^\circ$.

Figure 7.2 illustrates that an arbitrary operating point $\left\{\overline{Z}_{inj,0}, \overline{Z}_{th,0}\right\}$ can be mapped as $\left\{\overline{Z}_{inj,\star}, (Z_{th,0}\angle 90^\circ)\right\}$ by utilizing (7.10) where characteristics concerning $\Delta\delta$ and normalized voltage $V/E_{th,i}$ are preserved after the mapping. In order to visualize multiple operating points in the same impedance plane, further manipulation of (7.10) is needed such that the same normalized stability boundary can be applied to all of the k operating points for the k system generators.

7.2.2 Characteristics of the Normalized Injection Impedance Plane

For the purpose of normalizing the stability boundary for aperiodic small signal stability, it is relevant to consider how boundary appears in the injection impedance plane. In chapter 5 it was mentioned that the stability boundary appears as a circle with the following characteristics:

- With radius $r = Z_{th}/(2\sin\phi)$
- The center of the circle is located on the imaginary axis where $X_{inj} = -r$

In the following, the stability boundaries will be normalized in such way, that they appear as a unit circle centered at the origin of the normalized impedance plane. For that purpose, all impedance values $\overline{Z}_{inj,\star}$ have to be shifted by r in the direction of the imaginary axis and scaled down by factor r. For achieving that, the expression (7.10) can be manipulated:

$$\overline{Z}_{inj,\star,pu} = \frac{\overline{Z}_{inj,\star}}{r} + j = \frac{2\overline{Z}_{inj,\star}}{Z_{th,0}} + j \tag{7.11}$$

By applying (7.11), the characteristic lines for constant δ and V and the stability boundary can be used to visualize all of the k operating points $\left\{\overline{Z}_{inj,i}, \overline{Z}_{th,i}\right\}$ in the same impedance plane, where the same boundary applies for all operating points.

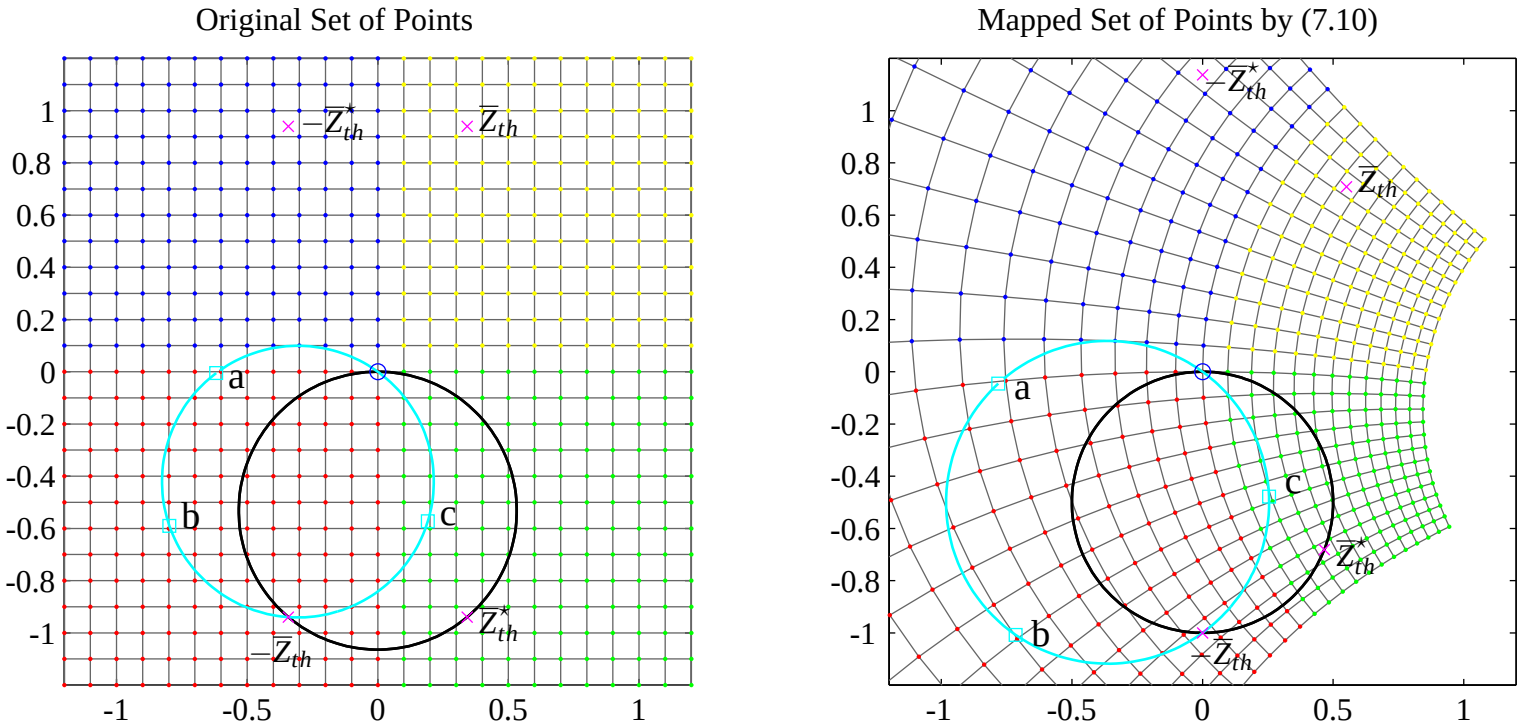

Figure 7.2: Illustration of the mapping of injection impedances. To the left, the critical boundary (in black) and the circle representing the conditions where $\Delta\delta = 36^{\circ}$ (in light blue), when $\overline{Z}_{th,0} = 1\angle 70^{\circ}$. To the right, mapping of all points in the left into a impedance plane where $\overline{Z}_{th,\star} = 1\angle 90^{\circ}$

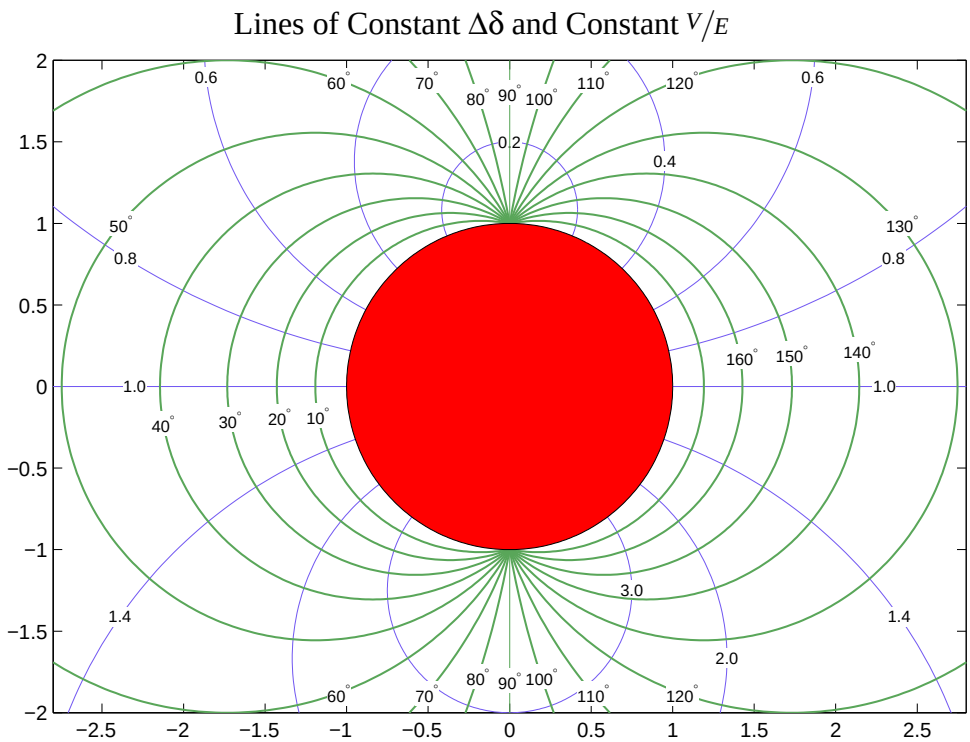

Figure 7.3: Illustration of the normalized injection impedance plane when (7.11) is used. The boundaries appear as a unit circle at the origin. The figure shows lines of constant voltage ratio V/E (blue lines) and lines of constant phase angle difference $\Delta\delta$ from the critical boundaries (green lines). These characteristics are valid for all operating points $\{\overline{Z}_{inj,i}, \overline{Z}_{th,i}\}$ that have been normalized by (7.11).

In figure 7.3, the appearance of the stability boundary and few lines of constant phase angle margin $\Delta\delta$ and normalized voltage magnitude V/E are visualized in the normalized injection impedance plane. An arbitrary operating point $\left\{\overline{Z}_{inj,i}, \overline{Z}_{th,i}\right\}$ can be mapped into this plane by applying (7.11).

Part III

Algorithms and Implementation

Chapter 8

Development of Test Bench Software

This chapter describes a test bench software that was written for the purpose of testing the suggested assessment method and to make the development and implementation of the assessment algorithms easier.

8.1 Objective

The development and test process of wide-area stability assessment algorithms can be quite time consuming, especially if the testing procedure is not carried out in a systematic and automatic way. For the purpose of testing real-time wide-area assessment algorithms, a sequence of synthetic PMU-snapshots is generated from a time domain simulation of a given power system incident. The sequence of PMU-snapshots is then used to emulate the system response following the considered incident, where a new snapshot is fed to the assessment algorithm once per cycle of system frequency. In this way, the real-time performance of the assessment method can be studied.

It is of high importance that the generation of synthetic PMU-measurements and the test of the assessment algorithms is carried out in automatic manner. If the test procedure is not automated, the following time consuming work is needed to be carried out manually:

- The synthetic PMU-measurements have to be generated for every new case study. This involves the time consuming work of finding the right variables in the output file, generate the PMU data and assign the data to the right bus.
- The network of concern must be represented when the assessment method is tested. This involves formulation of the system admittance matrix and manual assignment of the generated PMU-data to an appropriate node in the system.
- The analysis results need to be viewed and hence relevant information must be accessible. The work of accessing the data associated with each operating point is time consuming if manual search is used.

By automation of the above mentioned points, great amount of time is saved in the development and implementation process of the assessment algorithm, where different systems and operating scenarios can quickly be applied. Furthermore, by avoiding manual generation of PMU data, the risk of errors has been eliminated in that process.

For the above reasons, it was decided to develop a software that can function as a test-bench for wide-area assessment algorithms under development. The aim of the software is to automatically generate synthetic PMU-data from a simulated case scenario, and automatically obtain the necessary network information needed by the assessment algorithm. Furthermore, the software aims at visualizing the results from the algorithm and to provide an easy access to the necessary information associated with each visualized operating point.

8.2 Structural Overview

The software was written in C++. The main reason for choosing C++ instead of MATLAB is due to the flexibility for memory allocation in C++. When large systems with great amount of data are being analyzed, memory related problems might be experienced in MATLAB , while in C++ software the flexibility in the memory allocation can be utilized to avoid the problem.

A structural overview of the software is provided in figure 8.1. The figure shows four boxes that represent the main modules in the software. As an input, the software receives a PSS/E simulation case files that are used for the testing of the assessment algorithm.

The main objective of each module is listed below:

GUI Controller: This module is responsible for the interface between the user and the system. In this module, the user can select which PSS/E case scenario should be analyzed, start, stop and pause the emulation of the selected scenario.

Case Reader / PMU generation: This module reads the input data, which consists of PSS/E network (*.raw), dynamic (*.dyr) and simulation output data (*.out), together with a node position file (*.pos) which is used to represent the network in the viewer module. The PSS/E data is used to generate an initial graph representation of the system,

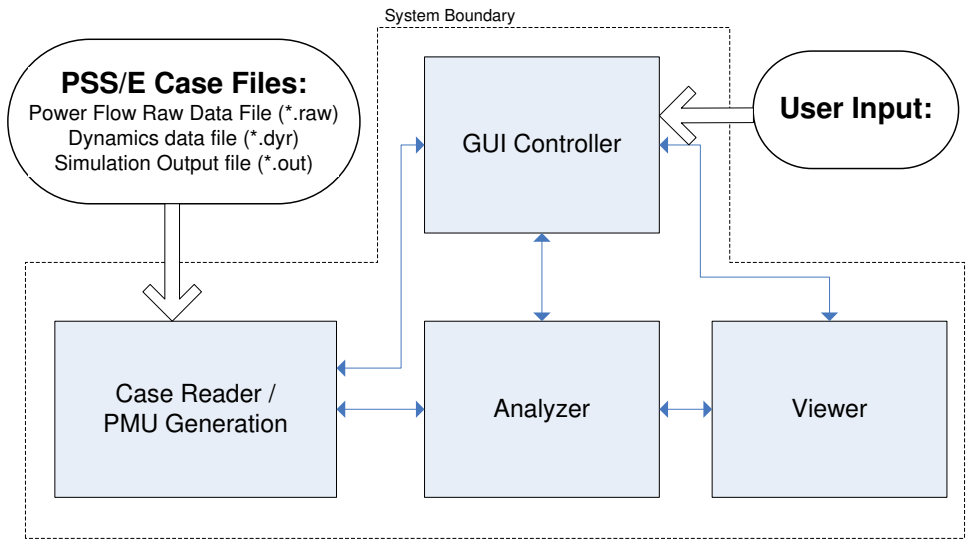

Figure 8.1: Structural overview of the test-bench software. The drawing shows the main modules in the software. The module "Analyzer" is where the assessment algorithms will be implemented for testing purposes.

where appropriate model and simulation output data is related to the nodes and edges in the graph. The module checks whether the PSS/E simulation output files contain enough variables to generate synthetic PMU-snapshots of the system conditions.

Analyzer: In this module, the wide-area assessment algorithms should be implemented. This module receives the system graph constructed in the "Case Reader" module. The system graph contains all the necessary system model information and information concerning the synthetic measurement data associated with each node and edge in the graph. Several different assessment methods could be implemented in the analyzer module, where the system graph provides all the necessary system information required for each method.

Viewer: This module is responsible for visualizing the assessment results where the observed operating points are held against their critical stability boundaries. Furthermore, a interface for plotting the PSS/E simulation results is provided. The viewer provides an interface as well for identifying each of the observed operating points.

8.3 Screen Shots

In this section, few screen shots are provided from the developed test-bench software. Figure 8.2 shows the graphical user interface where the user can select which simulated case scenario should be analyzed. Furthermore, the user can control the emulation of the case scenario by using the player control buttons. This enables the user to pause, move forward or backward the emulation at any time in order to investigate interesting system snapshots.

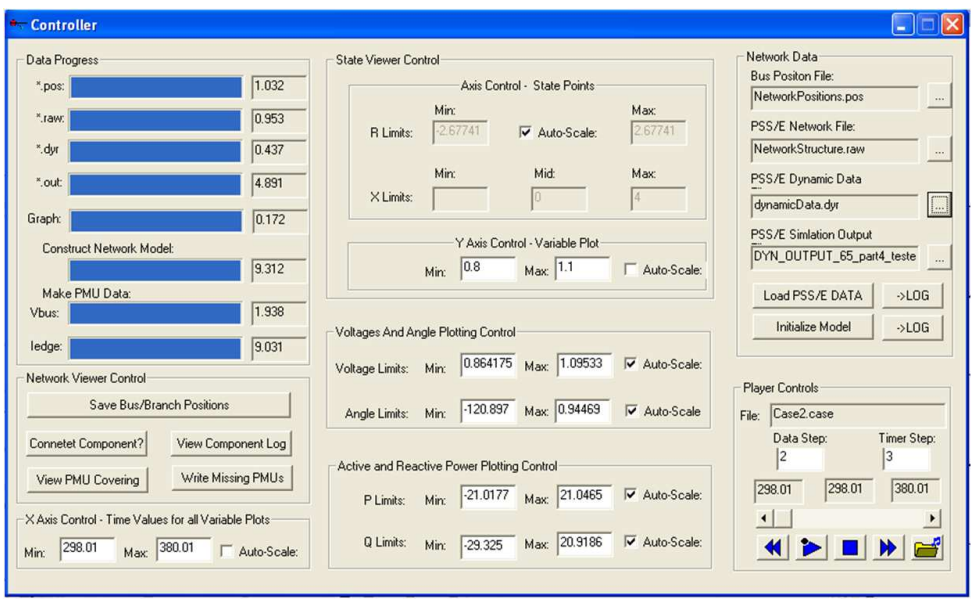

Figure 8.2: The Graphical User Interface. The user can specify the PSS/E case data to be used and control the emulation of the simulated event by using player control buttons (play, pause, fast forward, fast backward, etc.).

Figure 8.3 shows the "State Viewer" window. In this window, the observed operating points for the system machines are visualized together with their corresponding stability boundaries. By clicking on one of the operating points, an information regarding which generator is represented by the point and is percentage margin to the boundaries is provided. Furthermore, the selected operating point can be highlighted in the "Network Viewer" window, which enables a visual identification of the generators' locations in the grid. At the bottom in figure 8.3 the voltage magnitude at selected busses is plotted. A vertical line moves along the time axis, as the emulation is running,

which indicates the instance of time that is currently being analyzed.

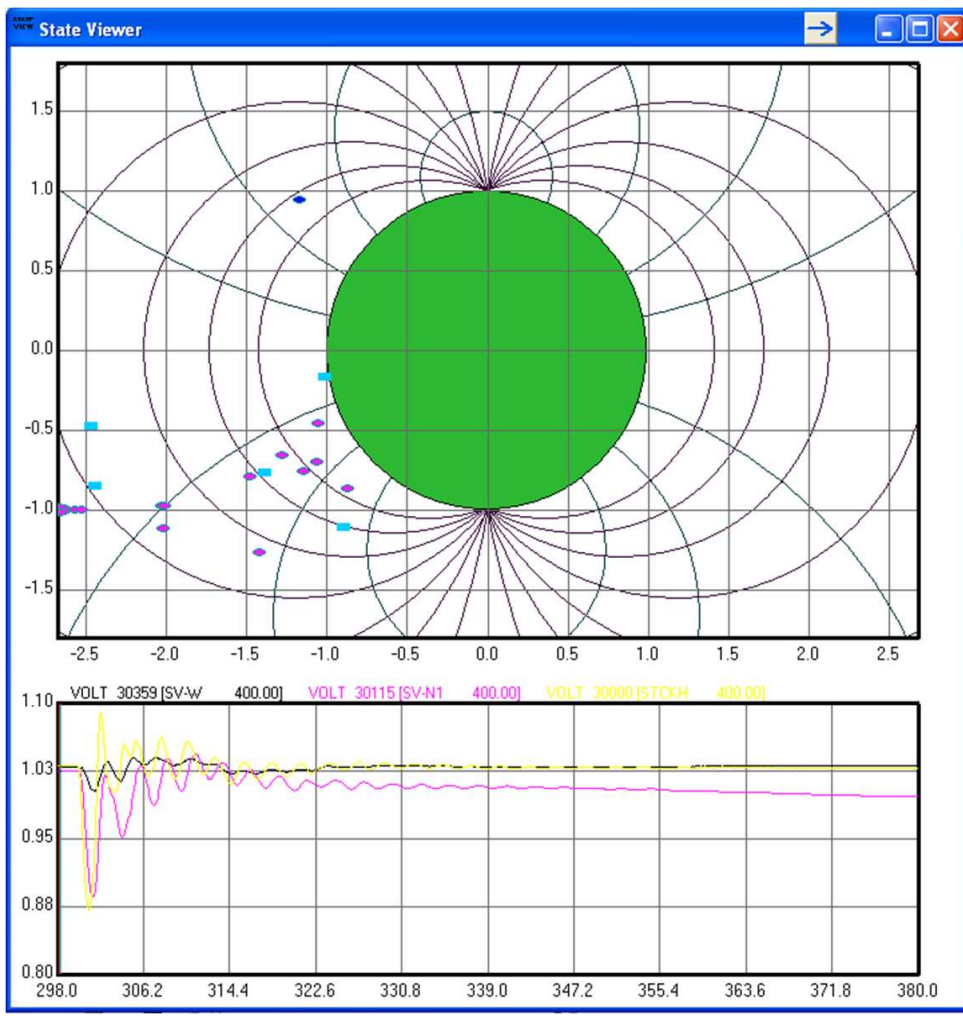

Figure 8.3: The State Point Viewer. Above, the stability boundaries are plotted together with lines of constant $\Delta\delta$ and V/E in the normalized impedance plane, as described in chapter 7. The system state points shown were mapped into the normalized impedances plane using (7.11). Each of the individual state points can be selected by a mouse click, resulting in the generator corresponding to the point becomes highlighted in the "Network Viewer" window. Below, a plot of system voltage magnitude at busses that can be chosen from the "Network Viewer" window can be seen.

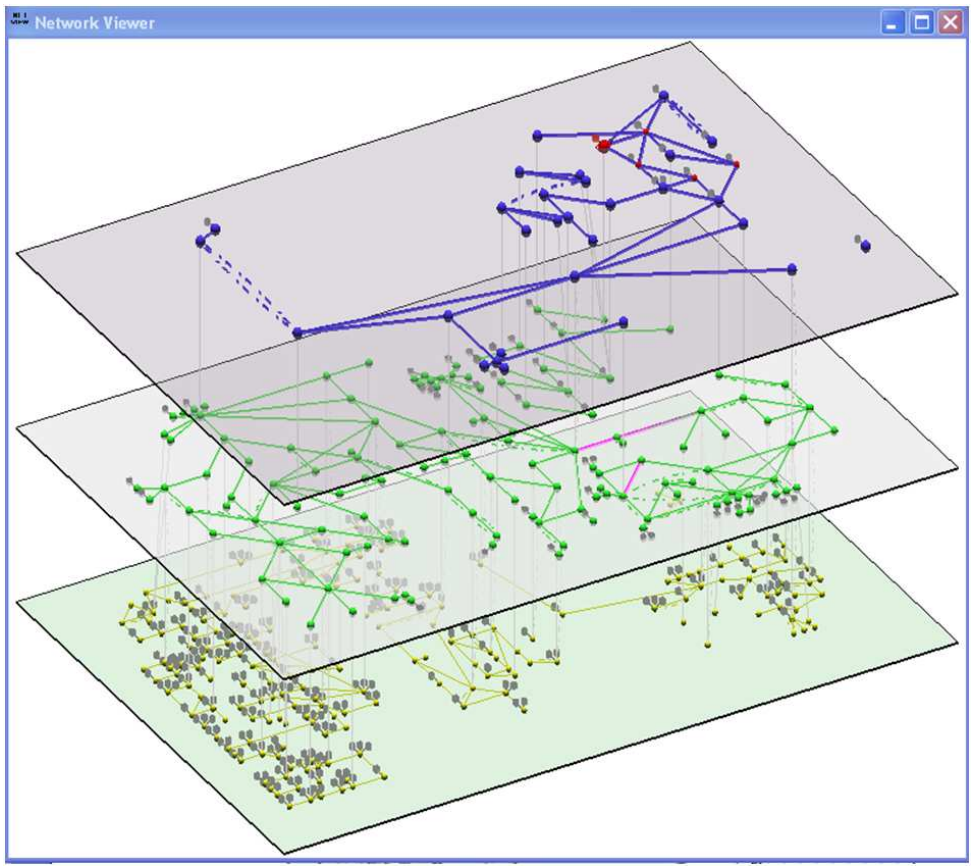

Figure 8.4: The Network Viewer. The systems busses, branches and generators are shown in a multilayered diagram. The different levels are used to illustrate different system voltage levels.

Figure 8.4 shows a screenshot from the "Network Viewer" window where the systems busses, branches and generators are shown in a multilayered diagram. The different levels are used to illustrate different system voltage levels. The position of the system busses is loaded from a *.pos file together with the PSS/E case files. It is possible to select each component (bus, branch or generator) in the diagram and plot the simulation results associated with the component. Furthermore, generators representing the state points that have selected in "State Viewer" window can be highlighted for easy identification of critical machines.

Figure 8.4 provides another screenshot from the "Network Viewer" window, where a top view of the system network is applied. The viewpoint of the network can be freely varied.

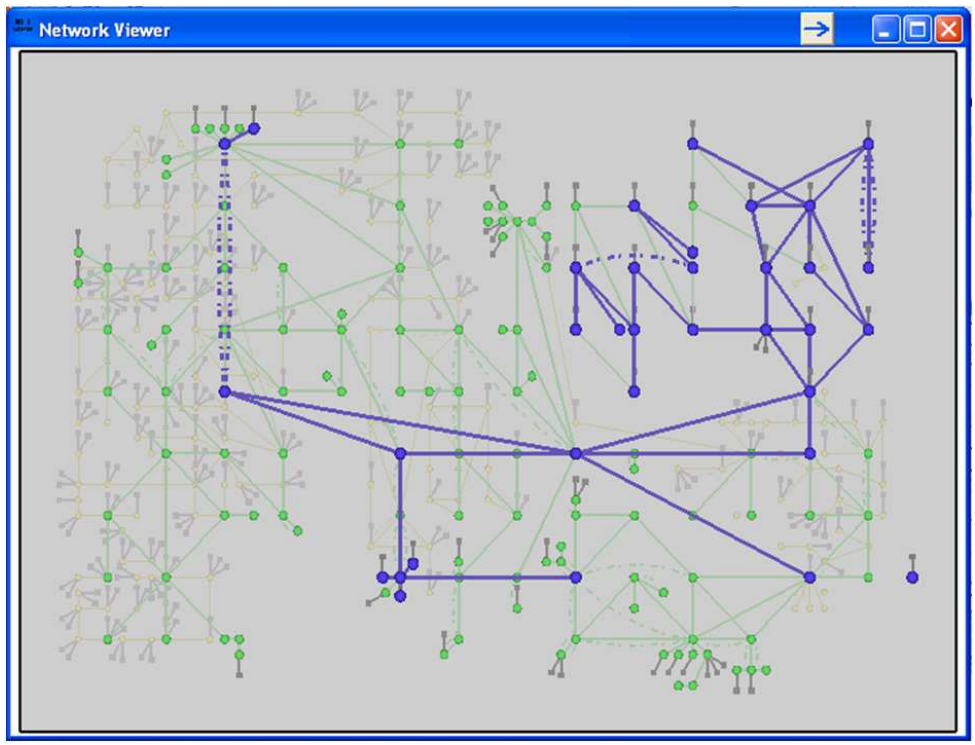

Figure 8.5: The same as in figure 8.4, where a top view of the system network is applied. The viewpoint of the network can be freely varied.

When a system component (bus, branch or generator) is selected in the "View Network" window, the simulation results associated with the component can be plotted in other windows. Figures 8.6 and 8.7 provide screenshots of the windows that plot the selected voltage magnitudes together with phase angle and the active and reactive flow in each end of a selected branch. A voltage phase angle reference can be chosen arbitrary in the "Network Viewer" window, resulting in voltage phase angles values relative to the reference bus, being plotted. An example of this can be seen in figure 8.6.

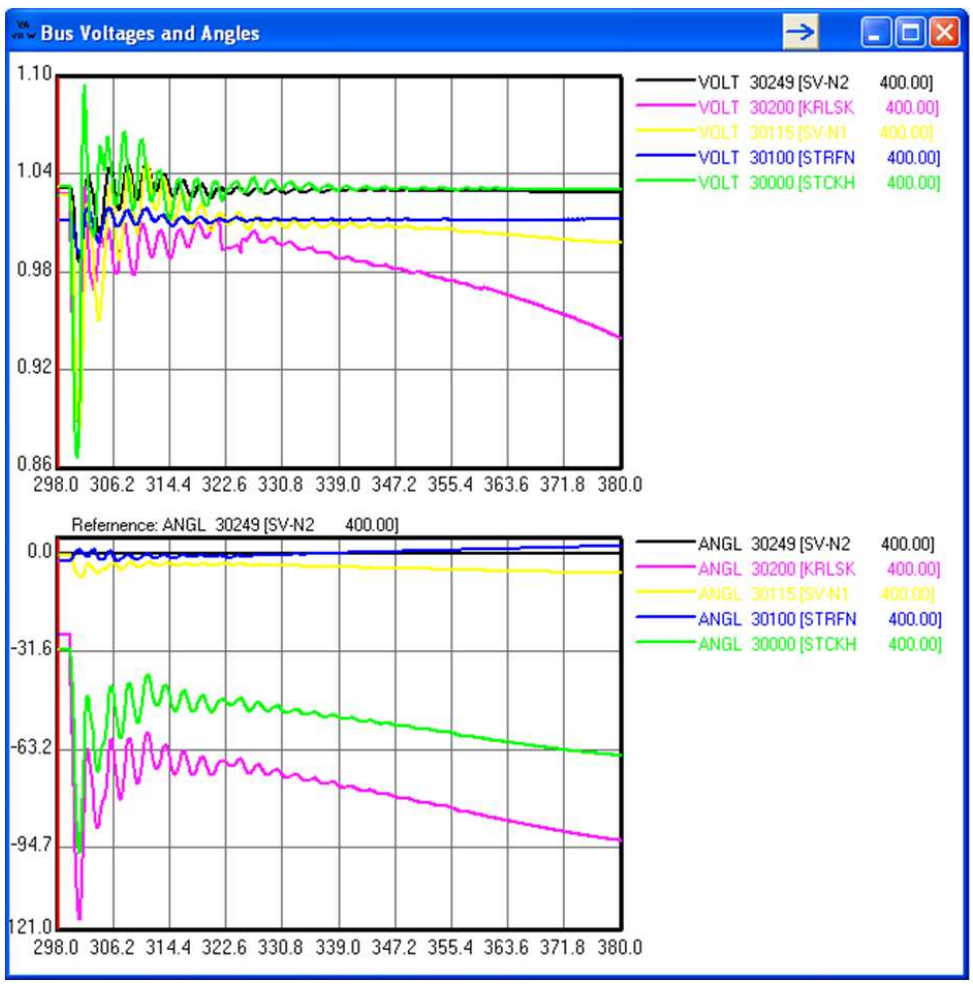

Figure 8.6: Plots of bus voltage magnitudes and voltage phase angles from busses selected in the "Network Viewer". A reference bus for the system phase angle can be chosen freely in the "Network Viewer". The phase angles on the selected busses are then plotted relative to the selected reference bus.

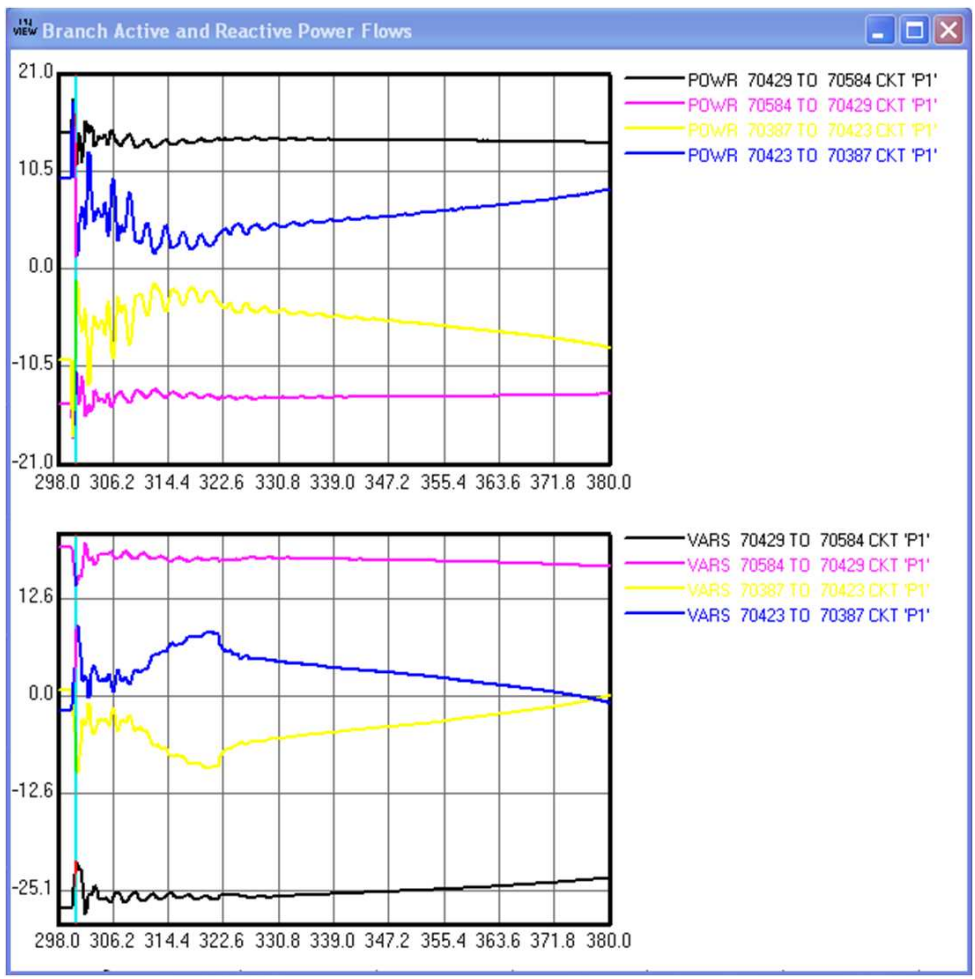

Figure 8.7: Plots of active and reactive power flow in branches selected in the "Network Viewer". Similar plots of the active and reactive outputs from selected generators can also be obtained.

Chapter 9

Algorithm and Implementation of the Method

Chapters 5-7 presented a method for assessing and visualizing aperiodic small signal stability of the system generators. This chapters concerns the implementation of the assessment method, where algorithm for fast assessment of the generators Thevenin impedance is presented as well as a special matrix ordering scheme that improves the computational efficiency of the presented algorithm. The chapter is concluded by presenting results from a time performance test of the algorithm.

9.1 System Representation

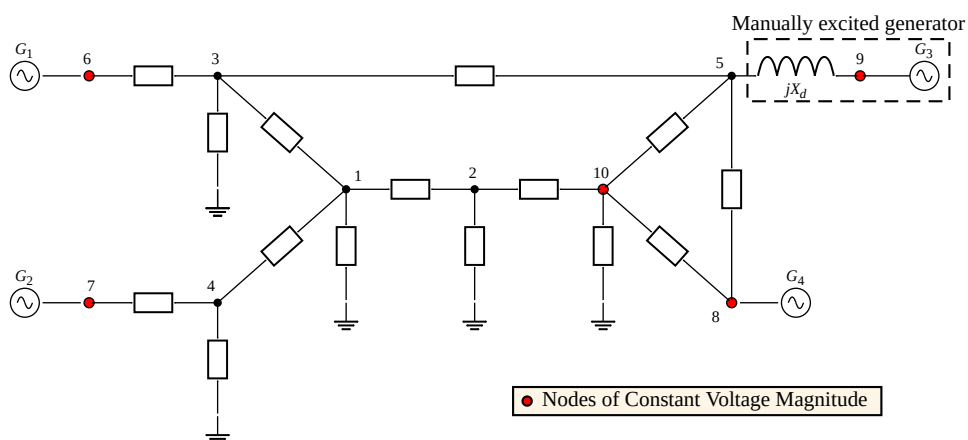

Figure 9.1: System used for illustrating how system nodes are indexed in the following. The nodes of constant steady state voltage magnitude are colored red, while nodes that are non-controlled are colored black. The voltage magnitude at node 10 is maintained constant by means of voltage control equipment such as a SVC. The node of constant voltage magnitude for generators G_1-G_4 is either at the terminal of the machines (nodes 6-8), or behind the direct axis reactance jX_d (internal node 9).

In the following description, an arbitrary system is represented in such a way that the system load is represented as impedances and power injections from

synchronous machines occur into nodes of constant voltage magnitude as described in chapter 6. Figure 9.1 provides an example of how a system is represented in the following, where an additional node has been added to the network due to the manual excitation of G_3. The system considered in the following, has characteristics as listed below:

- The number of system nodes is N
- The number of nodes of constant steady state voltage magnitude is M where $M \leq N$
- The number of synchronous generators is K

For the purpose of structuring the following description, the system nodes are indexed $i = 1 \ldots N$ in the following way:

- A node i in the range $1 \leq i \leq N - M$ represents a node of non-controlled voltage magnitude.
- A node i in the range $N - M < i \leq N$ represents a node of constant steady state voltage magnitude.
- The voltage controlled nodes are divided into two categories:
  - A node i in $N - M < i \leq N - M + K$, where voltage magnitude is maintained constant by a generator.
  - A node i in $N - M + K < i \leq N$, where voltage magnitude is maintained constant by means of synchronous condensers, SVCs etc.

This indexing is applied on the system in figure 9.1.

9.2 Algorithm

For the subsequent discussion, it is helpful to introduce the notation $\mathbf{A}_{i\star}$ and $\mathbf{A}_{\star i}$ to denote the ith row and column of $\mathbf{A}$ respectively. $\mathbf{A}_{i\star}$ is understood to be row vector and $\mathbf{A}_{\star i}$ is understood to be column vector.

The objective is to describe how the system Thevenin impedance, as seen from a node of constant voltage, can be determined. To begin with, the

system node voltage equation is provided:

$$\mathbf{I} = \mathbf{YV} \tag{9.1}$$

which can be expressed as:

$$\begin{bmatrix} i_1 \\ \vdots \\ i_{N-M} \\ \vdots \\ i_N \end{bmatrix} = \begin{bmatrix} y_{1,1} & \cdots & y_{N-M,1} & \cdots & y_{N,1} \\ \vdots & \ddots & \vdots & & \\ y_{1,N-M} & \cdots & y_{N-M,N-M} & & \vdots \\ \vdots & & & \ddots & \\ y_{1,N} & & \cdots & & y_{N,N} \end{bmatrix} \begin{bmatrix} V_1 \\ \vdots \\ V_{N-M} \\ \vdots \\ V_N \end{bmatrix} \tag{9.2}$$

Due to the chosen structure of the node indices, the system admittance matrix $\mathbf{Y}$ can be expressed in terms of sub-matrices in the following way:

$$\mathbf{Y} = \left[\begin{array}{c|c} \mathbf{Y}_{nc} & \mathbf{Y}_{link} \\ \hline \mathbf{Y}_{link}^T & \mathbf{Y}_{vc} \end{array}\right] \tag{9.3}$$

where $\mathbf{Y}_{nc}$ is the admittance matrix containing only the nodes of non-controlled voltage magnitude, $\mathbf{Y}_{vc}$ is the admittance matrix containing only nodes of controlled voltage magnitude and $\mathbf{Y}_{link}$ is an admittance matrix containing the elements that connect the two subsets of system nodes in $\mathbf{Y}_{nc}$ and $\mathbf{Y}_{vc}$ respectively.

The matrix $\mathbf{Y}_{nc}$ would be the system admittance matrix, if all nodes of constant voltage magnitude were short circuited. The objective is to determine the impedance $Z_{th,k}$ seen from a given node of constant voltage k ($N-M < k \leq N$), when all other nodes of constant voltage are shorted. For that purpose, the matrix $\mathbf{Y}_{nc}$ can be used together with the column of $\mathbf{Y}_{link}$, the row of $\mathbf{Y}_{link}^T$ and the diagonal element from $\mathbf{Y}_{vc}$ that corresponds to the node of interest. In the following $\mathbf{Y}_{link,\star k}$ is used to denote the column of $\mathbf{Y}_{link}$ corresponding to node k, $\mathbf{Y}_{link,k\star}^T$ is row vector of $\mathbf{Y}_{link}^T$ corresponding to node k and $\mathbf{Y}_{vc,(k,k)} = \mathbf{Y}(k,k)$ is the diagonal element of $\mathbf{Y}_{vc}$ corresponding to the node k.

The system impedance seen from the node k, can be determined by shorting all nodes of constant voltages except the node k and inject current of $1A$ into node k. The resulting voltage at node k is then equal to the system impedance

$Z_{th,k}$. The value of $Z_{th,k}$ can be determined from the admittance matrix for the system when all nodes of constant voltage have been shorted except node k. This matrix can be expressed as:

$$\mathbf{Y}_k = \left[\begin{array}{c|c} \mathbf{Y}_{nc} & \mathbf{Y}_{link,\star k} \\ \hline \mathbf{Y}_{link,k\star}^T & \mathbf{Y}_{vc,(k,k)} \end{array}\right] \tag{9.4}$$

The voltage at node k, when $1A$ current is injected into the node, can be obtained by the node equation $\mathbf{V} = \mathbf{Y}_k^{-1}\mathbf{I}$. Since the only non zero element in $\mathbf{I}$ is the last element in the vector, the system Thevenin impedance $Z_{th,k}$ is the last diagonal value in $\mathbf{Y}_k^{-1}$.

The Thevenin impedance for the other system generators can be obtained in the same way, where the matrix $\mathbf{Y}_k$ has to be reformulated by updating the values corresponding to $\mathbf{Y}_{link,\star k}, \mathbf{y}_{link,k\star}^T$ and $\mathbf{Y}_{vc,(k,k)}$ in $\mathbf{Y}_k$. A procedure for determining all of the K Thevenin impedance $Z_{th,k}$ is described in algorithm 9.1.

Algorithm 9.1: Computationally inefficient approach for determining the K Thevenin impedances $Z_{th,k}$ from a single PMU-snapshot.

Input: PMU-snapshot of the system conditions

Update matrices $\mathbf{Y}_{nc}$, $\mathbf{Y}_{link}$ and $\mathbf{Y}_{vc}$;
foreach *generator node k* $(M < k \leq N - M + K)$ **do**
    Construct $\mathbf{Y}_k$ from (9.4);
    Find the inverse of $\mathbf{Y}_k$;
    Find the value of $Z_{th,k}$ as the last diagonal element of $\mathbf{Y}_k^{-1}$;
end

The approach listed in algorithm 9.1 requires that the matrix inverse of the $(N-M+1)\times(N-M+1)$ matrix $\mathbf{Y}_k$, has to be determined K times, in order to determine all K Thevenin impedances. Matrix inversion is a computationally demanding operation, where for example the Gauss-Jordan inversion algorithm requires $O(n^3)$ arithmetic operations. For large systems, the above approach for determining the K Thevenin impedances would be inefficient and not suitable for real-time assessment of the system conditions.

The computational burden required for determining all of the K Thevenin impedances can be heavily reduced by utilizing useful characteristics of

the LU-factorization. It turns out that it is sufficient to determine the LU-factorization of the full $N \times N$ matrix $\mathbf{Y}$ only once in order to determine the K Thevenin impedances. This approach is described in next section.

9.2.1 Determining Thevenin Impedances from a LU-factorization

Useful Observation

In the previous section, it was shown that the Thevenin impedance $Z_{th,k}$ can be determined as the last diagonal element of $\mathbf{Y}_k^{-1}$. The admittance matrix $\mathbf{Y}_k$ can be decomposed into a product of a lower triangular matrix $\mathbf{L}$ and an upper triangular matrix $\mathbf{U}$ such as:

$$\mathbf{Y}_k = \mathbf{L}_k \mathbf{U}_k \tag{9.5}$$

where $\mathbf{L}$ and $\mathbf{U}$ have the following form:

$$\mathbf{L}_k = \begin{bmatrix} 1 & & & \\ l_{21} & 1 & & \\ \vdots & \vdots & \ddots & \\ l_{n1} & l_{n2} & \cdots & 1 \end{bmatrix}$$

and

$$\mathbf{U_k} = \begin{bmatrix} u_{11} & u_{12} & \cdots & u_{1n} \\ & u_{22} & \cdots & u_{2n} \\ & & \ddots & \vdots \\ & & & u_{nn} \end{bmatrix}$$

and $n = N - M$. The inverse of $\mathbf{Y}_k$ can be expressed as:

$$\mathbf{Y}_k^{-1} = \mathbf{U}_k^{-1} \mathbf{L}_k^{-1} \tag{9.6}$$

The inverse of $\mathbf{L}_k$ is also a lower triangular matrix with 1's on its diagonal. The last diagonal element of $\mathbf{Y}_k^{-1}$ can be determined as the vector product of the last row in $\mathbf{U}_k^{-1}$ and the last column of $\mathbf{L}_k^{-1}$, which has only the last

element as a non-zero element. Therefore, the last diagonal element of $\mathbf{Y}_k^{-1}$ can be expressed as:

$$\mathbf{Y}_k^{-1}(k,k) = \mathbf{U}_k^{-1}(k,k) = [\mathbf{U}_k(k,k)]^{-1} \tag{9.7}$$

This means that the Thevenin impedance can be determined when the LU-factorization of $\mathbf{Y}_k$ has been carried and therefore the full inverse of $\mathbf{Y}_k$ is not needed. The computational cost of LU-factorization of sparse matrices is much lower than the cost of matrix inverse; the exact value depends in a complicated way on the size of the matrix, the number of zeros in the matrix and its sparsity pattern.

Determining all Thevenin Impedances from a Single LU-factorization

It has been shown that the $Z_{th,k}$ can be determined from the last diagonal element of the $\mathbf{U}_k$ matrix from a LU-factorization of $\mathbf{Y}_k$. In the following, it will be shown how all of the K Thevenin impedances can be determined from a single LU-factorization of the full admittance matrix $\mathbf{Y}$.

For that purpose, it is useful to express $\mathbf{Y}_k(k,k)$ in terms of elements from $\mathbf{L}_k$ and $\mathbf{U}_k$:

$$\mathbf{Y}_k(k,k) = \sum_{i=1}^{k-1} \mathbf{L}_k(k,i)\mathbf{U}_k(i,k) + \mathbf{L}_k(k,k)\mathbf{U}_k(k,k) \tag{9.8}$$

Since $\mathbf{L}_k(k,k) = 1$, the last diagonal element in $\mathbf{U}_k$ can be determined as:

$$\mathbf{U}_k(k,k) = y_{th,k} = \mathbf{Y}_k(k,k) - \sum_{i=1}^{k-1} \mathbf{L}_k(k,i)\mathbf{U}_k(i,k) \tag{9.9}$$

In (9.3) the full system admittance matrix $\mathbf{Y}$ was expressed in terms of submatrices. Similarly, the resulting LU-factorization of $\mathbf{Y}$ can be expressed in terms of submatrices:

$$\mathbf{Y} = \left[\begin{array}{c|c} \mathbf{Y}_{nc} & \mathbf{Y}_{link} \\ \hline \mathbf{Y}_{link}^T & \mathbf{Y}_{vc} \end{array}\right] = \mathbf{LU} = \left[\begin{array}{c|c} \mathbf{L}_{nc} & 0 \\ \hline \mathbf{L}_{link} & \mathbf{L}_{vc} \end{array}\right] \left[\begin{array}{c|c} \mathbf{U}_{nc} & \mathbf{U}_{link} \\ \hline 0 & \mathbf{U}_{vc} \end{array}\right] \tag{9.10}$$

where:

$\mathbf{L}_{nc}$:	Lower triangular submatrix of $\mathbf{L}$ with same indices as $\mathbf{Y}_{nc}$ in (9.3)
$\mathbf{L}_{vc}$:	Lower triangular submatrix of $\mathbf{L}$ with same indices as $\mathbf{Y}_{vc}$ in (9.3)
$\mathbf{L}_{link}$:	Rectangular submatrix of $\mathbf{L}$ with same indices as $\mathbf{Y}_{link}^{T}$ in (9.3)
$\mathbf{U}_{nc}$:	Upper triangular submatrix of $\mathbf{U}$ with same indices as $\mathbf{Y}_{nc}$ in (9.3)
$\mathbf{U}_{vc}$:	Upper triangular submatrix of $\mathbf{U}$ with same indices as $\mathbf{Y}_{vc}$ in (9.3)
$\mathbf{U}_{link}$:	Rectangular submatrix of $\mathbf{U}$ with same indices as $\mathbf{Y}_{link}$ in (9.3)

LU-factorization of each of the K different $\mathbf{Y}_k$ matrices are needed to determine the K different Thevenin impedances. Due to the chosen indexing of the admittance matrix $\mathbf{Y}$, the submatrix $\mathbf{Y}_{nc}$ of $\mathbf{Y}_k$ in (9.4) will be the same for all of the K different $\mathbf{Y}_k$ matrices. This results in that the part of the LU-factorization corresponding to the matrix $\mathbf{Y}_{nc}$ ($\mathbf{L}_{nc}$ and $\mathbf{U}_{nc}$) will be the same in all K cases and therefore, they do not have to be recomputed every time a new Thevenin impedance is determined.

In fact, by considering (9.9) it can be seen that the only information needed from the resulting LU-factorization of the $\mathbf{Y}_k$ to determine the Thevenin impedance, is the last diagonal value of $\mathbf{U}_k$. This value can be determined from the last row in $\mathbf{L}_k$ and last column in $\mathbf{U}_k$. By letting $\mathbf{L}_{link,k\star}$ be the row in $\mathbf{L}_{link}$ that corresponds to system node k and $\mathbf{U}_{link,\star k}$ be the column of $\mathbf{U}_{link}$ corresponding to the same node, each of the Thevenin admittances $\overline{Y}_{th,k}$ seen from the node of injection can be determined as:

$$\overline{Y}_{th,k} = \mathbf{Y}_{vc,kk} - \mathbf{L}_{link,k\star}\mathbf{U}_{link,\star k} \tag{9.11}$$

where k ($N - M < k \leq N - M + K$) represent a node which voltage magnitude is maintained constant by a generator. The Thevenin impedance $\overline{Z}_{th,k}$ is found as the inverse of $\overline{Y}_{th,k}$.

All of the K values of $\overline{Z}_{th,k}$ can be determined from the matrices $\mathbf{L}_{link}$ and $\mathbf{U}_{link}$ together with the diagonal elements of $\mathbf{Y}_{vc}$. This means, that only a single LU-factorization of the full system admittance matrix $\mathbf{Y}$ is required for the assessment of the system aperiodic small signal stability of all K generators, which lays the foundation for a fast assessment algorithm.

9.2.2 Suggested Algorithm

Based on the the above analysis, algorithm 9.2 is suggested for carrying out an assessment of aperiodic small signal stability of all K system generators based on a single PMU-snapshot of the system conditions.

Algorithm 9.2: Suggested approach for determining the K Thevenin impedances $Z_{th,k}$ from a single PMU-snapshot.

Input: PMU-snapshot of the system conditions

foreach *PMU-snapshot* **do**
    Determine the K injection impedances $Z_{inj,k}$;
    Update the full system admittance matrix $\mathbf{Y}$;
    Decompose $\mathbf{Y}$ into $\mathbf{L}$ and $\mathbf{U}$;
    foreach *generator node k* $(N-M < k \leq N-M+K)$ **do**
        Determine $\overline{Y}_{th,k}$ by (9.11) and $\overline{Z}_{th,k} = \overline{Y}_{th,k}^{-1}$;
        Assess stability of the operating point $\left\{\overline{Z}_{inj,k}, \overline{Z}_{th,k}\right\}$ by (6.7);
        Determine the margin to the boundary by (7.5);
        Visualize the operating point and the boundary by (7.11);
    end
end

Algorithm 9.2 outlines how all of the K operating points can be determined by only carrying out one LU-factorization of the full system admittance matrix $\mathbf{Y}$.

9.3 Implementation of the Method

As mentioned in chapter 8, a test bench software was written in C++ for the purpose of developing and testing algorithms for wide-area stability assessment. The assessment method for aperiodic small signal stability was implemented into the test bench software, where the implementation of the method consisted of two routines:

Initialization Routine where the extended network representation was formulated, system nodes categorized, specialized matrix ordering scheme applied, the system admittance matrix generated, the LU-factorization

initialized and the PMU-data structured in such a way that the admittance matrix can be efficiently updated.

Snapshot Assessment Routine where the assessment algorithm 9.2 is implemented.

Figures 9.2 and 9.3 show block diagrams that describe the two main routines used as a software implementation of the assessment method. The figures refer to external software libraries and packages that were used for the implementation of the method. The external libraries and packages used for the implementation are:

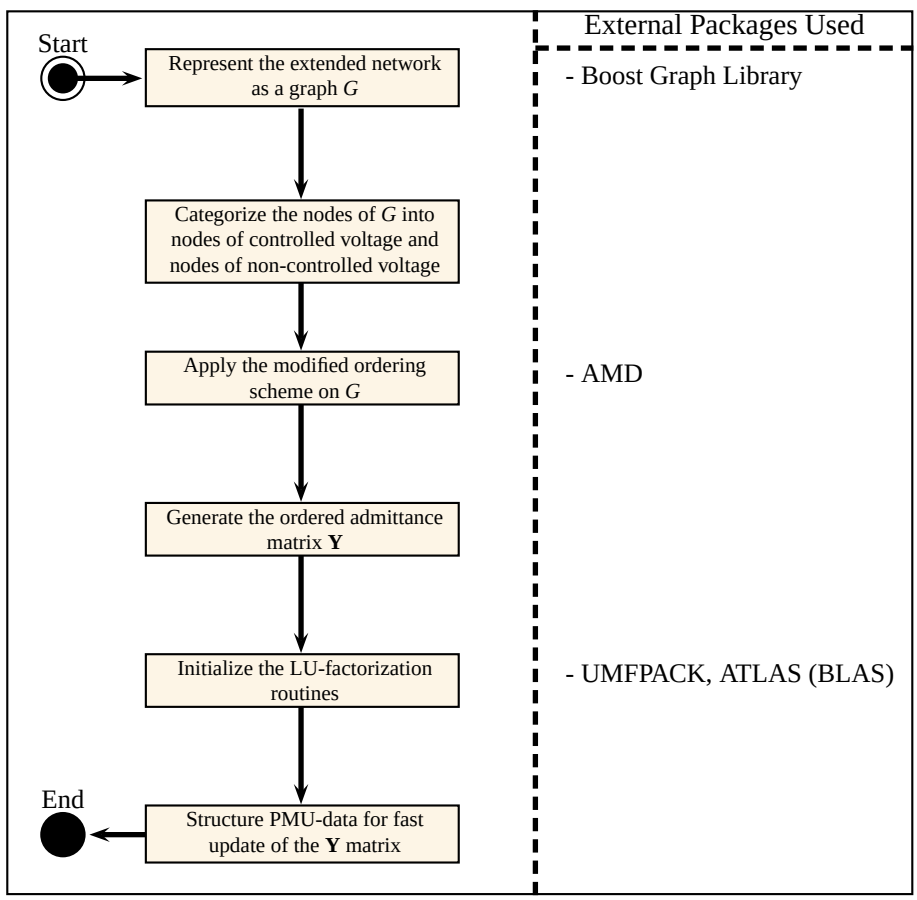

Figure 9.2: Overview of the steps involved for the initialization of the assessment method and the external software packages used in each step.

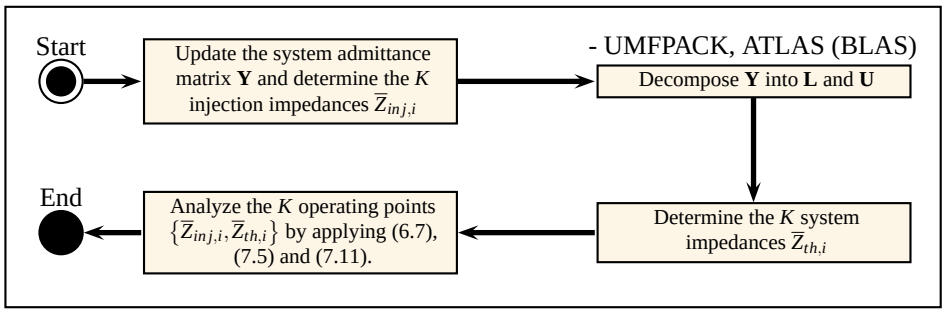

Figure 9.3: Involved steps in the assessment method which is executed when a new PMU-snapshot is received.

UMFPACK is a set of routines that implement LU-factorization algorithm for sparse matrices (Davis 2004).

ADM is a set of routines for carrying out the approximate minimum degree ordering algorithm to permute sparse matrices prior to LU-factorization (Amestoy et al. 2004).

ATLAS BLAS is a high performance implementation of BLAS (Basic Linear Algebra Subprograms) which is needed by the UMFPACK routines (Whaley et al. 2001). BLAS are a set of subroutines which provide a standard application programming interface for simple linear algebra operations. The BLAS operations are divided into 3 levels:

Level 1: Vector operations. Consist mainly of vector-scalar, norm, inner-product and rotation operations. These are $O(N)$ operations.

Level 2: Matrix-vector routines and Special Matrix Solvers. These are $O(N^2)$ operations.

Level 3: Matrix-matrix operations, which are $O(N^3)$ operations.

Boost graph library is a graph analysis toolkit that provides general purpose graph classes (Siek et al. 2002). It contains different choices of graph containers and efficient graph theory algorithms implemented as generic C++ template specifications.

In the following subsections, additional description is provided for few of the blocks in figures 9.2 and 9.3 that were of crucial significance for obtaining a computationally efficient implementation of the assessment method.

9.3.1 LU-factorization

The single most computationally demanding step in algorithm 9.2 is the LU-factorization of the **Y** matrix. Several software packages exist that contain efficient routines for carrying out LU-factorization of sparse matrices. One of these is the software package UMFPACK (Davis 2004) which is the choice of MATLAB for carrying out LU-factorization of sparse matrices.

The UMFPACK packages was chosen for carrying out the LU-factorization of the **Y** matrix in the project. UMFPACK requires the packages BLAS (for dense matrix operations) and AMD (for sparse matrix minimum degree ordering) to be implemented. Algorithm 9.2 was implemented using the C++ programming language and ATLAS library (Whaley et al. 2001) as a high performance implementation of BLAS.

The computational efficiency of algorithms for decomposition of sparse matrices is strongly depended on the number of fill-ins that are required for completing the decomposition. The fill-in of a matrix are the entries which change from an initial zero to a non-zero value during the execution of the decomposition algorithm. A higher number of fill-ins results in increased memory requirements and increased number of arithmetic operations for completing the matrix decomposition. The number of fill-ins can be reduced by switching rows and columns in the matrix according to a chosen matrix ordering scheme.

9.3.2 Matrix Ordering Schemes

For illustrating the effects that fill-ins have on the required number of arithmetic operations for decomposing a matrix **A** into upper and lower matrices, figures 9.4 and 9.5 are considered. The figures illustrate how the augmented matrix $[\mathbf{A}|\mathbf{I}]$ is decomposed into $[\mathbf{U}|\mathbf{R}]$ by row operations, where **U** and **R** are upper and lower triangular matrices respectively.

In figure 9.4 it can be seen that the initial coefficient matrix **A** is sparse, but as the elimination phase progresses, new non-zeros (or fill-ins) are introduced. After the first step, fill-ins were generated such that all initially zero elements of the coefficient matrix **A** became non-zero elements. Apart from increasing the storage requirement, the fill-ins enter into the calculation of subsequent elimination steps and thereby increase the number of arithmetic operations needed for completing the elimination process.

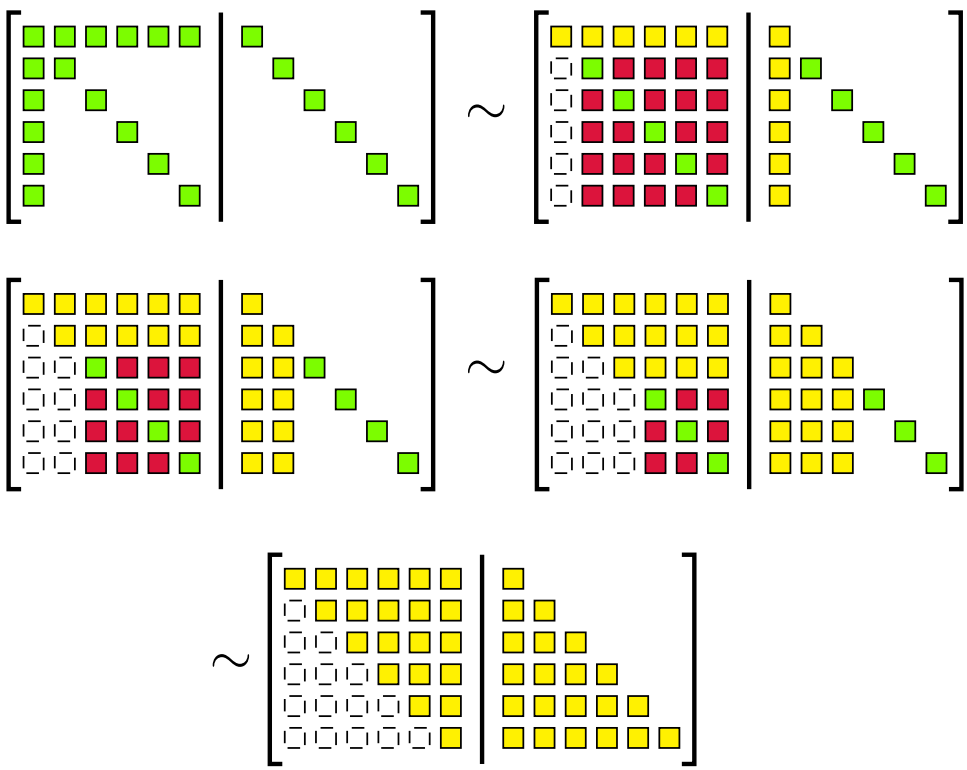

Figure 9.4: Decomposition of an augmented coefficient matrix [**A**|**I**] into [**U**|**R**], where **U** and **R** are upper and lower triangular matrices respectively. The green elements represent original elements of [**A**|**I**], the yellow elements are the one determined in each step and the red elements represent additional fill-ins created after the first step. The eliminated elements are shown as dashed boxes. The resulting upper and lower matrices have no sparsity.

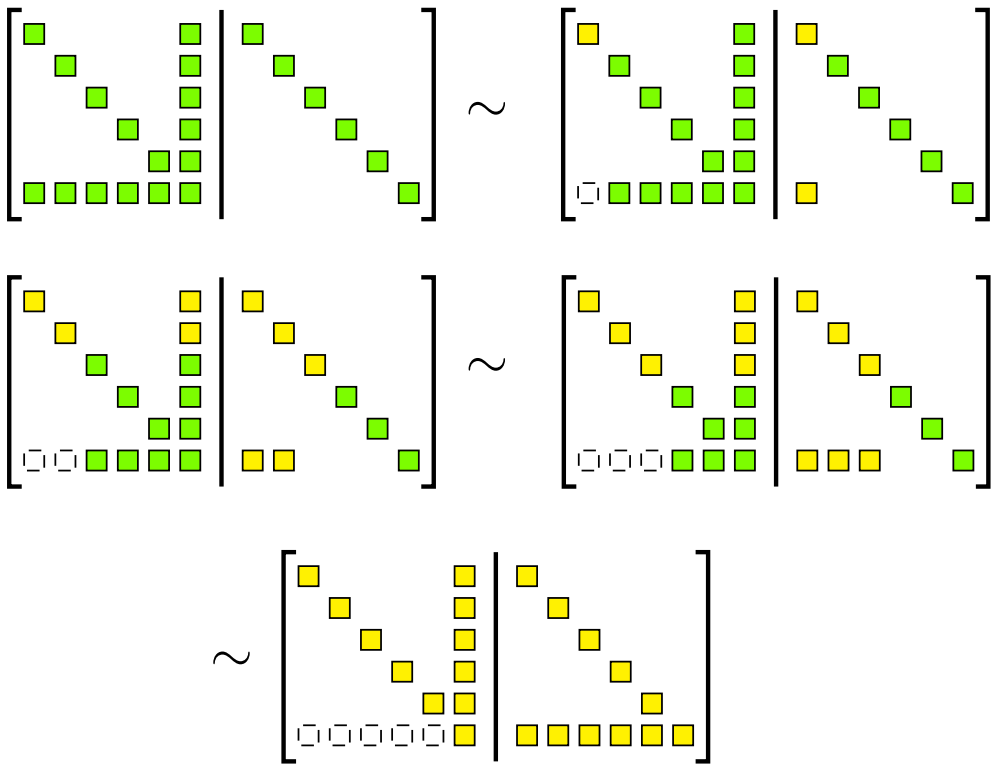

Figure 9.5: The same elimination steps of the same augmented matrix as in figure 9.4 except that the matrix **A** was re-ordered such that the first and the last rows and columns were swapped. The reordering results in that no fill-ins are generated during the elimination process and the resulting upper and lower matrices have the same sparsity structure as the original matrix.

The resulting upper and lower triangular matrices $[\mathbf{U}|\mathbf{R}]$ are both full triangular matrices, which results in increased storage requirements for **L** and **R**.

The amount of fill-ins generated in an elimination process can be heavily reduced by applying appropriate reordering scheme of the coefficient matrix **A**. This is illustrated in figure 9.5, where the last and the fist rows and columns of **A** have been swapped before the elimination process began. Due to the reordering, no fill-ins are generated in the elimination process and the resulting **L** and **R** matrices are therefore sparse.

Few algorithms exists for reordering sparse matrices, which aim at reducing

the storage requirement and increasing the computational efficiency for decomposition algorithms. The reverse Cuthill-McKee (Liu & Sherman 1975) and King's (King 1970) algorithms aim at reducing the bandwidth of the sparse matrix while the minimum degree algorithm (George & Liu 1989) reduces the number of non-zeros in the resulting matrix after a Choelsky factorization.

The above mentioned LU-factorization routine provided in UMFPACK, applies approximate minimum degree algorithm for its symmetric ordering strategies. The approximate minimum degree algorithms are implemented in the AMD ordering package (Amestoy et al. 2004).

Reordering the Admittance Matrix Y

None of the above mentioned ordering schemes can be used to reorder the admittance matrix **Y** in algorithm 9.2. The reason is that the assessment algorithm is dependent on the system admittance matrix being structured in a specific manner such that all K system admittances can be determined from a single LU-factorization. This requires that every node of uncontrolled voltage must have a lower index than every node of constant voltage. The result of this requirement is that a minimum degree algorithm cannot be applied on the full admittance matrix. Instead, specialized ordering schemes have to be applied such that the requirements for the structure of the admittance matrix are met.

Modified Ordering Scheme for Y

In order for algorithm 9.2 to function correctly, it is necessary that the nodes of non-controlled voltage are represented at the first $N-M$ indices of the full admittance matrix **Y**. A reordering of the full admittance matrix **Y** by the minimum degree ordering algorithm can therefore not be used, since it might results in that some of the voltage-controlled nodes would be indexed among the first $N-M$ indices of the reordered matrix.

For the purpose of reducing the fill-ins generated during the LU-factorization of the **Y** matrix, modified minimum degree ordering scheme was applied. The ordering consisted of finding the approximate minimum degree ordering of the $\mathbf{Y}_{uc}$ and $\mathbf{Y}_{vc}$ submatrices of **Y**. By reordering the submatrices individually, it is ensured that all nodes of uncontrolled voltages are represented before nodes of controlled voltages when the new ordering has been applied to **Y**.

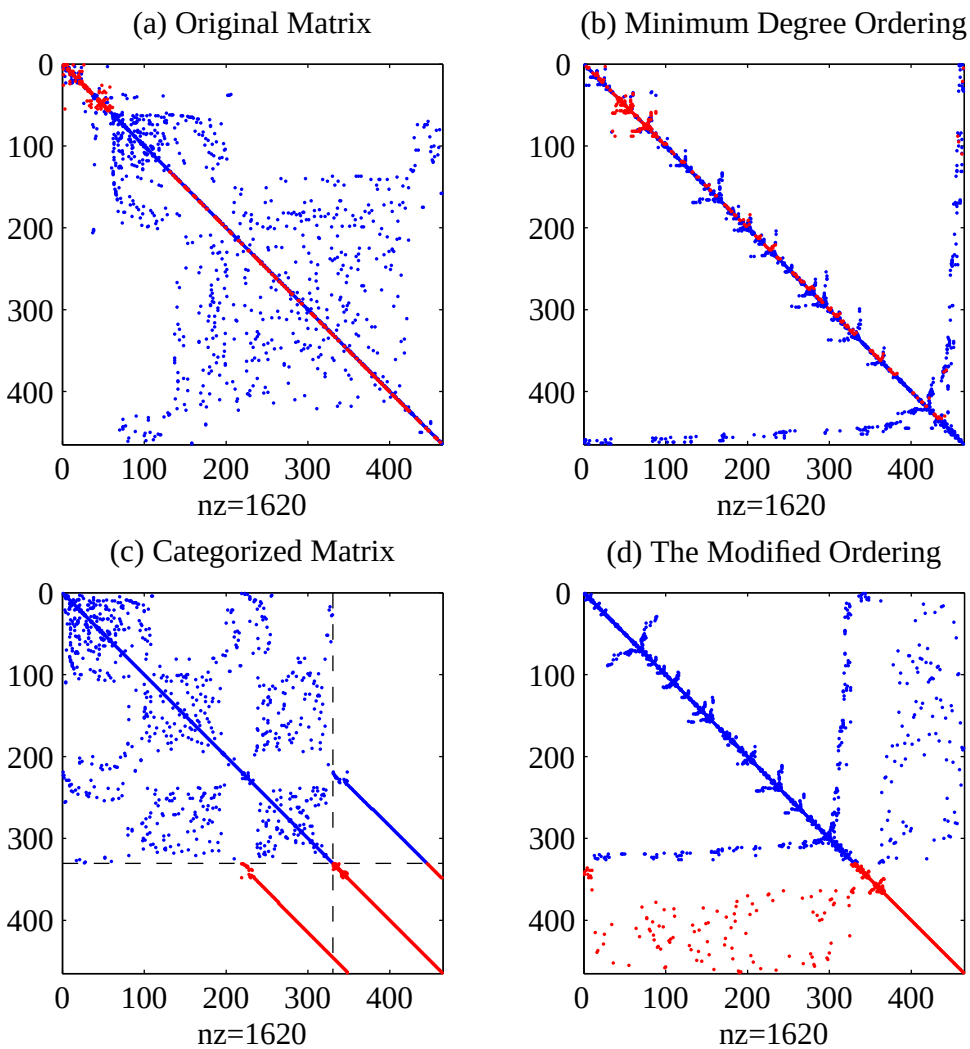

Figure 9.6: Illustration of the ordering scheme. a) The original unordered 464×464 admittance matrix $\mathbf{Y}$ with 1620 non-zero elements, where blue diagonal elements represent nodes of non-controlled voltage and red elements are nodes of constant voltage. b) Matrix structure after minimum degree ordering of the full matrix $\mathbf{Y}$. c) the matrix $\mathbf{Y}$ categorized into submatrices $\mathbf{Y}_{nc}, \mathbf{Y}_{vc}, \mathbf{Y}_{link}$ and $\mathbf{Y}_{link}^{T}$ as represented in (9.3). d) The chosen ordering scheme where minimum degree ordering was applied on $\mathbf{Y}_{nc}$ and $\mathbf{Y}_{vc}$ individually.

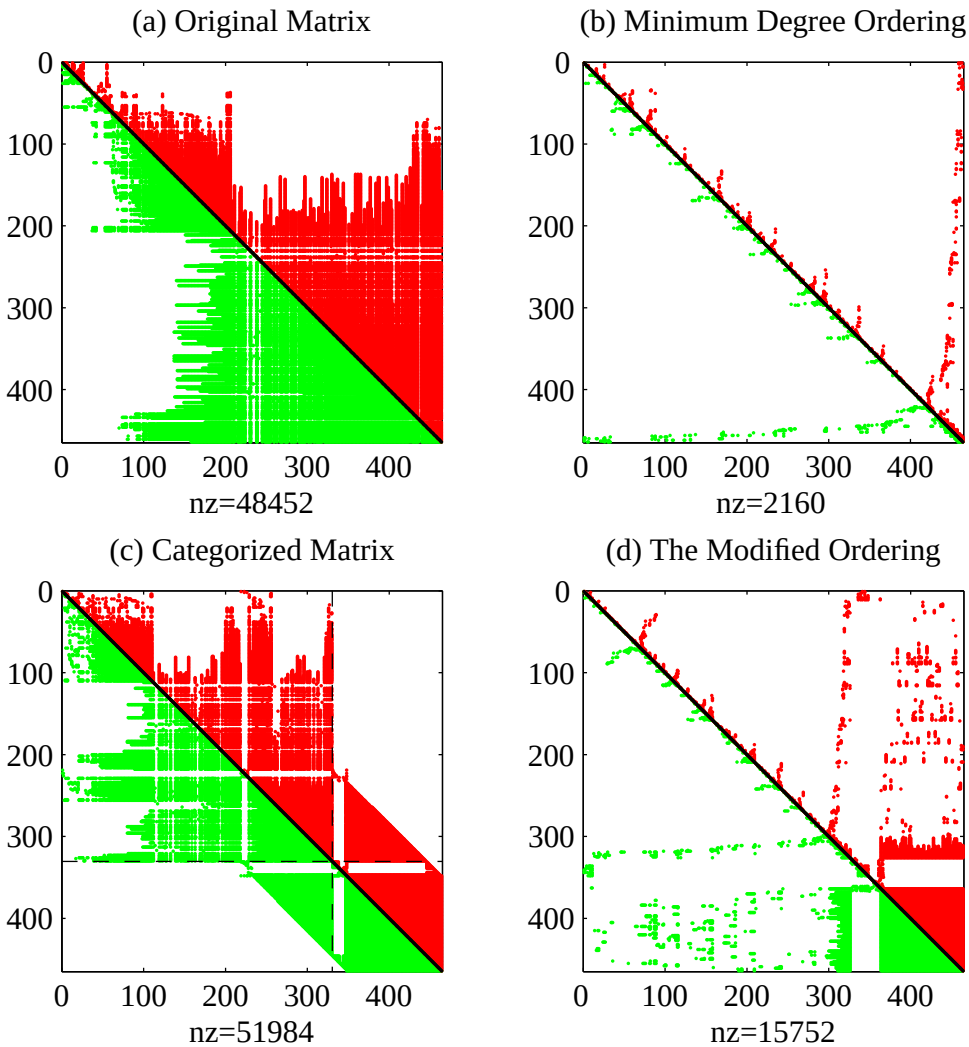

Figure 9.7: The sparsity patterns after LU-factorization of the four matrices in figure 9.6. The figure illustrates the non-zero elements of the matrix $\mathbf{L}+\mathbf{U}$, where the green elements are in $\mathbf{L}$ and the red elements are in $\mathbf{U}$. The number of generated fill-ins, during the factorization, is greatly affected by which ordering scheme is applied. By using the modified ordering scheme, the $\mathbf{L}$ and $\mathbf{U}$ matrices become quite sparse except for indices that correspond to the submatrice $\mathbf{Y}_{vc}$.

Figure 9.6 visualizes the steps involved in achieving the reordered admittance **Y** by showing the sparsity pattern at different stages. In (a) the original structure of the admittance matrix **Y** is shown, where nodes of uncontrolled voltage magnitude are represented as blue diagonal elements and nodes of controlled voltage are represented as red diagonal elements. In (b) the approximate minimum degree ordering of the full **Y** is shown for later comparison. Plot (c) shows the matrix where **Y** has been reordered and has the same structure as in (9.3) where $\mathbf{Y}_{nc}$ is the upper left submatrix and $\mathbf{Y}_{vc}$ is the lower left submatrix. In (d) the above modified minimum degree ordering scheme has been applied on **Y**. The difference between approximate minimum degree of the entire **Y** matrix and the modified scheme can be noticed by comparing (b) and (d).

The sparsity pattern of the resulting **L** and **U** matrices from a LU-factorization of the matrices in figure 9.6 is visualized in figure 9.7. The effect that the approximate minimum degree ordering has on the reduction of fill-ins is apparent by comparing (a) and (b). The number of non-zero elements in the matrix $\mathbf{L}+\mathbf{U}$ is more than 20 times larger in (a) than in (b). The matrices in (c) and (d) are categorized in such a way, that they can be used in algorithm 9.2. By applying the modified ordering, the number of non-zero elements in the $\mathbf{L}+\mathbf{U}$ matrix is greatly reduced in (d) compared to (c).

It is interesting to note that the most dense part of $\mathbf{L}+\mathbf{U}$ in (d) is in the $\mathbf{L}_{vc}$ and $\mathbf{U}_{vc}$ submatrices, and those matrices are not needed in-order to determine the K Thevenin impedances $\overline{Y}_{th,k}$, as can be seen in (9.11). This means, that the algorithms carrying out the LU-factorization could be modified in such a way that calculation of elements in $\mathbf{L}_{vc}$ and $\mathbf{U}_{vc}$ are not carried out. By doing so, a further increased computational efficiency of algorithm 9.2 would be achieved.

The modified ordering scheme for **Y**, presented in this section, contributes increased efficiency of the LU-factorization of the **Y** matrix, which is the single most computational demanding step in algorithm 9.2.

9.4 Performance Test

For the purpose of testing the efficiency of the assessment implementation, a test was carried out on a network containing 488 nodes and 672 branches and 144 generators. The test consisted of that a loop of 1000 iterations was

executed, where in each loop the LU-factorization of the system admittance matrix was determined, whereafter the Thevenin impedances for all 144 generators were determined. The total execution time for completing the loop was used to determine an average computational time for determining the Thevenin impedances from the system admittance matrix **Y**.

The test was carried out on a 64bit laptop machine having an Intel Core 2 Duo 2.26GHz processor and 8 GB RAM. The results from the test were that the 144 system Thevenin impedances for the system in context, could be determined in $\underline{7.86\,ms}$. The results mean that an aperiodic stability assessment of all 144 system generators can be carried out well within the time interval between two PMU-snapshots. Therefore, the assessment of the generators operating conditions can be updated once per cycle of system frequency, enabling full exploitation of the high repetition rate that PMUs can provide.

Part IV

Test of Method

Chapter 10

Full Scale Test - The Blackout on September 23, 2003

In this chapter describes a full scale test of the real-time assessment method. For the purpose of carrying the test out, a PSS/E simulation was conducted of the blackout in E-Denmark and S-Sweden that occurred September 23, 2003. The simulation output data was used to generate synthetic PMU-measurements from the event, which again were used for emulation of the blackout in the test-bench software described in chapter 8.

A detailed description of the blackout in E-Denmark and S-Sweden was provided in chapter 2 where the initial conditions were described and a time line of events was established. The simulation results presented in this chapter are based on this case description.

10.1 The Simulation Model

The model of the Scandinavian power system used to simulate the blackout is a combination of two models; a simplified model of the Scandinavian power system and a detailed model of the power system in E-Denmark. The two models where merged into a single model and used for the simulation. It was not possible to provide a detailed model of the Swedish power system within the time frame decided for the analysis of the blackout, and therefore the simplified model was used.

Figure 10.1 shows an overview drawing of the simplified model. The model is simplified in such way that all local production and consumption in certain area is aggregated into one equivalent generator and one equivalent load. The generator located in E-Denmark in figure 10.1 is replaced with the detailed Danish model which gives the resulting model used for the simulation of the blackout. The detailed Danish model consisted of 320 busses from $400\,kV$ to $50\,kV$ level, 480 branches and approximately 300 generators which includes distributed generation. The model details and data are not provided in the thesis due to a non-disclosure agreement with the Danish transmission

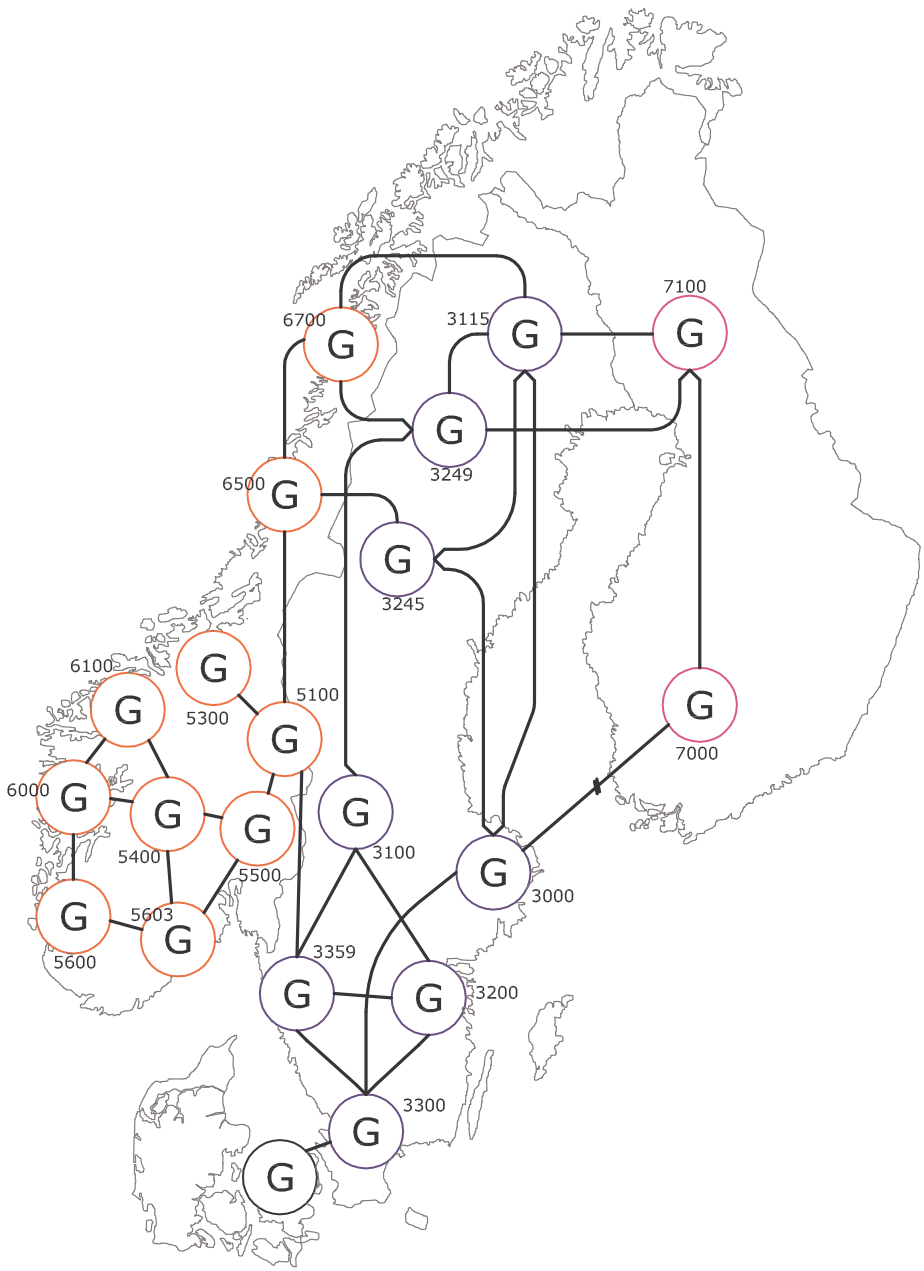

Figure 10.1: Overview drawing of the simplified Scandinavian model used for simulating the blackout on September 23, 2003. The generator in Zealand is replaced by a detailed model of the power system in Zealand.

system operators Energinet.dk, the provider of the model.

10.1.1 Applying Disturbances in the Simplified Model

For carrying out a time domain simulation of the blackout, it is necessary to identify the locations in the simplified model that corresponds to the actual fault locations. Figure 10.2 shows a diagram of the southern part of the Swedish power system and is used to relate the actual locations of involved generating units and tripped transmission lines to a corresponding location in the simplified model.

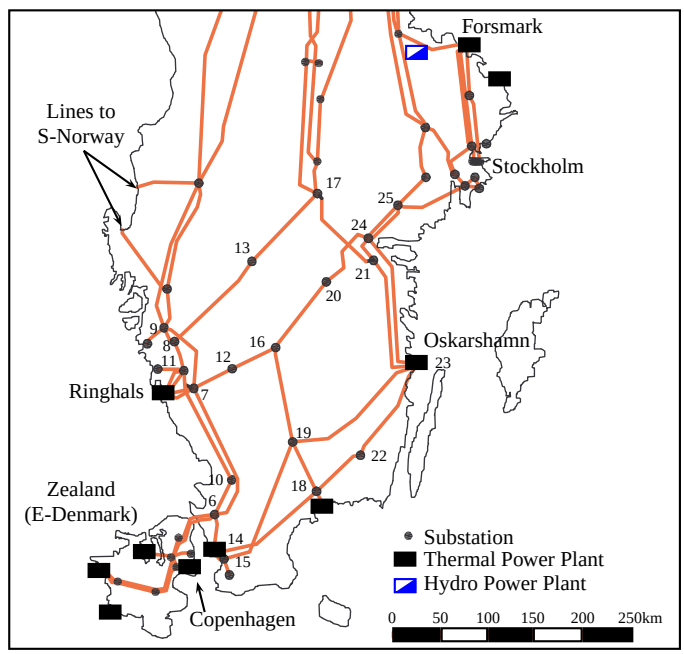

Figure 10.2: The southern part of the Swedish power system. The locations of the nuclear plants (Forsmark, Ringhals and Oskarshamn) have to be identified in the simple model in figure 10.1.

The first incident that played a role in the development of the blackout was the loss of the Oskarshamn unit. The Oskarhamn power plant is represented by the generator located at bus 3000 (in figure 10.1) which also represents the production at the Forsmark nuclear power plant located north of Stockholm. The Ringhals power plant is represented by the generator at bus 3359 and the Barsebäck, which was not operating the day of the blackout, is represented by the generator at bus 3300.

The loss of the Oskarshamn block and the two Ringhals blocks is simulated by splitting the generators at busses 3000 and 3359 into two, where the new generators represent the units that are disconnected during the simulation. Such modifications do not affect the dynamics represented by the model, since the sum of the machines size at each of the two busses is preserved after the modifications.

The line Halmsberg-Kimstad, between busses 17 and 21 in figure 10.2, was not in operation on September 23rd 2003. This line provides a connection between the mid and southern Sweden and in order to take this into consideration, the line between bus 3100 and bus 3200 is disconnected in the simplified model.

In chapter 2 a time line of events associated with the blackout was established. Table 10.1 provides an overview of the actual location of the involved events and their corresponding location in the simplified model.

Location of the incident	**Incident description**	**Component in model**	**How to simulate**
Oskarhamn block 3	Output lowered from 1.176MW to 800MW in 10s	Generator 2 at bus 3000	Reduce output by 376MW
Oskarhamn block 3	Output lowered from 800MW to 0MW in 10s	Generator 2 at bus 3000	Reduce output by 800MW, disconnect the unit.
Jutland	reserve DC-power activated	load at bus 3359	Add $\Delta P = -55MW$ to the load
Horred	Double busbar fault, four lines tripped	Line from 3359 to 3200 and line from 3359 to 3300	Switch both of the lines
Ringhals block 3 and 4	Both blocks are disconnected from the grid	Generator 2 at bus 3359	Disconnect the generator
Jytland	Loss of one of the DC-connections	load at bus 3359	Add $\Delta P = 250MW$ to the load

Table 10.1: The actual location of the involved events and their corresponding location in the simplified model.

10.2 Time Domain Simulation and Results

For the purpose of ensuring that the time domain simulation results reflect the actual situation on the September 23rd 2003, the simulated response was gradually fitted to a measurement data set of system frequency taken during the unfolding of the blackout. The data of the measured frequency was downloaded from the web page of Svenska Kraftnät[1]. A plot of the measured

[1] www.svk.se

values of the frequency is shown in figure 10.3. The figure shows measured frequency at the 220*kV* substation in Beckomberga.

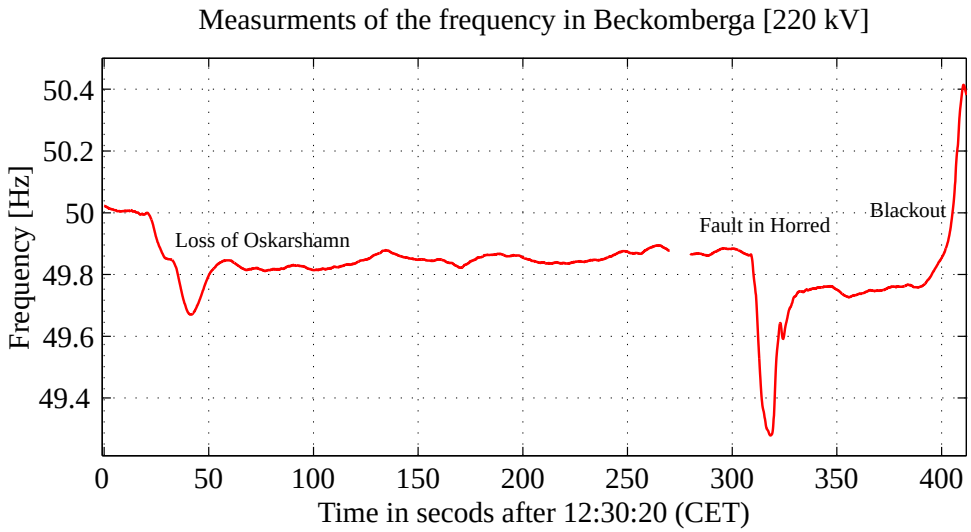

Figure 10.3: Available measurements of the frequency in Beckomberga at the time of the blackout on the September 23rd 2003. These measurements are found at the web page of Svenska Kraftnät *www.svk.se*. The measurements are used as reference for the time domain simulation of the blackout.

Figures 10.4 to 10.7 show the simulation results in the period from before the occurrence of the fault in Horred and until the blackout occurred. In figure 10.4, the measured values of the system frequency are compared to simulated values at bus 3100. The simulated frequency is well aligned with the measured values of the frequency. The increase in frequency experienced during the last 10 seconds of the simulation indicate that the instability mechanisms that caused the blackout have been captured by the simulation. The mechanisms of voltage instability do not play a role in the simulated blackout since the system ULTC-transformers and other load restorative dynamics were not represented in the simulation model. This means, even though an operational condition for voltage instability would have been achieved, there were no voltage instability mechanisms represented in the model that could be a driving force in a potential voltage instability.

A likely explanation of the observed increase in the system frequency for the last 10 seconds of the simulation is that the group of generators in Denmark and the remaining generators in the system are slowly losing synchronism.

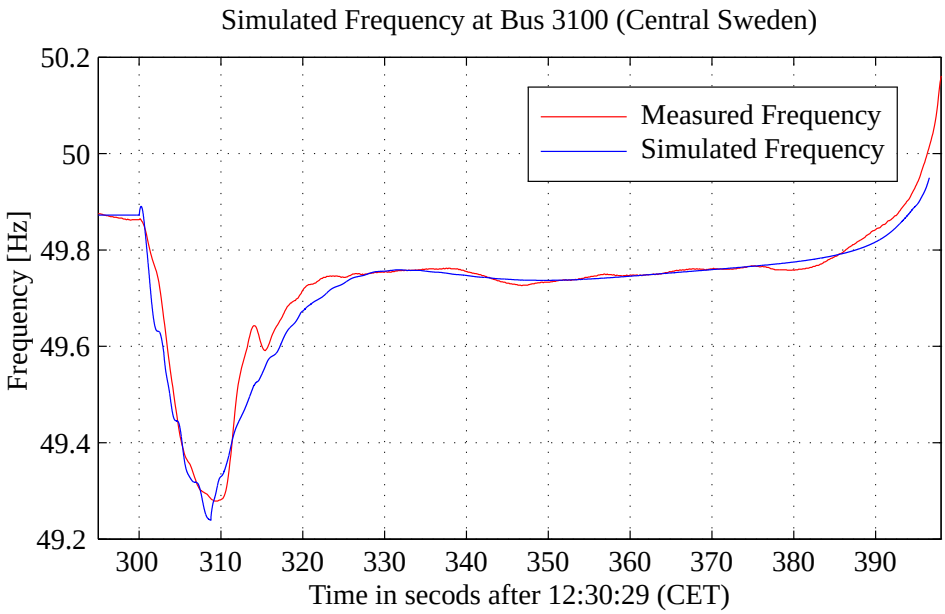

Figure 10.4: The simulated frequency at bus 3100 compared to measured values of the frequency at the time of the fault in Horred.

When the two subgroups of generators approach a phase angle separation of 180°, the voltage magnitude at intermediate busses begin to fall rapidly which results in a large reduction in the system consumption. The large reduction in the system consumption causes a rapid increase in the system frequency, similar to the one observed in figure 10.4.

In figure 10.5, the simulated flow of active and reactive power from E-Denmark to S-Sweden is shown. For comparison, the actual import of active and reactive power form E-Denmark to S-Sweden is provided in figure 10.6 (Elkraft System 2003). If the simulated values of delivered reactive power from E-Denmark are investigated, it can be seen that a reactive power is flowing into Denmark, which is the opposite to what happened in the actual case.

It can be seen from figure 10.6 that there was a great increase in the imported reactive power from E-Denmark to S-Sweden. The simulation result in figure 10.5 show therefore the opposite direction of the flow of reactive power. A flow pattern similar to the one observed in the actual case is given in figure 10.7. In this plot, the simulated flow from bus 3000 (the Stockholm area) to

bus 3300 (S-Sweden) is shown. It can be seen that the reactive power flow into the area increased very much during the last seconds before the black-out, which similar to the observed flow in the actual case. This indicates that the instability problems that caused the blackout, initially emerge in a different area in the simulated scenario compared to the actual case.

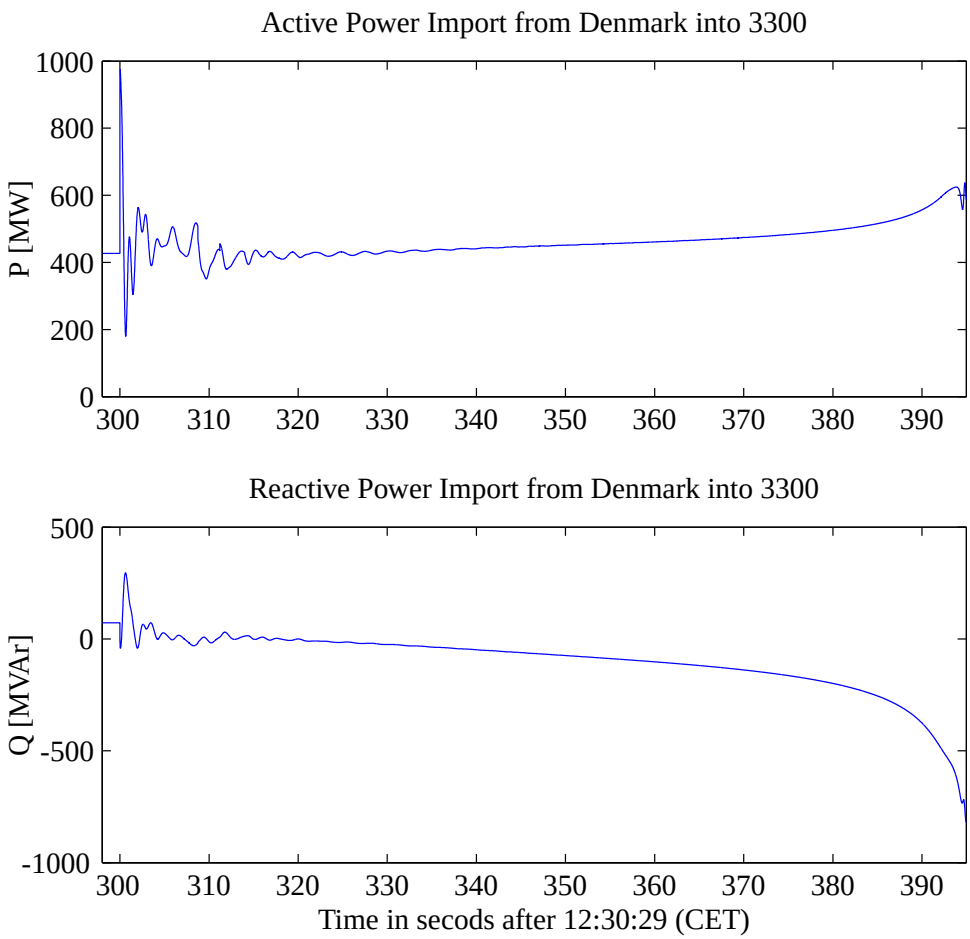

Figure 10.5: Results from the simulation of the blackout on the September 23rd 2003. The plots show the imported active and reactive power from E-Denmark to bus 3300, which corresponds to Söderåsen.

The simulated increase in reactive power injection to E-Denmark can be explained by that it were the Danish generators that were accelerating away from the remaining system generators. When a generator is loosing it syn-

chronism with remaining system generators and its internal rotor angle is approaching a 180 degree separation from others generators in the system, an increase of lagging armature current is experienced (Matsuki et al. 1992). The increase of the current flowing in the armature windings causes an increased reactive power demand by the generator which might explain the increase in reactive power import to E-Denmark during the last 10-15 seconds in the simulation results.

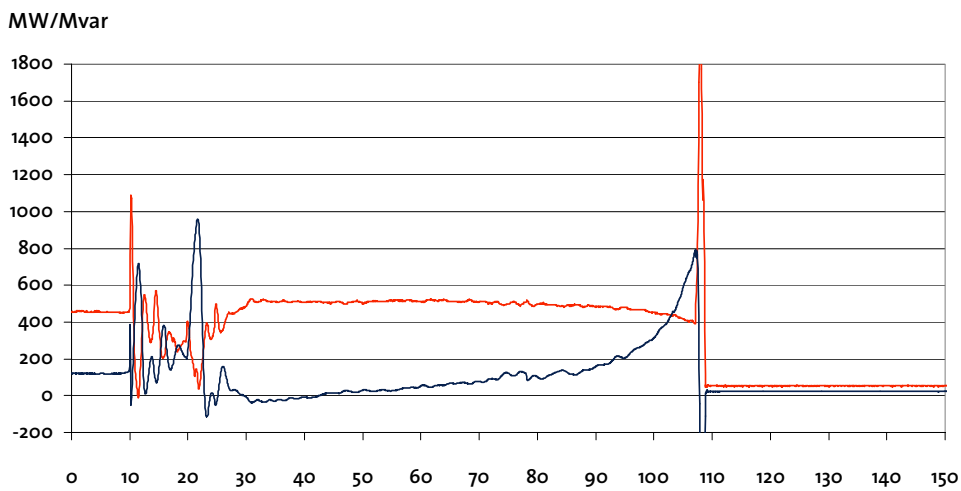

Figure 10.6: Measured values of imported active and reactive power from E-Denmark to Söderåsen, during and after the fault in Horred. The plot is taken from the official report from the Danish TSOs concerning the blackout (Elkraft System 2003, p.10). The red line represents delivered active power while the blue lines represents delivered reactive power.

It turned out to be difficult to imitate the actual development of the Blackout using the simplified model of the Scandinavian system. The greatest problem was the flow direction of the reactive power between E-Denmark and S-Sweden. A more detailed representation of the Swedish system is needed in order to accurately capture the resulting instability mechanism causing the blackout.

Even though it was not possible to simulate the blackout as it was seen from the Danish power system, it was possible to simulate a blackout that matched quite well with the actual measurements of system frequency from the time of the blackout. The simulation results will in the next section, be used to test the developed assessment method.

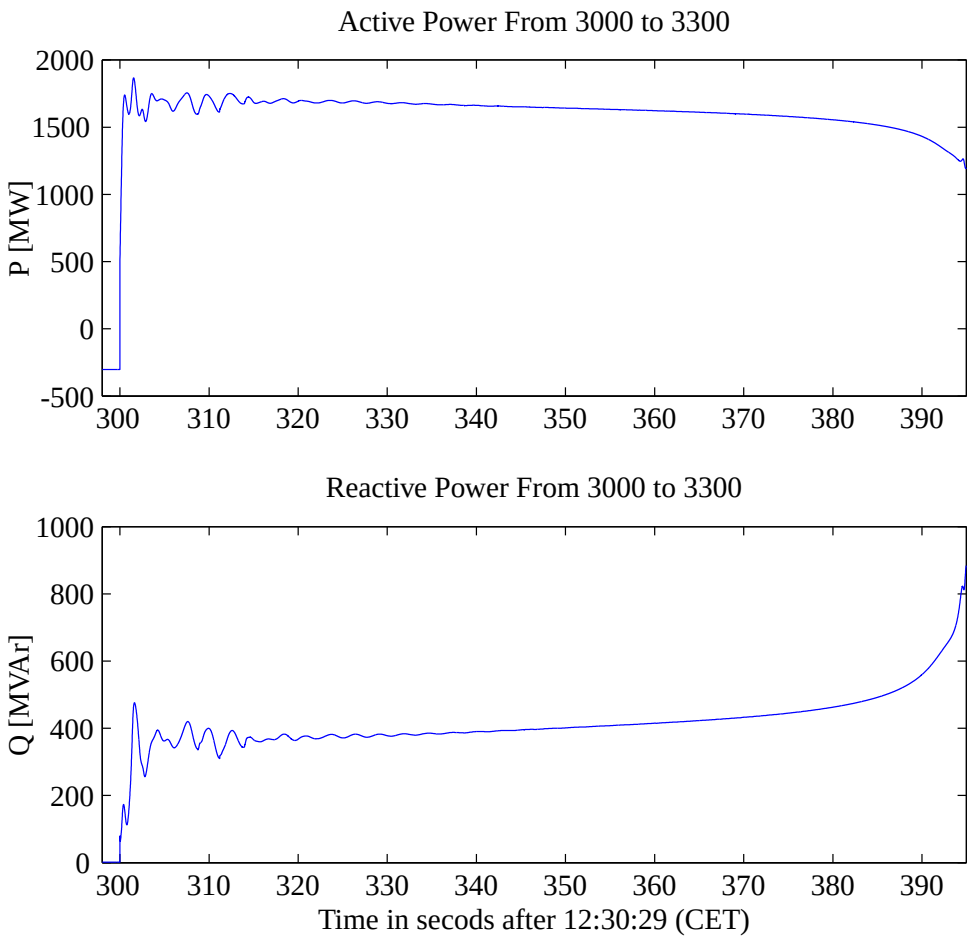

Figure 10.7: Simulation results for the active and reactive power flow from bus 3000 into bus 3300. These results are similar to the actual power flow from Denmark to Sweden under the development of the blackout, where a large increase in imported reactive power into the area is observed.

10.3 Test of the Method

The simulated blackout scenario was used to generate synthetic PMU measurements, and thereby a sequence of PMU-snapshots could be used as a test data for the developed assessment method. The results from the test of the assessment method are provided in figures 10.8 to 10.10.

Above, in figure 10.8 the simulated voltage magnitude at bus 3300 (S-Sweden)

in the simplified model is provided where five different snapshots are marked from I to V. The operating conditions for each of the snapshots I-V is provided in figure 10.8.(b), and in figures 10.9 and 10.10. The point of detected boundary crossover is represented by snapshot III and there elapsed approximately 54 s before a rapid decline in the voltage could be observed (snapshot V).

The plot (b) in figure 10.8 shows the system conditions at snapshot I, prior to the fault in Horred. The generators operating conditions are shown in the normalized injection impedance plane, as described in chapter 7. Two different shapes are used to represent the operating conditions, where the green circle represents a machine with a point of constant voltage magnitude behind X_d (manually excited) and the brown box shows where the operating point of a machine equipped with an AVR would be when an OXL has been activated. The squared points provide a security information, since they indicate where the operating point would be when a given machine protection has been activated. The operating point closest to the stability boundary has an active power margin of 2.5% when calculated according to (7.5).

The situation, when the most severe oscillations have decayed out following the disturbance in Horred, is shown by snapshot II in figure 10.9. The prefault situation is shown light dots and light gray lines link the new operating point to the prefault operating point. The margin of the most critical operating point is 0.3%. System has not yet settled to a stationary operating point, and therefore the operating points closest to the margin continue to slowly drift towards the boundaries.

Approximately 18 s later, the first machine crosses the stability boundaries. This situation is represented by snapshot III and is illustrated below in figure 10.9. The machine that crossed the boundaries is a 74 MVA machine in the Danish system. After the boundary crossover, other generators in the Danish part of the system slowly began to move towards the boundaries.

Approximately 27 s after the detected boundary crossover, a 310 MVA machine crossed the boundaries as shown by snapshot IV. The crossover of the second machine resulted in a more rapid movement of the operating points for the Danish generators towards the boundaries, which eventually resulted in a fast decline in the system bus voltages and a subsequent blackout.

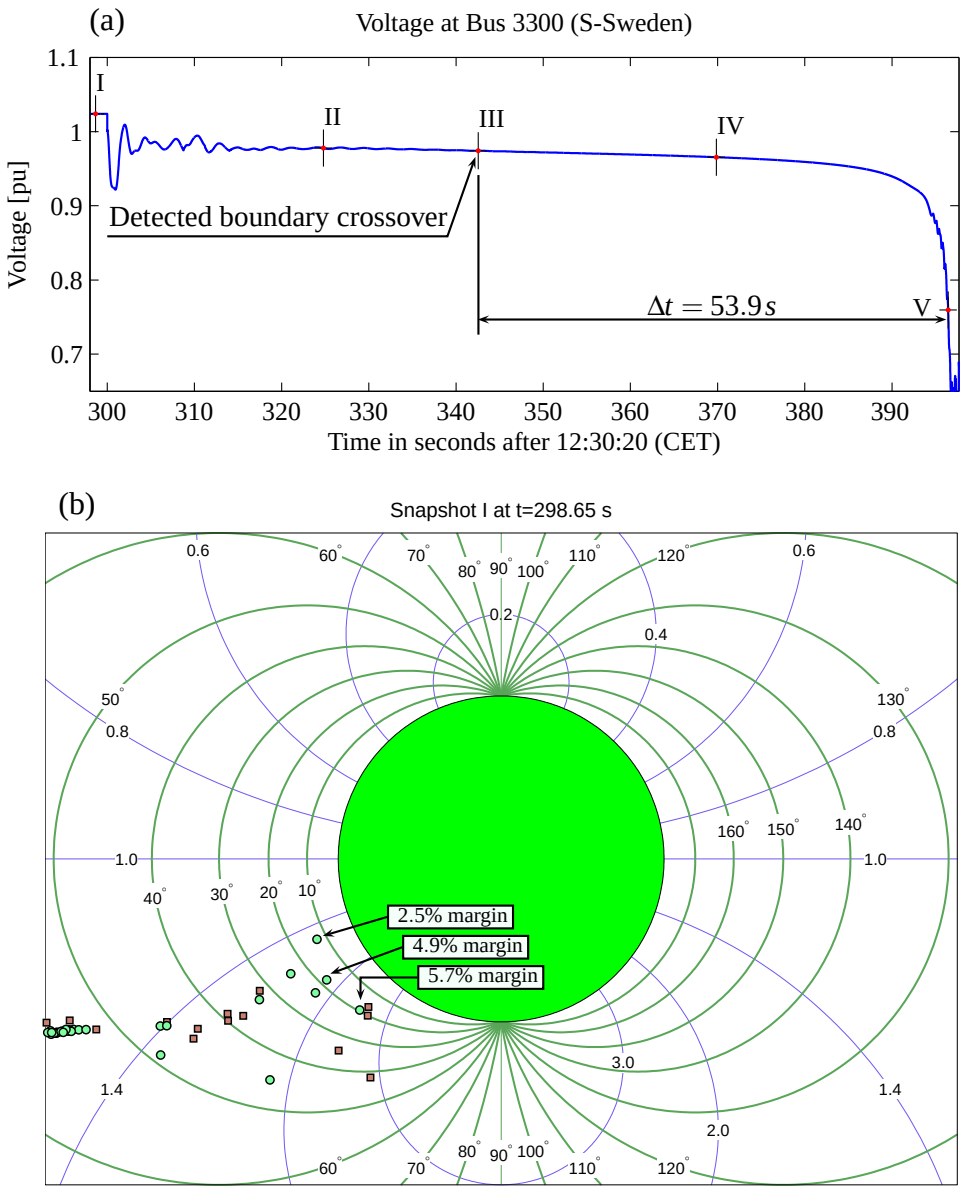

Figure 10.8: (a) plot of simulated voltage magnitude at bus 3300 (S-Sweden) for the period from before the double busbar fault in Horred and until the occurrence of the blackout. Five instances I-V are marked, which correspond to five snapshots provided in (b) and in figures 10.9 and 10.10. (b) is an assessment snapshot corresponding to point I, where the most critical point has an active power margin of 2.5%.

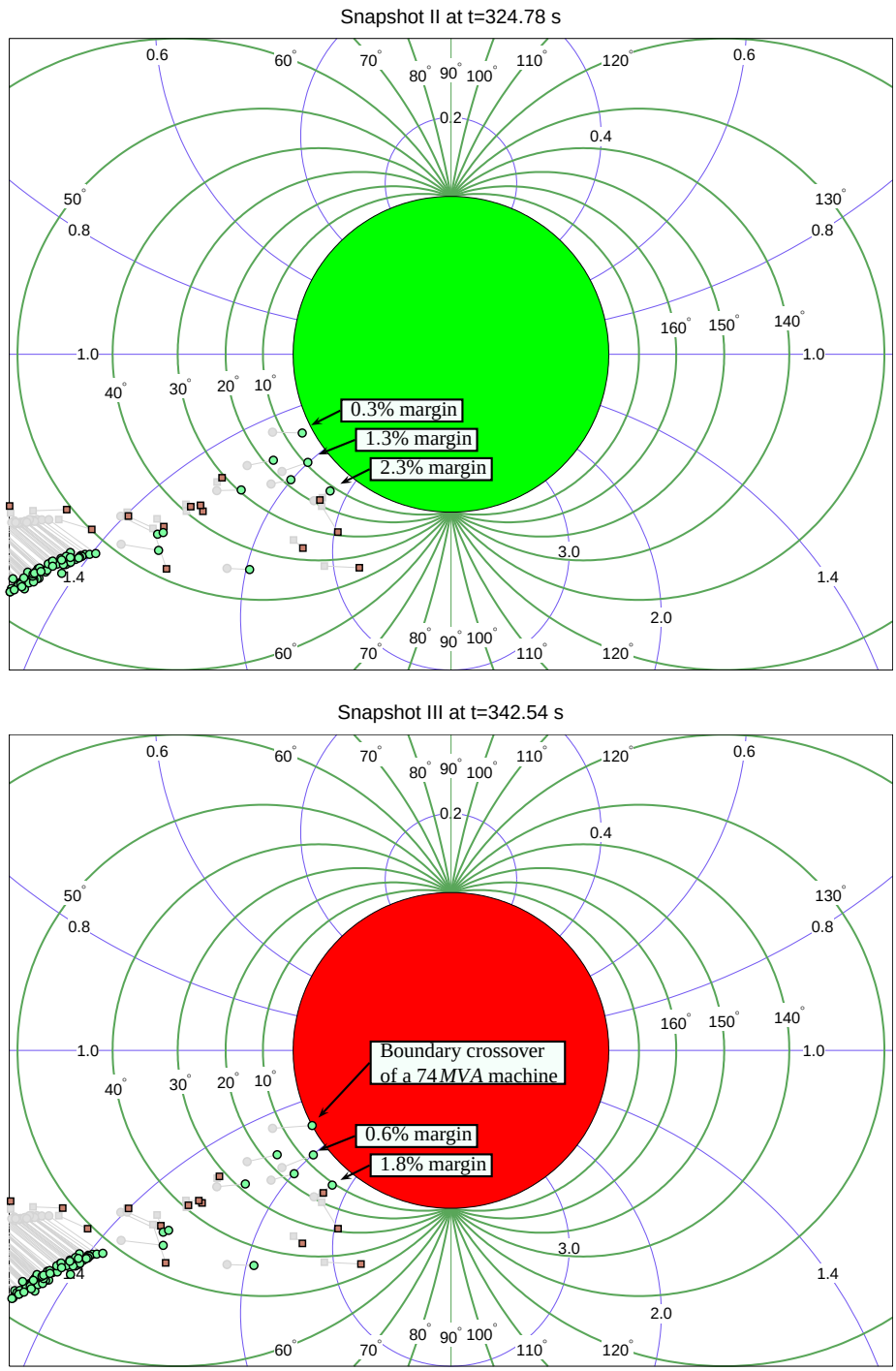

Figure 10.9: Assessment snapshots corresponding to point II (above) and III (below). Snapshot III shows when the first machine crossed the boundaries.

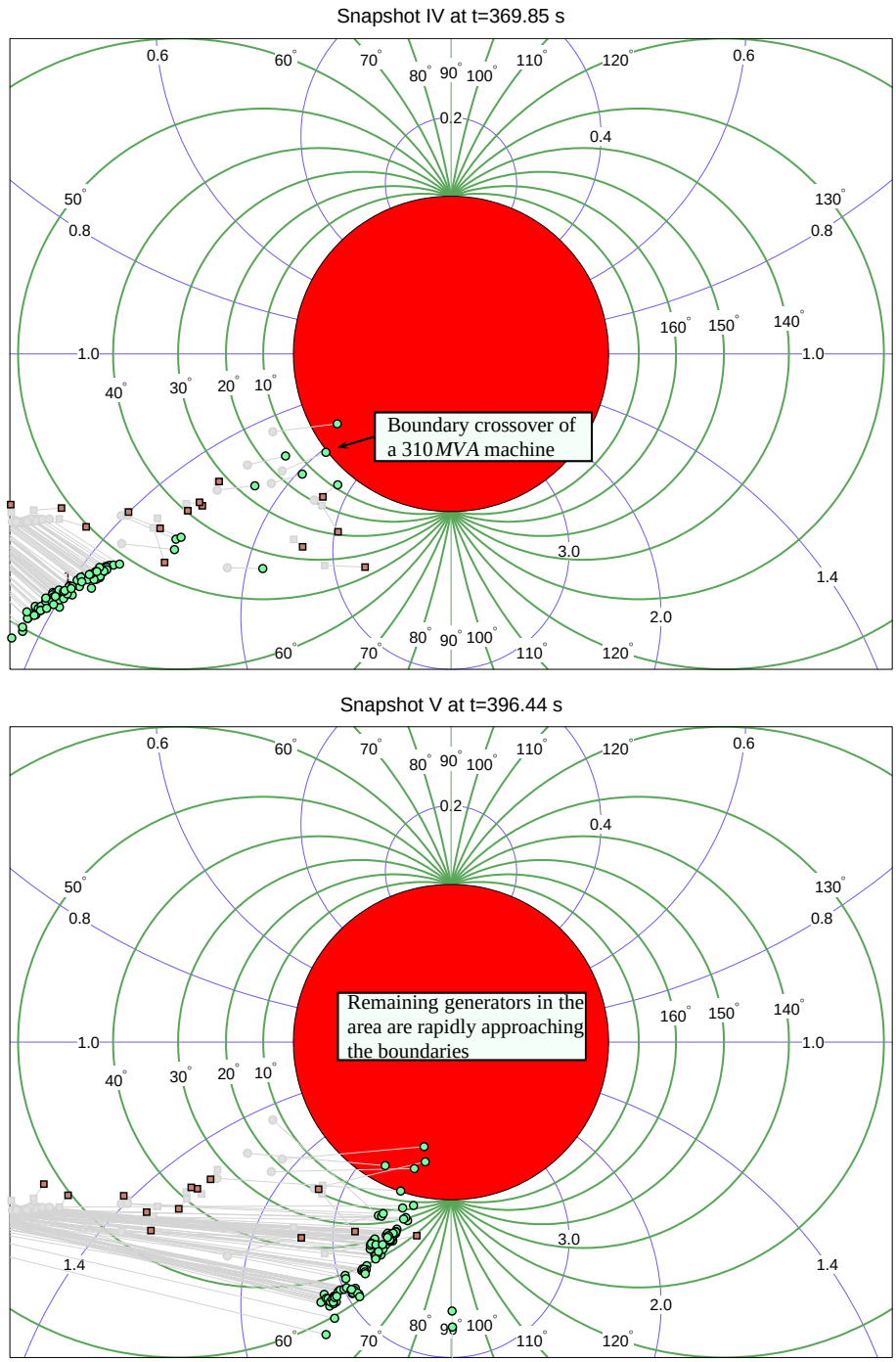

Figure 10.10: Snapshots IV and V represent an unstable situation. Snapshot V represents the condition approximately 54 s after the detected boundary crossover.

10.3.1 Discussion

The results from the test showed that the method was capable of detecting when the system machines crossed boundaries of aperiodic small signal stability. When the first machine crossed the boundary, the remaining machines in the Danish part of the system slowly began to move towards their boundaries. This process gradually continued until the second machine crossed its boundaries, which further deteriorated the situation and lead to a cascade of generators crossing their boundaries and consequently a blackout.

The time from, when the first machine crossed the critical operational boundaries until the simulated blackout occurred, was approximately $54s$. This means, that the system operators would have had a quite significant time window to take appropriate emergency actions for the purpose of avoiding the emerging blackout.

An even earlier warning for the emerging system blackout, could have been obtained if some minimum security margins would have been applied. Such security margin could be used to indicate the operator about a potential stability problem, when a given machine operating point exceeds the security boundaries. In this way, the operators are informed about which machines are the most critical ones and their distance to stability boundaries is obtained as well.

A further extension of the method would be to use the time information of previous operating points to predict future boundary crossover. In this way, a slowly drifting operating point could be identified as a potential threat, some time before an actual boundary crossover.

Part V

Conclusion and Perspective

Chapter 11

Conclusion and Future Outlook

In this chapter, a conclusion of the thesis is provided together with a discussion on future outlook for research based on the contributions from the project.

11.1 Conclusion

The overall purpose of the PhD project was to develop methods that in real-time provide an early warning for an emerging stability problem. The 2003 blackout in E-Denmark and S-Sweden was considered a case scenario of inspiration for the work. The blackout was caused by occurrence of two severe system disturbances within a time interval of five minutes. Following the second disturbance where initial oscillations had damped out, a period of approximately $80\,s$ with slowly decaying voltage magnitude was observed, before a system blackout was experienced. It was of interest to develop methods, that could in such situations give an early warning for the emerging blackout.

For achieving the project's overall purpose, several goals where defined that included derivation of stability boundaries, development of instability detection method and development of an algorithm for carrying out the stability assessment.

For the purpose of understanding the limitations imposed on the injection of power into transmission systems, analytical expressions were derived for the appearance of critical system boundaries and characteristic lines in the injection impedance plane. Boundaries described by the conditions where $\partial P/\partial V$, $\partial Q/\partial V$, $\partial P/\partial Q$, $\partial V/\partial Q$, $\partial V/\partial P$ and $\partial Q/\partial P$ become zero, were derived in terms of injection impedance. Analytical expressions for lines constant voltage magnitude, constant voltage phase angle, constant active power injection and reactive power injection were as well derived in the injection impedance plane.

The derived boundary where $\partial P/\partial Q = 0$ was used as a cornerstone for the development of a method for real-time assessment of aperiodic small signal

stability. The developed method carries out an element-wise assessment of aperiodic small signal stability where the stability of each system generator is determined from the knowledge of its injection impedance and the corresponding Thevenin system impedance seen from the generator. A test on a simple system illustrated that the method is capable of accurately detecting when a given machine crosses the boundaries for aperiodic small signal stability.

For an informative visualization of multiple operating points, a mapping of an arbitrary operating point was determined such that the stability boundary for the mapped point appeared as a unit circle in the normalized injection impedance plane. Furthermore, the mapping was derived in such a way that actual values of constant voltage ratio V/E and constant phase angle margin $\Delta\delta$ were represented in the normalized plane. This enabled an informative visualization of multiple operating points in the same plane where all points have the same unit circle as their stability boundaries.

In order to implement the developed assessment method, a fast algorithm was developed that determines the information required for carrying out the assessment from a PMU-snapshot of the system conditions. The algorithm was implemented in the test-bench software that was written for the purpose of testing the method. The algorithm was tested on a system containing 488 nodes and 672 branches and 144 generators. The aperiodic small signal stability of all 144 generators was determined in $7.86\,ms$.

A large scale test of the assessment method was carried out where a simulation of the blackout in E-Denmark and S-Sweden September 23, 2003 was used as a test case scenario. The simulation results were used to generate a synthetic PMU-snapshots of the system conditions which were used as an input to the assessment algorithm. The test results showed that the loss of aperiodic small signal stability of one machine was detected approximately $54\,s$ before the system blackout was experienced.

The test results show for the simulated case scenario that an aperiodic small signal instability was detected well before the actual blackout occurred. The detection of a boundary crossover could therefore be used as an early warning for an emerging blackout. An even earlier warning is received if a minimum margin to the stability boundary is used as a criteria. An early warning criteria which defines a minimum active power margin to be 2%, would

have resulted in an early warning immediately after the initial oscillations had decayed out in the simulated case scenario. The presented method could therefore be of high importance in emergency situations, where some system generators are prone to the loss of aperiodic small signal stability.

For methods that should provide an assessment of the system conditions during emergency operating conditions, it is of paramount importance that the computational times required for carrying out the assessment are short. The presented method fulfils these requirements, and in fact it is possible carry out the assessment of the 144 generators in the considered 488 node system in only $7.86\,ms$. This means that a full exploitation of the high repetition rate for PMU-measurements could be achieved. These results make the presented assessment method an attractive tool for real-time stability assessment in future emergency situations.

11.2 Future Outlook

By considering the contributions this project, several research topics can be identified which are based on, or even continue, the work carried out in the project. The identified future research topics related to the presented work are listed below:

- Further work on the stability assessment method
- Representation of Asynchronous Machines
- Security assessment of aperiodic small signal stability
- Improvements of the assessment algorithm computational time
- Visualizing other characteristic lines in the normalized impedance plane
- Utilizing Early Warning for Early Prevention of System Blackouts

Each of the above listed points will be elaborated in the following.

Further work on the stability assessment method

The time synchronized PMU-snapshot provide an information regarding the systems time domain trajectory. It could be useful to extend the current assessment method such that previously observed system conditions could be used to predict future system states. In this way, it becomes possible to

identify a critical operating point that is slowly moving towards the stability boundary before it crosses the boundary. Furthermore, an estimation of when the boundary is crossed could be obtained which provides an increased time window for system operators to apply appropriate countermeasures. It could as well be useful to express the margins to the stability boundaries in terms of system load increase. This requires a study of how the machines' stability boundaries and their injection impedances are affected by changes in system consumption. A margin expressed in terms of system loading level might have a greater practical value for the system operators than a margin for the rotor angle expressed in degrees.

Representation of Asynchronous Machines

With an increased utilization of wind energy in electric power systems, the share of power generations from asynchronous generators is increasing. Asynchronous generators are as well prone to stability problems when their mechanical input power is greater than the maximum amount of power that can be injected into the system at the point of their connection.

If the power from a asynchronous machine is injected into a system node of constant steady state voltage magnitude (voltage controlled node), the presented assessment method can be used to determine the boundaries of maximum injectable power. If, on the other hand, the power is not injected into a node of constant voltage, the power injection from the asynchronous machine must be represented in such a way that an assessment of its operating condition can be carried out.

Security Assessment of Aperiodic Small Signal Stability

A fast security assessment could be carried out by using the presented assessment method together with a method that can quickly determine the steady state post-fault conditions following a given contingency. In this way, a $N-1$ contingency study of aperiodic small signal stability could be carried out. This requires though that a method for fast determination of the $N-1$ steady state conditions is developed.

Improvements of the Assessment Algorithm Computational Time

A work can be carried out for improving the computational efficiency of the presented algorithm. By stopping the LU-factorization process when nodes of constant voltage magnitude are to be processed can results in a significant reduction of the number of fill-ins generated and hence a reduced

computational burden. Further reductions in computational burden could be obtained, if ordering algorithms are developed that reorder the rows and columns of $\mathbf{Y}_{link}^{T}$ and $\mathbf{Y}_{link}$ respectively for improving the efficiency.

Visualizing Other Characteristic Lines in the Normalized Impedance Plane

It was shown how the mapping of operating points into a normalized injection impedance plane could be carried out such that their actual values constant voltage ratio V/E and constant phase angle margin $\Delta\delta$ were represented in the normalized plane. For advancing the visualization of multiple operating points several other mappings of system characteristic could be of interest. The operating points could be mapped such that the values of two variables out of P, Q, V or $\Delta\delta$ is preserved after the mapping.

Utilizing Early Warning for Early Prevention of System Blackouts

The next natural step following the development of a method that provides an early warning for an emerging stability problem is to focus the research on methods that can automatically determine appropriate control actions for preventing the occurrence of the problem.

Bibliography

Amestoy, P., Enseeiht-Irit, Davis, T. & Duff, I. (2004), 'Algorithm 837: AMD, an Approximate Minimum Degree Ordering Algorithm', *ACM Transactions on Mathematical Software* **30**(3), 381–388.

Barbier, C. & Barret, J. (1980), 'An Analysis of Phenomena of Voltage Collapse on a Transmission System', *Revue Géneral de l'Electricité* **80**(10).

Breidablik, O., Giaver, F. & Glende, I. (2003), Innovative Measures to Increase the Utilization of Norwegian transmission, *in* 'Power Tech Conference Proceedings, 2003 IEEE Bologna', Vol. 1, p. 8 pp. Vol.1.

Breulmann, H., Grebe, E., Lösing, M. & Energie, R. (2000), 'Analysis and Damping of Inter-Area Oscillations in the UCTE/CENTREL Power System', *CIGRE 2000 Session, Paris, 27th August - 1st September 2000* .

Brucoli, M., Rossi, F., Torelli, F. & Trovato, M. (1985), 'A Generalized Approach to the Analysis of Voltage Stability in Electric Power Systems', *Electric Power Systems Research* **9**(1), 49–62.

Crary, S. (1945), *Power System Stability*, Vol. I, John Wiley & Sons, Inc.

Cutsem, T. & Vournas, C. (1998), *Voltage Stability of Electric Power Systems*, Power Electronics and Power systems Series, Kluwer. ISBN: 0-7923-8139-4.

Davis, T. (2004), 'Algorithm 832: UMFPACK V4.3 - An Unsymmetric-Pattern Multifrontal Method', *ACM Transactions on Mathematical Software* **30**(2), 196–199.

Dobson, I. & Chiang, H. (1989), 'Towards a Theory of Voltage Collapse in Electric Power Systems', *Systems & Control Letters* **13**(3), 253–262.

Dobson, I. & Parashar, M. (2010), A Cutset Area Concept for Phasor Monitoring, *in* '2010 IEEE Power and Energy Society General Meeting, July 2010, Minneapolis, MN USA'.

Dobson, I., Parashar, M. & Carter, C. (2010), Combining Phasor Measurements to Monitor Cutset Angles, *in* '2010 43rd Hawaii International Conference on System Sciences', pp. 1–9.

Elkraft System (2003), Strømafbrydelsen i Østdanmark og Sydsvergie 23. September 2003, Endelig Hændelsesrapport, Technical report, Elkraft System.

Gan, D., Thomas, R. & Zimmerman, R. (2000), 'Stability-Constrained Optimal Power Flow', *IEEE Transactions On Power Systems* **15**(2), 535–540.

George, A. & Liu, J. W. H. (1989), 'The Evolution of the Minimum Degree Ordering Algorithm', *SIAM Review* **31**(1), 1–19.

Glavic, M. & Van Cutsem, T. (2008), Detecting with PMUs the Onset of Voltage Instability Caused by a Large Disturbance, *in* '2008 IEEE Power & Energy Society General Meeting, VOLS 1-11', pp. 4945–4952.

Glavic, M. & Van Cutsem, T. (2009*a*), 'Wide-Area Detection of Voltage Instability From Synchronized Phasor Measurements. Part I: Principle', *IEEE Transactions On Power Systems* **24**(3), 1408–1416.

Glavic, M. & Van Cutsem, T. (2009*b*), 'Wide-Area Detection of Voltage Instability From Synchronized Phasor Measurements. Part II: Simulation Results', *IEEE Transactions On Power Systems* **24**(3), 1417–1425.

Hauer, J., Martin, K. & Lee, H. (2005), Evaluating the Dynamic Performance of Phasor Measurement Units: Experience in the Western Power System, Interim report, Western Electricity Coordinating Council (WECC) - Disturbance Monitoring Work Group.

Hiskens, I. (2001), 'Nonlinear Dynamic Model Evaluation from Disturbance Measurements', *IEEE Transactions on Power Systems* **16**(4), 702–710.

Julian, D., Schulz, R., Vu, K., Quaintance, W., Bhatt, N. & Novosel, D. (2000), Quantifying proximity to voltage collapse using the voltage instability predictor (vip), *in* 'Power Engineering Society Summer Meeting, 2000. IEEE', Vol. 2, IEEE, pp. 931–936.

Kimbark, E. (1956), *Power System Stability, Volume III: Synchronous Machines*, John Wiley & Sons, Inc.

King, I. P. (1970), 'An Automatic Reordering Scheme for Simultaneous Equations Derived from Network Analysis', *International Journal for Numerical Methods in Engineering* **2**(4), 523–533.

Kundur, P. (1994), *Power System Stability and Control*, *New York*, McGraw-Hill. ISBN: 0-07-035958.

Kundur, P., Paserba, J., Ajjarapu, V., Andersson, G., Bose, A., Canizares, C., Hatziargyriou, N., Hill, D., Stankovic, A., Taylor, C. et al. (2004), 'Definition and Classification of Power System Stability', *IEEE Transactions on Power Systems* **19**(3), 1387 – 1401.

Leirbukt, A., Uhlen, K., Palsson, M., Gjerde, J., Vu, K. & Kirkeluten, O. (2005), Voltage Monitoring and Control for Enhanced Utilization of Power Grids, *in* 'IEEE PES Power Systems Conference and Exposition, 2004', pp. 342–347.

Liscouski, B. & Elliot, W. (2004), Final Report on the August 14, 2003 Blackout in the United States and Canada: Causes and Recommendations, Technical report, A report to US Department of Energy.

Liu, J. & Sherman, A. (1975), 'Comparative analysis of the cuthill-mckee and the reverse cuthill-mckee ordering algorithms for sparse matrices', *SIAM Journal of Numerical Analysis* .

Makarov, Y., Lu, S., Guo, X., Gronquist, J., Du, P., Nguyen, T. & Burns, J. (2010), Wide Area Security Region Final Report, Technical report, Pacific Northwest National Laboratory (PNNL), Richland, WA (US).

Mao, A., Yu, J. & Guo, Z. (2005), PMU Placement and Data Processing in WAMS that Complements SCADA, *in* '2005 IEEE Power Engineering Society General Meeting, Vols, 1-3', pp. 780–783.

Martin, K., Hamai, D., Adamiak, M., Anderson, S., Begovic, M., Benmouyal, G., Brunello, G., Burger, J., Cai, J., Dickerson, B. et al. (2008), 'Exploring the IEEE Standard C37. 118–2005 Synchrophasors for Power Systems', *IEEE Transactions on Power Delivery* **23**(4), 1805–1811.

Matsuki, J., Okada, T. & Uenosono, C. (1992), 'Loss of Synchronism Process of a Synchronous Generator Described by its Internal Flux and Force Distributions', *IEEE Transactions on Energy Conversion* **7**(1), 177–182.

Moriso, G., Gao, B. & Kundur, P. (1993), 'Voltage Stability Analysis Using Static And Dynamic Approaches', *IEEE Transactions On Power Systems* **8**(3), 1159–1171.

Naduvathuparambil, B., Valenti, M. & Feliachi, A. (2002), Communication Delays in Wide Area Measurement Systems, *in* 'Proceedings Of The Thirty-Fourth Southeastern Symposium On System Theory', pp. 118–122.

Nagao, T. (1975), 'Voltage Collapse at Load Ends of Power Systems', *Electrical Engineering in Japan* **95**(4), 62–70.

Nguyen, T. & Pai, M. (2003), 'Dynamic Security-Constrained Rescheduling of Power Systems Using Trajectory Sensitivities', *IEEE Transactions on Power Systems* **18**(2), 848–854.

Nuqui, R. (2001), State Estimation and Voltage Security Monitoring using Synchronized Phasor Measurements, PhD thesis, Virginia Polytechnic Institute and State University.

Phadke, A. & de Moraes, R. (2008), 'The Wide World of Wide-Area Measurement', *IEEE Power and Energy Magazine* **6**(5), 52–65.

Phadke, A., Thorp, J. & Adamiak, M. (1983), 'A New Measurement Technique for Tracking Voltage Phasors, Local System Frequency, and Rate of Change of Frequency', *IEEE Transactions on Power Apparatus and Systems* **102**(5), 1025–1038.

Pourbeik, P., Kundur, P. & Taylor, C. (2006), 'The Anatomy of a Power Grid Blackout - Root Causes and Dynamics of Recent Major Blackouts', *Power and Energy Magazine, IEEE* **4**(5), 22–29.

Rehtanz, C. & Pouyan, P. (2006), Wide area monitoring and control for transmission capability enhancement, Technical report, CIGRE-Report, Working Group C4.6.01 on Power System Security Assessment.

Savulescu, S. (2006), *Real-Time Stability in Power Systems: Techniques for Early Detection of The Risk of Blackout*, Springer Verlag. ISBN:0-387-25626-1.

Siek, J., Lee, L. & Lumsdaine, A. (2002), *The Boost Graph Library: User Guide and Reference Manual*, Addison-Wesley Professional. 0-201-72914-8.

Skok, S., Ivankovic, I. & Cerina, Z. (2007), Applications Based on PMU Technology for Improved Power System Utilization, *in* 'Power Engineering Society General Meeting, 2007. IEEE', pp. 1–8.

Steinmetz, C. (1894), Complex Quantities and their Use in Electrical Engineering, *in* 'AIEE Proceedings of the International Electrical Congress, Chicago, USA', pp. 33–74.

Svenska Kraftnät (2003*a*), Elavbrottet 23 September 2003 - Händelser och Åtgärder, Technical Report Nr 1:2003, Svenska Kraftnät.

Svenska Kraftnät (2003*b*), The Blackout in Southern Sweden and Eastern Denmark, 23 September, 2003, Technical report, Svenska Kraftnät.

Taylor, C., Erickson, D., Martin, K., Wilson, R. & Venkatasubramanian, V. (2005), 'WACS-Wide-Area Stability and voltage Control System: R&D and Online Demonstration', *Proceedings of the IEEE* **93**(5), 892–906.

Taylor, C. W. (1994), *Power System Voltage Stability*, McGraw-Hill. ISBN: 0-07-113708-4.

Van Cutsem, T., Jacquemart, Y., Marguet, J. & Pruvot, P. (1995), 'A Comprehensive Analysis of Midterm Voltage Stability', *IEEE Transactions On Power Systems* **10**(3), 1173–1182.

Vandenberghe, F., Grebe, E., Klaar, D., Kleinekorte, K., Rodriguez, J.-M., Erven, H., Laffaye, H., Sabelli, C., Kropec, F., Tillwicks, T., Tassan, L., Callewaert, S., Mandozzi, M., Imhof, K., Janssens, N. & Bronckart, O. (2004), Final Report of the Investigation Committee on the 28 September 2003 Blackout in Italy, Technical report, UCTE.

Venkatasubramanian, V. M., Yue, X., Liu, G., Sherwood, M. & Zhang, Q. (2009), Wide-Area Monitoring and Control Algorithms for Large

Power Systems using Synchrophasors, *in* '2009 IEEE/PES Power Systems Conference And Exposition, Vol 1-3', pp. 821–825.

Voropai, N. & Efimov, D. (2008), Analysis of Blackout Development Mechanisms in Electric Power Systems, *in* 'Power and Energy Society General Meeting-Conversion and Delivery of Electrical Energy in the 21st Century, 2008 IEEE', pp. 1–7.

Weibel, M., Sattinger, W., Rothermann, P., Steinegger, U., Zima, M. & Biedenbach, G. (2006), 'Overhead Line Temperature Monitoring Pilot Project', *CIGRE 2006 Session,Paris, 27th August - 1st September 2006* .

Whaley, R. C., Petitet, A. & Dongarra, J. J. (2001), 'Automated Empirical Optimization of Software and the ATLAS Project', *Parallel Computing* **27**(1–2), 3–35.

Zhao, L. & Abur, A. (2005), 'Multi Area State Estimation Using Synchronized Phasor Measurements', *IEEE Transactions on Power Systems* **20**(2), 611–617.

Appendix A

Derivation of equation 5.1 on page 64

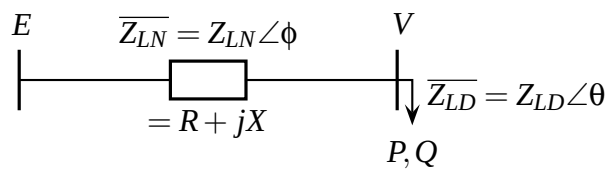

Figure A.1: The simple two bus system and the relevant notations used in the following.

It is desired to derive an expression that describes the relationship between the voltage V, delivered power P and delivered reactive power Q. The line current $\bar{I}$ can expressed as:

$$\bar{I} = \frac{\overline{E}}{\overline{Z}_{LN} + \overline{Z}_{LD}} \tag{A.1}$$

It is convenient to perform the following calculations in terms of the magnitude of the variables rather than using a complex number representation of the variables. When the complex voltage $\overline{E}$ is selected as reference for the system ($\overline{E} = E\angle 0$), the magnitude of the current can be written as:

$$I = \frac{E}{\sqrt{\left(Z_{LN}\cos(\theta) + Z_{LD}\cos(\phi)\right)^2 + \left(Z_{LN}\sin(\theta) + Z_{LD}\sin(\phi)\right)^2}} \tag{A.2}$$

This can also be written in simplified form as (Kundur 1994, p.961):

$$I = \frac{1}{\sqrt{F}}\frac{E}{Z_{LN}} \tag{A.3}$$

Where:

$$F = 1 + \left(\frac{Z_{LD}}{Z_{LN}}\right)^2 + 2\left(\frac{Z_{LD}}{Z_{LN}}\right)\cos(\theta - \phi) \tag{A.4}$$

The magnitude of the voltage V can be expressed as:

$$\begin{aligned} V &= Z_{LD} I \\ &= \frac{1}{\sqrt{F}} \frac{Z_{LD} E}{Z_{LN}} \end{aligned} \tag{A.5}$$

The supplied power to the load can be written as:

$$\begin{aligned} P &= VI\cos\phi \\ &= \frac{Z_{LD}}{F}\left(\frac{E}{Z_{LN}}\right)^2 \cos(\phi) \end{aligned} \tag{A.6}$$

As mentioned above, is it desired to find an expression for the relationship between the voltage V P and Q. For the purpose of doing so, the following expressions become useful:

$$\begin{aligned} \cos(\theta) &= \frac{R}{\sqrt{(R^2+X^2)}}, \qquad \sin(\theta) = \frac{X}{\sqrt{(R^2+X^2)}} \\ \cos(\phi) &= \frac{P}{\sqrt{(P^2+Q^2)}}, \qquad \sin(\phi) = \frac{Q}{\sqrt{(P^2+Q^2)}} \end{aligned} \tag{A.7}$$

By using (A.7), the expression $\cos(\theta - \phi)$ can be written as:

$$\cos(\theta - \phi) = \cos(\theta)\cos(\phi) + \sin(\theta)\sin(\phi) = \frac{RP + XQ}{\sqrt{(R^2+X^2)(P^2+Q^2)}} \tag{A.8}$$

The expression Z_{LD} represents the magnitude of the load impedance, which can be calculated as:

$$Z_{LD} = \frac{V^2}{S} = \frac{V^2}{\sqrt{P^2+Q^2}} \tag{A.9}$$

The expression Z_{LN} represents the magnitude of the line impedance which can be calculated as:

$$Z_{LN} = \sqrt{R^2 + X^2} \tag{A.10}$$

By using the expressions in (A.7),(A.8),(A.9) and (A.10), the expression in (A.6) can be rewritten as:

$$\begin{aligned}
P &= \frac{Z_{LD}}{F}\left(\frac{E}{Z_{LN}}\right)^2 \cos(\phi) \\
&= \frac{V^2 E^2 P}{Z_{LN}^2 (P^2+Q^2) F} \\
&= \frac{V^2 E^2 P}{Z_{LN}^2 (P^2+Q^2)\left(1+\left(\frac{Z_{LD}}{Z_{LN}}\right)^2 + 2\left(\frac{Z_{LD}}{Z_{LN}}\right)\cos(\theta-\phi)\right)} \\
&= \frac{V^2 E^2 P}{Z_{LN}^2 (P^2+Q^2)\left(1+\left(\frac{V^4}{Z_{LN}^2(P^2+Q^2)}\right) + 2\left(\frac{V^2(RP+XQ)}{Z_{LN}(P^2+Q^2)\sqrt{(R^2+X^2)}}\right)\right)} \\
&= \frac{V^2 E^2 P}{V^4 + V^2 2(RP+XQ) + (R^2+X^2)(P^2+Q^2)}
\end{aligned} \tag{A.11}$$

By rearranging (A.11) yields:

$$V^4 + V^2(2(RP+XQ) - E^2) + (R^2+X^2)(P^2+Q^2) = 0 \tag{A.12}$$

which is the same expression as (5.1) on page 64.

Appendix A. Derivation of equation 5.1 on page 64

Appendix B

Citations in the Voltage Collapse Histogram

[1] F. Mercede, J. Chow, H. Yan, and R. Fischl, "A framework to predict voltage collapse in power systems," *IEEE Trans. Power Syst.*, vol. 3, pp. 1807–1813, Nov 1988.

[2] Y. Sekine and H. Ohtsuki, "Cascaded voltage collapse," *IEEE Trans. Power Syst.*, vol. 5, pp. 250–256, Feb 1990.

[3] J. Chow, R. Fischl, and H. Yan, "On the evaluation of voltage collapse criteria," *IEEE Trans. Power Syst.*, vol. 5, pp. 612–620, May 1990.

[4] H. Chiang, I. Dobson, R. Thomas, J. Thorp, and L. Fekihahmed, "On voltage collapse in electric power systems," *IEEE Trans. Power Syst.*, vol. 5, pp. 601–611, May 1990.

[5] C. Demarco and T. Overbye, "An energy based security measure for assessing vulnerability to voltage collapse," *IEEE Trans. Power Syst.*, vol. 5, pp. 419–427, May 1990.

[6] M. Begovic and A. Phadke, "Dynamic simulation of voltage collapse," *IEEE Trans. Power Syst.*, vol. 5, pp. 1529–1534, Nov 1990.

[7] H. Ohtsuki, A. Yokoyama, and Y. Sekine, "Reverse action of on-load tap changer in association with voltage collapse," *IEEE Trans. Power Syst.*, vol. 6, pp. 300–306, Feb 1991.

[8] R. Schlueter, I. Hu, M. Chang, J. Lo, and A. Costi, "Methods for determining proximity to voltage collapse," *IEEE Trans. Power Syst.*, vol. 6, pp. 285–292, Feb 1991.

[9] T. Van Cutsem, "A method to compute reactive power margins with respect to voltage collapse," *IEEE Trans. Power Syst.*, vol. 6, pp. 145–156, Feb 1991.

[10] K. Iba, H. Suzuki, M. Egawa, and T. Watanabe, "Calculation of critical loading condition with nose curve using homotopy continuation method," *IEEE Trans. Power Syst.*, vol. 6, pp. 584–593, May 1991.

[11] T. Overbye and C. Demarco, "Voltage security enhancement using energy based sensitivities," *IEEE Trans. Power Syst.*, vol. 6, pp. 1196–1202, Aug 1991.

[12] F. Alvarado, Y. Hu, D. Ray, R. Stevenson, and E. Cashman, "Engineering foundations for the determination of security costs," *IEEE Trans. Power Syst.*, vol. 6, pp. 1175–1182, Aug 1991.

[13] B. Lee and K. Lee, "A study on voltage collapse mechanism in electric power systems," *IEEE Trans. Power Syst.*, vol. 6, pp. 966–974, Aug 1991.

[14] T. Overbye and C. Demarco, "Improved techniques for power system voltage stability assessment using energy methods," *IEEE Trans. Power Syst.*, vol. 6, pp. 1446–1452, Nov 1991.

[15] V. Ajjarapu and B. Lee, "Bifurcation theory and its application to nonlinear dynamic phenomena in an electrical power system," *IEEE Trans. Power Syst.*, vol. 7, pp. 424–431, Feb 1992.

[16] V. Ajjarapu and C. Christy, "The continuation power flow - a tool for steady-state voltage stability analysis," *IEEE Trans. Power Syst.*, vol. 7, pp. 416–423, Feb 1992.

[17] M. Pal, "Voltage stability conditions considering load characteristics," *IEEE Trans. Power Syst.*, vol. 7, pp. 243–249, Feb 1992.

[18] W. Lachs, D. Sutanto, and L. Coskerie, "Voltage instability in interconnected power systems - a simulation approach," *IEEE Trans. Power Syst.*, vol. 7, pp. 753–761, May 1992.

[19] C. Canizares, F. Alvarado, C. Demarco, I. Dobson, W. Long, M. Pal, and A. Semlyen, "Point of collapse methods applied to ac dc power-systems," *IEEE Trans. Power Syst.*, vol. 7, pp. 673–683, May 1992.

[20] Y. Hong and C. Liu, "A heuristic and algorithmic approach to VAR planning," *IEEE Trans. Power Syst.*, vol. 7, pp. 505–512, May 1992.

[21] F. Galiana, Z. Zeng, and I. Dobson, "Analysis of the load flow behavior near a jacobian singularity," *IEEE Trans. Power Syst.*, vol. 7, pp. 1362–1369, Aug 1992.

[22] I. Hiskens, C. McLean, and M. Pal, "SVC behavior under voltage collapse conditions," *IEEE Trans. Power Syst.*, vol. 7, pp. 1078–1087, Aug 1992.

[23] P. Lof, G. Andersson, and D. Hill, "Voltage stability indexes for stressed power-systems," *IEEE Trans. Power Syst.*, vol. 8, pp. 326–335, Feb 1993.

[24] T. Lie, R. Schlueter, P. Rusche, and R. Rhoades, "Method of identifying weak transmission network stability boundaries," *IEEE Trans. Power Syst.*, vol. 8, pp. 293–301, Feb 1993.

[25] B. Lee and K. Lee, "Dynamic and static voltage stability enhancement of power systems," *IEEE Trans. Power Syst.*, vol. 8, pp. 231–238, Feb 1993.

[26] A. Kurita, H. Okubo, D. Klapper, N. Miller, W. Price, K. Oki, S. Agematsu, J. Sanchezgasca, K. Wirgau, and T. Younkins, "Multiple time-scale power-system dynamic simulation," *IEEE Trans. Power Syst.*, vol. 8, pp. 216–223, Feb 1993.

[27] D. Hill, R. Fischl, M. Pal, W. Xu, Y. Mansour, C. Nwankpa, and L. Xu, "Nonlinear dynamic load models with recovery for voltage stability studies," *IEEE Trans. Power Syst.*, vol. 8, pp. 166–176, Feb 1993.

[28] C. Canizares and F. Alvarado, "Point of collapse and continuation methods for large ac dc systems," *IEEE Trans. Power Syst.*, vol. 8, pp. 1–8, Feb 1993.

[29] Z. Zeng, F. Galiana, B. Ooi, and N. Yorino, "A simplified approach to estimate maximum loading conditions in the load flow problem," *IEEE Trans. Power Syst.*, vol. 8, pp. 646–654, May 1993.

[30] T. Overbye, "Use of energy methods for online assessment of power-system voltage security," *IEEE Trans. Power Syst.*, vol. 8, pp. 452–458, May 1993.

[31] C. Nwankpa and R. Hassan, "A stochastic based voltage collapse indicator," *IEEE Trans. Power Syst.*, vol. 8, pp. 1187–1194, Aug 1993.

[32] N. Miller, R. Daquila, K. Jimma, M. Sheehan, and G. Comegys, "Voltage stability of the Puget Sound system under abnormally cold weather conditions," *IEEE Trans. Power Syst.*, vol. 8, pp. 1133–1142, Aug 1993.

[33] R. Jean-Jumeau and H. Chiang, "Parameterizations of the load-flow equations for eliminating ill-conditioning load flow solutions," *IEEE Trans. Power Syst.*, vol. 8, pp. 1004–1012, Aug 1993.

[34] N. Flatabo, O. Fosso, R. Ognedal, T. Carlsen, and K. Heggland, "A method for calculation of margins to voltage instability applied on the norwegian system for maintaining required security level," *IEEE Trans. Power Syst.*, vol. 8, pp. 920–928, Aug 1993.

[35] I. Dobson and L. Lu, "New methods for computing a closest saddle node bifurcation and worst-case load power margin for voltage collapse," *IEEE Trans. Power Syst.*, vol. 8, pp. 905–913, Aug 1993.

[36] J. Deuse and M. Stubbe, "Dynamic simulation of voltage collapses," *IEEE Trans. Power Syst.*, vol. 8, pp. 894–904, Aug 1993.

[37] J. Chow, Q. Zhu, R. Fischl, and M. Kam, "Design of a decision fusion rule for power-system security assessment," *IEEE Trans. Power Syst.*, vol. 8, pp. 858–864, Aug 1993.

[38] F. Bourgin, G. Testud, B. Heilbronn, and J. Verseille, "Present practices and trends on the french power-system to prevent voltage collapse," *IEEE Trans. Power Syst.*, vol. 8, pp. 778–788, Aug 1993.

[39] H. Chiang, C. Liu, P. Varaiya, F. Wu, and M. Lauby, "Chaos in a simple power-system," *IEEE Trans. Power Syst.*, vol. 8, pp. 1407–1417, NOV 1993.

[40] W. Xu and Y. Mansour, "Voltage stability analysis using generic dynamic load models," *IEEE Trans. Power Syst.*, vol. 9, pp. 479–486, Feb 1994.

[41] T. Tuan, J. Fandino, N. Hadjsaid, J. Sabonnadiere, and H. Vu, "Emergency load shedding to avoid risks of voltage instability using indicators," *IEEE Trans. Power Syst.*, vol. 9, pp. 341–348, Feb 1994.

[42] T. Overbye, I. Dobson, and C. Demarco, "Q-V curve interpretations of energy measures for voltage security," *IEEE Trans. Power Syst.*, vol. 9, pp. 331–337, Feb 1994.

[43] F. Alvarado, I. Dobson, Y. Hu, M. Pai, and N. Pal, "Computation of closest bifurcations in power systems," *IEEE Trans. Power Syst.*, vol. 9, pp. 918–928, May 1994.

[44] V. Ajjarapu, P. Lau, and S. Battula, "An optimal reactive power planning strategy against voltage collapse," *IEEE Trans. Power Syst.*, vol. 9, pp. 906–917, May 1994.

[45] Y. Mansour, W. Xu, F. Alvarado, and C. Rinzn, "SVC placement using critical modes of voltage instability," *IEEE Trans. Power Syst.*, vol. 9, pp. 757–763, May 1994.

[46] T. Overbye, "A power flow measure for unsolvable cases," *IEEE Trans. Power Syst.*, vol. 9, pp. 1359–1365, Aug 1994.

[47] C. Canizares, "On bifurcations, voltage collapse and load modeling," *IEEE Trans. Power Syst.*, vol. 10, pp. 512–522, Feb 1995.

[48] A. Panvini and T. Yohn, "Field assessment of generators reactive capability," *IEEE Trans. Power Syst.*, vol. 10, pp. 288–296, Feb 1995.

[49] T. Overbye, "Computation of a practical method to restore power flow solvability," *IEEE Trans. Power Syst.*, vol. 10, pp. 280–287, Feb 1995.

[50] P. Lof, G. Andersson, and D. Hill, "Voltage dependent reactive power limits for voltage stability studies," *IEEE Trans. Power Syst.*, vol. 10, pp. 220–228, Feb 1995.

[51] M. Begovic and R. Mills, "Load identification and voltage stability monitoring," *IEEE Trans. Power Syst.*, vol. 10, pp. 109–116, Feb 1995.

[52] P. Nedwick, A. Mistr, and E. Croasdale, "Reactive management - a key to survival in the 1990s," *IEEE Trans. Power Syst.*, vol. 10, pp. 1036–1042, May 1995.

[53] J. Lu, C. Liu, and J. Thorp, "New methods for computing a saddle-node bifurcation point for voltage stability analysis," *IEEE Trans. Power Syst.*, vol. 10, pp. 978–985, May 1995.

[54] F. Gubina and B. Strmcnik, "Voltage collapse proximity index determination using voltage phasors approach," *IEEE Trans. Power Syst.*, vol. 10, pp. 788–793, May 1995.

[55] H. Chiang and R. Jean-Jumeau, "A more efficient formulation for computation of the maximum loading points in electric power systems," *IEEE Trans. Power Syst.*, vol. 10, pp. 635–641, May 1995.

[56] T. Vancutsem, "An approach to corrective control of voltage instability using simulation and sensitivity," *IEEE Trans. Power Syst.*, vol. 10, pp. 616–622, May 1995.

[57] H. Chiang and R. Jean-Jumeau, "Toward a practical performance index for predicting voltage collapse in electric-power systems," *IEEE Trans. Power Syst.*, vol. 10, pp. 584–590, May 1995.

[58] T. Lie, "Method of identifying the strategic placement for compensation devices," *IEEE Trans. Power Syst.*, vol. 10, pp. 1448–1453, Aug 1995.

[59] C. Vournas, "Voltage stability and controllability indexes for multimachine power systems," *IEEE Trans. Power Syst.*, vol. 10, pp. 1183–1194, Aug 1995.

[60] T. Vancutsem, Y. Jacquemart, J. Marguet, and P. Pruvot, "A comprehensive analysis of midterm voltage stability," *IEEE Trans. Power Syst.*, vol. 10, pp. 1173–1182, Aug 1995.

[61] J. Barquin, T. Gomez, and F. Pagola, "Estimating the loading limit margin taking into account voltage collapse areas," *IEEE Trans. Power Syst.*, vol. 10, pp. 1952–1962, NOV 1995.

[62] G. Ejebe, G. Irisarri, S. Mokhtari, O. Obadina, P. Ristanovic, and J. Tong, "Methods for contingency screening and ranking for voltage stability analysis of power systems," *IEEE Trans. Power Syst.*, vol. 11, pp. 350–356, Feb 1996.

[63] K. Yabe, J. Koda, K. Yoshida, K. Chiang, P. Khedkar, D. Leonard, and N. Miller, "Conceptual designs of AI-based systems for local prediction of voltage collapse," *IEEE Trans. Power Syst.*, vol. 11, pp. 137–144, Feb 1996.

[64] T. Overbye and R. Klump, "Effective calculation of power system low-voltage solutions," *IEEE Trans. Power Syst.*, vol. 11, pp. 75–80, Feb 1996.

[65] C. Parker, I. Morrison, and D. Sutanto, "Application of an optimisation method for determining the reactive margin from voltage collapse in reactive power planning," *IEEE Trans. Power Syst.*, vol. 11, pp. 1473–1478, Aug 1996.

[66] A. Berizzi, P. Bresesti, P. Marannino, G. Granelli, and M. Montagna, "System-area operating margin assessment and security enhancement against voltage collapse," *IEEE Trans. Power Syst.*, vol. 11, pp. 1451–1459, Aug 1996.

[67] C. Canizares, A. deSouza, and V. Quintana, "Comparison of performance indices for detection of proximity to voltage collapse," *IEEE Trans. Power Syst.*, vol. 11, pp. 1441–1447, Aug 1996.

[68] L. Wang and A. Girgis, "On-line detection of power system small disturbance voltage instability," *IEEE Trans. Power Syst.*, vol. 11, pp. 1304–1311, Aug 1996.

[69] Y. Chen, "Weak bus-oriented optimal multi-objective VAR planning," *IEEE Trans. Power Syst.*, vol. 11, pp. 1885–1890, NOV 1996.

[70] A. Melo, J. Mello, and S. Granville, "The effects of voltage collapse problems in the reliability evaluation of composite systems," *IEEE Trans. Power Syst.*, vol. 12, pp. 480–486, Feb 1997.

[71] N. Yorino, S. Harada, and H. Cheng, "A method to approximate a closest loadability limit using multiple load flow solutions," *IEEE Trans. Power Syst.*, vol. 12, pp. 424–429, Feb 1997.

[72] R. Klump and T. Overbye, "Assessment of transmission system loadability," *IEEE Trans. Power Syst.*, vol. 12, pp. 416–422, Feb 1997.

[73] A. Borghetti, R. Caldon, A. Mari, and C. Nucci, "On dynamic load models for voltage stability studies," *IEEE Trans. Power Syst.*, vol. 12, pp. 293–299, Feb 1997.

[74] S. Greene, I. Dobson, and F. Alvarado, "Sensitivity of the loading margin to voltage collapse with respect, to arbitrary parameters," *IEEE Trans. Power Syst.*, vol. 12, pp. 262–268, Feb 1997.

[75] H. Chiang, C. Wang, and A. Flueck, "Look-ahead voltage and load margin contingency selection functions for large-scale power systems," *IEEE Trans. Power Syst.*, vol. 12, pp. 173–179, Feb 1997.

[76] J. Mello, A. Melo, and S. Granville, "Simultaneous transfer capability assessment by combining interior point methods and Monte Carlo simulation," *IEEE Trans. Power Syst.*, vol. 12, pp. 736–742, May 1997.

[77] A. deSouza, C. Canizares, and V. Quintana, "New techniques to speed up voltage collapse computations using tangent vectors," *IEEE Trans. Power Syst.*, vol. 12, pp. 1380–1387, Aug 1997.

[78] F. Gubina and B. Strmcnik, "A simple approach to voltage stability assessment in radial networks," *IEEE Trans. Power Syst.*, vol. 12, pp. 1121–1126, Aug 1997.

[79] Y. Hong, C. Pan, and W. Lin, "Fast calculation of a voltage stability index of power systems," *IEEE Trans. Power Syst.*, vol. 12, pp. 1555–1560, NOV 1997.

[80] T. Overbye and R. Klump, "Determination of emergency power system voltage control actions," *IEEE Trans. Power Syst.*, vol. 13, pp. 205–210, Feb 1998.

[81] L. Hajagos and B. Danai, "Laboratory measurements and models of modern loads and their effect on voltage stability studies," *IEEE Trans. Power Syst.*, vol. 13, pp. 584–591, May 1998.

[82] A. Berizzi, P. Finazzi, D. Dosi, P. Marannino, and S. Corsi, "First and second order methods for voltage collapse assessment and security enhancement," *IEEE Trans. Power Syst.*, vol. 13, pp. 543–549, May 1998.

[83] C. Liu, C. Chang, and M. Su, "Neuro-fuzzy networks for voltage security monitoring based on synchronized phasor measurements," *IEEE Trans. Power Syst.*, vol. 13, pp. 326–332, May 1998.

[84] R. Rajaraman, F. Alvarado, A. Maniaci, R. Camfield, and S. Jalali, "Determination of location and amount of series compensation to increase power transfer capability," *IEEE Trans. Power Syst.*, vol. 13, pp. 294–300, May 1998.

[85] C. Vournas and G. Manos, "Modelling of stalling motors during voltage stability studies," *IEEE Trans. Power Syst.*, vol. 13, pp. 775–781, Aug 1998.

[86] G. Ejebe, J. Tong, J. Waight, J. Frame, X. Wang, and W. Tinney, "Available transfer capability calculations," *IEEE Trans. Power Syst.*, vol. 13, pp. 1521–1527, NOV 1998.

[87] R. Schlueter, "A voltage stability security assessment method," *IEEE Trans. Power Syst.*, vol. 13, pp. 1423–1438, NOV 1998.

[88] Z. Feng, V. Ajjarapu, and D. Maratukulam, "Practical minimum load shedding strategy to mitigate voltage collapse," *IEEE Trans. Power Syst.*, vol. 13, pp. 1285–1291, NOV 1998.

[89] T. Van Cutsem, C. Moisse, and R. Mailhot, "Determination of secure operating limits with respect to voltage collapse," *IEEE Trans. Power Syst.*, vol. 14, pp. 327–333, Feb 1999.

[90] S. Greene, I. Dobson, and F. Alvarado, "Contingency ranking for voltage collapse via sensitivities from a single nose curve," *IEEE Trans. Power Syst.*, vol. 14, pp. 232–238, Feb 1999.

[91] C. Canizares and Z. Faur, "Analysis of SVC and TCSC Controllers in voltage collapse," *IEEE Trans. Power Syst.*, vol. 14, pp. 158–165, Feb 1999.

[92] S. Johansson, "Mitigation of voltage collapse caused by armature current protection," *IEEE Trans. Power Syst.*, vol. 14, pp. 591–599, May 1999.

[93] J. Momoh, Y. Makarov, and W. Mittelstadt, "A framework of voltage stability assessment in power system reliability analysis," *IEEE Trans. Power Syst.*, vol. 14, pp. 484–491, May 1999.

[94] L. Pereira and D. DeBerry, "The role of less-economic generating units in the open access transmission era," *IEEE Trans. Power Syst.*, vol. 14, pp. 1133–1136, Aug 1999.

[95] K. Vu, M. Begovic, D. Novosel, and M. Saha, "Use of local measurements to estimate voltage-stability margin," *IEEE Trans. Power Syst.*, vol. 14, pp. 1029–1034, Aug 1999.

[96] B. Long and V. Ajjarapu, "The sparse formulation of ISPS and its application to voltage stability margin sensitivity and estimation," *IEEE Trans. Power Syst.*, vol. 14, pp. 944–951, Aug 1999.

[97] C. Rehtanz, "Systemic use of multifunctional SMES in electric power systems," *IEEE Trans. Power Syst.*, vol. 14, pp. 1422–1427, NOV 1999.

[98] L. Vargas, V. Quintana, and R. Miranda, "Voltage collapse scenario in the Chilean interconnected system," *IEEE Trans. Power Syst.*, vol. 14, pp. 1415–1421, NOV 1999.

[99] L. Pereira and D. DeBerry, "Double contingency transmission outages in a generation and reactive power deficient area," *IEEE Trans. Power Syst.*, vol. 15, pp. 416–420, Feb 2000.

[100] Z. Feng, V. Ajjarapu, and B. Long, "Identification of voltage collapse through direct equilibrium tracing," *IEEE Trans. Power Syst.*, vol. 15, pp. 342–349, Feb 2000.

[101] L. Braz, C. Castro, and C. Murari, "A critical evaluation of step size optimization based load flow methods," *IEEE Trans. Power Syst.*, vol. 15, pp. 202–207, Feb 2000.

[102] A. Berizzi, Y. Zeng, P. Marannino, A. Vaccarini, and P. Scarpellini, "A second order method for contingency severity assessment with respect to voltage collapse," *IEEE Trans. Power Syst.*, vol. 15, pp. 81–87, Feb 2000.

[103] B. Venkatesh, G. Sadasivam, and M. Khan, "A new optimal reactive power scheduling method for loss minimization and voltage stability margin maximization using successive multi-objective fuzzy LP technique," *IEEE Trans. Power Syst.*, vol. 15, pp. 844–851, May 2000.

[104] Z. Feng, V. Ajjarapu, and D. Maratukulam, "A comprehensive approach for preventive and corrective control to mitigate voltage collapse," *IEEE Trans. Power Syst.*, vol. 15, pp. 791–797, May 2000.

[105] T. Zhu, S. Tso, and K. Lo, "An investigation into the OLTC effects on voltage collapse," *IEEE Trans. Power Syst.*, vol. 15, pp. 515–521, May 2000.

[106] R. Wang and R. Lasseter, "Re-dispatching generation to increase power system security margin and support low voltage bus," *IEEE Trans. Power Syst.*, vol. 15, pp. 496–501, May 2000.

[107] R. Schlueter, S. Liu, and K. Ben-Kilani, "Justification of the voltage stability security assessment and diagnostic procedure using a bifurcation subsystem method," *IEEE Trans. Power Syst.*, vol. 15, pp. 1105–1111, Aug 2000.

[108] Z. Jia and B. Jeyasurya, "Contingency ranking for on-line voltage stability assessment," *IEEE Trans. Power Syst.*, vol. 15, pp. 1093–1097, Aug 2000.

[109] L. Vargas and C. Canizares, "Time dependence of controls to avoid voltage collapse," *IEEE Trans. Power Syst.*, vol. 15, pp. 1367–1375, NOV 2000.

[110] B. Chowdhury and C. Taylor, "Voltage stability analysis: V-Q power flow simulation versus dynamic simulation," *IEEE Trans. Power Syst.*, vol. 15, pp. 1354–1359, NOV 2000.

[111] A. de Souza, J. de Souza, and A. da Silva, "On-line voltage stability monitoring," *IEEE Trans. Power Syst.*, vol. 15, pp. 1300–1305, NOV 2000.

[112] H. Wan, J. McCalley, and V. Vittal, "Risk based voltage security assessment," *IEEE Trans. Power Syst.*, vol. 15, pp. 1247–1254, Nov 2000.

[113] Q. Wu, D. Popovic, D. Hill, and C. Parker, "Voltage security enhancement via coordinated control," *IEEE Trans. Power Syst.*, vol. 16, pp. 127–135, Feb 2001.

[114] S. Greene, I. Dobson, and F. Alvarado, "Sensitivity of transfer capability margins with a fast formula," *IEEE Trans. Power Syst.*, vol. 17, pp. 34–40, Feb 2002.

[115] A. Flueck, R. Gonella, and J. Dondeti, "A new power sensitivity method of ranking branch outage contingencies for voltage collapse," *IEEE Trans. Power Syst.*, vol. 17, pp. 265–270, May 2002.

[116] B. Lee, H. Song, S. Kwon, G. Jang, J. Kim, and V. Ajjarapu, "A study on determination of interface flow limits in the KEPCO system using modified continuation power flow (MCPF)," *IEEE Trans. Power Syst.*, vol. 17, pp. 557–564, Aug 2002.

[117] M. Ni, J. McCalley, V. Vittal, and T. Tayyib, "Online risk-based security assessment," *IEEE Trans. Power Syst.*, vol. 18, pp. 258–265, Feb 2003.

[118] B. Milosevic and M. Begovic, "Voltage-stability protection and control using a wide-area network of phasor measurements," *IEEE Trans. Power Syst.*, vol. 18, pp. 121–127, Feb 2003.

[119] W. Rosehart, C. Canizares, and V. Quintana, "Effect of detailed power system models in traditional and voltage-stability-constrained optimal power-flow problems," *IEEE Trans. Power Syst.*, vol. 18, pp. 27–35, Feb 2003.

[120] N. Yorino, E. El-Araby, H. Sasaki, and S. Harada, "A new formulation for FACTS allocation for security enhancement against voltage collapse," *IEEE Trans. Power Syst.*, vol. 18, pp. 3–10, Feb 2003.

[121] K. Chen, A. Hussein, M. Bradley, and H. Wan, "A performance-index guided continuation method for fast computation of saddle-node bifurcation in power systems," *IEEE Trans. Power Syst.*, vol. 18, pp. 753–760, May 2003.

[122] M. Pandit, L. Srivastava, and J. Sharma, "Fast voltage contingency selection using fuzzy parallel self-organizing hierarchical neural network," *IEEE Trans. Power Syst.*, vol. 18, pp. 657–664, May 2003.

[123] W. Rosehart, C. Canizares, and V. Quintana, "Multiobjective optimal power flows to evaluate voltage security costs in power networks," *IEEE Trans. Power Syst.*, vol. 18, pp. 578–587, May 2003.

[124] M. Ni, J. McCalley, V. Vittal, S. Greene, C. Ten, V. Ganugula, and T. Tayyib, "Software implementation of online risk-based security assessment," *IEEE Trans. Power Syst.*, vol. 18, pp. 1165–1172, Aug 2003.

[125] C. Aumuller and T. Saha, "Investigating the impact of powerformer on voltage stability by dynamic simulation," *IEEE Trans. Power Syst.*, vol. 18, pp. 1142–1148, Aug 2003.

[126] D. Alves, L. da Silva, C. Castro, and V. da Costa, "Continuation fast decoupled power flow with secant predictor," *IEEE Trans. Power Syst.*, vol. 18, pp. 1078–1085, Aug 2003.

[127] M. Larsson and D. Karlsson, "Coordinated system protection scheme against voltage collapse using heuristic search and predictive control," *IEEE Trans. Power Syst.*, vol. 18, pp. 1001–1006, Aug 2003.

[128] C. Vournas and M. Karystianos, "Load tap changers in emergency and preventive voltage stability control," *IEEE Trans. Power Syst.*, vol. 19, pp. 492–498, Feb 2004.

[129] N. Yorino, H. Li, S. Harada, A. Ohta, and H. Sasaki, "A method of voltage stability evaluation for branch and generator outage contingencies," *IEEE Trans. Power Syst.*, vol. 19, pp. 252–259, Feb 2004.

[130] A. de Souza, L. Honorio, G. Torres, and G. Lambert-Torres, "Increasing the loadability of power systems through optimal-local-control actions," *IEEE Trans. Power Syst.*, vol. 19, pp. 188–194, Feb 2004.

[131] W. Freitas, A. Morelato, and W. Xu, "Improvement of induction generator stability using braking resistors," *IEEE Trans. Power Syst.*, vol. 19, pp. 1247–1249, May 2004.

[132] A. Berizzi, P. Marannino, M. Merlo, M. Pozzi, and F. Zanellini, "Steady-state and dynamic approaches for the evaluation of loadability margins in the presence of secondary voltage regulation," *IEEE Trans. Power Syst.*, vol. 19, pp. 1048–1057, May 2004.

Appendix B. Voltage Collapse Histogram Citations

[133] N. Amjady, "A framework of reliability assessment with consideration effect of transient and voltage stabilities," *IEEE Trans. Power Syst.*, vol. 19, pp. 1005–1014, May 2004.

[134] P. Kundur, J. Paserba, V. Ajjarapu, G. Andersson, A. Bose, C. Canizares, N. Hatziargyriou, D. Hill, A. Stankovic, C. Taylor, T. Van Cutsem, and V. Vittal, "Definition and classification of power system stability," *IEEE Trans. Power Syst.*, vol. 19, pp. 1387–1401, Aug 2004.

[135] F. Dong, B. Chowdhury, M. Crow, and L. Acar, "Improving voltage stability by reactive power reserve management," *IEEE Trans. Power Syst.*, vol. 20, pp. 338–345, Feb 2005.

[136] W. Marszalek and Z. Trzaska, "Singularity-induced bifurcations in electrical power systems," *IEEE Trans. Power Syst.*, vol. 20, pp. 312–320, Feb 2005.

[137] A. Gamm, I. Golub, A. Bachry, and Z. Styczynski, "Solving several problems of power systems using spectral and singular analyses," *IEEE Trans. Power Syst.*, vol. 20, pp. 138–148, Feb 2005.

[138] N. Yorino, H. Li, and H. Sasaki, "A predictor/corrector scheme for obtaining Q-limit points for power flow studies," *IEEE Trans. Power Syst.*, vol. 20, pp. 130–137, Feb 2005.

[139] C. Roman and W. Rosehart, "Complementarity model for generator buses in OPF-based maximum loading problems," *IEEE Trans. Power Syst.*, vol. 20, pp. 514–516, Feb 2005.

[140] N. Amjady and M. Esmaili, "Application of a new sensitivity analysis framework for voltage contingency ranking," *IEEE Trans. Power Syst.*, vol. 20, pp. 973–983, May 2005.

[141] Y. Kataoka and Y. Shinoda, "Voltage stability limit of electric power systems with generator reactive power constraints considered," *IEEE Trans. Power Syst.*, vol. 20, pp. 951–962, May 2005.

[142] A. Esmin, G. Lambert-Torres, and A. de Souza, "A hybrid particle swarm optimization applied to loss power minimization," *IEEE Trans. Power Syst.*, vol. 20, pp. 859–866, May 2005.

[143] M. Gibescu, C. Liu, H. Hashimoto, and H. Taoka, "Energy-based stability margin computation incorporating effects of ULTCs," *IEEE Trans. Power Syst.*, vol. 20, pp. 843–851, May 2005.

[144] W. Freltas, L. Da Silva, and A. Morelato, "Small-disturbance voltage stability of distribution systems with induction generators," *IEEE Trans. Power Syst.*, vol. 20, pp. 1653–1654, Aug 2005.

[145] R. Guedes, L. Alberto, and N. Bretas, "Power system low-voltage solutions using an auxiliary gradient system for voltage collapse purposes," *IEEE Trans. Power Syst.*, vol. 20, pp. 1528–1537, Aug 2005.

[146] L. Zarate, C. Castro, J. Ramos, and E. Ramos, "Fast computation of voltage stability security margins using nonlinear programming techniques," *IEEE Trans. Power Syst.*, vol. 21, pp. 19–27, Feb 2006.

[147] A. Sode-Yome, N. Mithulananthan, and K. Lee, "A maximum loading margin method for static voltage stability in power systems," *IEEE Trans. Power Syst.*, vol. 21, pp. 799–808, May 2006.

[148] J. A. Ramirez and J. L. Murillo-Perez, "Steady-state voltage stability with StatCom," *IEEE Trans. Power Syst.*, vol. 21, pp. 1453–1454, Aug 2006.

[149] C. D. Vournas, V. C. Nikolaidis, and A. A. Tassoulis, "Postmortem analysis and data validation in the wake of the 2004 Athens blackout," *IEEE Trans. Power Syst.*, vol. 21, pp. 1331–1339, Aug 2006.

[150] E. A. Leonidaki, D. P. Georgiadis, and N. D. Hatziargyriou, "Decision trees for determination of optimal location and rate of series compensation to increase power system loading margin," *IEEE Trans. Power Syst.*, vol. 21, pp. 1303–1310, Aug 2006.

[151] F. W. Mohn and A. C. Z. de Souza, "Tracing PV and QV curves with the help of a CRIC continuation method," *IEEE Trans. Power Syst.*, vol. 21, pp. 1115–1122, Aug 2006.

[152] D. Yang and V. Ajjarapu, "Critical eigenvalues tracing for power system analysis via continuation of invariant subspaces and projected Arnoldi method," *IEEE Trans. Power Syst.*, vol. 22, pp. 324–332, Feb 2007.

[153] J.-R. Shin, B.-S. Kim, J.-B. Park, and K. Y. Lee, "A new optimal routing algorithm for loss minimization and voltage stability improvement in radial power systems," *IEEE Trans. Power Syst.*, vol. 22, pp. 648–657, May 2007.

[154] S. R. Torres, W. H. Peralta, and C. A. Castro, "Power system loading margin estimation using a neuro-fuzzy approach," *IEEE Trans. Power Syst.*, vol. 22, pp. 1955–1964, Nov 2007.

[155] I. El-Samahy, K. Bhattacharya, C. Canizares, M. F. Anjos, and J. Pan, "A procurement market model for reactive power services considering system security," *IEEE Trans. Power Syst.*, vol. 23, pp. 137–149, Feb 2008.

[156] V. C. Nikolaidis and C. D. Vournas, "Design strategies for load-shedding schemes against voltage collapse in the Hellenic System," *IEEE Trans. Power Syst.*, vol. 23, pp. 582–591, May 2008.

[157] V. Donde, V. Lopez, B. Lesieutre, A. Pinar, C. Yang, and J. Meza, "Severe multiple contingency screening in electric power systems," *IEEE Trans. Power Syst.*, vol. 23, pp. 406–417, May 2008.

[158] C. D. Vournas and T. Van Cutsem, "Local identification of voltage emergency situations," *IEEE Trans. Power Syst.*, vol. 23, pp. 1239–1248, Aug 2008.

[159] S. M. Halpin, K. A. Harley, R. A. Jones, and L. Y. Taylor, "Slope-permissive under-voltage load shed relay for delayed voltage recovery mitigation," *IEEE Trans. Power Syst.*, vol. 23, pp. 1211–1216, Aug 2008.

[160] S. M. Halpin, R. A. Jones, and L. Y. Taylor, "The MVA-Volt index: A screening tool for predicting fault-induced low voltage problems on bulk transmission systems," *IEEE Trans. Power Syst.*, vol. 23, pp. 1205–1210, Aug 2008.

[161] J. Hazra and A. K. Sinha, "Identification of Catastrophic Failures in Power System Using Pattern Recognition and Fuzzy Estimation," *IEEE Trans. Power Syst.*, vol. 24, pp. 378–387, Feb 2009.

[162] H. Liu, L. Jin, J. D. McCalley, R. Kumar, V. Ajjarapu, and N. Elia, "Planning Reconfigurable Reactive Control for Voltage Stability Limited Power Systems," *IEEE Trans. Power Syst.*, vol. 24, pp. 1029–1038, May 2009.

[163] E. Haesen, C. Bastiaensen, J. Driesen, and R. Belmans, "A Probabilistic Formulation of Load Margins in Power Systems With Stochastic Generation," *IEEE Trans. Power Syst.*, vol. 24, pp. 951–958, May 2009.

[164] R. Diao, K. Sun, V. Vittal, R. J. O'Keefe, M. R. Richardson, N. Bhatt, D. Stradford, and S. K. Sarawgi, "Decision Tree-Based Online Voltage Security Assessment Using PMU Measurements," *IEEE Trans. Power Syst.*, vol. 24, pp. 832–839, May 2009.

[165] F. Capitanescu, T. Van Cutsem, and L. Wehenkel, "Coupling Optimization and Dynamic Simulation for Preventive-Corrective Control of Voltage Instability," *IEEE Trans. Power Syst.*, vol. 24, pp. 796–805, May 2009.

[166] M. Glavic and T. Van Cutsem, "Wide-Area Detection of Voltage Instability From Synchronized Phasor Measurements. Part I: Principle," *IEEE Trans. Power Syst.*, vol. 24, pp. 1408–1416, Aug 2009.

Appendix B. Voltage Collapse Histogram Citations

www.elektro.dtu.dk

Centre for Electric Technology (CET)
Department of Electrical Engineering
Technical University of Denmark
Elektrovej 325
2800 Kgs. Lyngby, Denmark
Tel: (+45) 45 25 35 00
Fax: (+45) 45 88 61 11
E-mail: cet@elektro.dtu.dk

ISBN: 978-87-92465-95-5